

JUN 03 1986

AUG 05 1986

NASA
Technical
Paper
2491

C2
March 1986

**Mach 6 Flow Field Surveys
Beneath the Forebody of
an Airbreathing Missile**

**Patrick J. Johnston
and James L. Hunt**

PROPERTY OF U.S. AIR FORCE
AEDC TECHNICAL LIBRARY

**TECHNICAL REPORTS
FILE COPY**

NASA

**NASA
Technical
Paper
2491**

1986

**Mach 6 Flow Field Surveys
Beneath the Forebody of
an Airbreathing Missile**

**Patrick J. Johnston
and James L. Hunt**

*Langley Research Center
Hampton, Virginia*



National Aeronautics
and Space Administration

**Scientific and Technical
Information Branch**

SUMMARY

Wall static, local stream static, and pitot pressure surveys were made on the windward side of a hypersonic airbreathing missile at Mach 6 at full-scale length Reynolds numbers. The model was preheated to near adiabatic wall temperature to minimize the effect of heat transfer on boundary layer characteristics.

In the inviscid part of the flow field, the experimental mass flow ratios agreed with trends predicted by a three-dimensional method-of-characteristics solution. At the forward survey station, experimental bow shock locations were closer to the body surface than had been predicted, but this is thought to be the result of the blunt nose tip required for the theoretical solution.

The results showed that the boundary layer was transitional or turbulent at zero angle of attack and laminar at angles of attack of 4° and 8° at a longitudinal station 3.5 diameters downstream of the nose. The boundary layer, which had a bell-shaped thickness distribution across the body, affected the mass flow distribution out to the bow shock and decreased the mass flow available to the engine inlet.

Even though the tests were performed at full-scale Mach and Reynolds numbers, factors such as the wind tunnel wall boundary layer noise, the difference in wall temperature ratios between the test and flight hardware, and the blunt nose of the full-scale vehicle versus the sharp model nose could alter the transition location at full scale relative to that occurring in the tests. A delay in boundary layer transition could cause transition to occur aft of the inlet compression ramp and thus subject the inlet flow to boundary layer separation or other adverse effects.

INTRODUCTION

For the past several years, experimental and analytical studies of scramjet-powered hypersonic missiles have been conducted at the NASA Langley Research Center (refs. 1 and 2). One of the more attractive concepts evolving from these studies was a two-stage long-range surface-to-air vehicle designed to cruise at Mach 6. As envisioned in these studies, the second stage of this missile would incorporate a dual-mode scramjet engine that would be attached to the fuselage undersurface to take advantage of forebody precompression. This precompression increases the mass flow captured by the inlet, thereby reducing the engine size and especially its weight relative to that required by an inlet operating in the free stream. Studies such as those of reference 3 have shown that reduced engine weight and good inlet performance are critical factors in achieving the long ranges desired.

For aft-mounted lower-surface inlets such as those postulated for use on these vehicles, it was assumed that the inlet would ingest not only the nonuniform forebody inviscid flow but also an as-yet-undefined boundary layer on the vehicle forebody. This assumption was based on the premise that the inviscid inlet design contours could be altered in an appropriate way to take into account the forebody boundary layer displacement thickness. Advocates of this approach, which probably

stems from the inlet concept proposed for the Langley scramjet engine module (ref. 4), point out that boundary layer diverters cause unnecessary drag and aggravate aerodynamic heating problems at hypersonic speeds and that the ramjet or scramjet is much more tolerant of nonuniform flow than, for example, a turbojet.

Before the inlet design and performance can be evaluated, in even a preliminary way, the characteristics of the flow ahead of the inlet must be known or assumed. For preliminary inlet sizing and engine performance calculations, it is usually assumed that the flow can be described by an average of the flow conditions between the shock and the body surface on an equivalent tangent cone. Unfortunately, however, flow distortions caused by streamwise and lateral body curvature, for instance, can make such assumptions uncertain at best.

A much better insight into the character of the flow can be gained by computational fluid dynamic methods, and a number of computer codes are emerging to calculate both the inviscid and viscous flows about arbitrary bodies. However, these programs are large and highly specialized, and are only now becoming available for engineering design purposes. It is frequently desirable to calibrate these codes by a comparison of their outputs with experimental data, which at hypersonic speeds are extremely sparse. In view of these circumstances, the present investigation was undertaken to experimentally survey the flow field beneath the forebody of a representative hypersonic airbreathing missile configuration and to present the data with sufficient accuracy to make them useful in testing and calibrating recently developed flow prediction computer codes.

The data obtained in this investigation consist of wall static as well as pitot and static pressure surveys at two stations beneath the fuselage of a 0.15-scale missile model at Mach 6 and angles of attack from 0° to 8° . Most of the data were obtained at 8° because it is near the cruise angle of attack for maximum trimmed lift-to-drag ratio.

The experiments were conducted in the Langley 20-Inch Mach 6 Tunnel at a length Reynolds number of 8.9×10^6 . These conditions match flight conditions at 96 000 ft, which is near the optimum cruise altitude.

SYMBOLS

D	body diameter (2.121 in.)
M	Mach number
\dot{m}	mass flow per unit area
N	panel index
p	static pressure, psia
p_t	total pressure, psia
p'_t	pitot pressure, psia
u	velocity in boundary layer

X,Y,Z model ordinates (see fig. 1(b))

x longitudinal distance from nose, in.

y spanwise distance from model centerline, in.

z distance from model surface perpendicular to free stream direction, in.

α angle of attack, deg

γ ratio of specific heats

Subscripts:

l body length (21.0 in.)

l local

w wall

δ boundary layer thickness

∞ free stream

APPARATUS AND TESTS

A photograph of the complete 0.15-scale missile model is shown in figure 1(a) and a sketch of the forebody showing the survey stations and locations of the wall static orifices is shown in figure 1(b). A photograph of the sting-supported forebody model mounted in the inverted position in the Langley 20-Inch Mach 6 Tunnel is shown in figure 2. Ordinates for the body are given in table I for a full-scale vehicle length of 140 in. A three-degree-of-freedom electrically driven survey mechanism attached to the tunnel ceiling and equipped with independent three-axis digital position readouts was used to mount the survey rakes.

Pitot pressures were measured by a five-tube horizontal rake with 0.25-in. spacing, which was situated so that the end tube was in the vertical plane of the body centerline. The rake probes consisted of 0.030-in. (outside diameter) stainless-steel tubing that was flattened to an average height of 0.024 in. to obtain better resolution in the boundary layer.

Static pressures in the flow field were measured in separate tests by a two-tube rake with a spacing of 0.50 in. and a 0.06-in-diameter probe. Between tests, this rake was moved laterally in 0.25-in. increments to provide the same spanwise coverage as the pitot rake. In this way, the static pressures 0.50 in. off the model centerline vertical plane were recorded twice to provide a check on the accuracy, repeatability, and calibration of the static probes. As discussed in reference 5, accurate probe measurements of static pressure in supersonic streams are not straightforward and the problem is accentuated at hypersonic speeds because of the increased thickness of the probe boundary layer. Appendix A contains a further discussion of the static pressure measurements for these tests and the method used to calibrate the probes.

One side of the model was equipped with four surface static pressure orifices (fig. 1) located 0.25-in. apart at the first survey station. Pressure tubing was laid in milled slots in the surface. These slots were then filled with high-temperature plastic and orifices were drilled into the tubing.

Prior to each test, the model was preheated to near adiabatic wall temperature (as determined by a thermocouple) by passing low-pressure air (50 psia) at approximately 400°F through the test section with the model in place. The model was then retracted and the tunnel flow established with a downstream ejector as a vacuum source. When the desired nominal stagnation conditions of 265 psia and 400°F were achieved, the model was injected into the stream and the survey probe was brought into electrical contact with the model surface. This procedure established a datum for the probe z position. During the tests, the probes were intermittently driven away from the body surface and the pressures and vertical position were recorded on magnetic tape.

It should be emphasized that the static pressure survey z locations were not necessarily at the same values as the pitot surveys; therefore, to obtain both pitot and static pressure values at a given z , faired values of static pressure were used. This approach was taken because the variation of static pressure from the body surface to the shock was more gradual than that of pitot pressure, and this interpolation was therefore easier and more accurate.

The z location of the bow shock was determined by the rapid drop in pitot pressure as opposed to the more gradual changes in pressure indicated by the static probes. The shock position indicated by the static pressure probes did not always coincide with that indicated by the pitot probes because of slight misalignments and a less rigid probe design for the static probes. A distance of about 33 probe diameters was allowed before the tubes were structurally supported in order to minimize possible pressure feedback.

During the tests, a single pitot tube was mounted 7.6 in. off the tunnel floor to measure free-stream pitot pressure (fig. 2), from which Mach number, stream static pressure, and other parameters could be calculated.

The survey data were normalized by measured stagnation pressure or calculated stream static pressure at each sample station to account for any change in stream conditions caused by tunnel throat expansion during the test.

All the pitot and static pressures were measured by diaphragm transducers with automatic range detection features. The ranges were from 0 to 1, 3, 10, 30, 100, 300, and 1000 mm of mercury. Tunnel stagnation pressure and temperature were measured by a diaphragm gauge and an iron-constantan thermocouple, respectively.

Table II provides a summary of the kinds of data obtained in this investigation

THEORETICAL METHODS

Flow characteristics at the wall and downstream of the bow shock were calculated by tangent cone (ref. 6) and tangent wedge (ref. 7) methods. Parameters in the flow field were also calculated by the three-dimensional method-of-characteristics (MOC) code of reference 8. This computer program cannot handle body

cross sections with sharp corners; therefore, the right-angle intersection of the lower surface and the body sides was replaced (using trial and error methods) by a 6.47:1 ellipse. A comparison of the theoretical and experimental body cross-section shapes is shown in figure 3.

The MOC solution requires that the body have a small spherical nose cap. This nose tip, which has a diameter of about 3 percent of the body diameter, produced entropy gradients normal to the surface which persisted well beyond the last body station surveyed experimentally. In the comparisons to follow, this entropy layer is shown along with extrapolations to the wall which attempt to eliminate the mass flow defect caused by this inviscid phenomenon. In general, the thickness of the entropy gradient did not exceed about 10 percent of the body diameter, which amounts to about 10 to 15 percent of the shock layer thickness.

It is appropriate to note here that a successful computer MOC solution could not be achieved on this particular body at $\alpha = 0^\circ$ and that the data for this angle of attack were obtained by extrapolations from successful solutions at $\alpha = 1.5^\circ$, 2° , 4° , and 8° .

PRESENTATION OF DATA

Typical data from mass flow surveys across the shock layer at the forward fuselage survey station ($x/D = 3.5$) and the aft survey station ($x/D = 5.4$) are shown in figures 4 and 5, respectively. Data, of which these are representative, were integrated for various spanwise stations across the semispan to determine the contours of cumulative mass flow ratios shown in figure 6 for the forward survey station ($x/D = 3.5$) and figure 7 for the aft survey station ($x/D = 5.4$).

Body centerline vertical-plane pitot pressure surveys in the boundary layer are shown in figures 8 and 9 for the forward and aft fuselage survey stations, respectively. The spanwise variation of fuselage boundary layer depth is shown in figures 10 and 11. The effect of angle of attack on the body centerline vertical-plane boundary layer and its displacement thickness is shown in figure 12. Similar results are shown in figure 13 for the average boundary layer thickness across the body.

Body centerline vertical-plane boundary layer velocity profiles at the forward station are shown in figure 14 and similar data are given in figure 15 for the aft station. Representative surface oil flow patterns are shown in figure 16.

Appendix B presents wall static pressure measurements, and appendix C contains comparisons of theoretical and experimental bow shock locations, detailed flow field pitot and static pressure results, and local Mach numbers and mass flow ratios.

DISCUSSION

Mass Flow Distributions

Figures 4 and 5 show representative mass flow ratio distributions across the shock layer on the body centerline vertical plane at the two longitudinal survey stations. At the forward survey station (fig. 4), the experimental mass flows

exceed the predicted values over most of the depth of the shock layer and may be associated with the displacement effect of the boundary layer near the vehicle nose. It may be noted in this figure that there is a 50-percent increase in mass flow from the edge of the boundary layer out to the shock. This large gradient is not predicted by tangent cone methods, but the average mass flow ratio is predicted reasonably well.

The entropy defect, which is reflected by the decrease in mass flow adjacent to the wall predicted by the inviscid three-dimensional MOC theory, is illustrated in figure 4. Also shown is the extrapolation to the wall which attempts to eliminate this defect in subsequent integrations to obtain realistic inviscid cumulative mass flow ratios.

A representative mass flow distribution across the shock layer at the aft survey station is shown in figure 5. At this fuselage station, the gradient from the body to the shock is much smaller than at the forward station and the agreement between theory and experiment is better. At this station, it was coincidental that the depth of the inviscid theoretical momentum defect was approximately the same as the boundary layer thickness.

Shock Shapes and Mass Flow Contours

Figures 6 and 7 illustrate the experimental and theoretical shock locations and cumulative mass flow contours across the body semispan at the forward and aft survey stations.

When the probe was passed across the bow shock there was an abrupt decrease in pitot pressure, but a certain amount of interpolation was necessary to define the shock position because of the finite number of vertical sampling locations at the five spanwise stations. At the forward station (fig. 6) the experimental bow shock was always inside the predicted location, but this difference decreased with increasing angle of attack. The predicted shock standoff was greater than the experiment standoff, and this difference was probably caused by the 3-percent nose bluntness required for the MOC theory. The better agreement at $\alpha = 8^\circ$ indicates that this bluntness effect was subordinated at higher angles of attack. As a matter of interest, the quasi-two-dimensional engine originally envisioned for this configuration (ref. 1) had inlet side plates that extended to $z/D = 0.382$; if the inlet were situated at the forward survey station there might be an impingement problem at angles of attack greater than 8° .

At the aft survey station (fig. 7) the shock standoff was much greater than at the forward station, and the agreement between theory and experiment was better.

Figures 6 and 7 show contours of cumulative mass flow across the body semispan at the forward and aft survey stations, respectively. The fairings, especially the slopes at $y/D = 0$, were based on flow field symmetry considerations. In general, the agreement between theory and experiment improved with increasing angle of attack because the boundary layer was much thinner and its associated displacement effects less at higher angles of attack. As will be shown subsequently, the boundary layer tends to accumulate on the vehicle centerline vertical plane, and this thickening causes bell-shaped distributions of the mass flow contours (i.e., a decrease of cumulative mass flow on the body plane of symmetry). This distribution persists from the body out to the bow shock.

At the forward station (fig. 6) at a constant value of z/D , the mass flow is predicted to increase toward the edge of the body, and this theoretical trend is verified by the experimental data.

One would surmise that a two-dimensional engine of the height mentioned earlier (i.e., $z/D = 0.382$) would, at full capture, swallow a mass flow ratio of unity. Visual inspection of the curves in figure 6(a) shows that for such an inlet height, the mass flow captured would be only about 0.9 stream mass flow. To achieve a mass capture of 1.0 at this angle of attack, the inlet (and probably the engine weight) would have to be considerably larger, with an area approximately equal to that under the curve with the triangle symbols.

At the aft fuselage station (fig. 7), no surveys were taken at $\alpha = 0^\circ$ and only pitot surveys were made at $\alpha = 4^\circ$; thus, no mass flow results are available at these angles of attack. MOC results at $\alpha = 4^\circ$ are shown in figure 7(a) along with shock shapes determined experimentally from pitot pressure surveys. The spanwise gradients in mass flow were much smaller here than at the forward station.

At an angle of attack of 8° (fig. 7(b)) the experimental mass flow contours have the same bell-shaped characteristic noted earlier at the forward survey station. At a fixed value of z/D the theoretical contours of figure 7 shows that the mass flow ratio diminishes toward the edge of the body. This trend reflects the fact that the flow is spilling around the sharp edges of the body. There appears to be better agreement between theory and experiment at this aft fuselage station, especially over the outer portions of the body.

The results in figures 6 and 7 show that at a fixed value of z/D , there is a considerable reduction in mass flow between the forward and aft survey stations. This reduction is probably related to the amount of spilloff around the edge of the body's flat lower surface. Such a reduction in mass flow would not, of course, be anticipated from Newtonian impact concepts because the lower surface of the body is flat. The axial defect in mass flow is another factor to be considered in selecting the inlet location for a bottom-mounted engine.

One of the outstanding advantages claimed for bottom-mounted engines on hypersonic vehicles is the increase in local mass flow with angle of attack. This is generally referred to as precompression. An insight into the magnitude of these benefits of precompression can be gained from figure 6. Compare the area under the cumulative mass flow ratio curve with a value of 1.0 at $\alpha = 0^\circ$ (fig. 6(a)) with that under the same curve at $\alpha = 8^\circ$ (fig. 6(c)). This area ratio, 11.1, represents the amount of precompression produced at $\alpha = 8^\circ$.

Boundary Layer Results

At the outset, it should be noted that precise definitions of the height of the fuselage boundary layer were more difficult to make on this body than on a flat plate or other simple shape having negligible streamwise or transverse pressure gradients. This situation is illustrated in figures 8 and 9, which show the body centerline vertical-plane pitot pressure surveys adjacent to the model surface on an expanded vertical scale. In some instances, the pitot pressures in the boundary layer faired so smoothly to those in the inviscid flow that it was quite difficult to determine the boundary layer edge. Examples of this problem are shown in figure 8 at $\alpha = 0^\circ$ and figure 9 at $\alpha = 8^\circ$.

In contrast to the foregoing examples, the $\alpha = 4^\circ$ and 8° surveys at the forward survey station exhibited an overshoot in pitot pressure which increased with angle of attack. Here, the vertical location of the maximum value of this overshoot was taken as the edge of the boundary layer, as indicated by the horizontal lines on either side of the curves in figure 8. These pitot pressures were used to define the edge Mach number and velocity ratio profiles which follow. As may be seen by the pitot pressure profiles presented in appendix C, the overshoot illustrated in figure 8 was characteristic of the data, especially toward the edge of the body at $\alpha = 0^\circ$ and at all spanwise locations at $\alpha = 4^\circ$ and 8° . The magnitude of the overshoot approached 15 to 30 percent of the local inviscid pitot pressure. According to reference 9, this overshoot is a probe diameter to boundary layer height ratio effect, and of course would be most evident at condition where the boundary layer height is relatively small (for example, at positive angles of attack or near the edge of the body).

Spanwise boundary layer distribution.- The variation in height of the boundary layer across the semispan is shown in figure 10 for the forward survey station and in figure 11 for the aft station. At both stations, it is apparent that the boundary layer has a bell-shaped distribution across the body and that the centerline thickness at $\alpha = 8^\circ$ has approximately tripled in the nearly two body diameters of length between the two survey stations.

As noted previously, considerable difficulty was experienced in accurately defining the edge of the boundary layer from pitot pressure profiles at certain combinations of angle of attack and lateral tube location. This difficulty resulted in considerable scatter in the boundary layer height distribution across the body, as illustrated by the results at the outboard stations in figure 11. There are a variety of reasons for this scatter, the most obvious being large outflows toward the edge of the body which thinned the boundary layer and may have affected the pitot pressure sensed by the probes. (Examples of the outflow will be shown in a subsequent figure.)

References 10 and 11 showed that accumulation of the boundary layer on the centerline was characteristic of flat-bottomed bodies at hypersonic speeds and that a moderate amount of lateral curvature could remedy the situation. However, additional systematic experimental research will be required to identify the geometric parameters which control the phenomenon.

To provide a frame of reference regarding the relative sizes of the boundary layer and the inlet, the capture area outline of a quasi-two-dimensional inlet, suggested in reference 2, is shown in figures 10 and 11. Note that in figure 10 at $\alpha = 0^\circ$, the centerline boundary layer depth is nearly 30 percent of the inlet height.

Longitudinal boundary layer distribution.- Figure 12 shows the variation of the centerline vertical-plane boundary layer and displacement thickness with angle of attack for the two survey stations. At $\alpha = 4^\circ$ and 8° , the total boundary layer thickness at the aft station increased by factors of 2 and 3.2, respectively, over those at the forward station, and the displacement thickness was actually less than at the forward station. This reduction in displacement thickness is attributed to mass depletion in the boundary layer caused by spilloff at the edge of the body. In fact, the displacement thickness at the aft station was only about half that

of a $1/11$ -power profile (ref. 12). As will be shown subsequently, this profile describes the velocity profile at this station reasonably well.

The spanwise boundary layer profiles of figures 10 and 11 were integrated to determine the average height across the body, and these results are shown in figure 13. For reference, the height of the quasi-two-dimensional inlet was $0.382D$. Thus, at the forward station, the average boundary layer height varied from about 15 percent of the inlet height at $\alpha = 0^\circ$ to about 6.5 percent of the inlet height at $\alpha = 8^\circ$. At the aft station, however, the average boundary layer height was essentially constant at 21 percent of the quasi-two-dimensional inlet height.

Boundary layer velocity profiles.- Body centerline vertical-plane velocity profiles at the forward survey station are shown in figure 14. At $\alpha = 0^\circ$, the experimental profile is near that of $1/5$ -power profile, and therefore indicates that the flow is transitional or turbulent. At $\alpha = 4^\circ$ and 8° , however, the profiles are essentially linear and are characteristic of a laminar boundary layer on an adiabatic surface at hypersonic Mach numbers (ref. 13). On the basis of the data shown in figure 14, transition occurred at or ahead of the first survey station at $\alpha = 0^\circ$ and moved aft at positive angles of attack. This trend is in agreement with the transition movement data on an insulated-wall 5° half-angle cone reported in reference 14, although the data from that study are limited to Mach numbers less than 4.63. This movement of transition with angle of attack is the opposite of that found on two-dimensional or planar bodies, as reported, for example, in reference 15.

That transition occurred near the forward body survey station at $\alpha = 0^\circ$ was substantiated by the results of reference 16, which used the preferred nonintrusive method (phase change paint) to detect the location of transition on power law bodies at $\alpha = 0^\circ$ at Mach 6 in the same wind tunnel. At the unit Reynolds number of the present tests, the cone and higher power law body (Exponent = 0.75) had boundary layer transition locations very near that for the forward survey station on the present missile body at $\alpha = 0^\circ$. The extreme sensitivity of transition location to body shape and nose bluntness at the Reynolds numbers of interest here is indicated by the fact that transition moved from a location at about half the body length for the cone to completely off the body base on the parabolic (Exponent = 0.50) body in the tests of reference 16.

Experimental boundary layer profiles for the aft survey station are presented in figure 15, which shows the data compared with $1/7$ - and $1/11$ -power profiles. The similarity of experimental profiles with the $1/11$ -power profile indicates that the flow is turbulent. The higher than theoretical velocity ratios shown in figure 15 are probably attributable to distortions caused by edge bleedoff at this aft station on the body.

Additional evidence that boundary layer transition occurred between the two survey stations is provided by the lower surface oil flow patterns in figure 16. In each photograph, the wider spanwise strips indicate the longitudinal survey stations and the narrow line is a nose-fuselage parting line. Of particular interest is figure 16(b) at $\alpha = 4^\circ$, which shows an elliptical zone centered on the body meridian in which the random oil dots either did not move or moved only slightly relative to the large smearing that occurred at the more outboard stations. During

these tests, the oil pattern was observed by closed-circuit television of the side of the model. At $\alpha = 4^\circ$ the model was retracted before too much smearing destroyed the oil pattern, as was the case at $\alpha = 8^\circ$.

Another interesting pattern at $\alpha = 4^\circ$ was the large outflow, approximately 43° , at the edges of the body. Although these oil patterns reflect what is occurring deep in the boundary layer adjacent to the surface, large outflows mean that inlets with sidewalls similar to those postulated for this configuration will have large flow turning angles and strong shocks emanating from the inlet sidewall leading edges. In fact, the flows may be near shock detachment even at a free-stream Mach number of 6. This situation suggests that the width of the engine be restricted to much less than the body width to avoid large flow deflections.

The photograph of the oil pattern about the complete configuration (fig. 16(d)) at $\alpha = 4^\circ$ shows a zone of separation just ahead of the 6° inlet compression ramp and a multitude of vortices on both the ramp and the cowl exterior for this unstarted condition.

Evidence (e.g., ref. 17) now suggests that boundary layer transition data obtained in conventional wind tunnels at supersonic speeds may be suspect because of facility-generated disturbances that destabilize the laminar boundary layer. For this and other reasons, relating the present transition results to flight, even at the same Reynolds number, is somewhat speculative. For example, nose bluntness is known to delay the onset of transition. The present model has a "sharp" nose, but a flight article would, for thermal protection considerations, require a moderate amount of nose bluntness. The model surfaces are relatively smooth, whereas the flight article would have manufacturing imperfections such as gaps, fasteners, joints, and other irregularities. At hypersonic speeds the boundary layer becomes more difficult to trip (ref. 18), and these discontinuities may not be sufficient to promote turbulence. The model was deliberately raised to adiabatic wall temperatures, whereas a flight vehicle would have heat transfer into the wall, which will alter the energy balance in the boundary layer. Thus, considering all these factors, there is a good possibility that in flight the inlet would have to ingest a laminar boundary layer at cruise conditions.

CONCLUSIONS

A flow field survey was made beneath the forebody of a hypersonic airbreathing missile at Mach 6. The results, in the form of pitot and static pressure distributions across the shock layer, were used to determine local mass flow ratios, and these were compared with available theoretical results. This study yielded the following conclusions:

1. In the inviscid flow field, the three-dimensional inviscid method-of-characteristics (MOC) theory can be relied upon to yield good indications of the local mass flow profiles and shock layer thickness. The predictions, especially where transverse gradients normal to the body were large, were superior to average mass flows predicted by tangent cone methods.

2. As a result of overexpansion, the mass flow ratio in the shock layer at zero angle of attack was below 1.0 over most of the flow field. Significant increases in mass flow were produced as the angle of attack increased.

3. The boundary layer significantly perturbed the flow beneath the body by accumulating in the centerline vertical plane. The effect of this thickening persisted out to the bow shock.

4. At zero angle of attack, the boundary layer was transitional or turbulent at an axial station about 3.5 diameters aft of the nose but was laminar at this station as the angle of attack increased. This aftward movement of transition with angle of attack agrees with previous results obtained on a 5° cone at lower Mach numbers but is opposite to that measured on planar bodies.

5. Based on the current state of the art regarding the location of boundary layer transition, there is a good possibility that in flight the transition region could occur well aft on the vehicle. Conflicting effects such as nose bluntness, which delays transition, and surface roughness, which tends to promote transition, make it impossible to determine whether, in fact, the inlet will have to contend with ingesting a more easily separated laminar boundary layer.

NASA Langley Research Center
Hampton, VA 23665-5225
July 25, 1985

TABLE I.- BODY ORDINATES FOR FULL-SCALE VEHICLE LENGTH OF 140 INCHES

x = 0		
N	y	z
1	0	-1.6770
2		
3		
4		
5		
6		
7		
8		
9		
10		
11		
12		
13		
14		
15		
16		
17		
18		
19		
20		
21		
22		
23		
24		
25		
26		
27		
28		
29		
30		
31		
32		
33		
34		
35		
36		
37		

x = 6		
N	y	z
1	0	0.5631
2	.1590	.5611
3	.3168	.5427
4	.4731	.5147
5	.6261	.4713
6	.7728	.4107
7	.9171	.3437
8	1.0504	.2580
9	1.1801	.1658
10	1.2992	.0615
11	1.4094	-.0532
12	1.5099	-.1755
13	1.5940	-.3106
14	1.6781	-.4456
15	1.7446	-.5889
16	1.7960	-.7395
17	1.8474	-.8900
18	1.8730	-1.0463
19	1.8903	-1.2044
20	1.9076	-1.3625
21	1.9076	-1.3625
22	1.9076	-1.3625
23	1.8746	-1.6899
24	1.7903	-2.0080
25	1.6484	-2.3053
26	1.4559	-2.5729
27	1.2196	-2.8025
28	.9427	-2.9807
29	.6440	-3.1152
30	.3277	-3.2018
31	0	-3.2380
32		
33		
34		
35		
36		
37		

x = 10		
N	y	z
1	0	1.9678
2	.2588	1.9640
3	.5163	1.9471
4	.7714	1.9056
5	1.0214	1.8384
6	1.2607	1.7410
7	1.4964	1.6338
8	1.7129	1.4932
9	1.9241	1.3434
10	2.1164	1.1717
11	2.2953	.9845
12	2.4559	.7832
13	2.5919	.5628
14	2.7279	.3425
15	2.8328	.1075
16	2.9157	-.1378
17	2.9985	-.3832
18	3.0382	-.6380
19	3.0660	-.8954
20	3.0938	-1.1529
21	3.0938	-1.1529
22	3.0938	-1.1529
23	3.0403	-1.6845
24	2.9039	-2.2011
25	2.6743	-2.6842
26	2.3622	-3.1191
27	1.9792	-3.4925
28	1.5302	-3.7827
29	1.0455	-4.0016
30	.5320	-4.1427
31	0	-4.2017
32		
33		
34		
35		
36		
37		

TABLE I.- Continued

x = 14		
N	y	z
1	0	3.2871
2	.3524	3.2852
3	.7041	3.2788
4	1.0527	3.2292
5	1.3950	3.1433
6	1.7219	3.0125
7	2.0444	2.8691
8	2.3386	2.6758
9	2.6269	2.4723
10	2.8861	2.2350
11	3.1294	1.9793
12	3.3437	1.7014
13	3.5276	1.4001
14	3.7116	1.0989
15	3.8495	.7768
16	3.9610	.4415
17	4.0726	.1066
18	4.1238	-.2414
19	4.1612	-.5923
20	4.1985	-.9433
21	4.1985	-.9433
22	4.1985	-.9433
23	4.1261	-1.6658
24	3.9413	-2.3680
25	3.6307	-3.0252
26	3.2074	-3.6168
27	2.6881	-4.1254
28	2.0787	-4.5209
29	1.4205	-4.8198
30	.7229	-5.0121
31	0	-5.0925
32	↓	↓
33	↓	↓
34	↓	↓
35	↓	↓
36	↓	↓
37	↓	↓

x = 18		
N	y	z
1	0	4.4891
2	.4321	4.4841
3	.8611	4.4346
4	1.2859	4.3591
5	1.7019	4.2416
6	2.1009	4.0781
7	2.4933	3.8967
8	2.8565	3.6649
9	3.2093	3.4150
10	3.5342	3.1328
11	3.8343	2.8216
12	4.1085	2.4903
13	4.3377	2.1238
14	4.5669	1.7572
15	4.7488	1.3682
16	4.8890	.9593
17	5.0293	.5504
18	5.0994	.1258
19	5.1465	.3039
20	5.1937	-.7336
21	5.1975	-.7337
22	5.1937	-.7337
23	5.1044	-1.6293
24	4.8765	-2.5000
25	4.4940	-3.3159
26	3.9707	-4.0501
27	3.3289	-4.6824
28	2.5752	-5.1749
29	1.7603	-5.5472
30	.8961	-5.7872
31	0	-5.8872
32	↓	↓
33	↓	↓
34	↓	↓
35	↓	↓
36	↓	↓
37	↓	↓

x = 22		
N	y	z
1	0	5.4760
2	.4951	5.4551
3	.9857	5.3870
4	1.4714	5.2922
5	1.9464	5.1507
6	2.4036	4.9623
7	2.8523	4.7516
8	3.2715	4.4903
9	3.6762	4.2041
10	4.0548	3.8873
11	4.4010	3.5325
12	4.7247	3.1600
13	4.9907	2.7417
14	5.2568	2.3235
15	5.4756	1.8824
16	5.6394	1.4145
17	5.8032	.9467
18	5.8895	.4612
19	5.9447	-.0314
20	6.0000	-.5240
21	6.0002	-.5241
22	6.0000	-.5241
23	5.8975	-1.5629
24	5.6358	-2.5733
25	5.1972	-3.5219
26	4.5938	-4.3758
27	3.8539	-5.1133
28	2.9833	-5.6894
29	2.0405	-6.1258
30	1.0391	-6.4071
31	0	-6.5240
32	↓	↓
33	↓	↓
34	↓	↓
35	↓	↓
36	↓	↓
37	↓	↓

TABLE I.- Continued

x = 28		
N	y	z
1	0	6.2626
2	.5426	6.2572
3	1.0830	6.2293
4	1.1689	6.1489
5	2.1445	6.0130
6	2.6489	5.8161
7	3.1453	5.5960
8	3.6040	5.3089
9	4.0499	4.9991
10	4.4590	4.6460
11	4.8377	4.2569
12	5.1814	3.8403
13	5.4699	3.3803
14	5.7584	2.9203
15	5.9847	2.4307
16	6.1607	1.9171
17	6.3368	1.4035
18	6.4233	.8699
19	6.4824	.3301
20	6.5415	-.2096
21	6.5415	-1.3016
22	6.5415	-2.3936
23	6.4442	-3.2149
24	6.1882	-4.0005
25	5.7715	-4.7174
26	5.2336	-5.3431
27	4.5918	-5.8652
28	3.8671	-6.2674
29	3.0922	-6.5518
30	2.2877	-6.7346
31	1.4627	-6.8154
32	1.2189	↓
33	.9751	
34	.7314	
35	.4876	
36	.2438	
37	0	↓

x = 32		
N	y	z
1	0	6.5564
2	.5542	6.5509
3	1.1062	6.5234
4	1.6539	6.4443
5	2.1913	6.3074
6	2.7085	6.1119
7	3.2167	5.8902
8	3.6894	5.6043
9	4.1472	5.2914
10	4.5713	4.9382
11	4.9613	4.5439
12	5.3202	4.1250
13	5.6182	3.6574
14	5.9163	3.1898
15	6.1550	2.6935
16	6.3375	2.1699
17	6.5199	1.6462
18	6.6123	1.1022
19	6.6736	.5511
20	6.7350	0
21	6.7350	-1.7661
22	6.7350	-3.5322
23	6.6451	-4.1955
24	6.4013	-4.8176
25	6.0249	-5.3703
26	5.5523	-5.8436
27	5.0028	-6.2253
28	4.4027	-6.5260
29	3.7628	-6.7232
30	3.1065	-6.8506
31	2.4379	-6.9097
32	2.0316	↓
33	1.6253	
34	1.2190	
35	.8126	
36	.4063	
37	0	↓

x = 36		
N	y	z
1	0	6.7645
2	.5661	6.7609
3	1.1286	6.7002
4	1.6861	6.6071
5	2.2323	6.4576
6	2.7580	6.2512
7	3.2742	6.0185
8	3.7555	5.7240
9	4.2209	5.4013
10	4.6540	5.0404
11	5.0512	4.6368
12	5.4196	4.2102
13	5.7240	3.7327
14	6.0284	3.2552
15	6.2753	2.7498
16	6.4621	2.2153
17	6.6489	1.6807
18	6.7453	1.1255
19	6.8083	.5628
20	6.8712	0
21	6.8712	-2.2881
22	6.8712	-4.5762
23	6.7904	-5.0827
24	6.5661	-5.5428
25	6.2415	-5.9389
26	5.8474	-6.2667
27	5.4028	-6.5219
28	4.9321	-6.7301
29	4.4328	-6.8540
30	3.9262	-6.9351
31	3.4131	-6.9751
32	2.8443	↓
33	2.2754	
34	1.7066	
35	1.1377	
36	.5689	
37	0	↓

TABLE I.- Continued

x = 40		
N	y	z
1	0	6.9108
2	.5742	6.8957
3	1.1438	6.8245
4	1.7081	6.7217
5	2.2604	6.5632
6	2.7921	6.3492
7	3.3139	6.1087
8	3.8012	5.8081
9	4.2719	5.4786
10	4.7114	5.1123
11	5.1137	4.7021
12	5.4888	4.2702
13	5.7977	3.7857
14	6.1065	3.3012
15	6.3593	2.7895
16	6.5492	2.2472
17	6.7391	1.7049
18	6.8384	1.1420
19	6.9025	.5710
20	6.9665	0
21	6.9665	-2.7548
22	6.9665	-5.5095
23	6.8938	-5.8624
24	6.7002	-6.1668
25	6.4391	-6.4159
26	6.1361	-6.6128
27	5.8059	-6.7598
28	5.4641	-6.8794
29	5.1090	-6.9525
30	4.7500	-6.9968
31	4.3882	-7.0207
32	3.6568	↓
33	2.9255	↓
34	2.1941	↓
35	1.4627	↓
36	.7314	↓
37	0	↓

x = 44		
N	y	z
1	0	7.0068
2	.5794	6.9841
3	1.1537	6.9061
4	1.7224	6.7968
5	2.2786	6.6325
6	2.8141	6.4135
7	3.3396	6.1679
8	3.8309	5.8634
9	4.3051	5.5293
10	4.7488	5.1595
11	5.1544	4.7449
12	5.5340	4.3096
13	5.8458	3.8205
14	6.1576	3.3314
15	6.4143	2.8155
16	6.6062	2.2682
17	6.7981	1.7209
18	6.8994	1.1528
19	6.9641	.5764
20	7.0289	0
21	7.0289	-3.1507
22	7.0289	-6.3014
23	6.9623	-6.5056
24	6.8161	-6.6660
25	6.6338	-6.7853
26	6.4345	-6.8737
27	6.2257	-6.9364
28	6.0139	-6.9874
29	5.7985	-7.0214
30	5.5813	-7.0394
31	5.3634	-7.0504
32	4.4695	↓
33	3.5756	↓
34	2.6817	↓
35	1.7878	↓
36	.8939	↓
37	0	↓

x = 51		
N	y	z
1	0	7.0699
2	.5828	7.0422
3	1.1600	6.9597
4	1.7316	6.8462
5	2.2905	6.6781
6	2.8285	6.4558
7	3.3564	6.2069
8	3.8503	5.8997
9	4.3268	5.5627
10	4.7733	5.1906
11	5.1811	4.7731
12	5.5636	4.3355
13	5.8773	3.8434
14	6.1910	3.3513
15	6.4503	2.8327
16	6.6436	2.2820
17	6.8369	1.7313
18	6.9394	1.1599
19	7.0046	.5800
20	7.0699	0
21	↓	-3.5350
22	↓	-7.0700
23	↓	↓
24	↓	↓
25	↓	↓
26	↓	↓
27	↓	↓
28	↓	↓
29	↓	↓
30	↓	↓
31	↓	↓
32	5.8916	↓
33	4.7133	↓
34	3.5349	↓
35	2.3566	↓
36	1.1783	↓
37	0	↓

TABLE I.- Concluded

x = 120		
N	y	z
1	0	7.0699
2	.5828	7.0422
3	1.1600	6.9597
4	1.7316	6.8462
5	2.2905	6.6781
6	2.8285	6.4558
7	3.3564	6.2069
8	3.8503	5.8997
9	4.3268	5.5627
10	4.7733	5.1906
11	5.1811	4.7731
12	5.5636	4.3355
13	5.8773	3.8434
14	6.1910	3.3513
15	6.4503	2.8327
16	6.6436	2.2820
17	6.8369	1.7313
18	6.9394	1.1599
19	7.0046	.5800
20	7.0699	0
21	↓	-3.5350
22		-7.0700
23		↓
24		
25		
26		
27		
28		
29		
30		
31		
32	5.8916	
33	4.7133	
34	3.5349	
35	2.3566	
36	1.1783	
37	0	

x = 140		
N	y	z
1	0	7.0699
2	.5828	7.0422
3	1.1600	6.9597
4	1.7316	6.8462
5	2.2905	6.6781
6	2.8285	6.4558
7	3.3564	6.2069
8	3.8503	5.8997
9	4.3268	5.5627
10	4.7733	5.1906
11	5.1811	4.7731
12	5.5636	4.3355
13	5.8773	3.8434
14	6.1910	3.3513
15	6.4503	2.8327
16	6.6436	2.2820
17	6.8369	1.7313
18	6.9394	1.1599
19	7.0046	.5800
20	7.0699	0
21	↓	↓
22		
23		
24		
25		
26		
27		
28		
29		
30		
31		
32	5.8916	
33	4.7133	
34	3.5349	
35	2.3566	
36	1.1783	
37	0	

TABLE II.- SUMMARY OF TEST DATA

(a) Forward survey station

[$x/D = 3.5$]

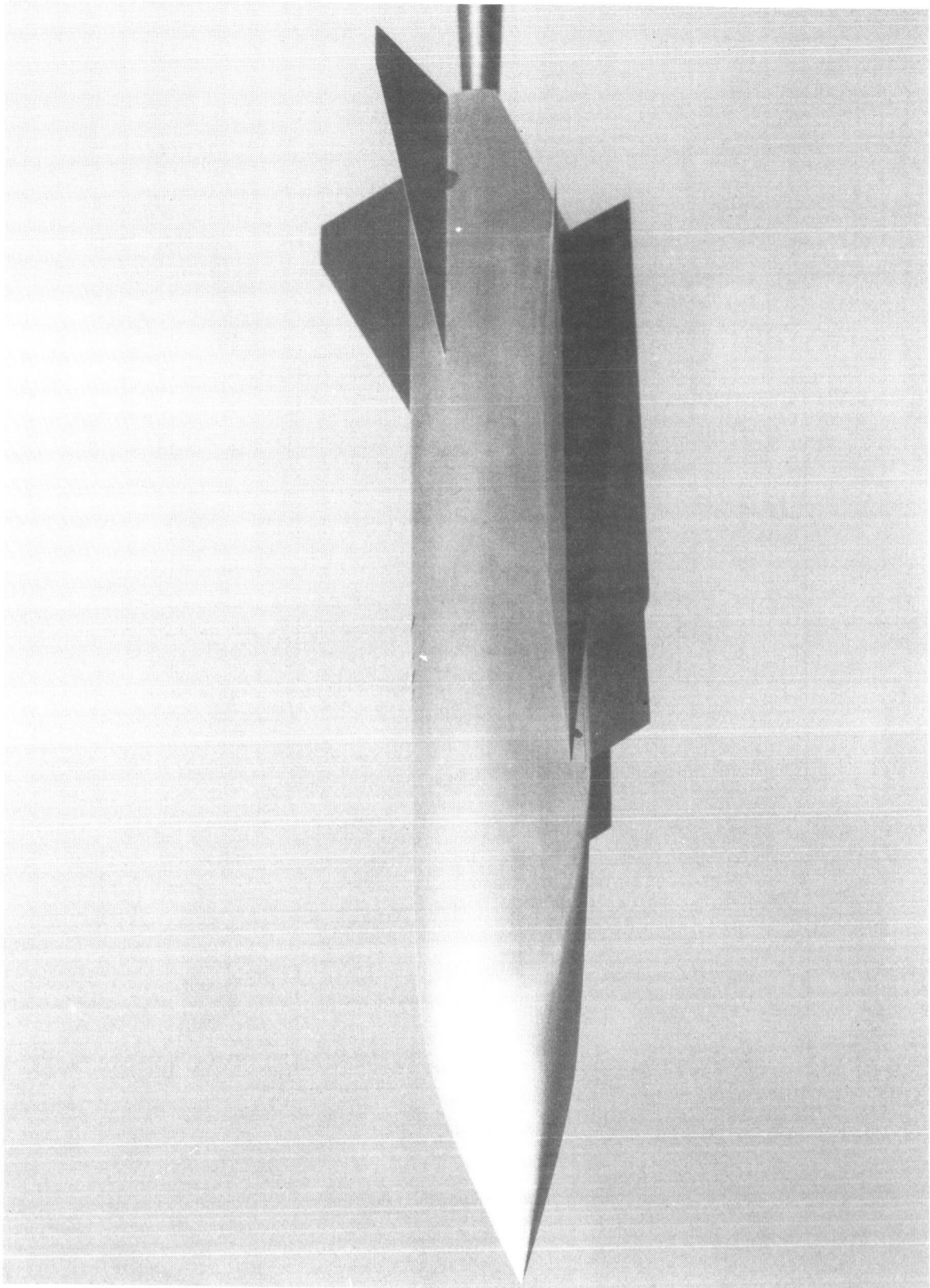
α , deg	Type of data obtained for y/D of -				
	0	0.118	0.236	0.354	0.471
0	W* P S	W P	W P S	W P	P S
4	W P S	W P	W P S	W P	
8	W P S	W P S	W P S	W P S	P S

(b) Aft survey station

[$x/D = 5.4$]

α , deg	Type of data obtained for y/D of -				
	0	0.118	0.236	0.354	0.471
4	P	P	P	P	P
8	P S	P S	P S	P S	P S

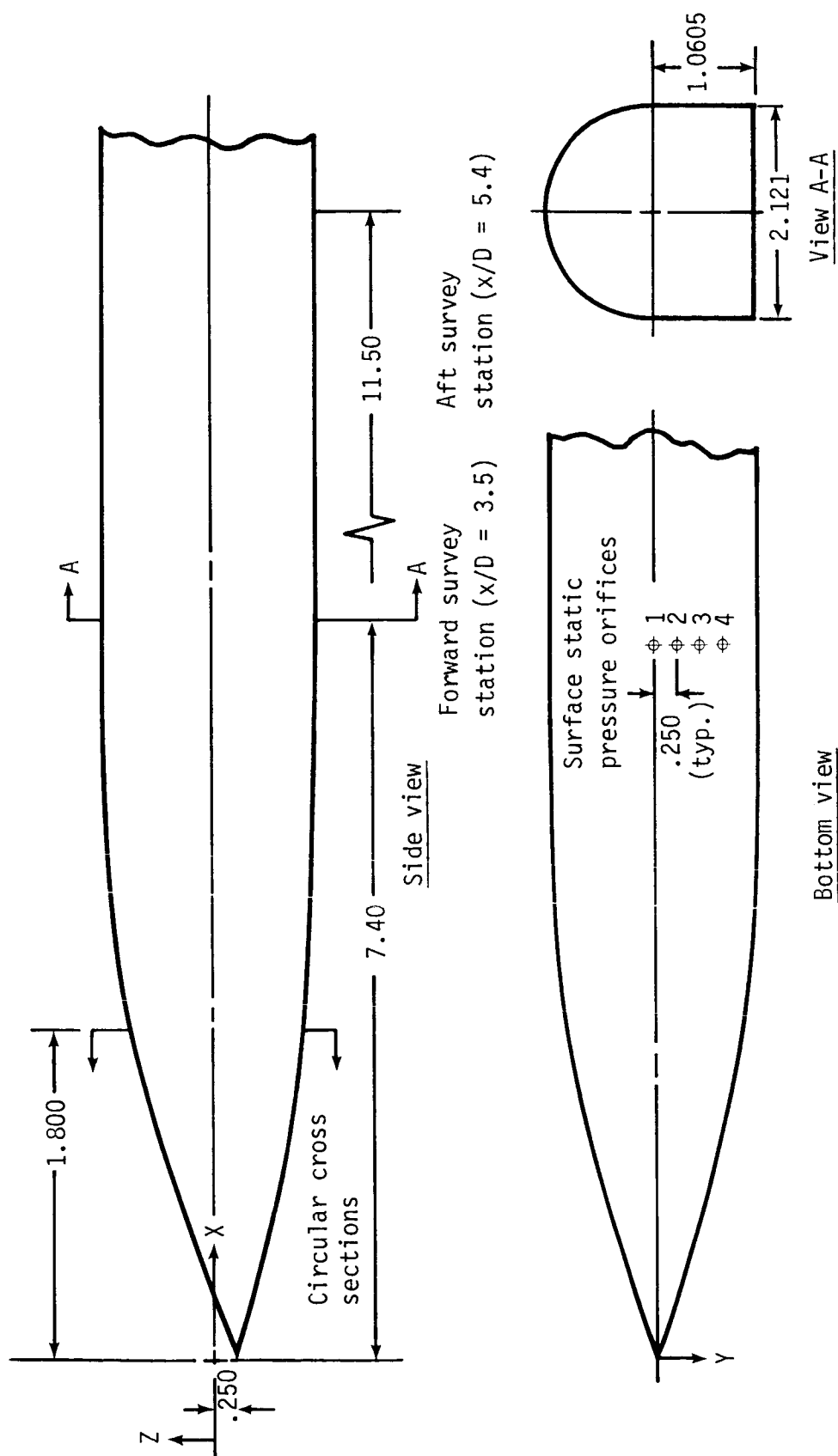
*W = Wall static pressure; P = Pitot pressure survey;
S = Static probe survey.



L-81-3262

(a) Side view.

Figure 1.- Photograph and sketch of 0.15-scale model of an airbreathing hypersonic missile.



(b) Fuselage forebody. (Dimensions in inches.)

Figure 1.- Concluded.

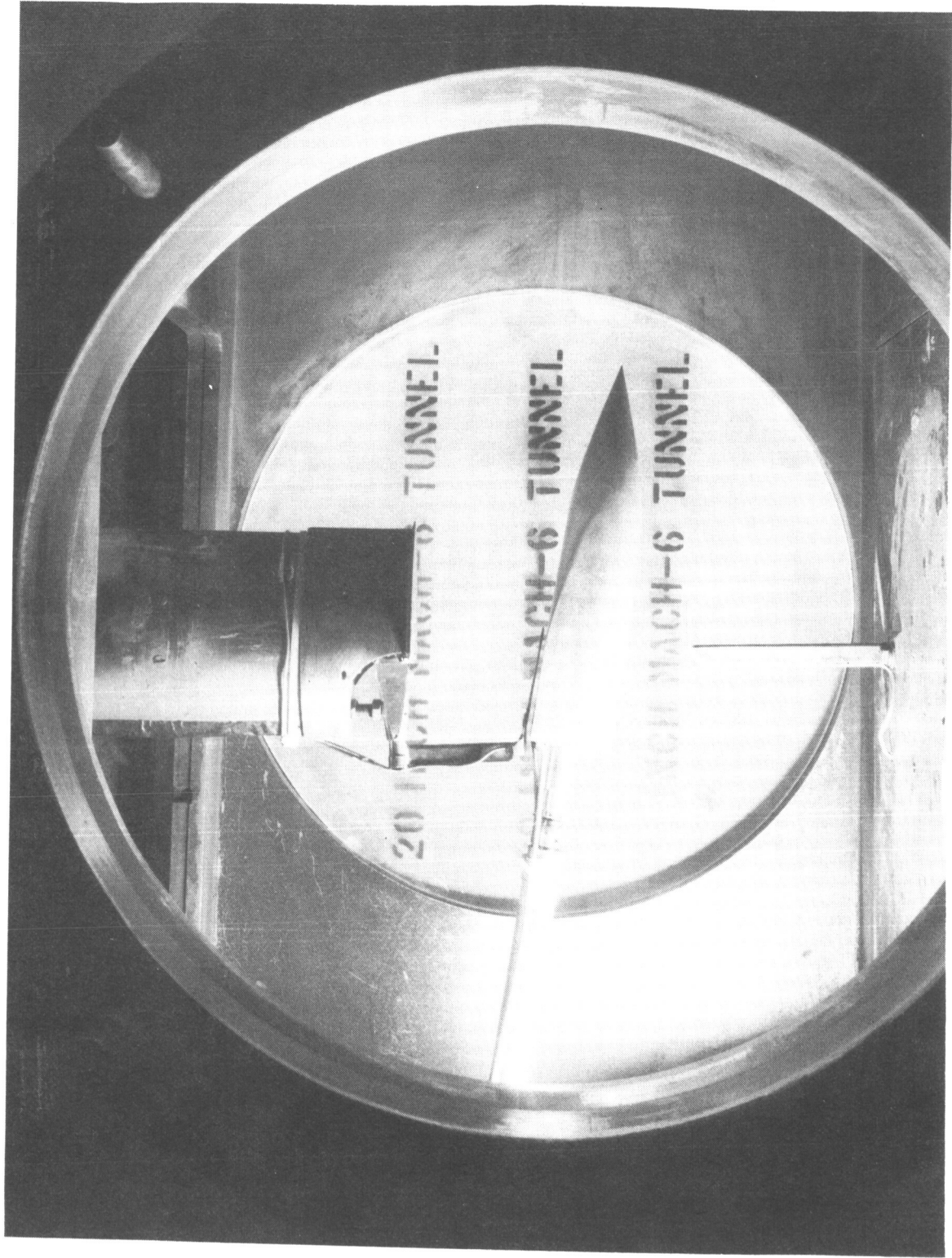


Figure 2.- Forebody model mounted in Langley 20-Inch Mach 6 Tunnel.

L-82-4136

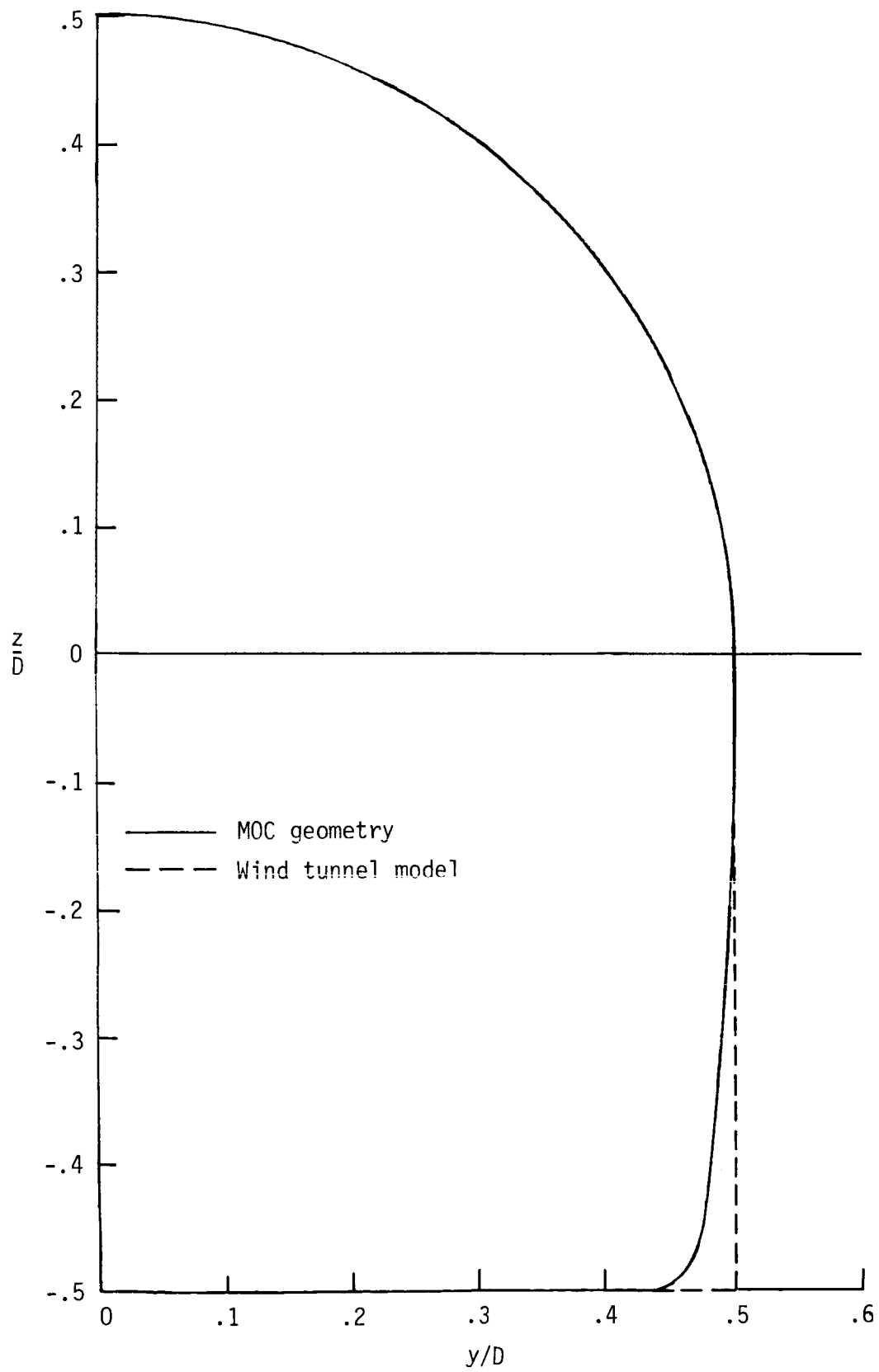


Figure 3.- Wind tunnel and theoretical model cross sections.

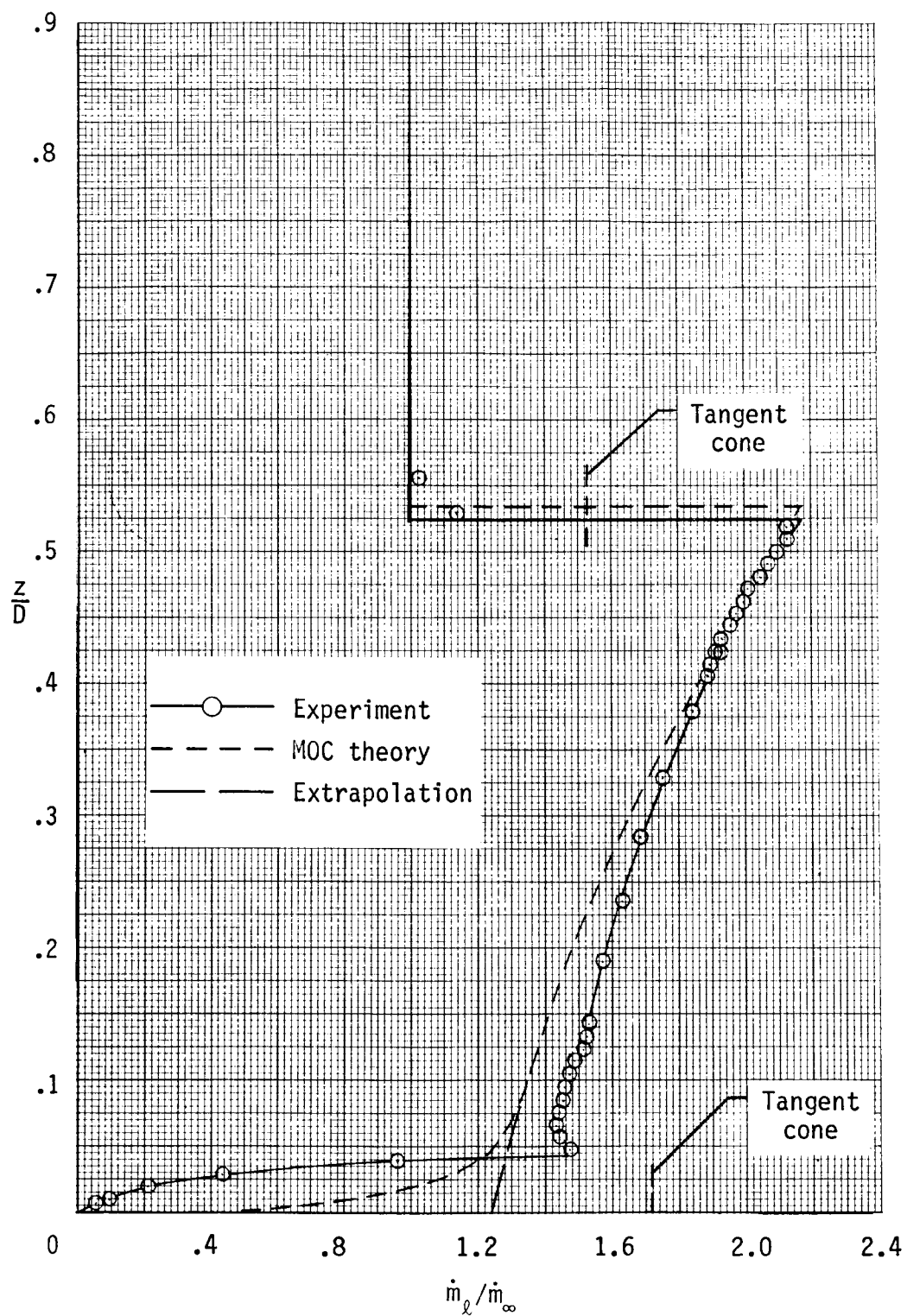


Figure 4.- Body centerline vertical-plane mass flow distribution at forward survey station ($x/D = 3.5$) at $\alpha = 8^\circ$.

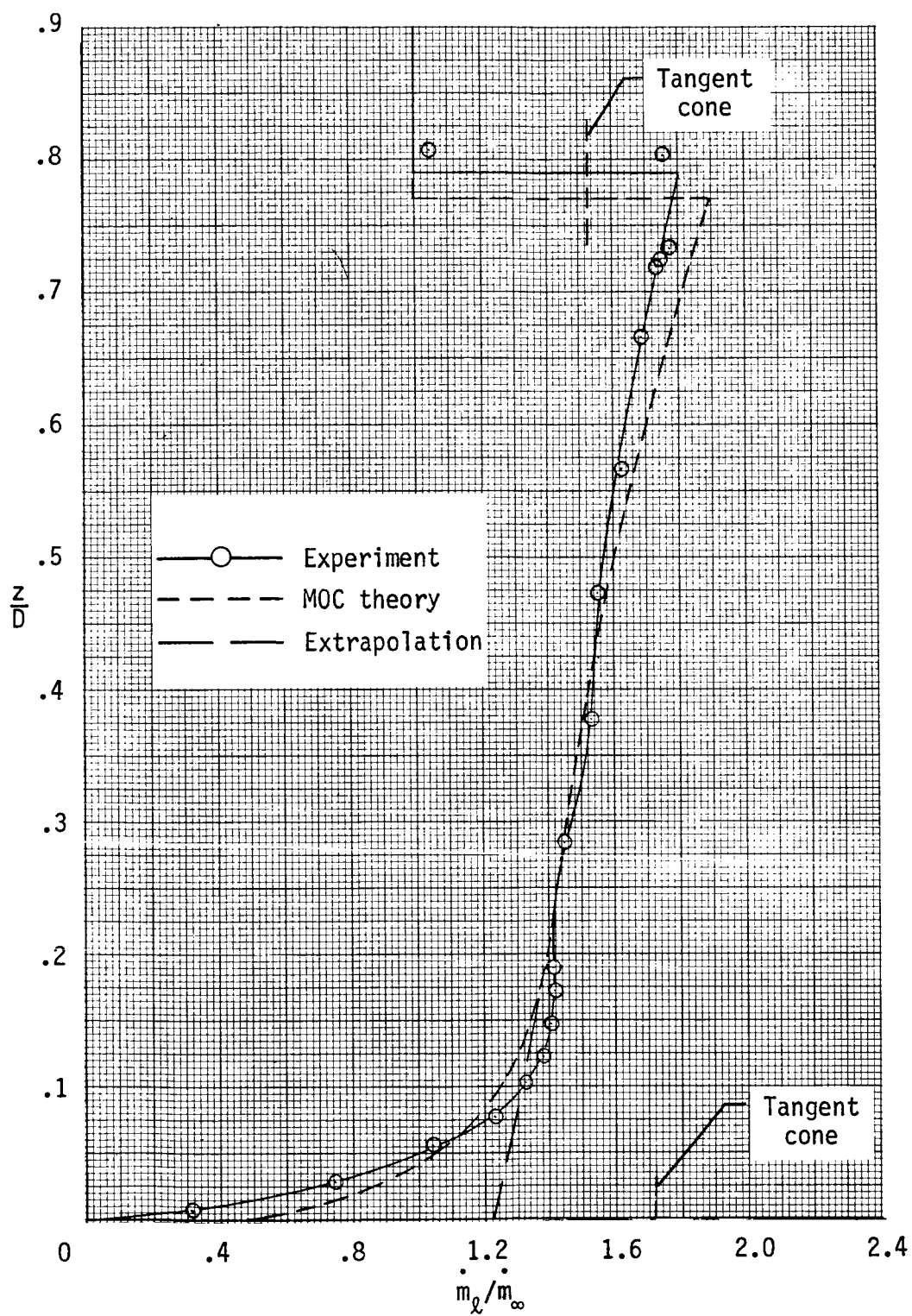
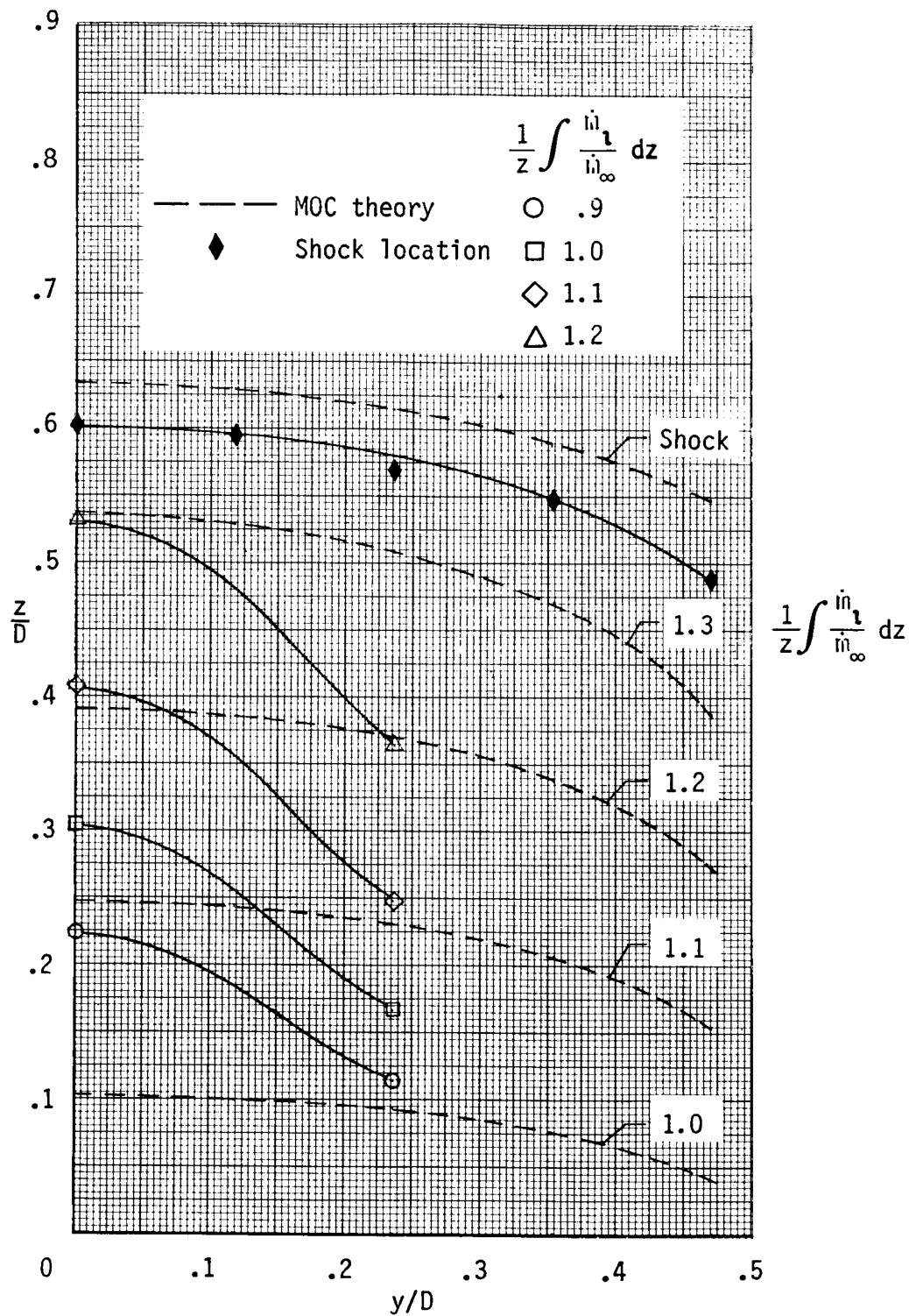
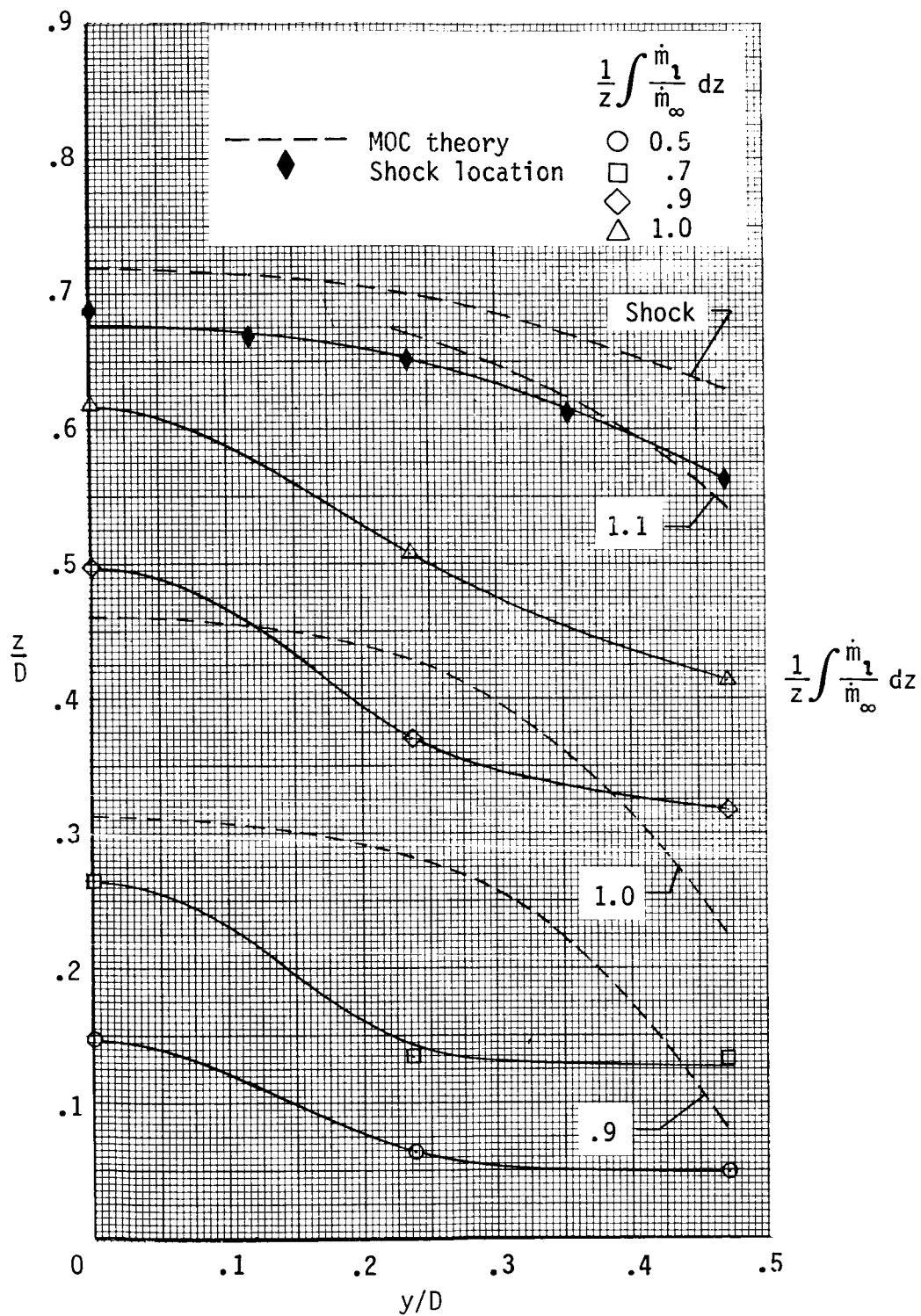


Figure 5.- Body centerline vertical-plane mass flow distribution at aft survey station ($x/D = 5.4$) at $\alpha = 8^\circ$.



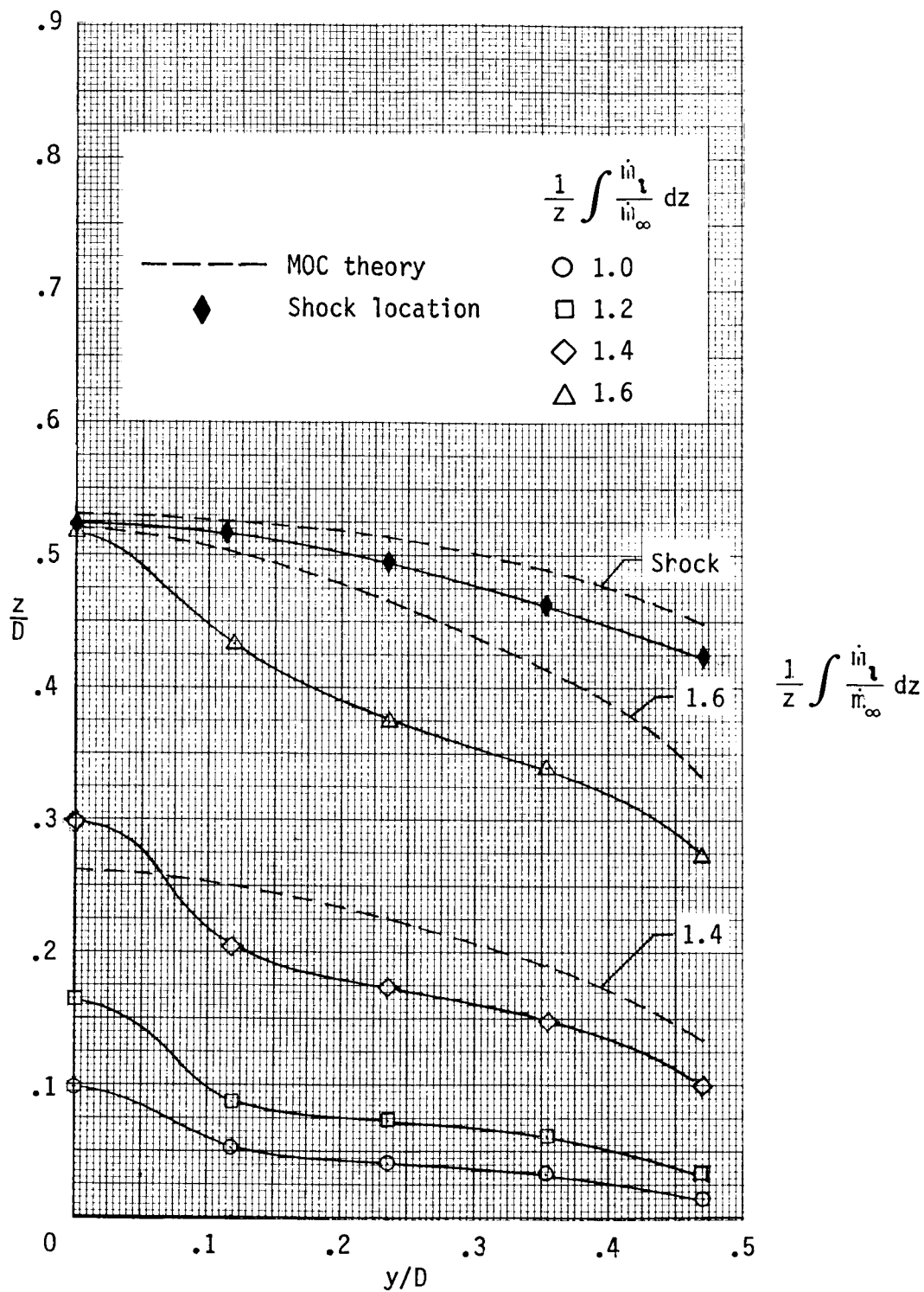
(a) $\alpha = 0^\circ$.

Figure 6.- Cumulative mass flow ratio contours across body semispan at $x/d = 3.5$.



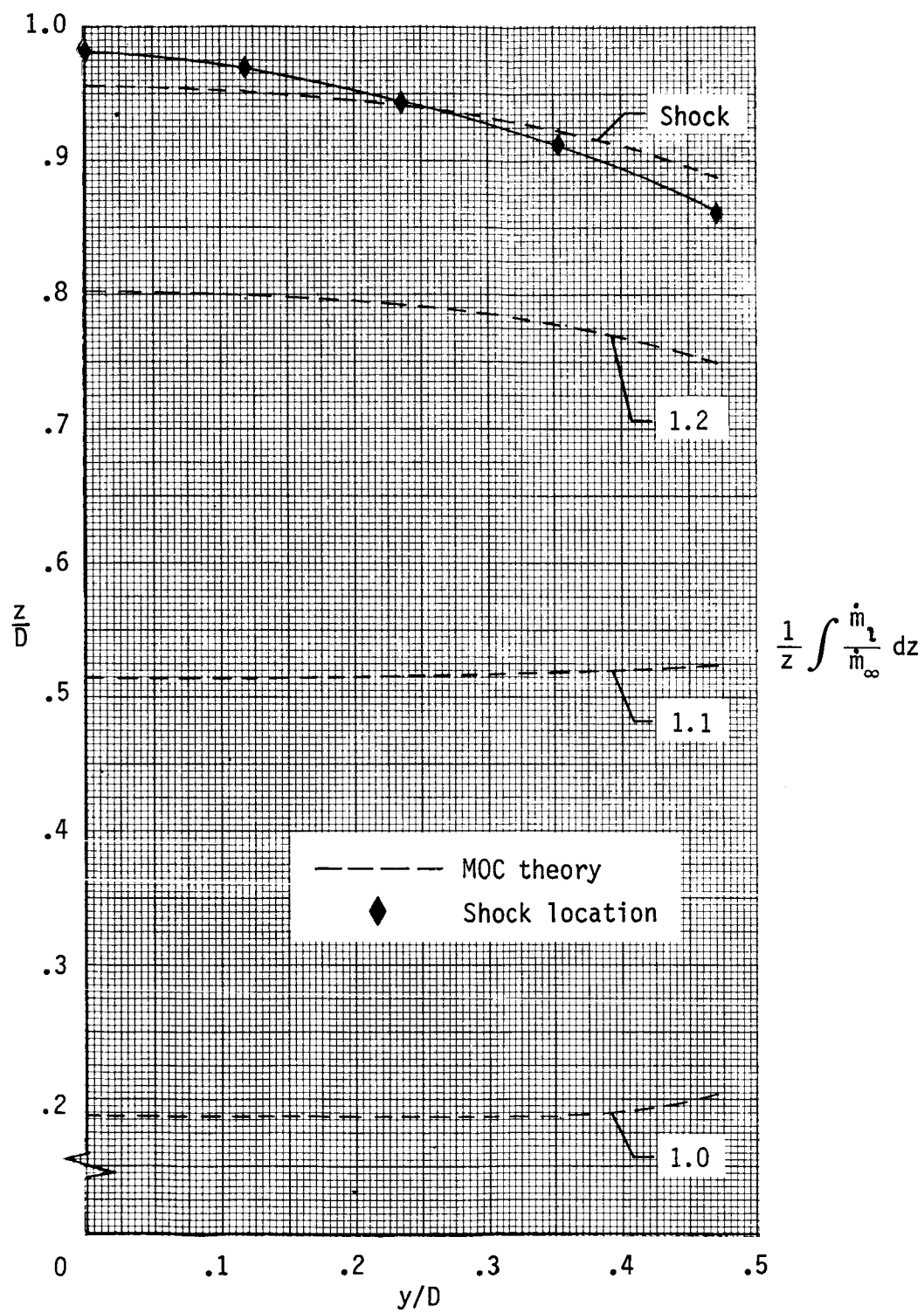
(b) $\alpha = 4^\circ$.

Figure 6.- Continued.



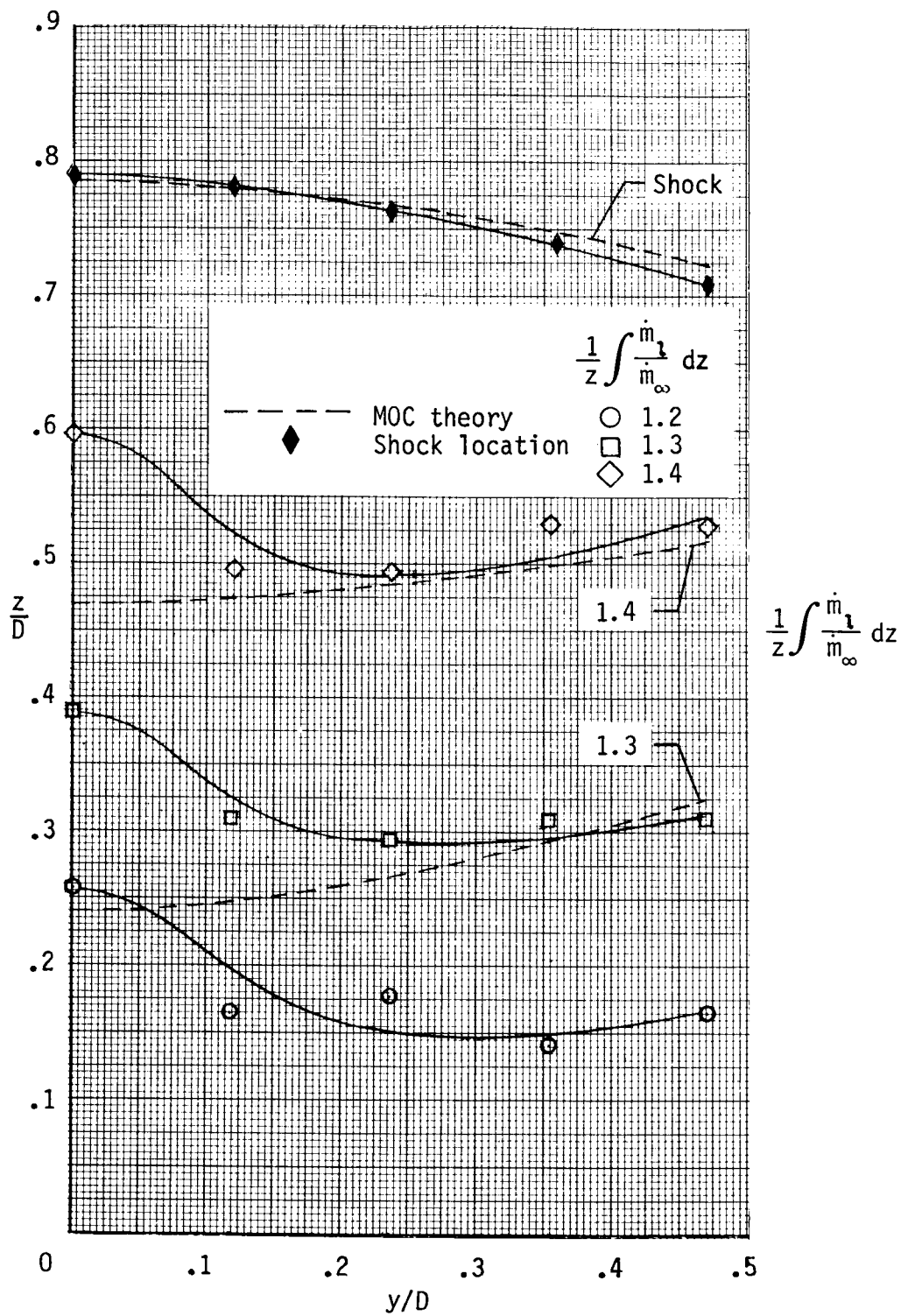
(c) $\alpha = 8^\circ$.

Figure 6.- Concluded.



(a) $\alpha = 4^\circ$.

Figure 7.- Cumulative mass flow ratios across body semispan at $x/d = 5.4$.



(b) $\alpha = 8^\circ$.

Figure 7.- Concluded.

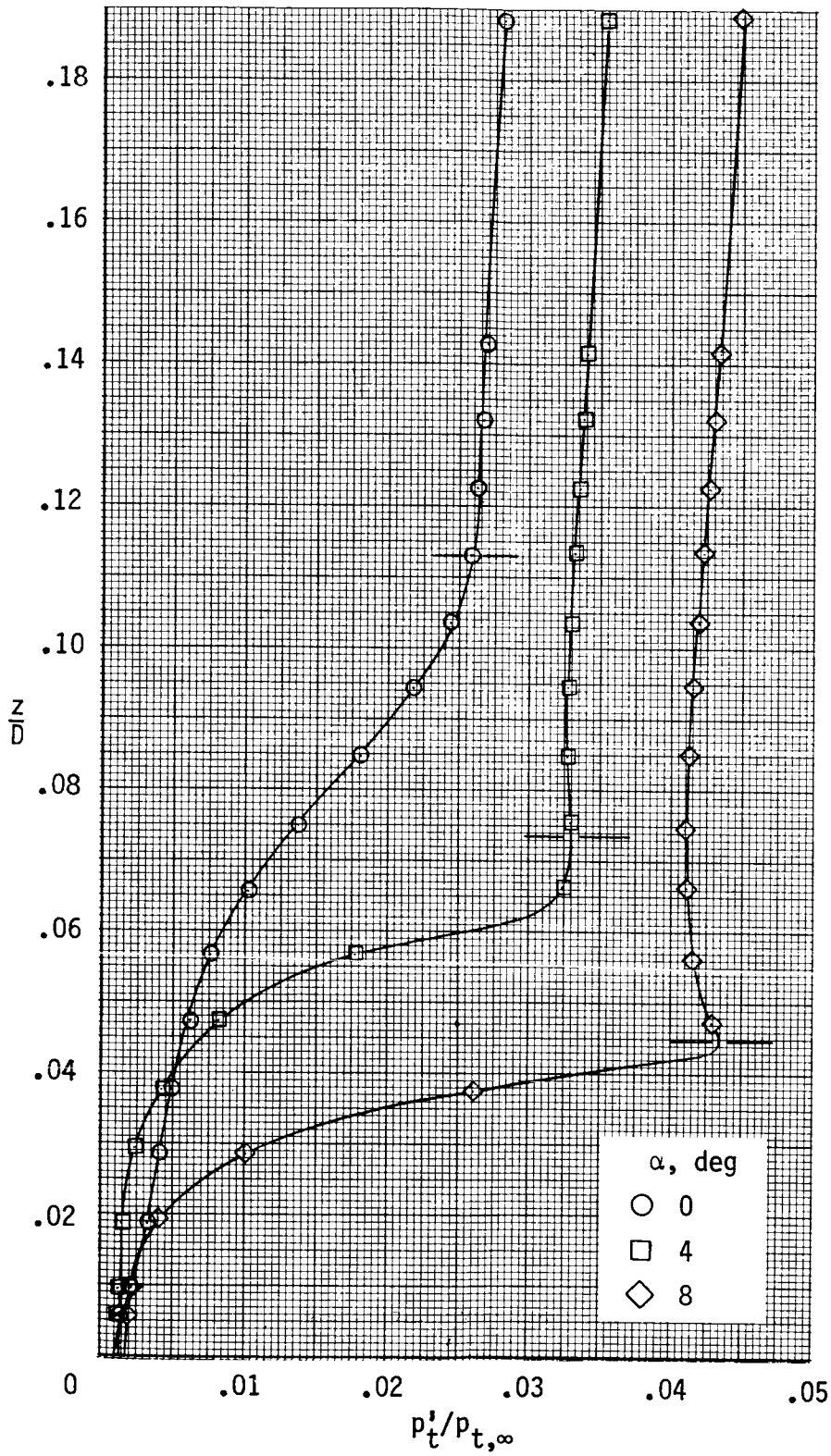


Figure 8.- Body centerline vertical-plane pitot pressure profiles adjacent to model surface at forward survey station ($x/D = 3.5$). Horizontal lines indicate assumed edge of boundary layer.

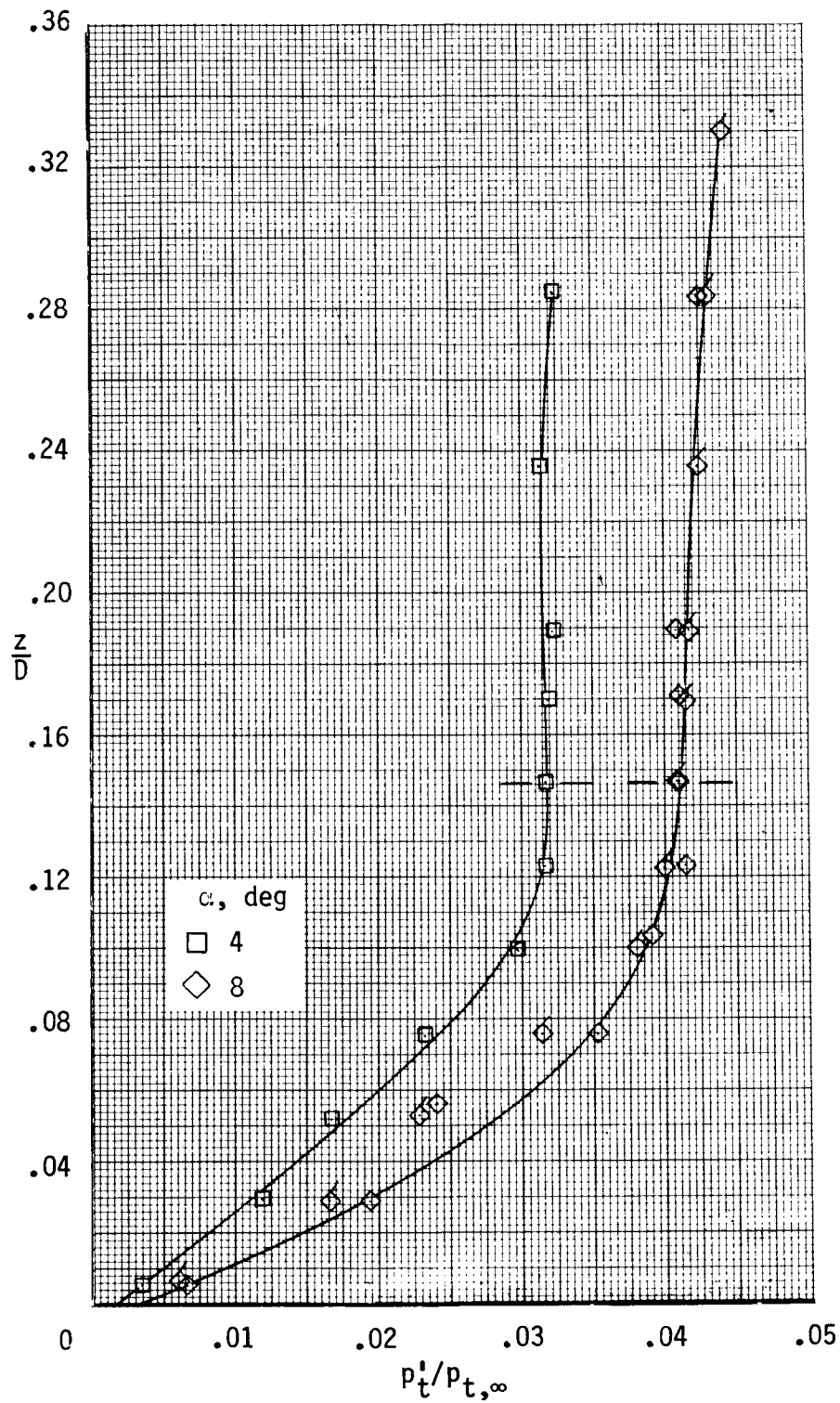


Figure 9.- Body centerline vertical-plane pitot pressure profiles adjacent to wall at aft survey station ($x/D = 5.4$). Horizontal lines indicate assumed edge of boundary layer. Symbols with flags denote data from a repeated test.

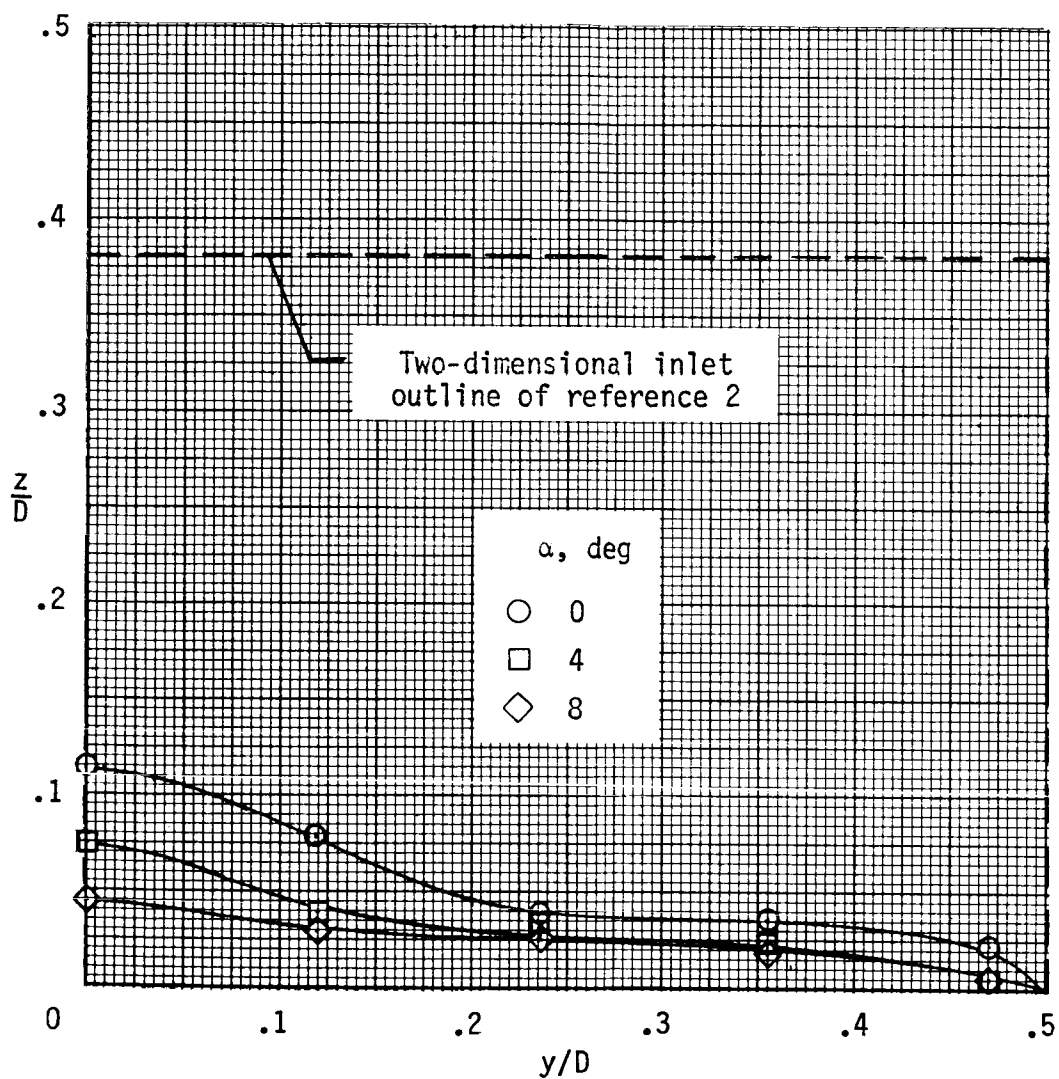


Figure 10.- Boundary layer thickness across body semiwidth at forward survey station ($x/D = 3.5$).

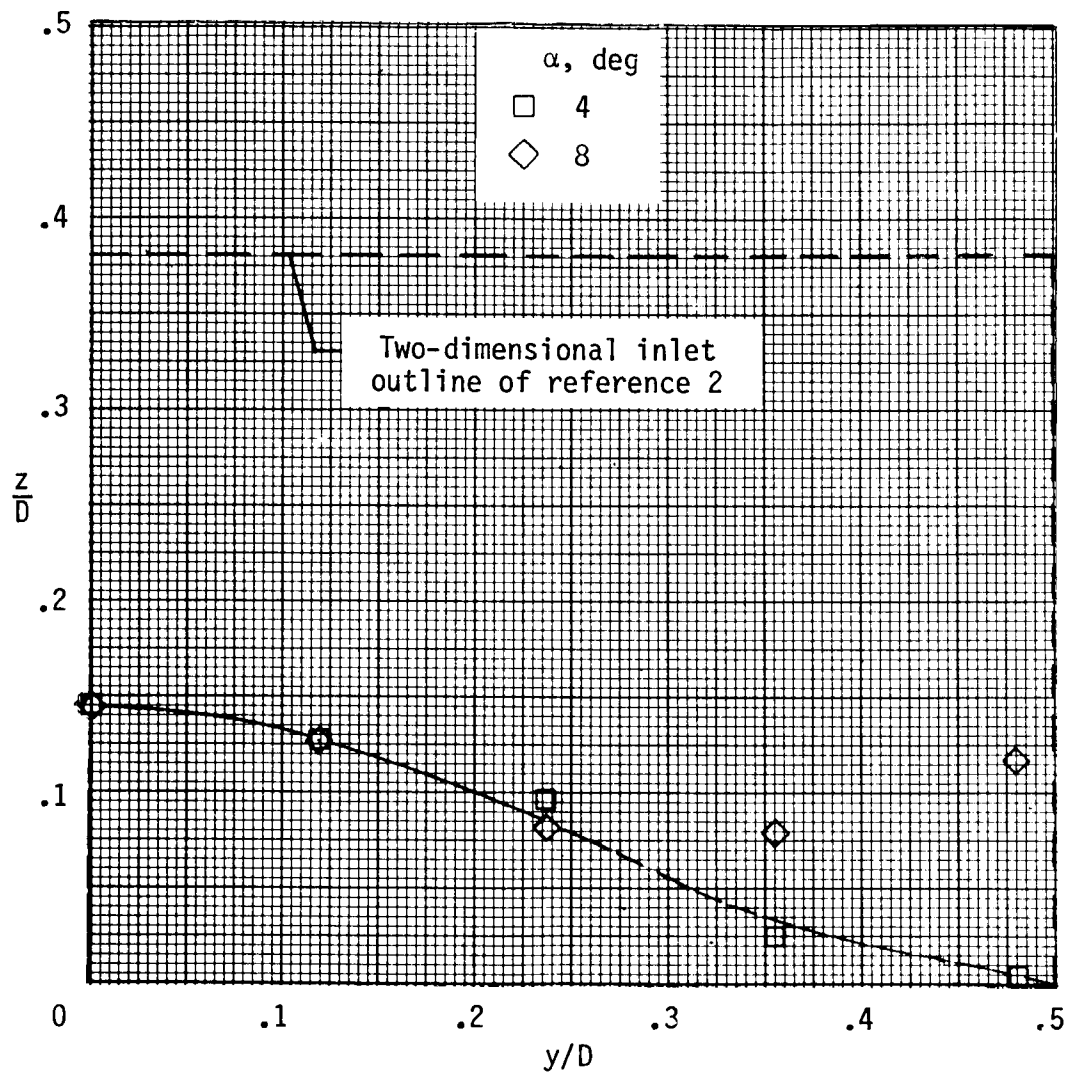
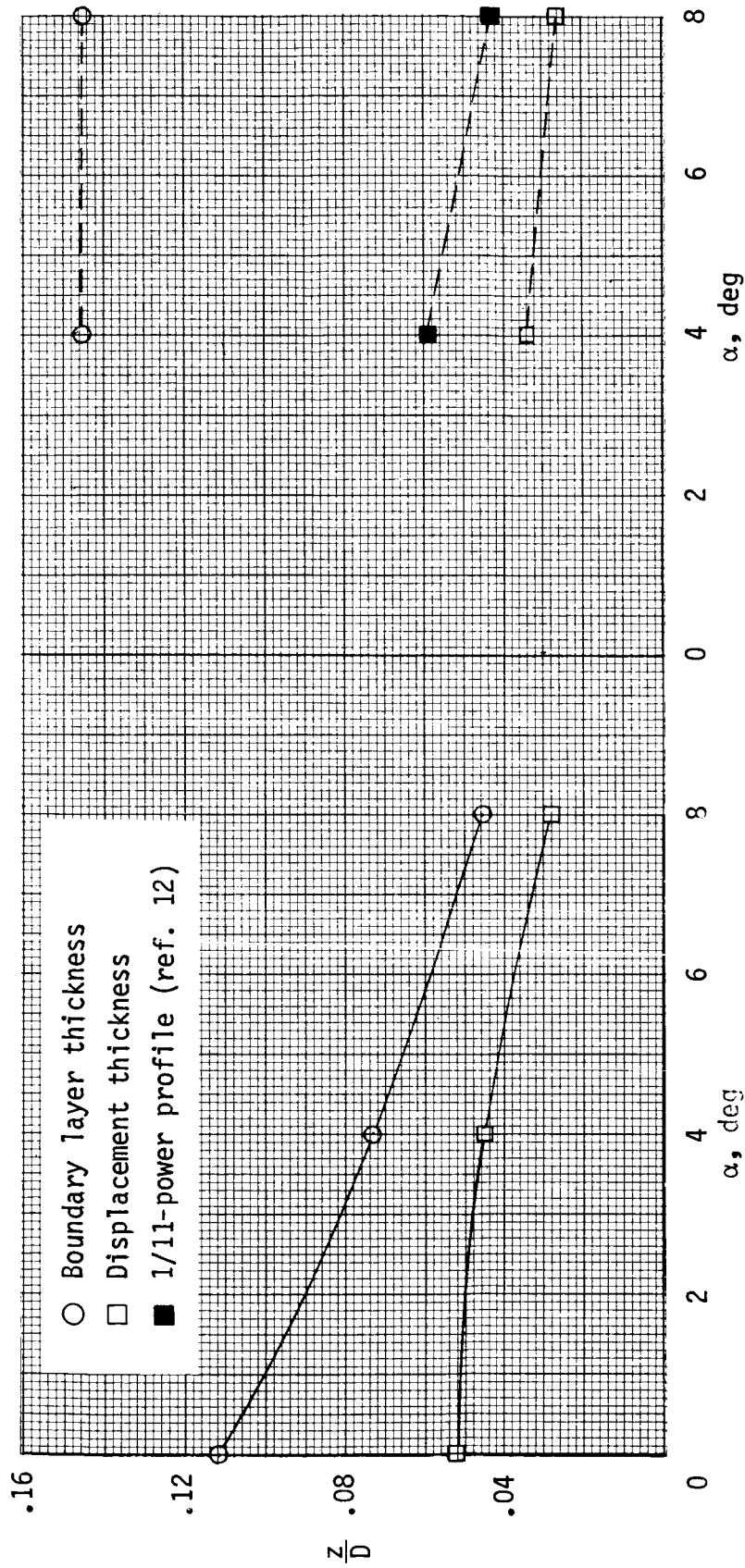


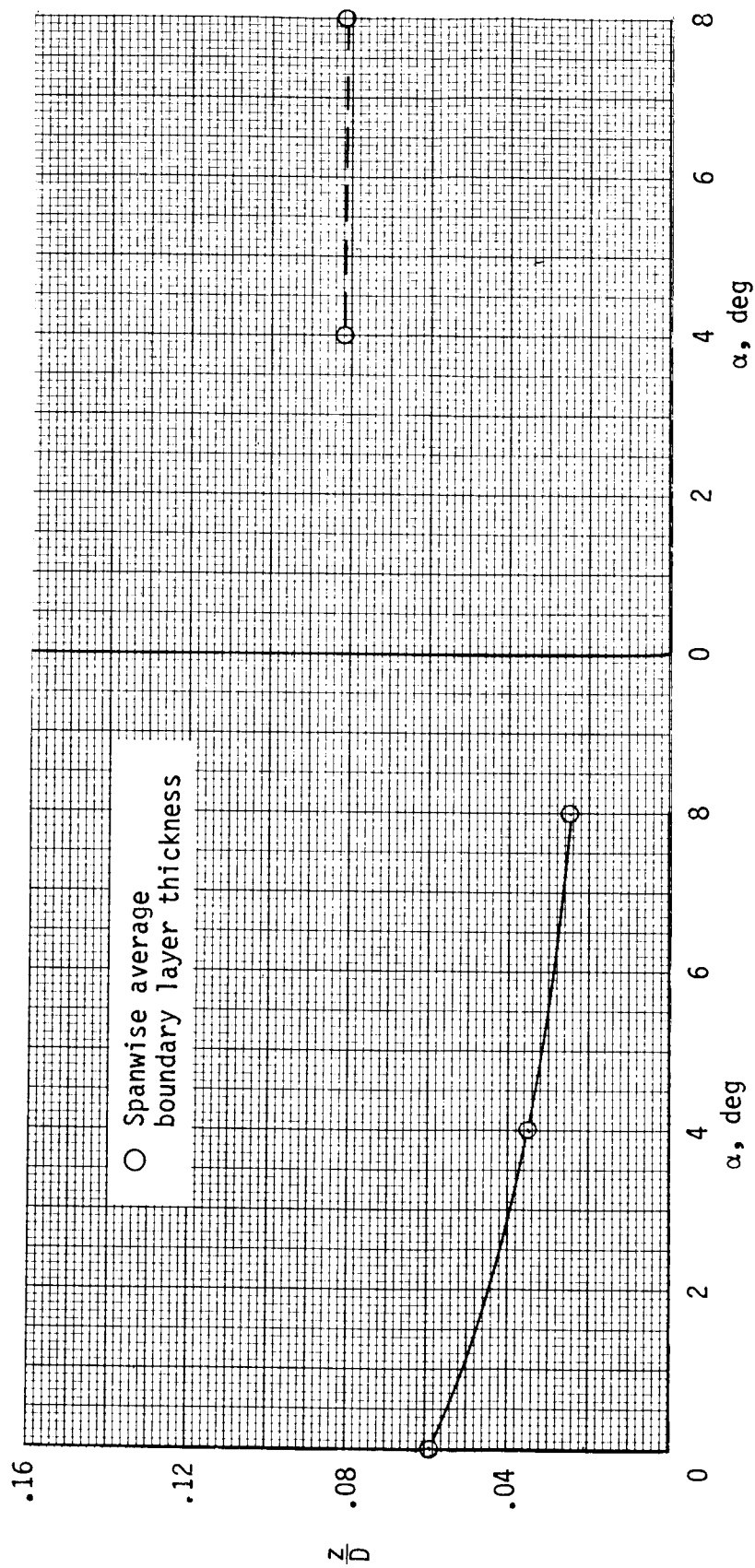
Figure 11.- Boundary layer thickness across body semiwidth at aft survey station ($x/D = 5.4$).



(a) Forward survey station ($x/D = 3.5$).

(b) Aft survey station ($x/D = 5.4$).

Figure 12.- Boundary layer thickness and displacement thickness on body centerline vertical plane.



(a) Forward survey station ($x/D = 3.5$).

(b) Aft survey station ($x/D = 5.4$).

Figure 13.- Effect of angle of attack on spanwise average boundary layer thickness.

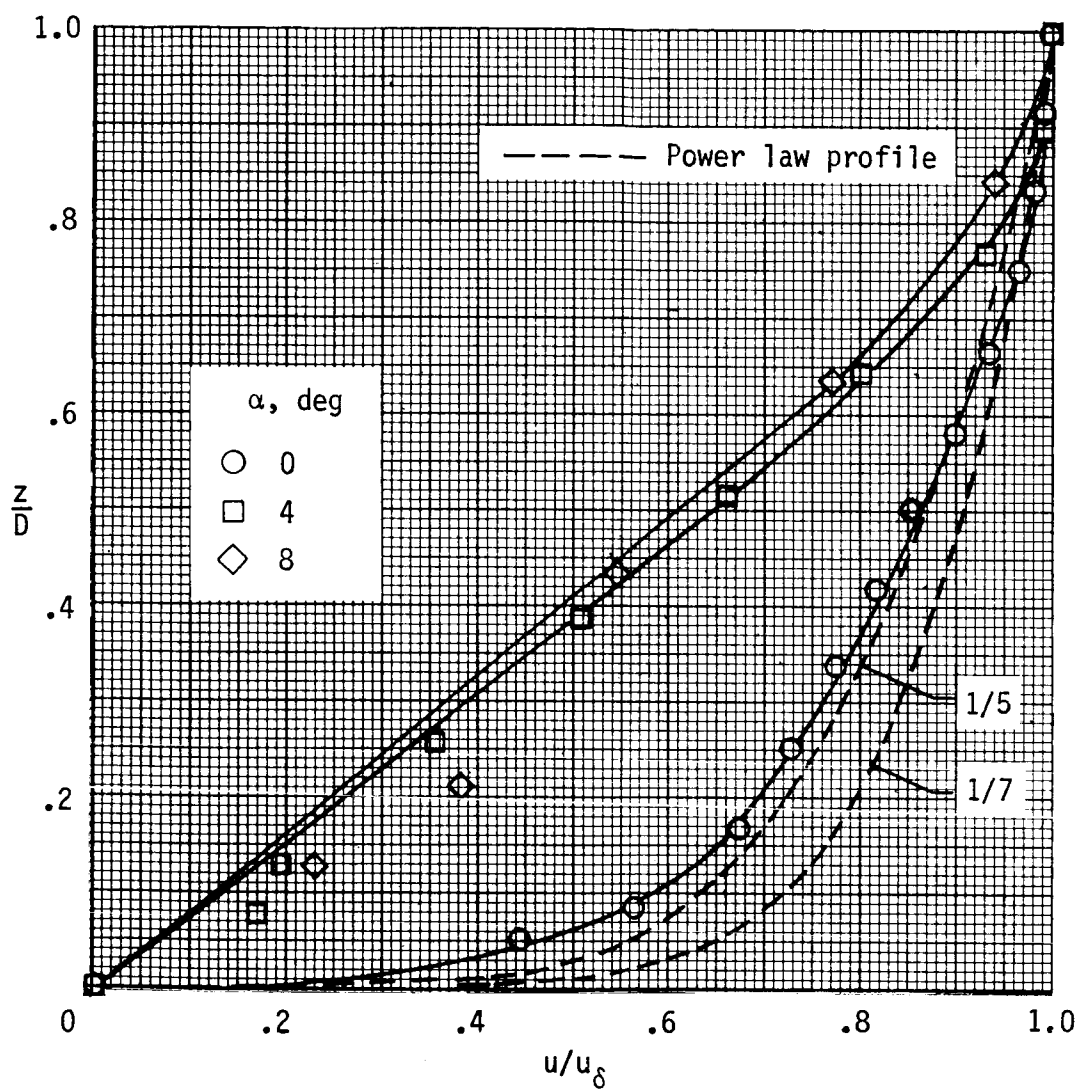


Figure 14.- Boundary layer velocity profiles on body centerline vertical plane at forward survey station ($x/D = 3.5$).

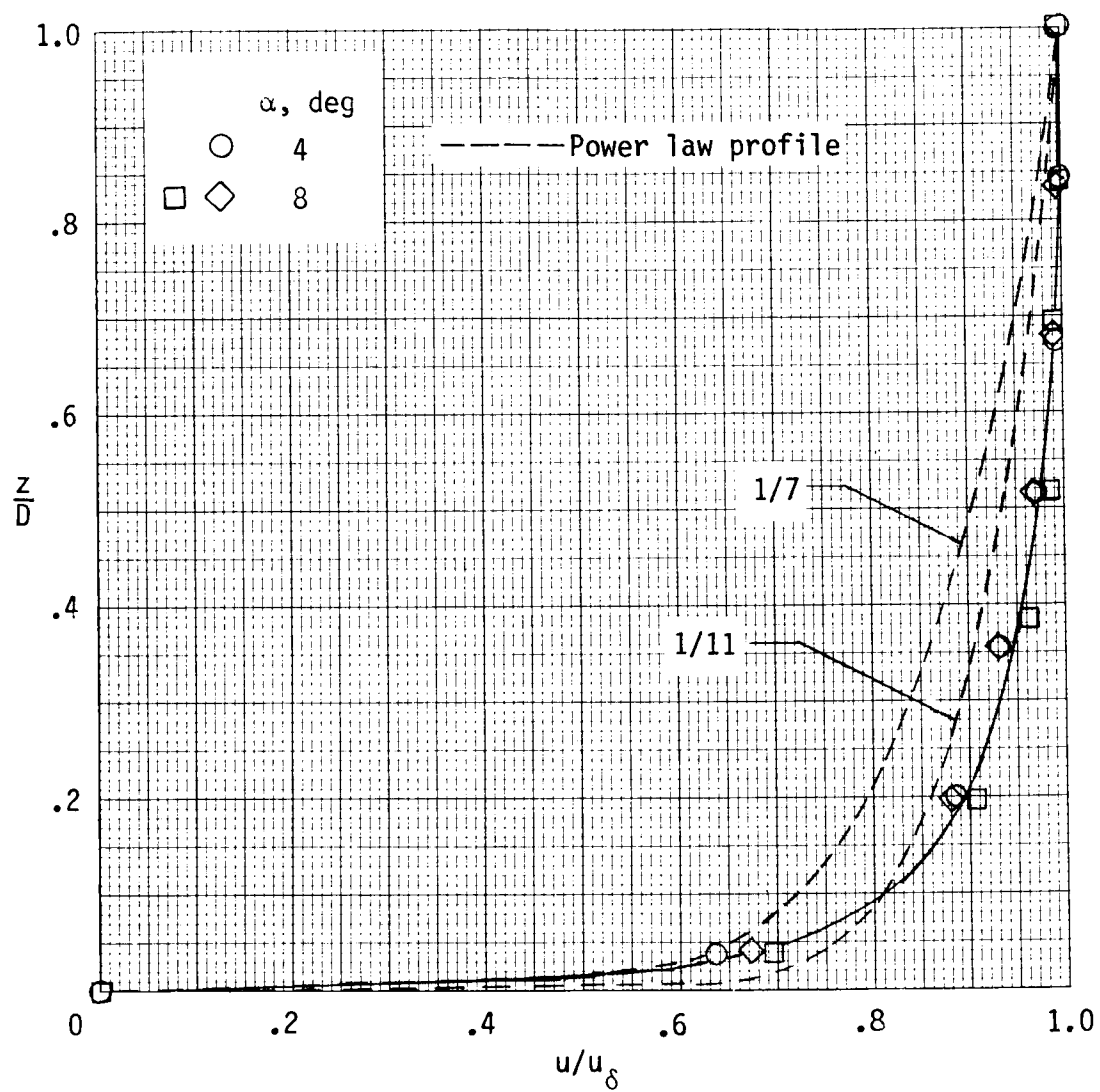
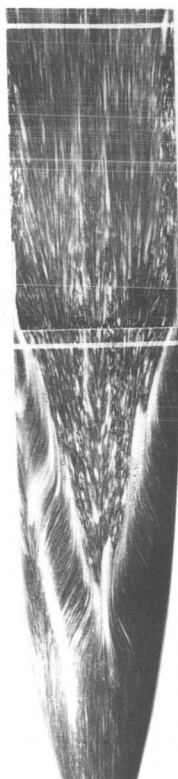
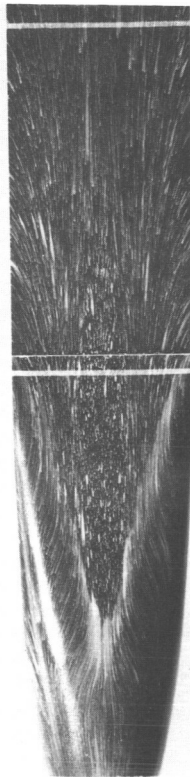


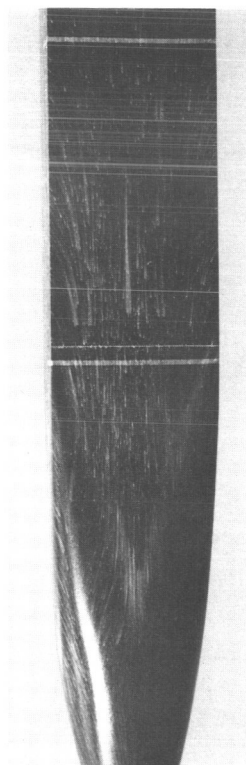
Figure 15.- Boundary layer velocity profiles on body centerline vertical plane at aft survey station ($x/D = 5.4$).



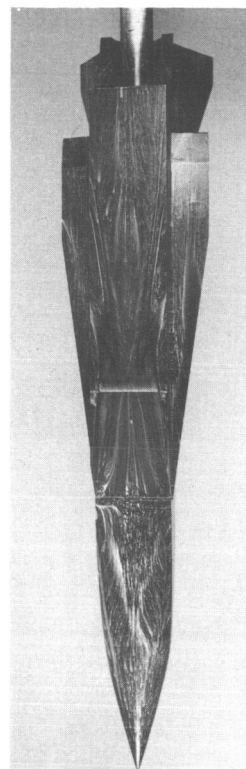
(a) $\alpha = 0^\circ$.



(b) $\alpha = 4^\circ$.



(c) $\alpha = 8^\circ$.



(d) $\alpha = 4^\circ$; complete configuration.

Figure 16.- Oil flow patterns on lower surface. L-85-125

APPENDIX A

PRESSURE MEASUREMENTS AND PROBE CALIBRATIONS

The measurement of static pressure in supersonic streams is not straightforward (see, for example, ref. 19), and at hypersonic speeds the problems are compounded by the induced pressure on the probe caused by the growth of the boundary layer along the surface of the probe (ref. 20).

A typical static pressure probe for use in supersonic streams consists of a high-fineness-ratio cylinder with a relatively shallow angle conical tip. For such a probe, static pressure taps are located at least 10 diameters aft of the cone-cylinder juncture so that they are downstream of most of the compression region following the shoulder. The disadvantage of this type of probe at high Mach numbers is that the recompression region stretches farther downstream as the Mach number increases; thus even greater distance is required from the shoulder to the orifices to avoid the recompression zone. Simultaneously, however, the growth of the boundary layer effectively distorts the cylinder to some type of power law body shape so that the local pressure, in the limit of extremely high Mach numbers, never reaches stream pressure for reasonable values of length-to-diameter ratio (ref. 21).

To overcome the foregoing difficulties with cone-cylinder probes, a short static pressure probe has been developed which lends itself to supersonic flow field surveys. The design and calibration of this probe are described in reference 5. The great advantage of this probe design is that the orifices are situated only about two diameters downstream of the tip. In addition, according to reference 5, the probe is relatively insensitive to angle of attack. This characteristic can be important in surveying flow fields about bodies in supersonic streams, as in the present study, since the flow direction varies from parallel to the surface near the body to the free-stream direction beyond the vehicle bow shock. In the present study, the probes were bent to some intermediate angle approximately halfway between the body angle of attack and the free-stream direction according to the calibration in reference 5, this should not have had a large effect on the measured probe static pressures. In the present surveys, in addition to probe angle-of-attack effects, there were large cross-probe velocity and pressure gradient especially in the boundary layer and at the edge of the body. The effect of these gradients on the probe readings is unknown.

As discussed in reference 5, the probes were calibrated in uniform Mach 2.5 and 4.0 streams, where the calibration factors (i.e., the ratios of measured to known or calculated stream pressure) were essentially unity. In the present study, of course, it was necessary to determine whether these calibration factors remained at 1.0 up to Mach 6. The probe calibrations at Mach 6 were obtained during the static pressure surveys as follows: The flow field surveys were initiated at the model surface and data were taken at random intervals through the model shock layer. The final frames were recorded with the probes in the free stream. (To be certain that there was no interference from the model shock, the last frame was taken with the model completely retracted from the tunnel flow.) The ratios of these free-stream probe readings to the calculated stream static pressures obtained from $p_{t,\infty}$ and $p'_{t,\infty}$ (as measured in the stagnation chamber and by a free-stream pitot tube, respectively) were then calculated. The resulting Mach 6.0 correction factors

ranged from 1.50 to 1.72; the scatter depended on model angle of attack and therefore on the angle to which the probes were bent. Following the tests at the forward survey station in the present study, the two probes were retested in the Mach 4.0 facility used in reference 5 to confirm that their calibration was indeed unity at this Mach number.

In the absence of any probe calibration data at intermediate Mach numbers between 4 and 6, it was assumed that the static probe calibration factors varied linearly from 1.0 to Mach 4 to whatever value was measured at Mach 6 free-stream conditions for the individual tests in the present investigation. (Because of the wind-tunnel throat shrinkage as a result of heat soak, the stream Mach number varied slightly with test duration.) The corrected local static pressure and Mach number were then determined by iteration using p_t' , measured static pressure, and the Rayleigh pitot equation from reference 22

$$\frac{p_{t,l}}{p_l} = \left[\frac{(\gamma + 1)M_l}{2} \right]^{\gamma/(\gamma-1)} \left[\frac{\gamma + 1}{2\gamma M_l^2 - (\gamma - 1)} \right]^{1/(\gamma-1)} \quad (1)$$

The ratio of local to free-stream mass flow, \dot{m}_l/\dot{m}_∞ , was then calculated from

$$\frac{\dot{m}_l}{\dot{m}_\infty} = \frac{p_l}{p_\infty} \frac{M_l}{M_\infty} \left(\frac{1 + M_l^2/5}{1 + M_\infty^2/5} \right)^{1/2} \quad (2)$$

using the corrected local pressures and Mach numbers and the free-stream Mach number at that point in time during the test.

As noted in the main body of the paper, the two-probe static pressure fixture was moved laterally to provide the same coverage as the five-tube pitot rake. It was therefore possible to compare the individual probe readings for the survey 0.5 in. off the body centerline for three test conditions: at the forward station at $\alpha = 0^\circ$ and 8° , and at the aft station at $\alpha = 8^\circ$. (See table II.)

For the first test condition, at $\alpha = 0^\circ$, the data from the probes were in exceptional agreement with the uncorrected static pressures, never differing by more than $0.05p_\infty$ throughout the flow field. For the second test condition, at $\alpha = 8^\circ$ at the forward station, the uncorrected pressures from the two probes differed by about $0.15p_\infty$. However, this difference ultimately caused only a 0.2-percent difference in local mass flow ratio. In the third test condition, at the aft survey station at $\alpha = 8^\circ$, the difference in the uncorrected station pressures grew to an average of $0.25p_\infty$. When these data were corrected, the differences increased to about $0.75p_\infty$ because the local Mach numbers and therefore the correction factors themselves were large. Static pressure differences of this magnitude resulted in differences in calculated local Mach numbers on the order of 1.0, and for the survey at $y/D = 0.236$ the calculated flow field Mach numbers exceeded the stream value of 6.0 and therefore ostensibly indicated an expansion across the bow shock. As will be seen subsequently, this situation happened again at the aft station at $\alpha = 8^\circ$ at $y/D = 0.354$. Fortunately, these uncertainties in

p_ℓ/p_∞ and their exaggerated effects on M_ℓ had little effect on local mass flow ratio, which, of course, was the parameter of most interest here. The relative sensitivity of Mach number and mass flow ratio can be demonstrated by assuming a 10-percent error in static pressure; the resulting change in Mach number would be 12 percent, but the change in mass flow ratio would be only 2 percent. A thorough review of the static pressure data gave no clue as to the source of this large discrepancy, but, in the end, the survey data yielding the larger values of p_ℓ/p_∞ were presented simply because they yielded local flow field Mach numbers always less than M_∞ .

APPENDIX B

WALL STATIC PRESSURES

The spanwise distribution of wall static pressures at the forward survey station is shown in figure B1. Although only half the model was instrumented with orifices, flow symmetry about the centerline was assumed in this figure in order to provide a better indication of the pressures across the entire body. The data are compared with tangent cone, tangent wedge, and three-dimensional MOC theories. The experimental data exceeded tangent cone and MOC predictions, with the highest pressure across the body occurring near the middle of the semispan. The favorable gradients (decreasing pressure) from this point toward the body centerline probably encouraged the thickening of the boundary layer at the centerline, as noted earlier. Pressure relief at the edge of the body for the MOC theory resulted from the edge rounding discussed previously. The most outboard experimental pressure was lower because of boundary layer bleed-off.

The variation of wall static pressure with angle of attack is shown in figure B2 for the four orifices at the forward survey station. At positive angles of attack, the experimental data fall about midway between tangent wedge and tangent cone theories. Similar results were obtained at Mach 6 on flat-surface bodies of widely different cross-section shapes in the tests reported in reference 1. These results suggest the need to develop a better pressure-deflection algorithm than the widely used tangent cone or tangent wedge methods.

In general, the three-dimensional MOC theory predicted the lowest pressure, with the results at the most outboard orifice indicating the influence of the body edge rounding required by that method.

The body centerline vertical-plane longitudinal static pressure distribution obtained from the three-dimensional MOC theory is shown in figure B3 at angles of attack of 4° and 8° . These results show that after the highly favorable gradient on the nose, the pressures continue to fall down the length of the body and thus provide a gradient favorable for the maintenance of laminar flow.

As indicated by the symbols at $x/D = 3.5$, the experimental pressures on the centerline were greater than had been predicted. Since the model was not instrumented for wall static pressures at the aft survey station ($x/D = 5.4$), and since these pressures are required to determine boundary layer velocity ratios, a linear extrapolation from the forward survey station was made, as shown in the figure, in order to calculate the boundary layer velocity ratios.

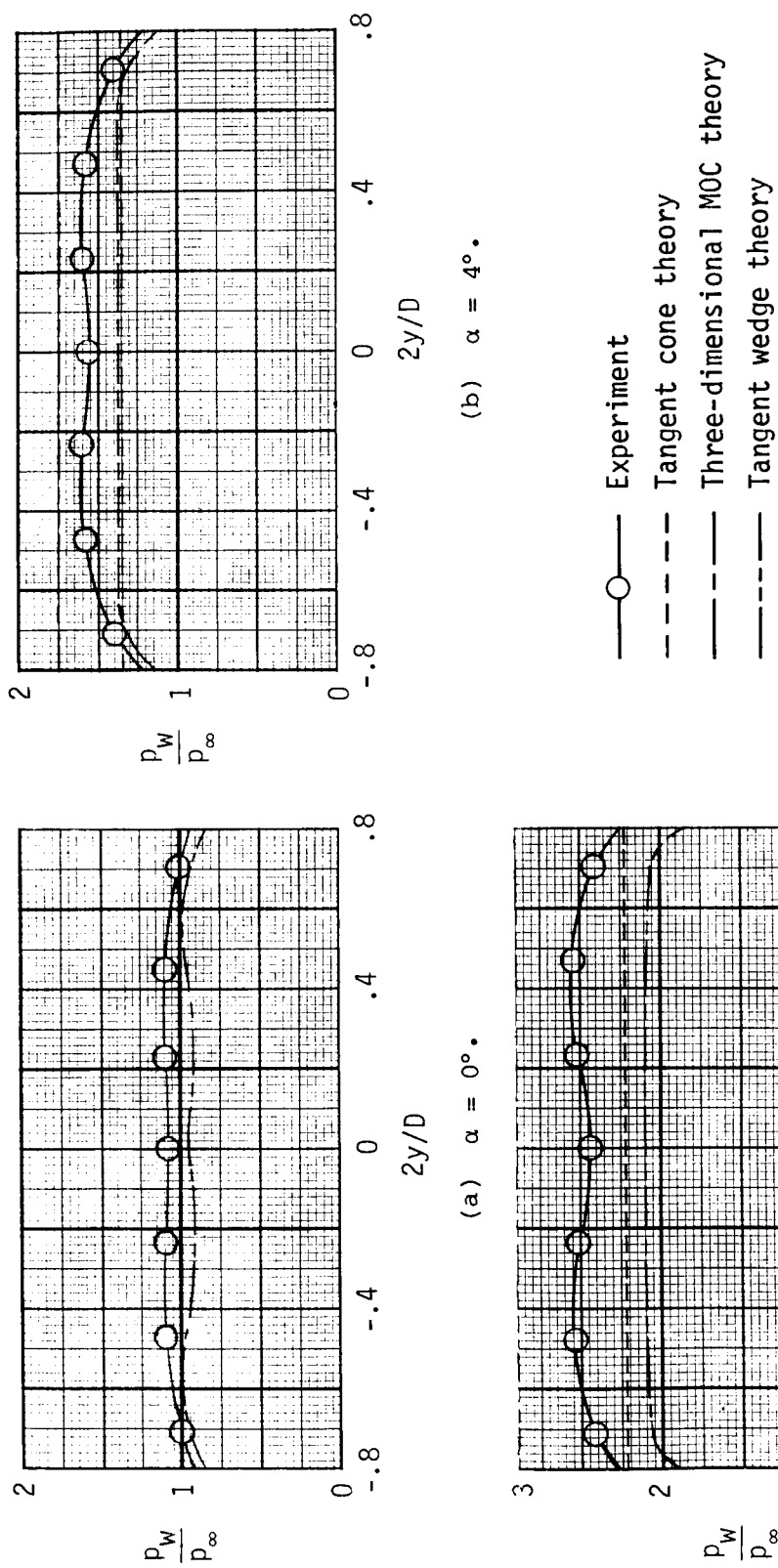
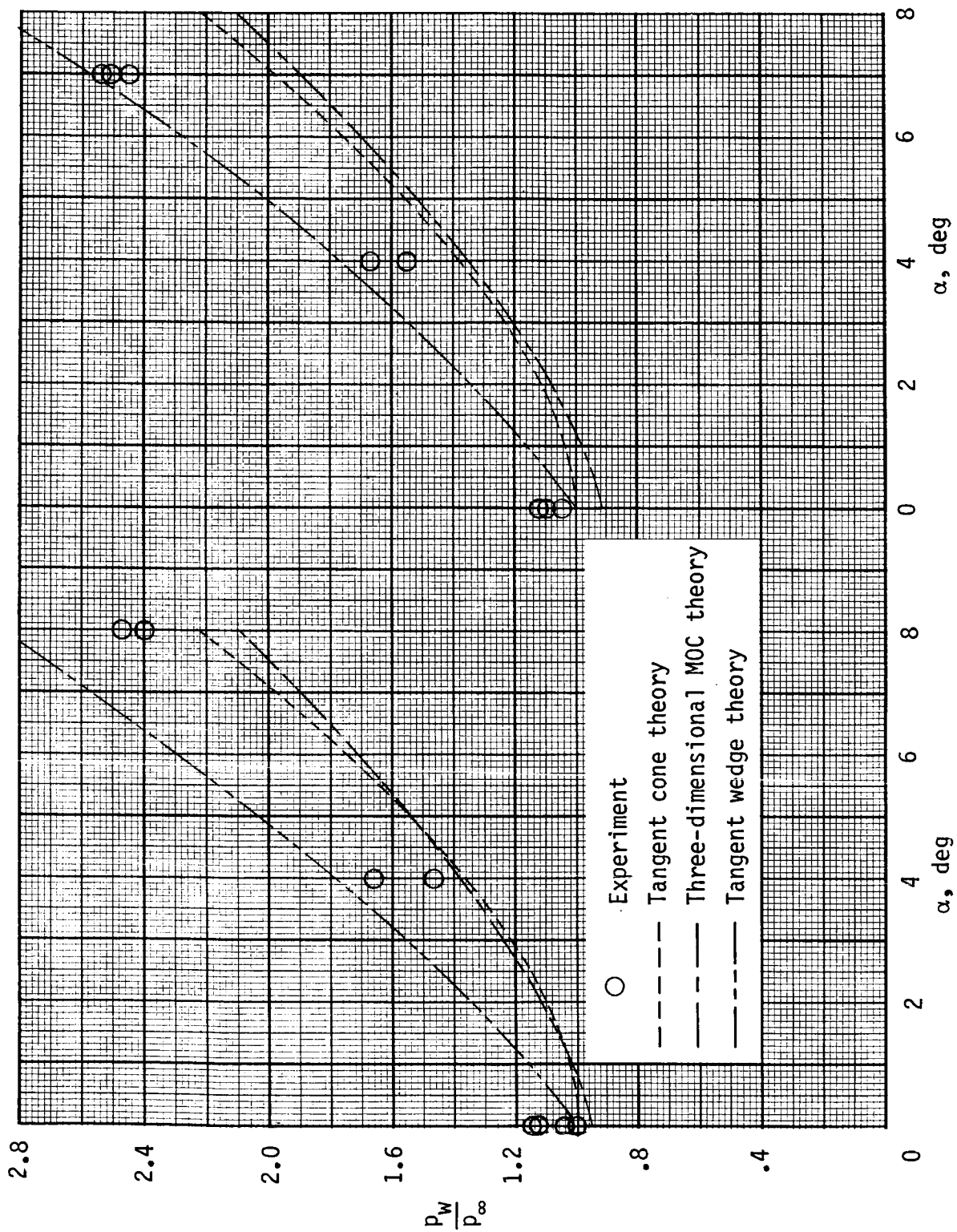
(c) $\alpha = 8^\circ$.

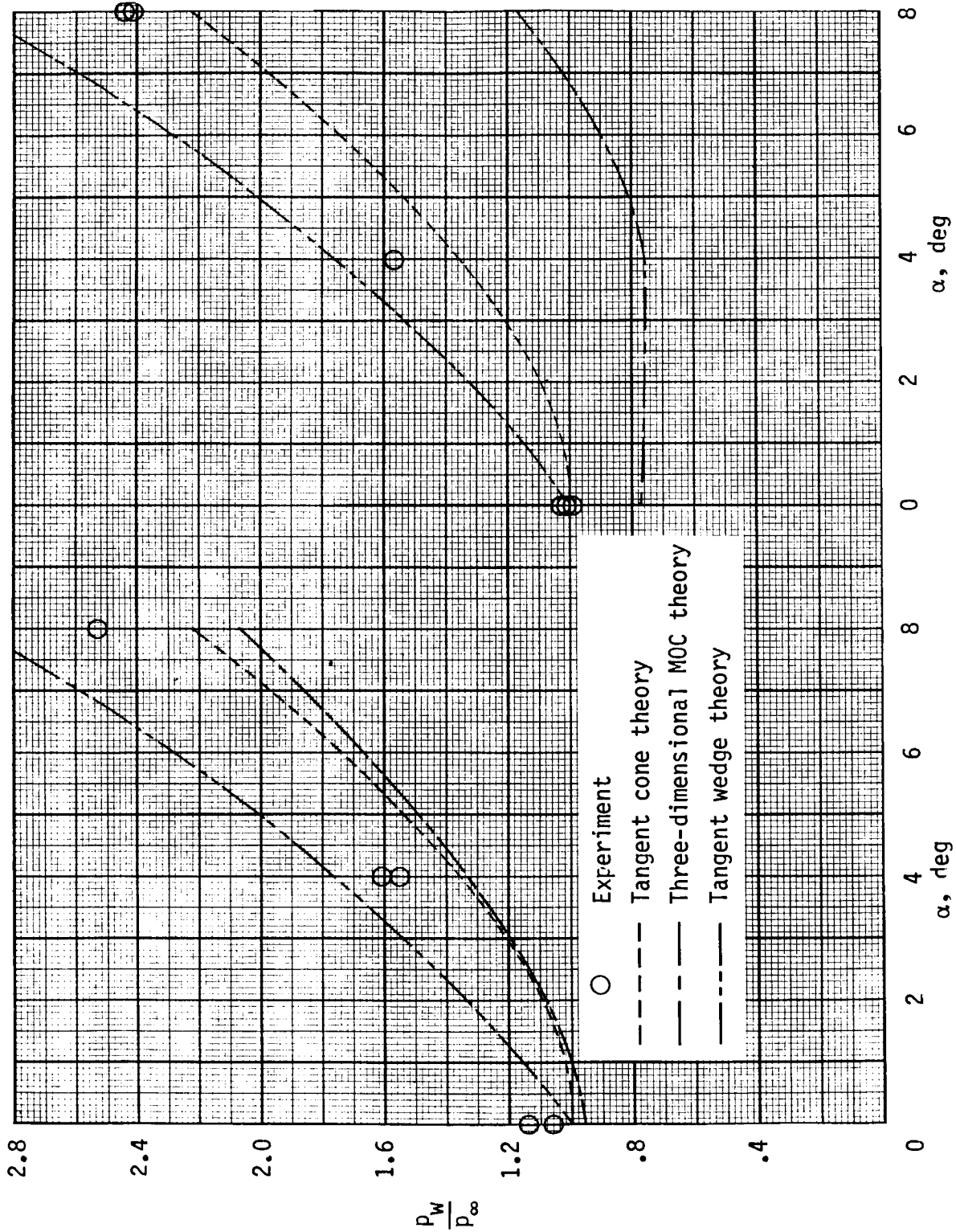
Figure B1.-- Wall static pressures at forward survey station.



(a) Orifice no. 1; $Y/D = 0$.

(b) Orifice no. 2; $Y/D = 0.118$.

Figure B2.-- Wall static pressures at $x/D = 3.5$.

(c) Orifice no. 3; $y/D = 0.265$.(d) Orifice no. 4; $y/D = 0.354$.

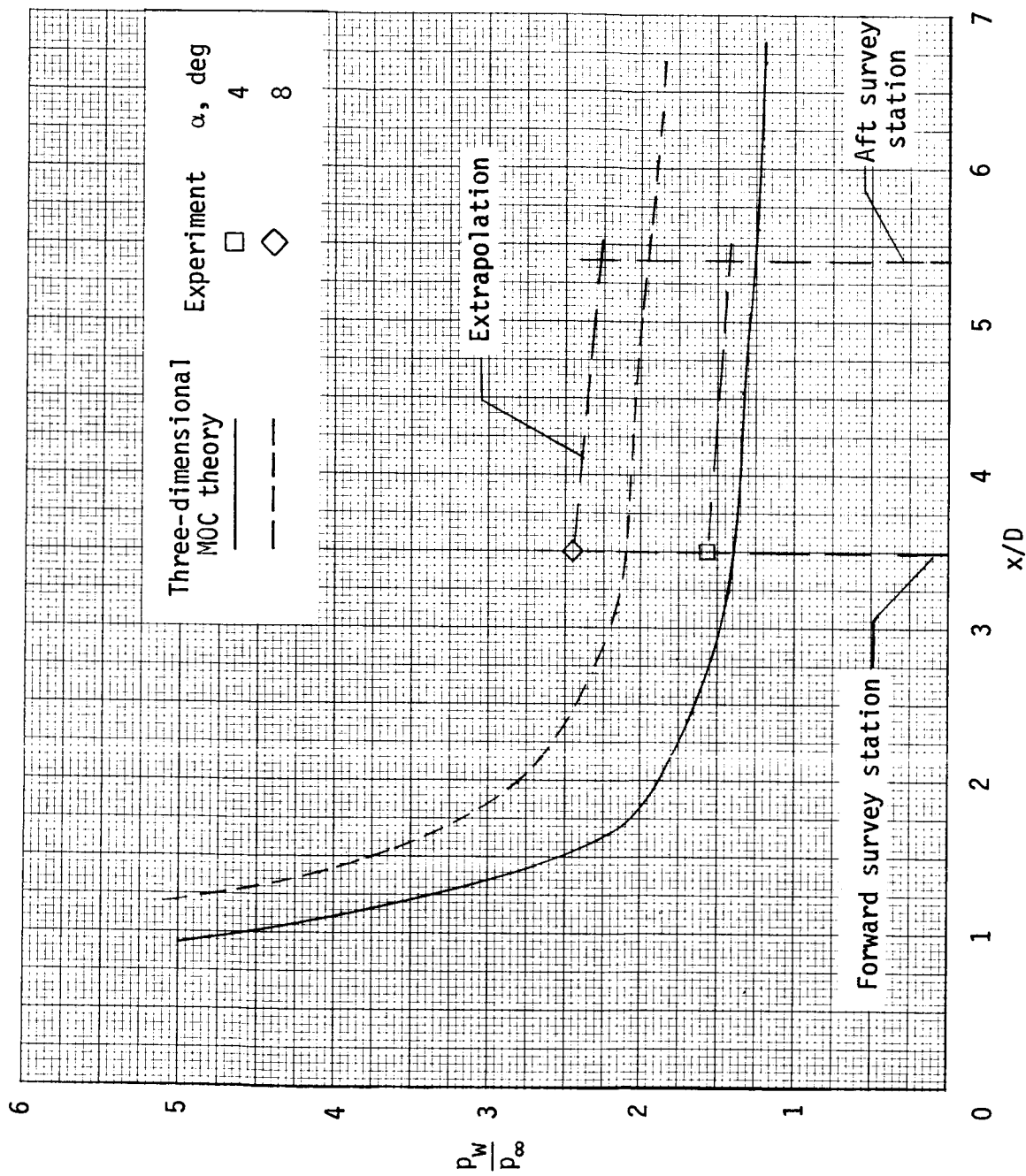


Figure B3.- Fuselage bottom centerline vertical-plane longitudinal static pressure distribution and method used to obtain wall static pressure at aft survey station.

APPENDIX C

DETAILED FLOW FIELD MEASUREMENTS

Forward Survey Station Results at $\alpha = 0^\circ$

Pitot pressure.- Pitot surveys for the five spanwise stations at $x/D = 3.5$ are shown in figure C1. At the two outermost stations, the pitot pressures exhibit an overshoot at the boundary layer edge which, as will be seen subsequently at positive angles of attack, was the rule rather than the exception at the forward survey station. This characteristic may be related either to the probe interference effect noted in reference 9 or to substantial spanwise velocity and angularity flow gradients which influence the pitot pressure readings.

The entropy gradient resulting from the blunt nose tip required for the inviscid MOC solution is evident in figure C1. The extrapolation of the MOC theoretical pressures to the wall is also shown in this figure. Efforts were made to predict the wall value of pitot pressure across the initial nose shock with conical shock theory and the assumption of isentropic flow downstream; however, the resulting pitot pressures were excessive, especially for stations off the plane of symmetry.

Static pressure.- Results of the static pressure probe surveys at $\alpha = 0^\circ$ are shown in figure C2. As noted in table II, no static pressure data were taken at $y/D = 0.118$ and 0.354 , but available MOC results at these stations are shown in figures C2(b) and C2(d) for completeness.

Figure C2(a) shows both the corrected and uncorrected static pressure surveys on the model centerline vertical plane. These data illustrate several important points that have been alluded to elsewhere in the paper. The first is the probe correction factor. As indicated by the free-stream uncorrected data shown here, the correction factor in this case at $\alpha = 0^\circ$ at Mach 6 was 1.521. As indicated in appendix A, the correction factor was unity at Mach 4; consequently no corrections were applied to the probe readings at Mach numbers below that. In figure C2(a) at heights above $z/D = 0.084$ (where the indicated local Mach number reached 4.0) the corrected static pressures change rapidly with height because this is a region of very large Mach number gradient (see fig. C3(a)) and because of the ramp-type correction factor assumed between Mach 4 and 6.

The second point to be noted is that the curves were faired in this and subsequent figures to the wall value of static pressure as indicated by the surface static pressure orifice. As will be seen in later figures, there was a good deal of scatter in the static pressure data when the probe was adjacent to the wall. This scatter was probably the result of both wall interference effects and large spanwise flow gradients toward the edge of the body, either of which would affect the probe readings.

Finally, it should be noted that the static probes had a relatively large diameter compared to the boundary layer thickness either at the edge of the body or at higher angles of attack. In many instances, if the erratic probe readings adjacent to the wall were ignored, it was relatively easy to visually extrapolate the static probe data to the wall static values and thus gain some insight whether there were static pressure gradients across the boundary layer. A constant static

pressure across the boundary layer is assumed in classical incompressible boundary layer theory but is not necessarily true when M^2 is large (ref. 23).

Finally, the corrected static pressure data at the shock were faired with shock positions determined from the pitot pressure data. These were much more abrupt than the measured static pressure data, which were obviously influenced by the effects of probe diameter and pressure gradients.

When the data in figures C2(a), C2(c), and C2(e) are compared, the static pressure gradients at the wall appear to increase toward the outermost survey station, although this increase is difficult to demonstrate precisely because of the lack of a wall static orifice at the most outboard station and the occurrence of the aforementioned erratic variations in both pitot and static pressure there.

In the shock layer, the corrected probe static pressures exceeded the MOC prediction on the vehicle axis (fig. C2(a)) but gradually fell below the predicted values toward the edge of the body (fig. C2(e)).

Mach number.— The shock layer Mach number distributions in figure C3 were determined from the Rayleigh pitot equation and the corrected static pressures of the previous figure. At hypersonic speeds, the Mach number is extremely sensitive to static pressure, and considerable scatter is evident in figure C3 and subsequent figures that depict this parameter. The extraneous data in the vicinity of the shock are caused by the static probes crossing the inclined shock at a slightly different z value than was obtained in the pitot pressure surveys. These data were ignored in the fairings.

Mass flow ratio.— The local mass flow ratios, \dot{m}/\dot{m}_∞ , across the flow field are shown in figure C4. In the inviscid flow between the boundary layer and the shock there appear to be some small but consistent deviations between the theory and experiment across the body; nevertheless, the MOC mass flow predictions appear to be sufficiently accurate to determine the available mass flow at the inlet.

Forward Survey Station Results at $\alpha = 4^\circ$

Pitot pressure.— The surveys at $\alpha = 4^\circ$ were terminated before the shock position was reached on the body centerline vertical plane. The outermost three probes had penetrated into the free stream and the centerline vertical-plane shock position was therefore determined by extrapolation. The data in figure C5 show a progressive divergence away from the MOC theory at the outboard stations. In addition, the aforementioned pitot pressure overshoot at the edge of the boundary layer is more widespread than at $\alpha = 0^\circ$ and occurred at all five spanwise survey stations.

As noted previously, tangent cone theory is frequently used to estimate local conditions in windward flow fields at hypersonic speeds. Parameters obtained with this method at the shock and on the body surface are shown here and on later figures by vertical lines at those flow field boundaries. The obvious shortcomings of this method are evident in figure C5; the method does not predict the nearly 2:1 pitot pressure gradient measured across the shock layer of this body at $\alpha = 4^\circ$.

Static pressure.- Only two spanwise stations were surveyed at $\alpha = 4^\circ$: $y/D = 0.0$ and 0.236 . These data are shown in figure C6 along with the MOC theory predictions.

In the body centerline vertical plane (fig. C6(a)) the corrected probe static pressures were easily extrapolated to the experimental value measured at the wall. Such a fairing indicated negligible static pressure gradients across the boundary layer. At $y/D = 0.236$ (fig. C6(c)), however, the static pressure at the wall was substantially higher than the corrected probe pressures, and a fairing through the data as shown in the figure indicates a static pressure gradient across the boundary layer. These data are similar to results at $\alpha = 0^\circ$. However, at $\alpha = 4^\circ$ it appears that the transverse boundary layer gradients increased with spanwise distance. Since the probes were shown to be relatively insensitive to angle of attack (ref. 5), the off-centerline plane data presented here may have been influenced by spanwise static pressure gradients across the probe itself.

For the two spanwise stations at which experimental data were available, the corrected static pressures appear to be decreasing in the spanwise direction, whereas the MOC theory predicted a nearly constant pressure. In the vertical direction, the tangent cone method indicates the characteristic decrease in static pressure across the shock layer, as indicated by the vertical lines. This trend is opposite to the experimental and MOC theory pressure variation.

Mach number.- The variation of local Mach number across the flow field at $\alpha = 4^\circ$ is shown in figure C7. Here, the agreement of experimental data with MOC theory across the inviscid part of the flow field is believed to be good considering the sensitivity of Mach number to static pressure. The tangent cone method over-predicted the Mach number at the surface and predicted a much smaller loss in Mach number at the bow shock.

Mass flow ratio.- As indicated in figure C8, the mass flow ratios predicted by the MOC theory are in excellent agreement with the experimental data for the two spanwise stations for which experimental data are available. The tangent cone method, on the other hand, overpredicts the mass flow at the wall and grossly under-predicts the mass flow at the shock. Even an average of these two values, which is often used to make preliminary estimates of inlet mass flow, would clearly under-predict the actual mass flow available to an inlet at this longitudinal body survey station where the transverse gradients caused by forebody curvature are large.

Forward Survey Station Results at $\alpha = 8^\circ$

Pitot pressure.- Figure C9 shows the pitot pressure survey results at $\alpha = 8^\circ$. This is the angle of attack of primary interest because it is approximately the cruise angle of attack for maximum trimmed lift-drag ratio.

At $\alpha = 8^\circ$, the experimental pressures exceed the MOC theory predictions over the inner half of the flow field in the body centerline vertical plane, and this discrepancy spreads to the shock at the more outboard survey station. As before, the shock and wall pitot pressures predicted by the tangent cone method are indicated by vertical lines. It appears that an average of these two values is more accurate at $\alpha = 8^\circ$ than at lower angles of attack.

The overshoot in pitot pressure at the boundary layer edge is more prominent than at lower angles of attack because the boundary layer is thinner. In addition,

flow irregularities adjacent to the body at the outboard survey station (fig. C9(e)) are more pronounced than at lower angles of attack.

Static pressure.- None of the corrected experimental static pressure surveys (fig. C10) exhibited the positive pressure gradients from the body to the shock predicted by MOC theory. Extrapolating the corrected static pressures to the measured wall static pressure indicated negative pressure gradients across the boundary layer at least out to the spanwise station at $y/D = 0.236$. Beyond this station, irregularities in the flow (evidenced by both pitot and static pressures) made it difficult to discern how the static pressure varied across the boundary layer.

At the shock, the jump in experimental static pressure was much less than was predicted by MOC theory.

Mach number.- As shown in figure C11, the experimental flow field Mach numbers were consistently higher than was predicted by MOC theory because of the lower than predicted static pressures. The large scatter in the experimental Mach numbers in the vicinity of the bow shock in figure C11 is attributed to the fact that the static pressure probes did not cross the shock at the same indicated z/D value as the pitot probes because of slight misalignments or deflection of the static probes under aerodynamic loads. As indicated by the fairings in the figure, these data were considered erroneous and were ignored in the fairings at the shock. The pitot and static pressure excursions noted previously result in large and rapid changes in indicated Mach number adjacent to the body at the outer two survey stations (figs. C11(d) and C11(e)).

Mass flow ratio.- Mass flow ratio distributions for the five spanwise stations are given in figure C12. At $\alpha = 8^\circ$, the experimental mass flow ratios exceeded those predicted by MOC theory, especially at the inboard stations and in that portion of the flow field closest to the body. These discrepancies continued to the shock at stations outboard of $y/D = 0.236$. Tangent cone mass flow ratios at the shock were only about half the difference between free stream and the maximum measured in the flow field. On the other hand, the tangent cone values at the wall were too large, so that the average value was, in fact, very near that measured. This agreement is fortuitous and would only be applicable to full-capture inlets with cowl lips at the bow shock.

Aft Survey Station Results at $\alpha = 4^\circ$

As indicated in table II, only pitot surveys were made at $\alpha = 4^\circ$ at the aft survey station; consequently, Mach number and mass flow ratios could not be determined. Complete MOC theory results and experimental pitot pressures are presented in figure C13. Only MOC predictions and tangent cone results at the shock and wall are given in figure C14 to C16.

Pitot pressure.- The experimental pitot pressure data in figure C13 show good overall agreement with MOC theory in the inviscid part of the shock layer. In the vicinity of the boundary layer edge, data at this fuselage station exhibit a somewhat different character than similar data at $x/D = 3.5$ in that, for most spanwise stations, the overshoot is more rounded.

It should be noted that the pitot pressure gradient from the wall to the bow shock is only about half that measured at the forward survey station ($x/D = 3.5$). At the $x/D = 5.4$ body station at 4° angle of attack, the average of the two tangent cone predictions of the pitot pressure appears to give reasonable results for this parameter.

Static pressure, Mach number, and mass flow ratio distributions across the shock layer as obtained from the MOC theory are shown in figures C14 to C16.

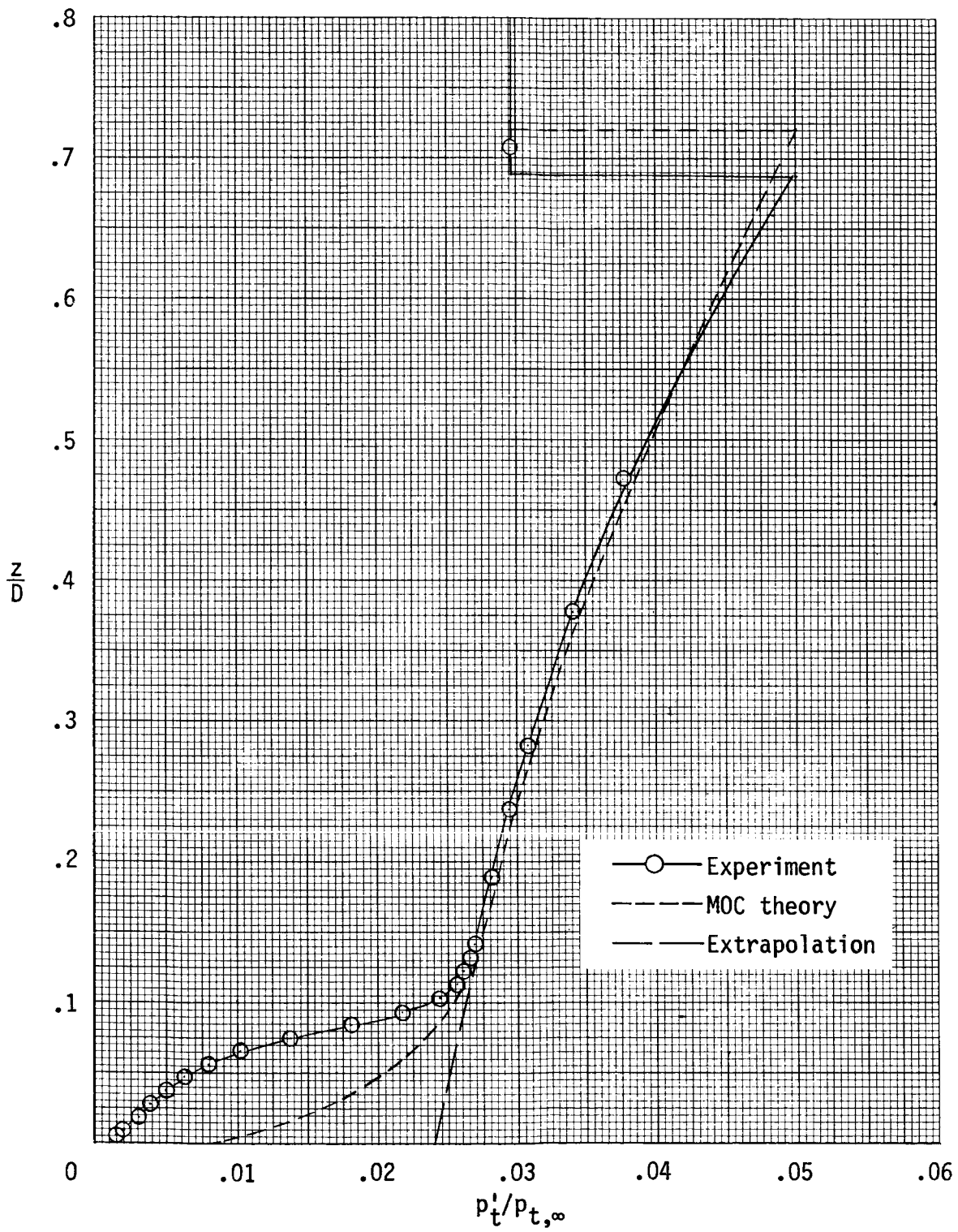
Aft Survey Station Results at $\alpha = 8^\circ$

Pitot pressure.— The experimental pitot pressure data (figs. C17(a) to C17(e)) show consistently good agreement with MOC theory predictions, but there seem to be certain systematic deviations over the inner portion of the shock layer which were not predicted by the theory.

Static pressure.— The static probe results at the aft survey station are shown in figure C18. Unlike the theoretical trend, which shows the static pressure increasing from the body to the shock, the experimental data in the body centerline vertical plane exhibit a decrease in pressure out to about the middle region of the shock layer and then a near constant pressure region beyond that point. At the more outboard stations, the experimental pressures have the same trend as the theory. Figure C18(c) shows the data obtained at $y/D = 0.236$ from the two static probes. The uncorrected static pressure data (not shown) from the two probes showed a consistent $0.25p_\infty$ difference across the flow field and a difference of $0.14p_\infty$ with the probes in the free stream. The latter determined the magnitude of the Mach number correction, which was applied to the uncorrected probe readings. The combination of these two factors contributed to the large differences in static pressure shown in figure C18(c), which averaged about $0.75p_\infty$. This was the largest error in static pressure measured in the tests. In other situations where data from two probes were available for comparison, the differences in uncorrected static pressure were $0.1p_\infty$ (or less) and the free-stream values were such that the Mach number corrections made the two sets of data indistinguishable. In the Mach number and mass flow data which follow, the higher values of static pressure from figure C18(c) were used simply because they yielded Mach numbers in the flow field less than M_∞ .

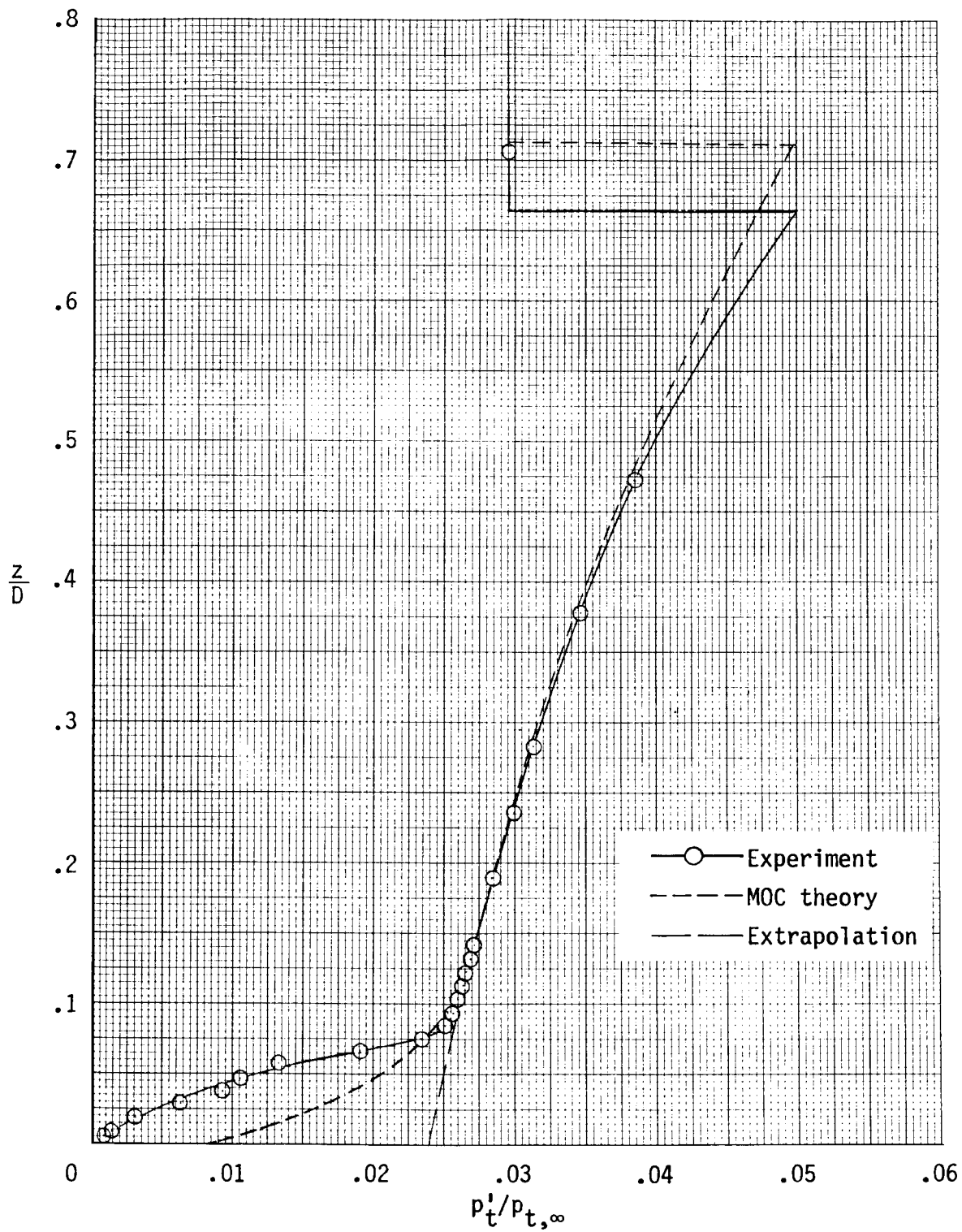
Mach number.— Because the corrected static pressures fell below the MOC predictions, the experimental Mach numbers in figure C19 were substantially higher than predicted, especially in the outer portions of the flow field. An example of the extreme sensitivity of Mach number to static pressure is indicated in figure C19(d), which shows that over the outer half of the shock layer, the indicated local Mach number obtained from pitot and corrected static pressures actually exceeded the stream Mach number and showed an erroneous decrease in Mach number across the bow shock.

Mass flow ratio.— Mass flow ratio distributions across the shock layer at $\alpha = 8^\circ$ are shown in figure C20. The agreement with the mass flows predicted by MOC theory was better than that found at the forward survey station at an equivalent angle of attack. It is coincidental that the decrease in mass flow caused by the boundary layer nearly matched the mass flow defect attributed to the entropy layer that was caused by the spherical nose cap required for the MOC solution.



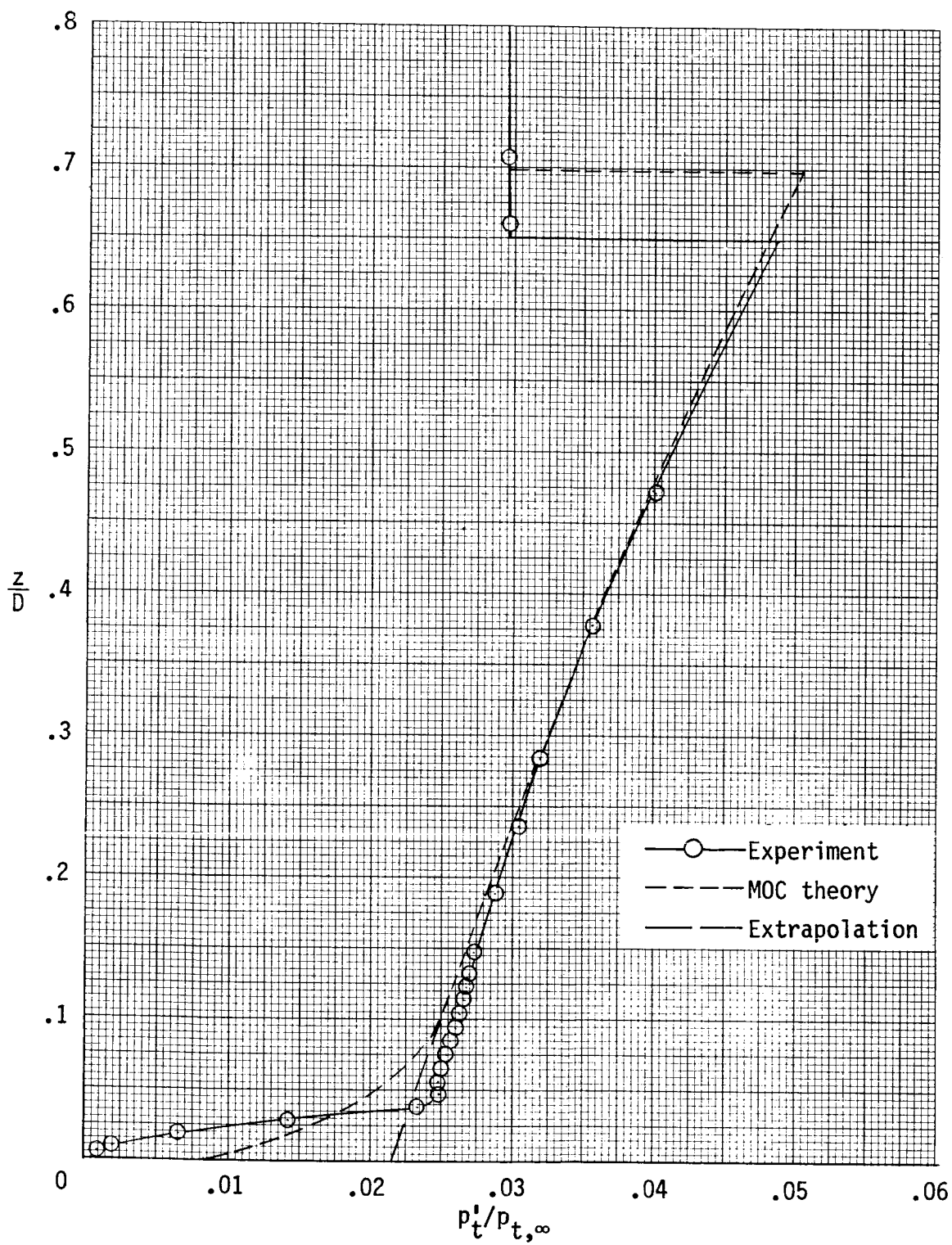
(a) $y/D = 0$.

Figure C1.- Pitot pressure survey at forward survey station
($x/D = 3.5$) at $\alpha = 0^\circ$.



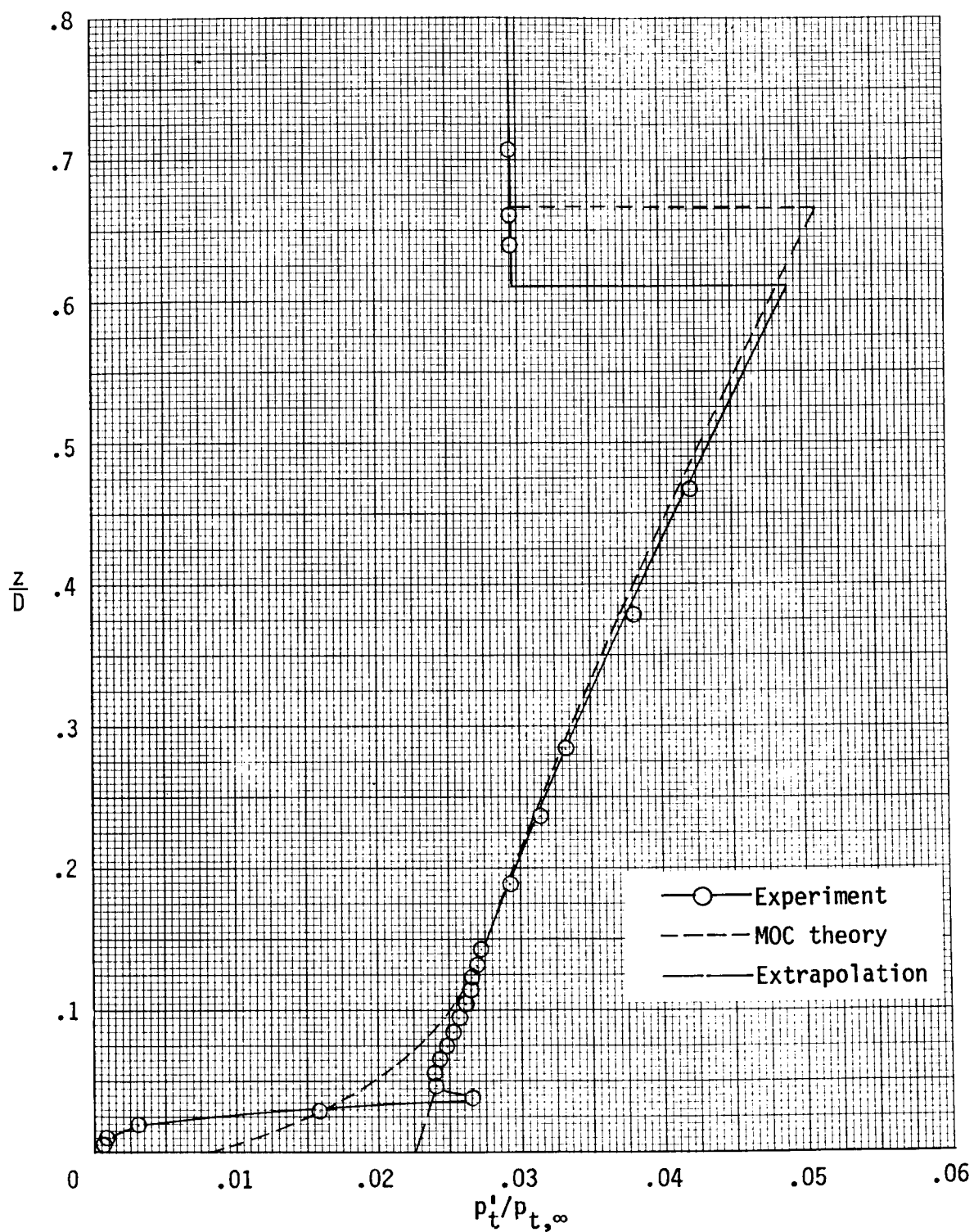
(b) $y/D = 0.118$.

Figure C1.- Continued.



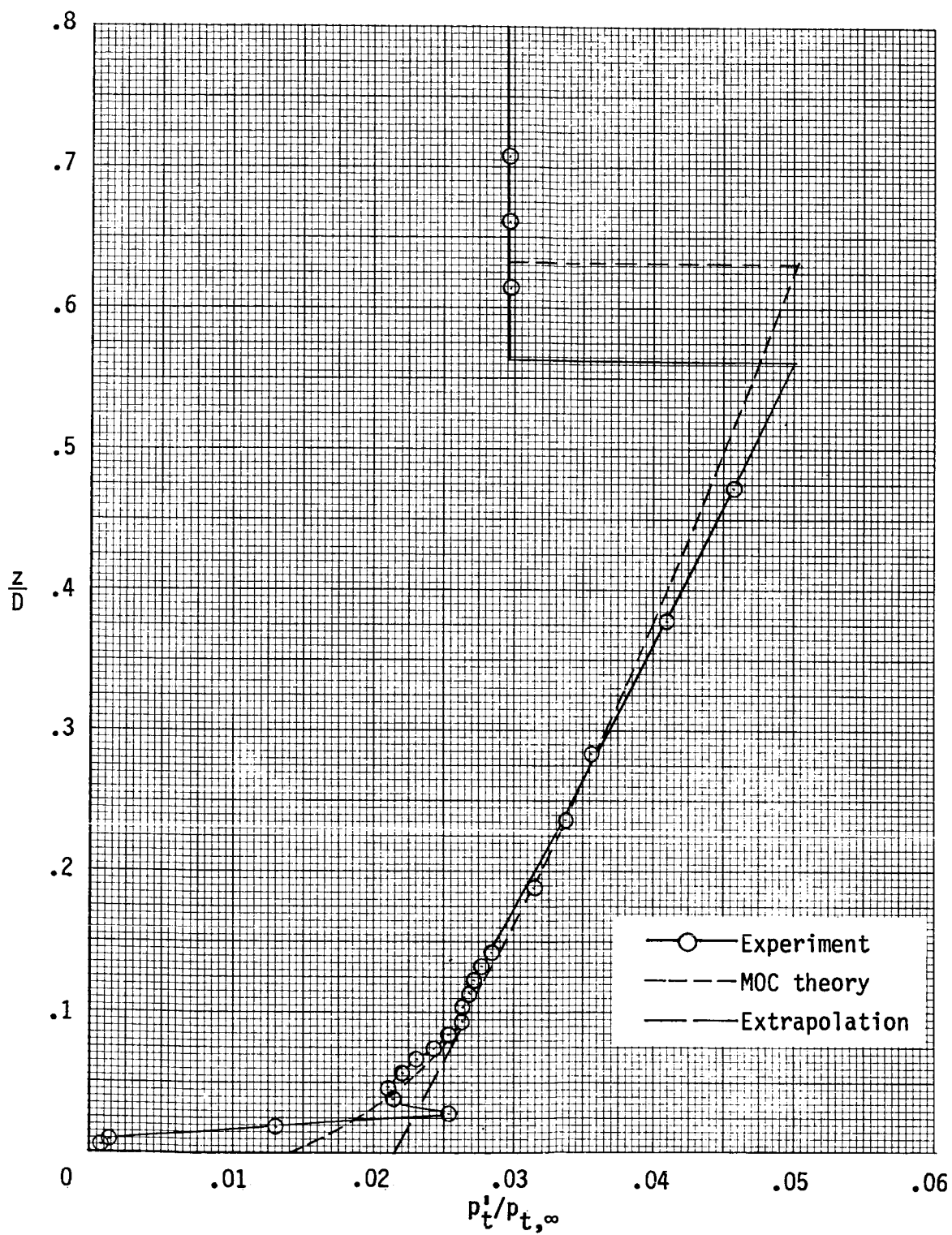
(c) $y/D = 0.236$.

Figure C1.- Continued.



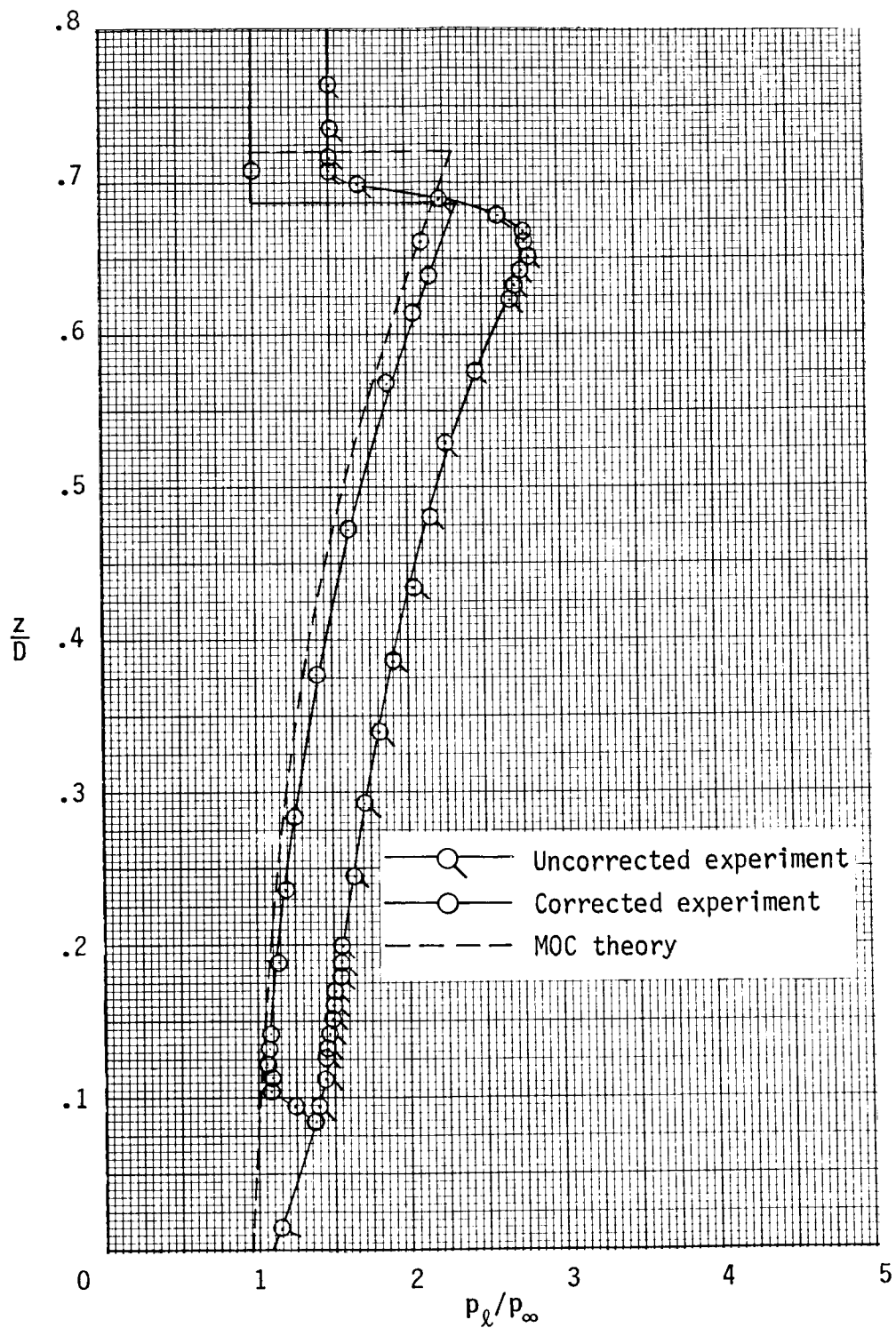
(d) $y/D = 0.354$.

Figure C1.- Continued.



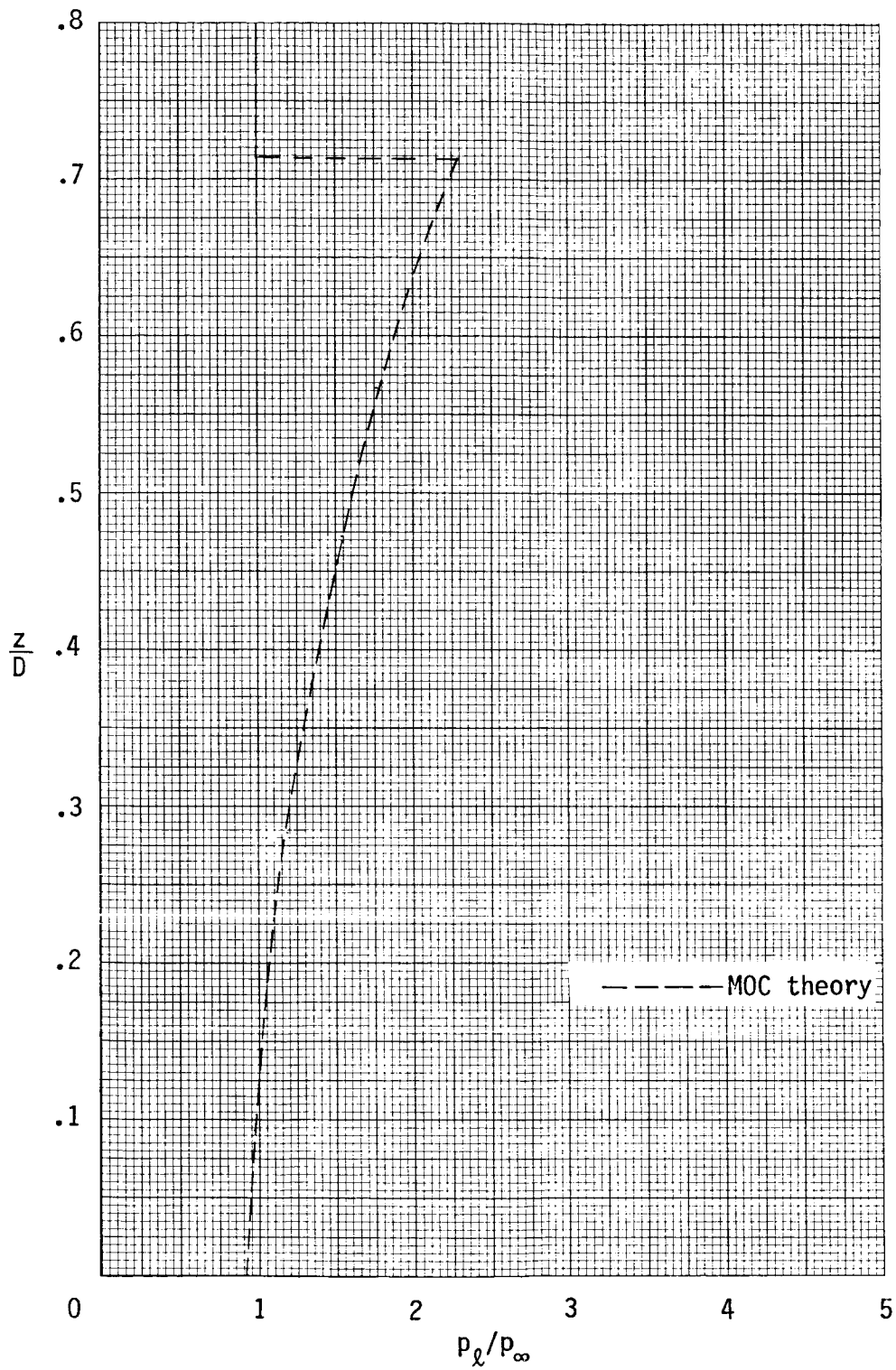
(e) $y/D = 0.472$.

Figure C1.- Concluded.



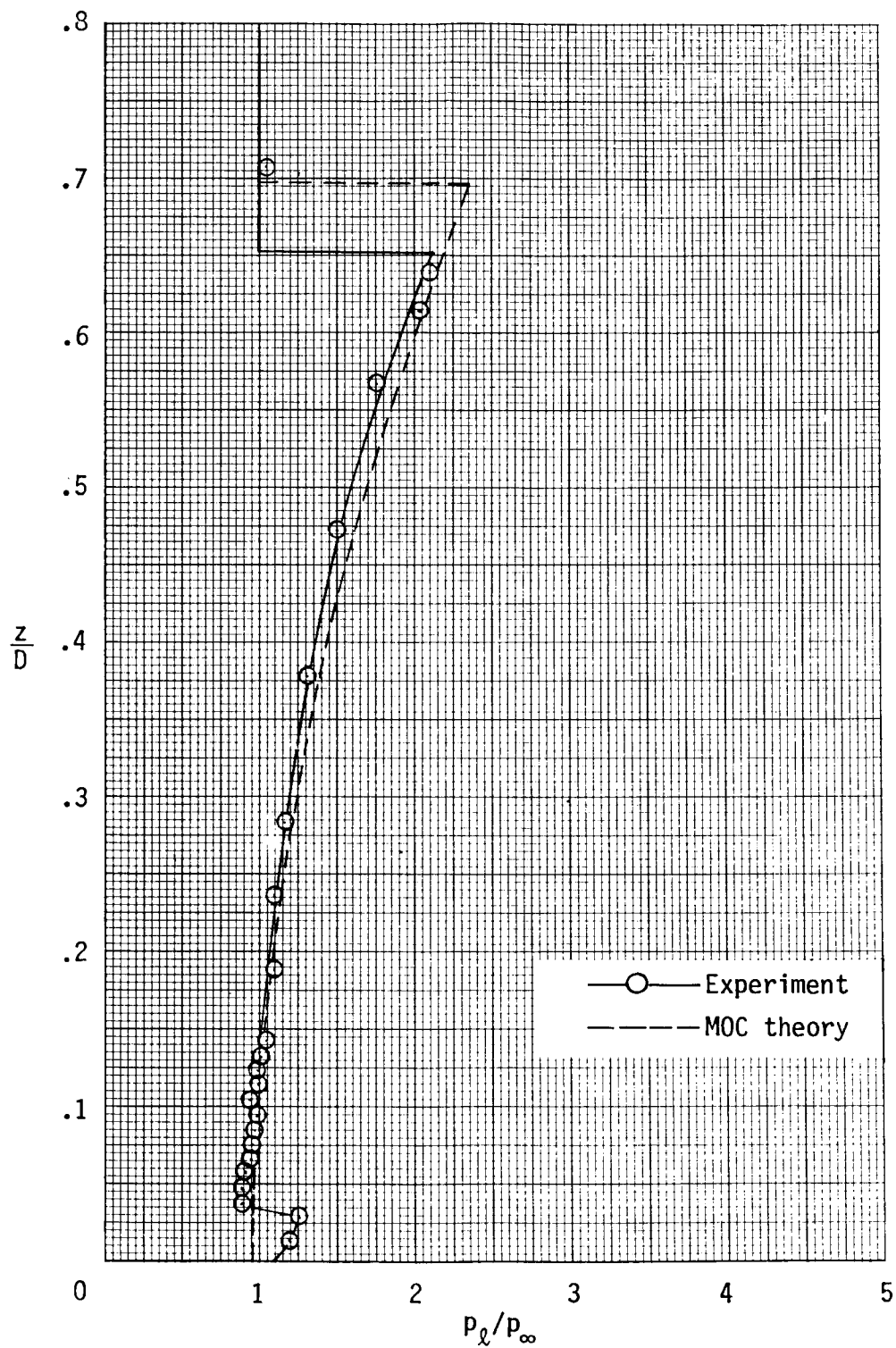
(a) $y/D = 0$.

Figure C2.- Static pressure survey at forward survey station ($x/D = 3.5$) at $\alpha = 0^\circ$.



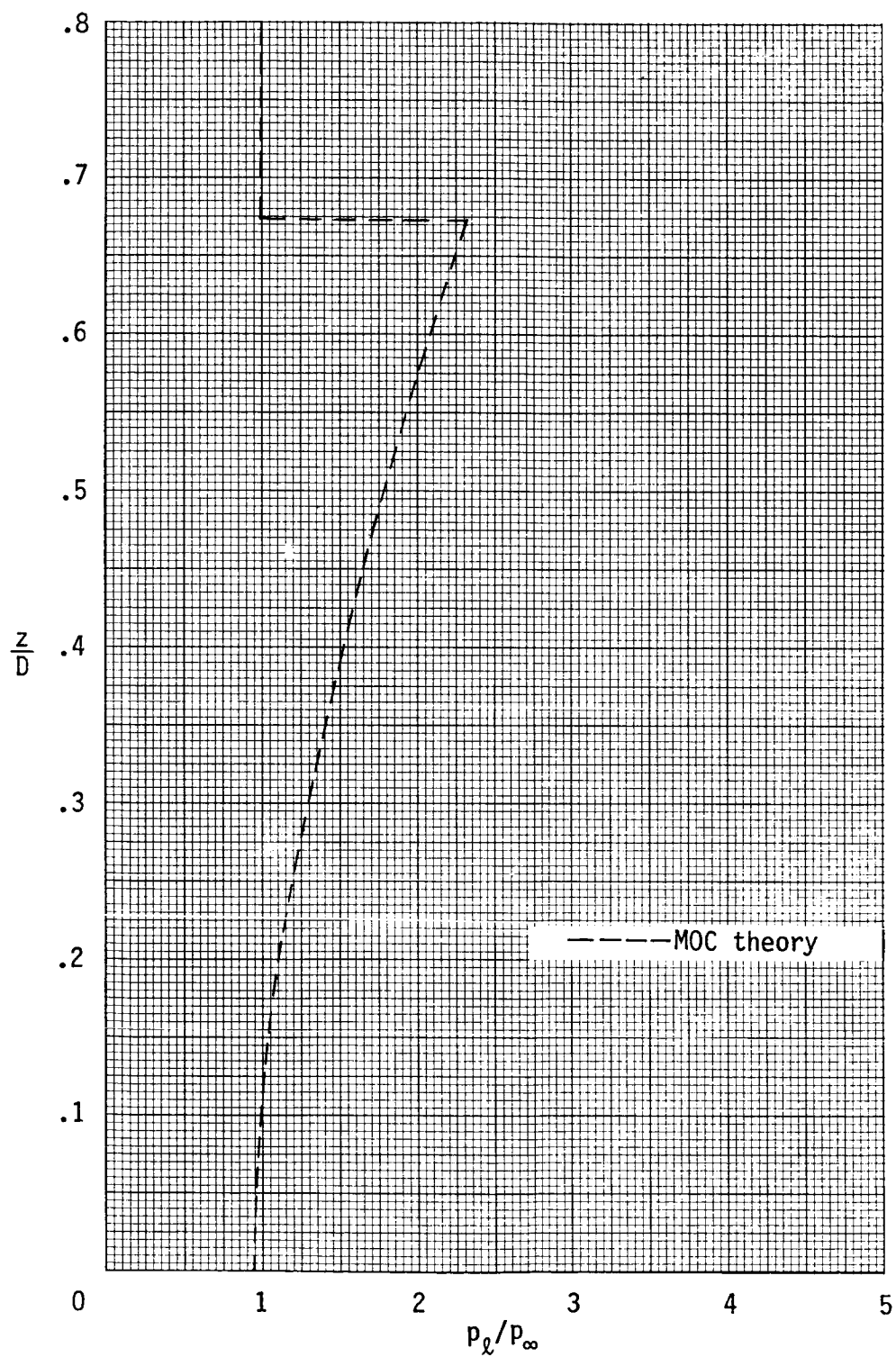
(b) $y/D = 0.118$.

Figure C2.- Continued.



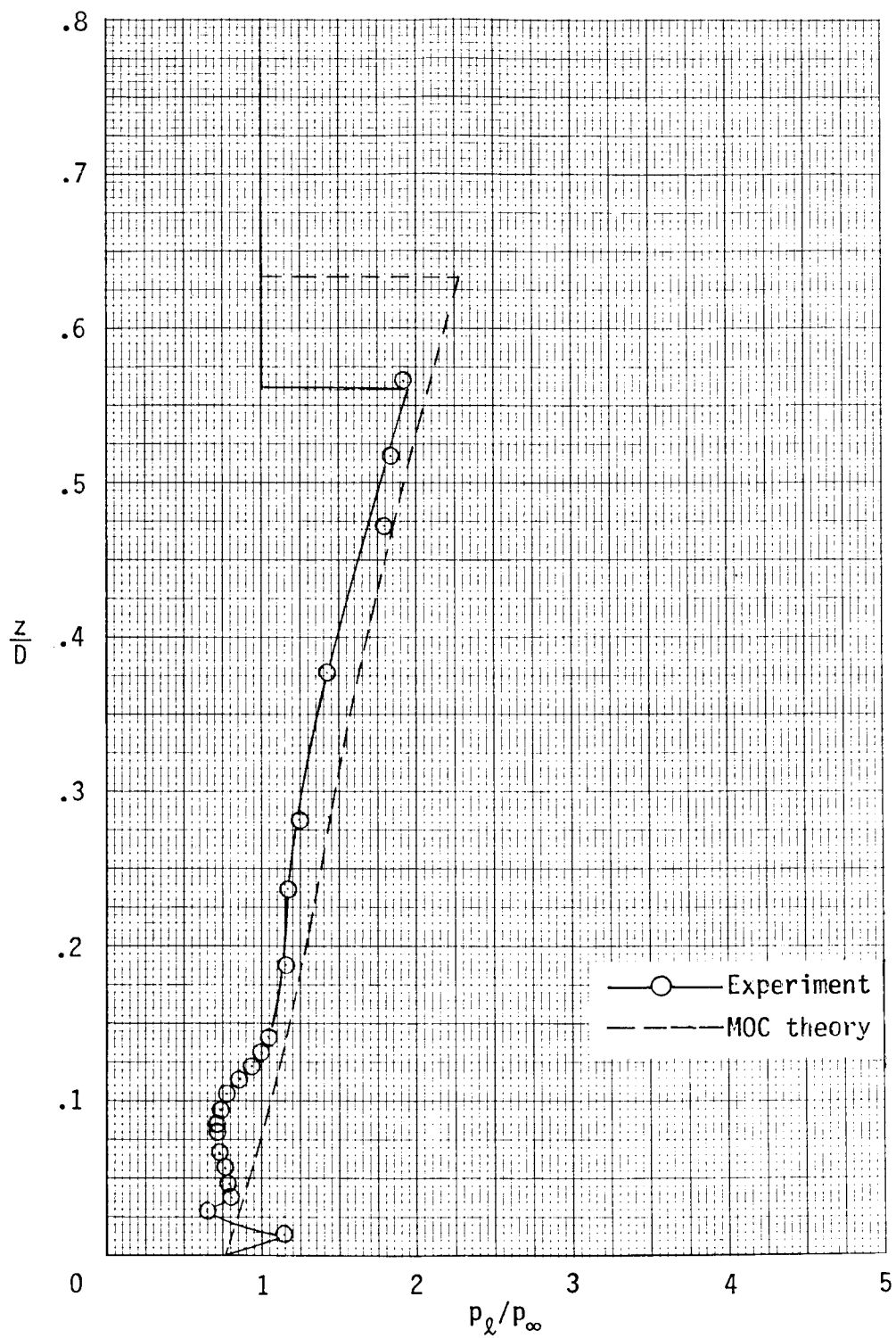
(c) $y/D = 0.236$.

Figure C2.- Continued.



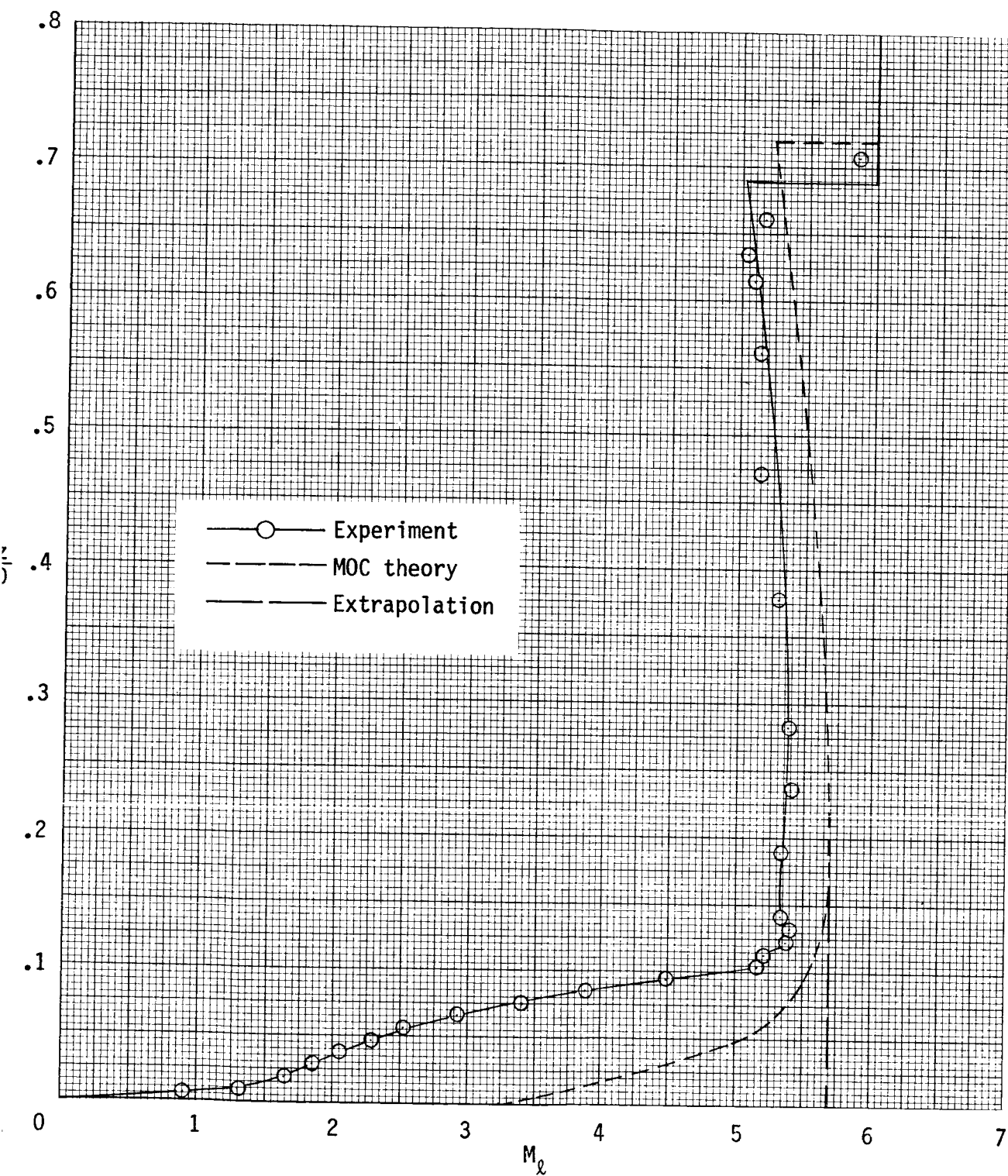
(d) $y/D = 0.354$.

Figure C2.- Continued.



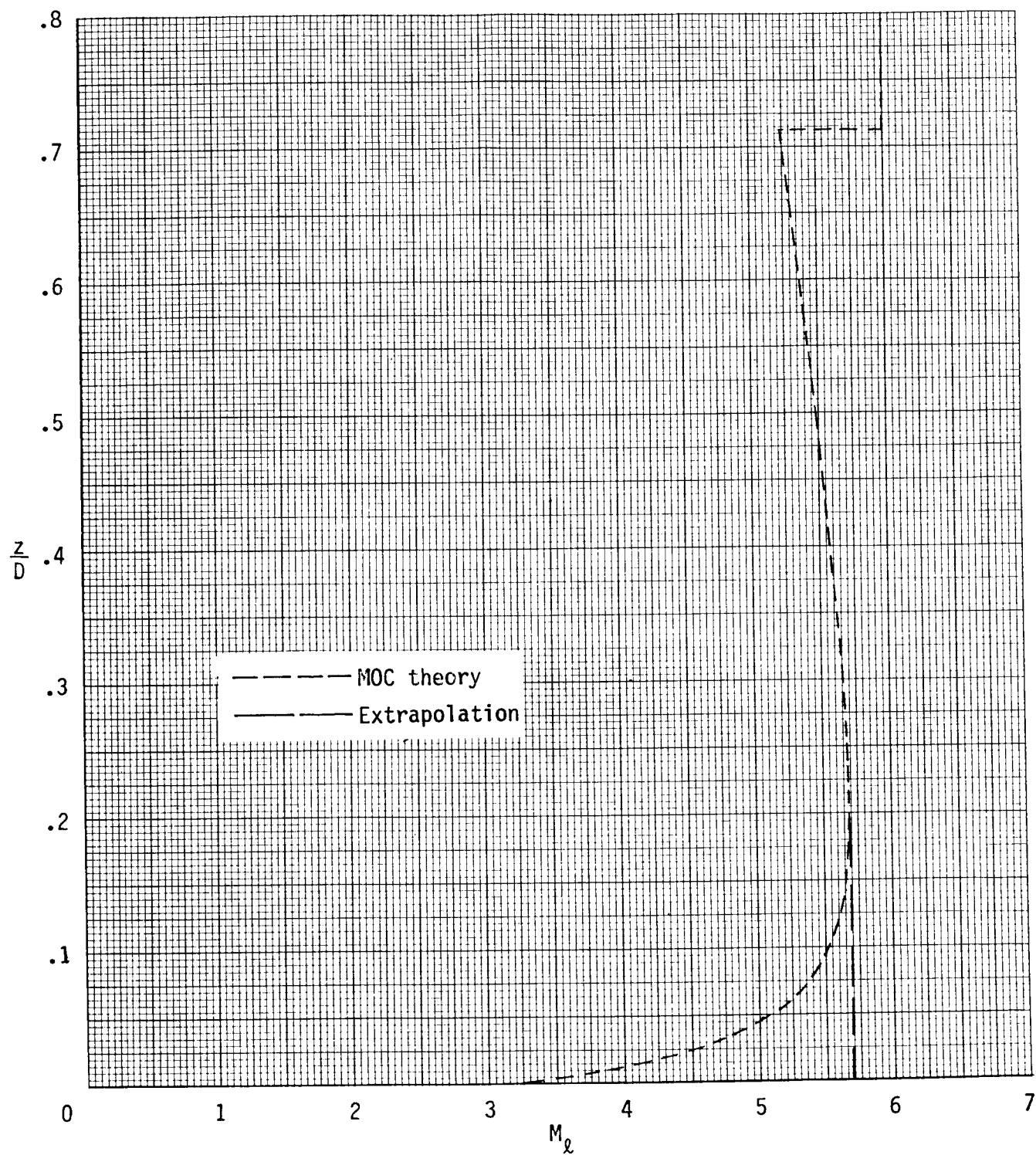
(e) $y/D = 0.472$.

Figure C2.- Concluded.



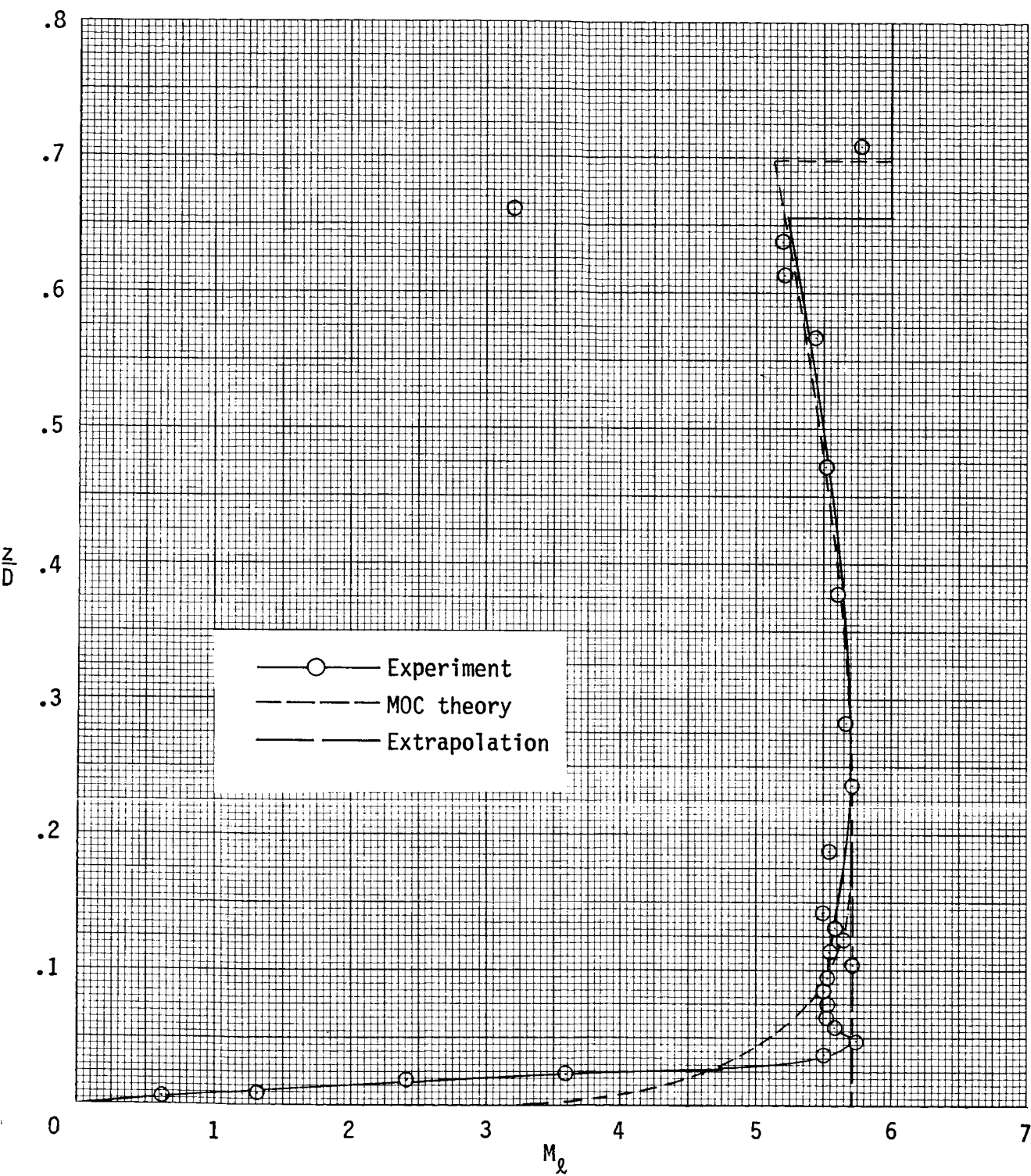
(a) $y/D = 0$.

Figure C3.- Local Mach number distribution at forward survey station ($x/D = 3.5$) at $\alpha = 0^\circ$.



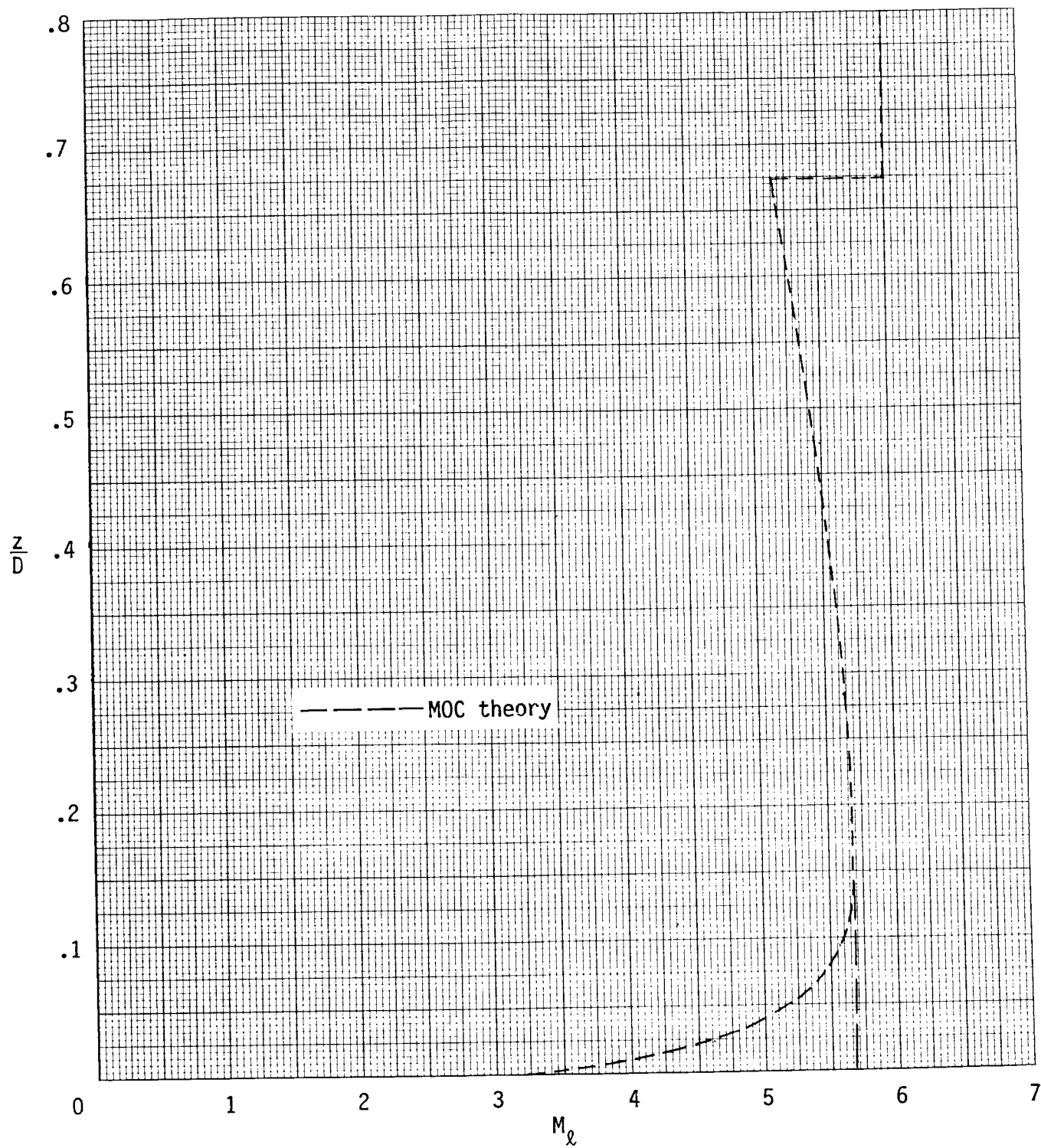
(b) $y/D = 0.118$.

Figure C3.- Continued.



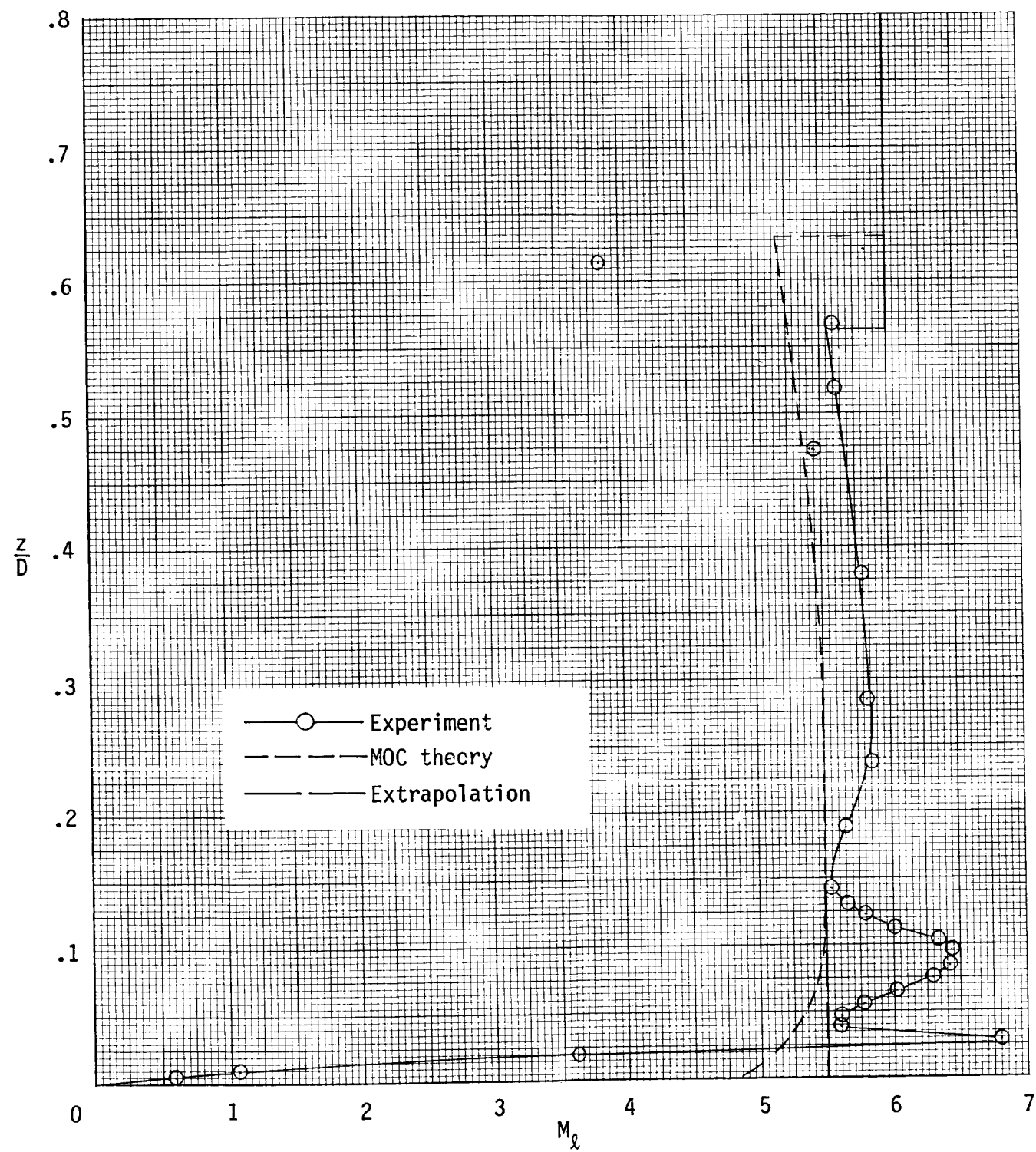
(c) $y/D = 0.236$.

Figure C3.- Continued.



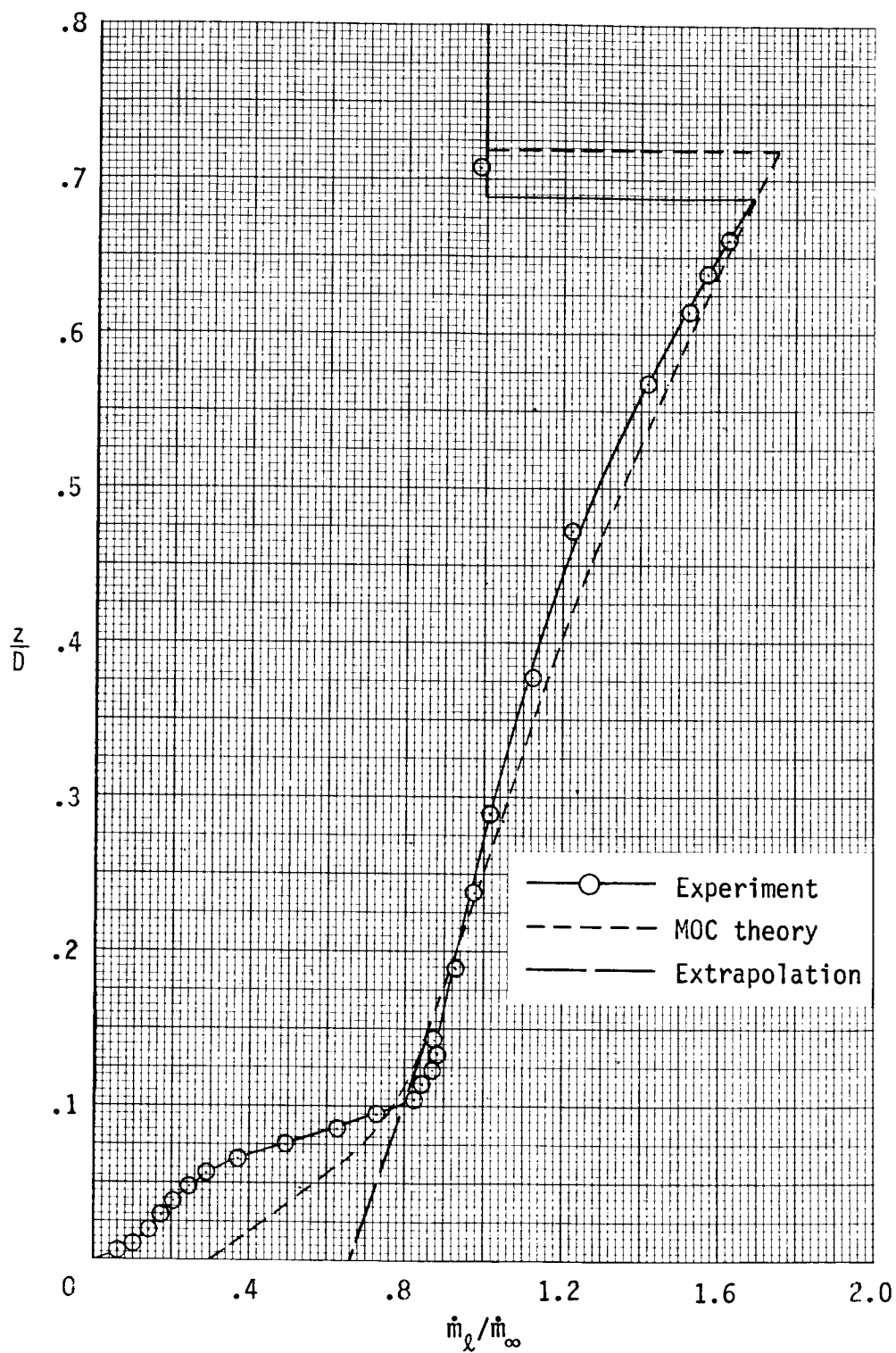
(d) $y/D = 0.354$.

Figure C3.- Continued.



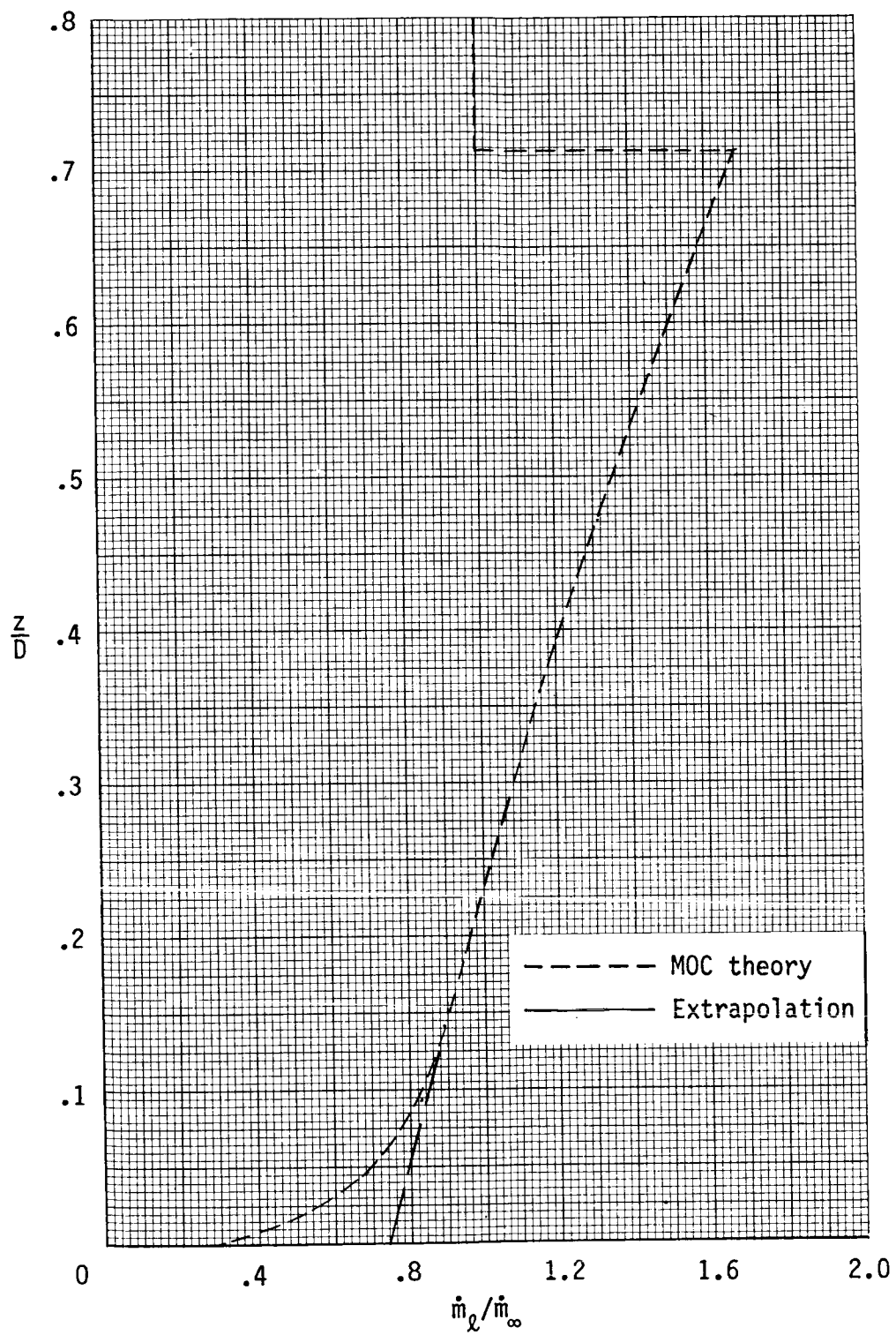
(e) $y/D = 0.472$.

Figure C3.- Concluded.



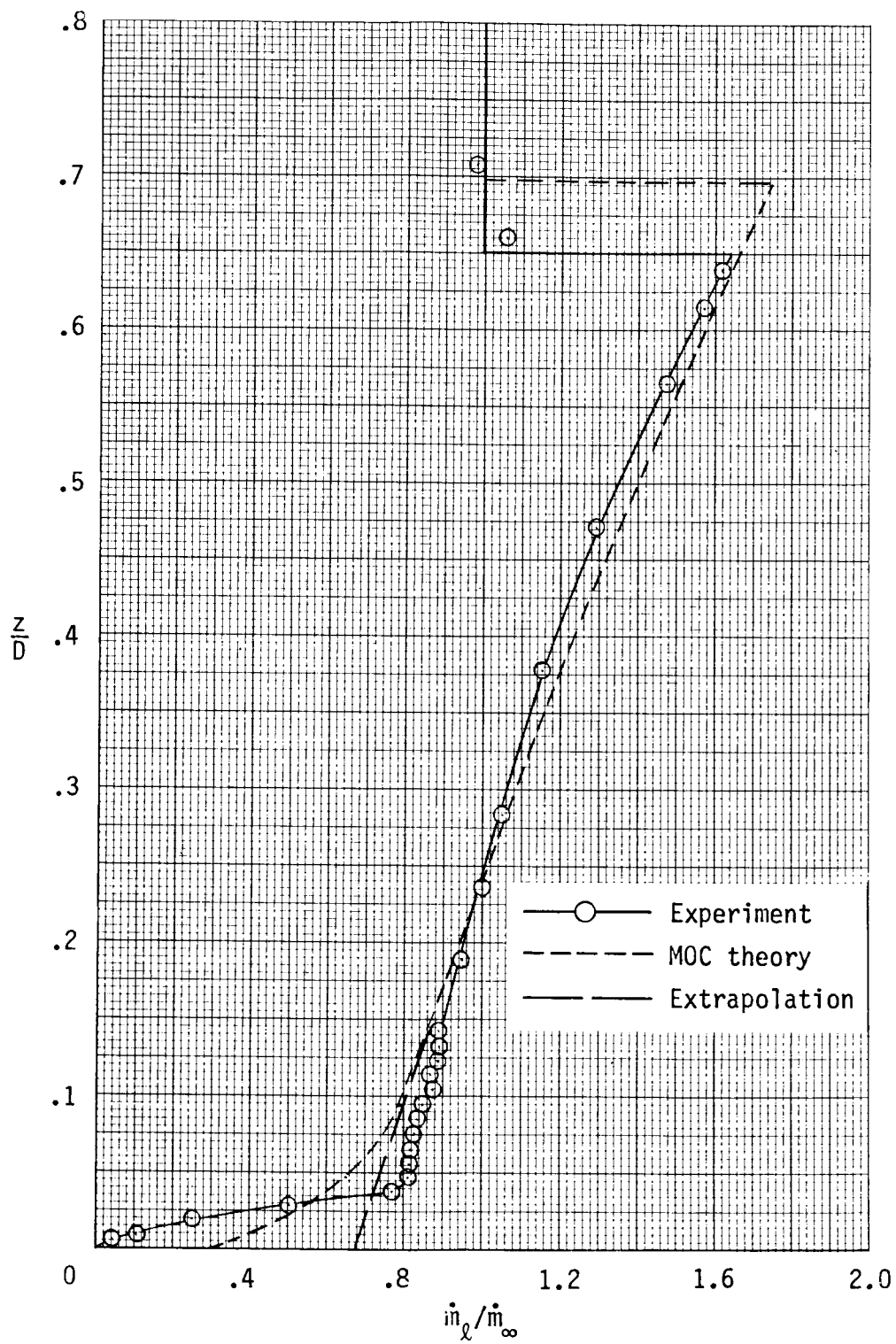
(a) $y/D = 0$.

Figure C4.- Local mass flow ratios at forward survey station ($x/D = 3.5$) at $\alpha = 0^\circ$.



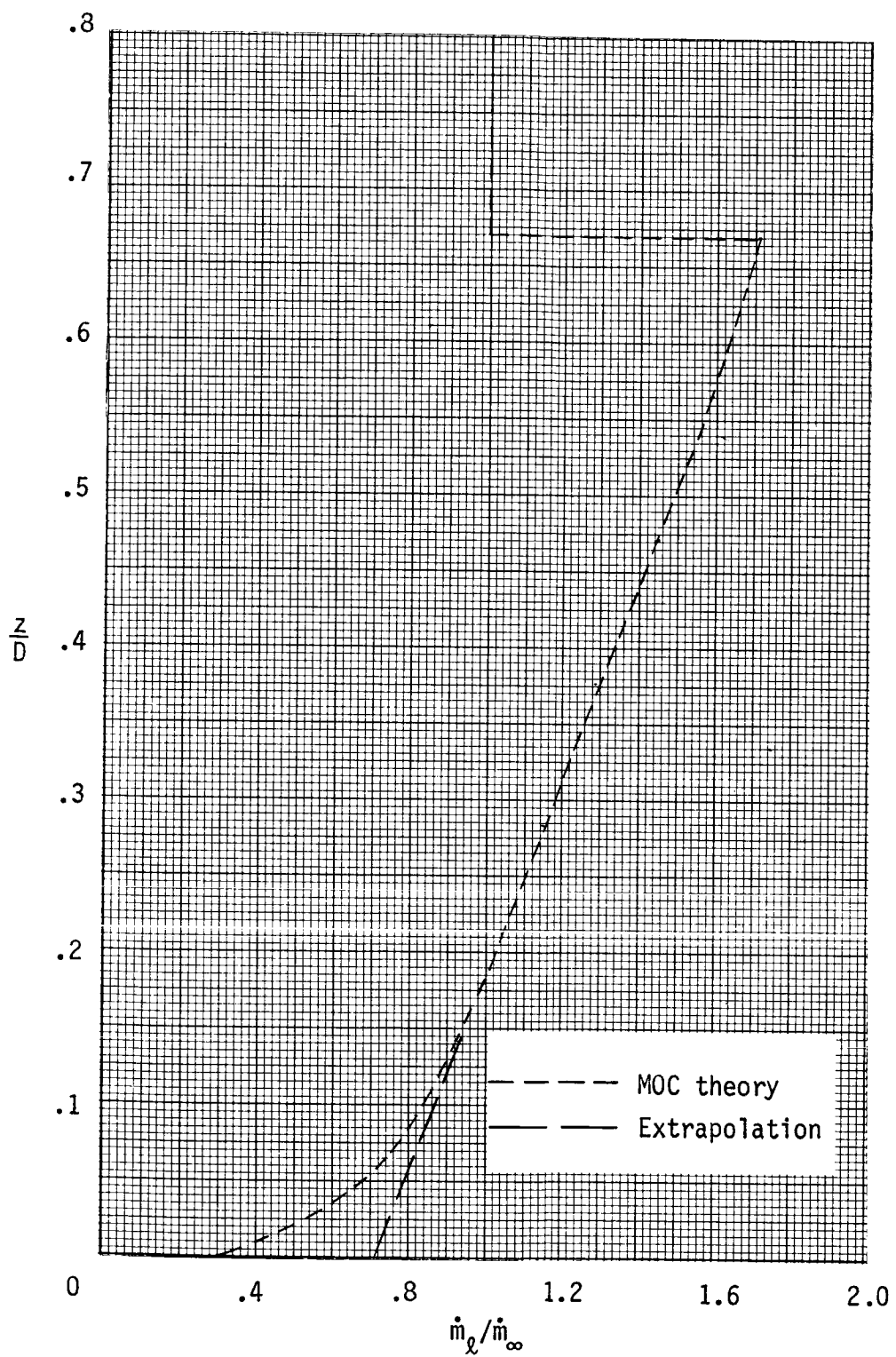
(b) $y/D = 0.118$.

Figure C4.- Continued.



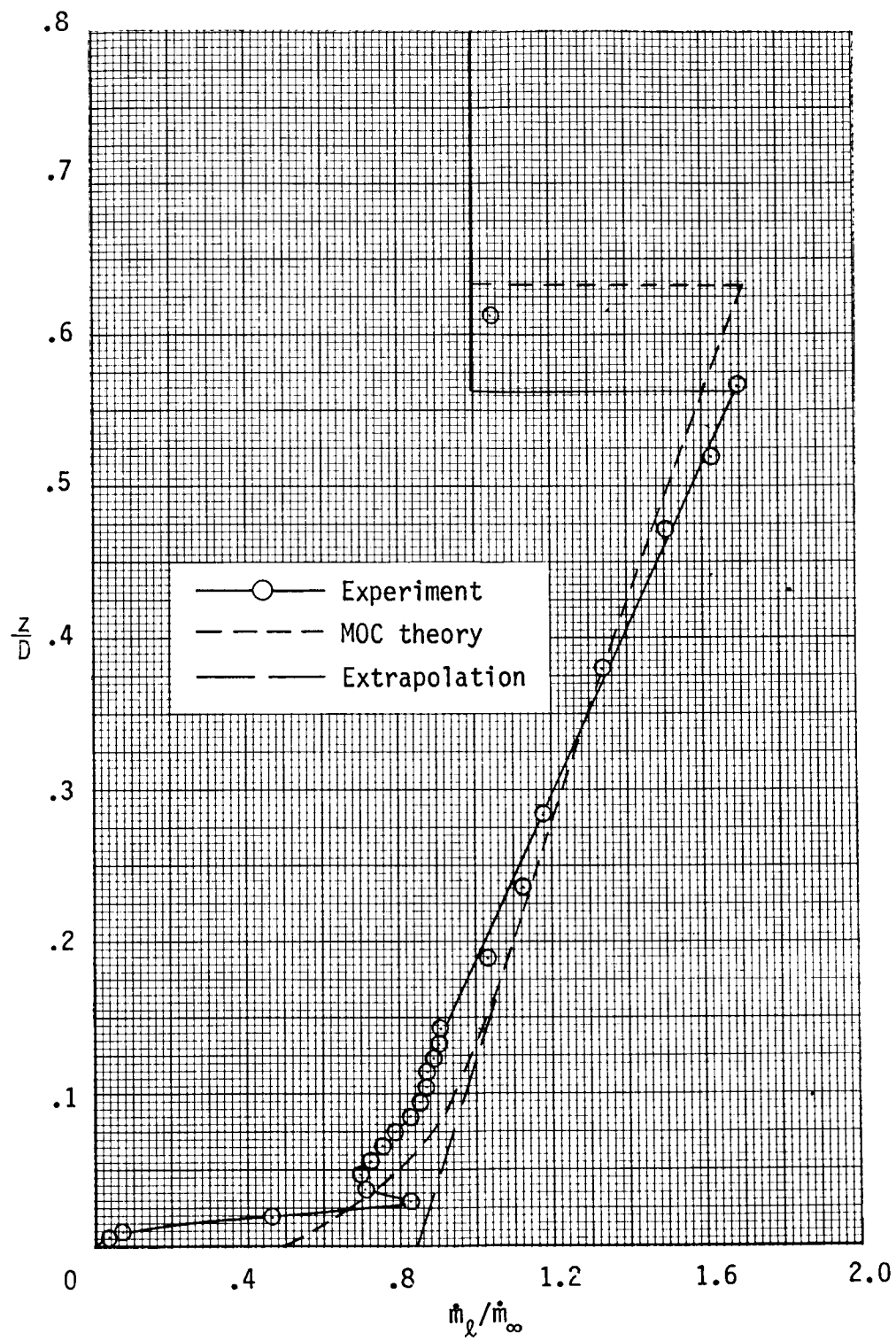
(c) $y/D = 0.236$.

Figure C4.- Continued.



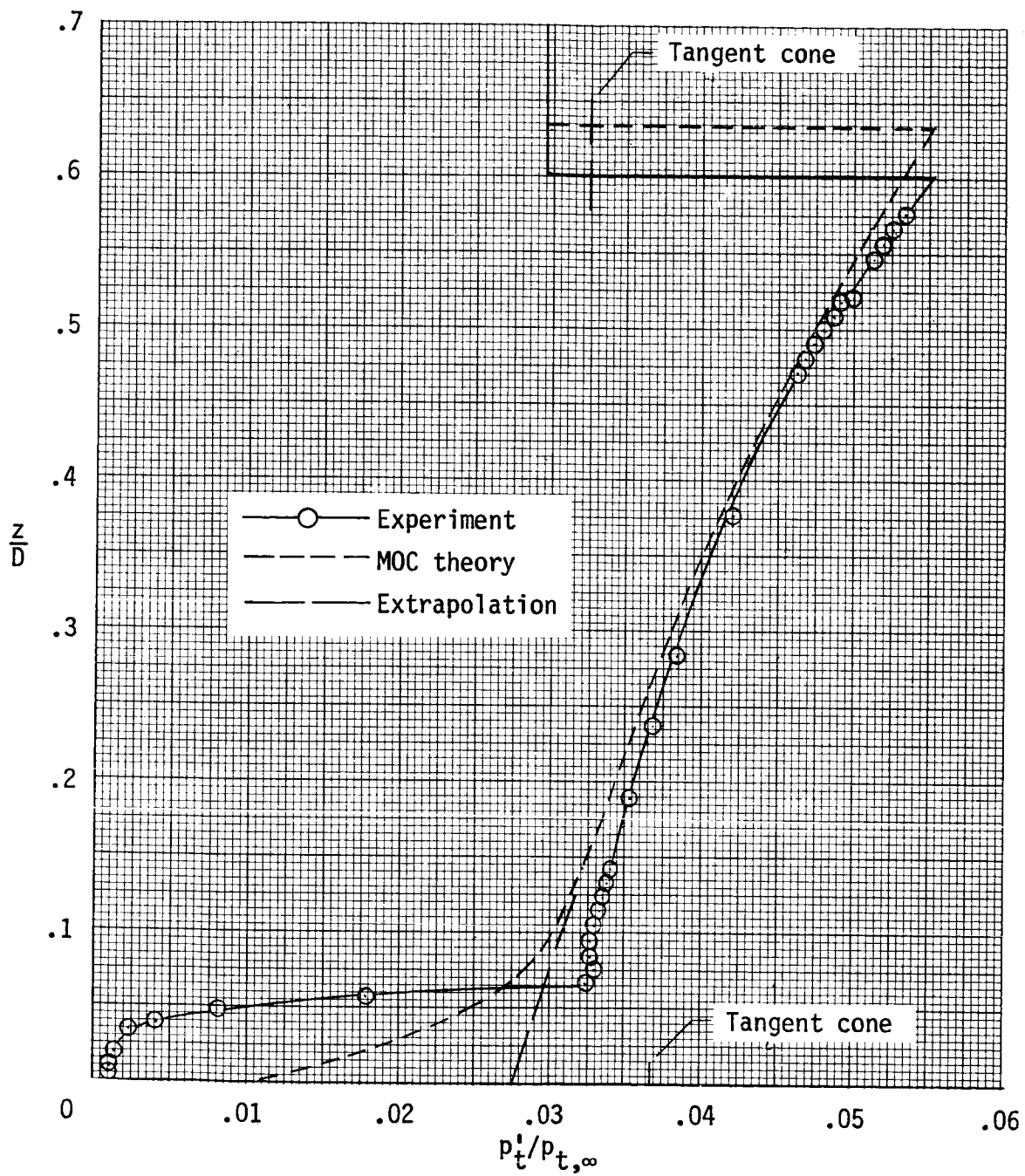
(d) $y/D = 0.354$.

Figure C4.- Continued.



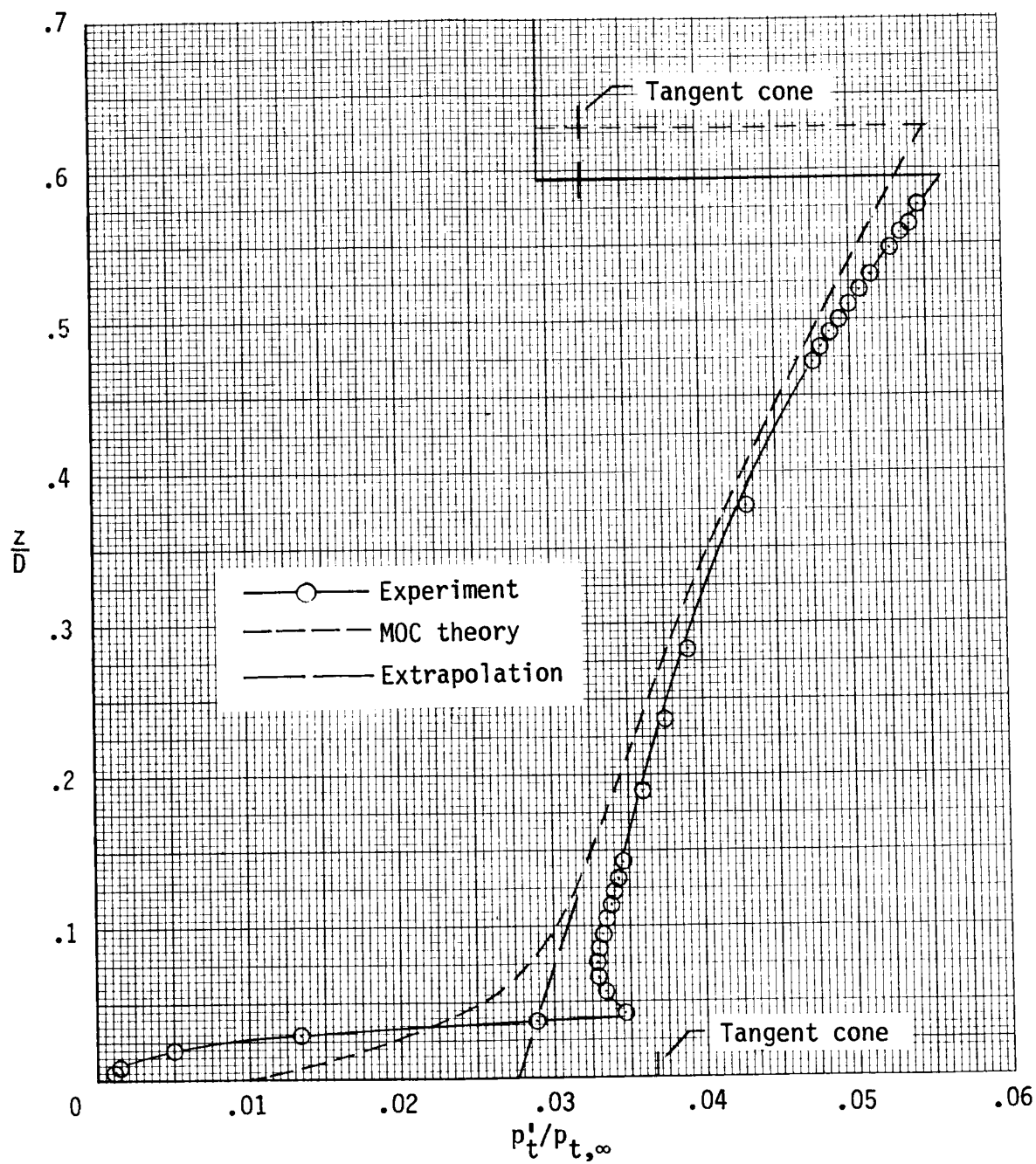
(e) $y/D = 0.472$.

Figure C4.- Concluded.



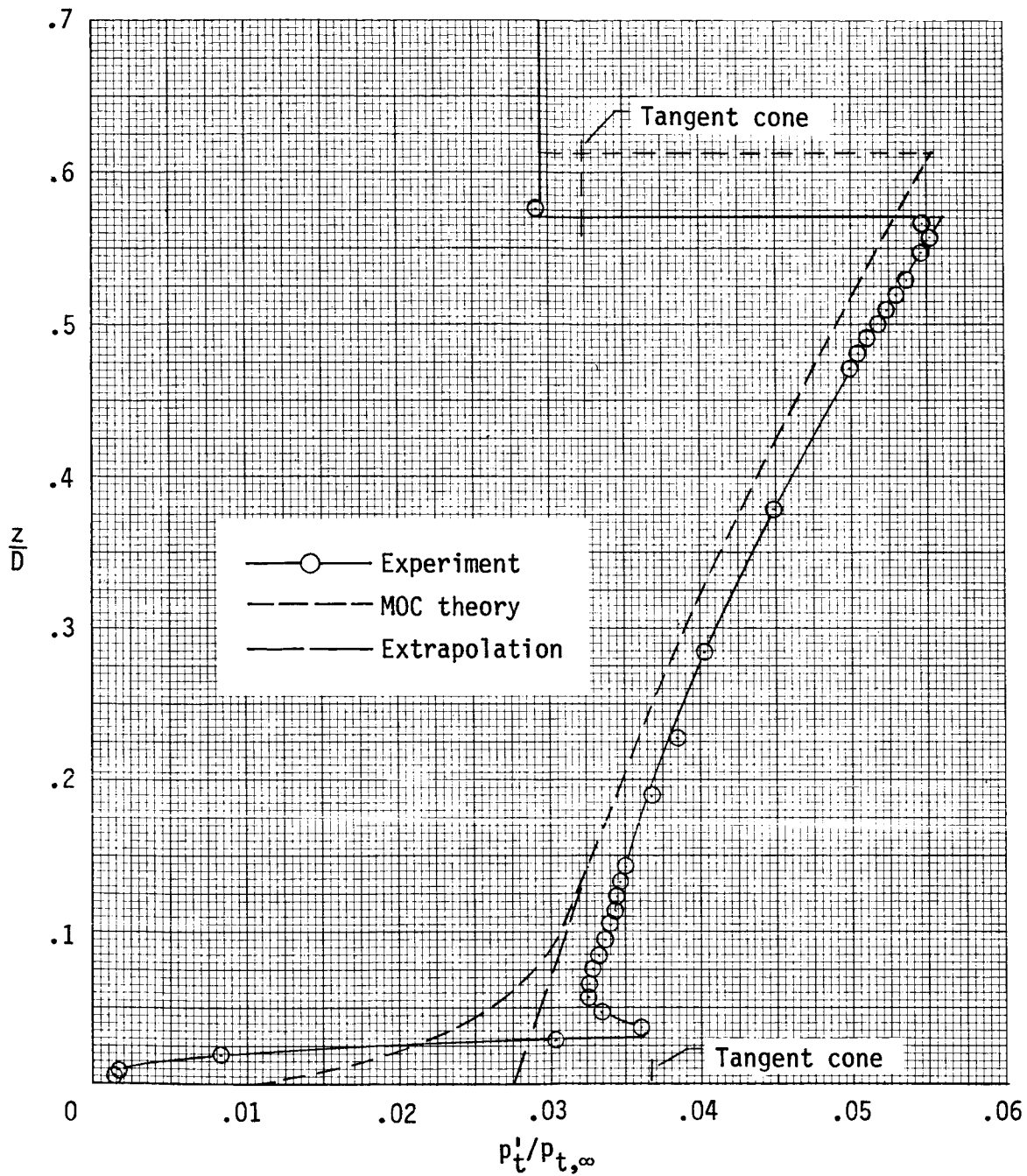
(a) $y/D = 0$.

Figure C5.- Pitot pressure survey at forward survey station
($x/D = 3.5$) at $\alpha = 4^\circ$.



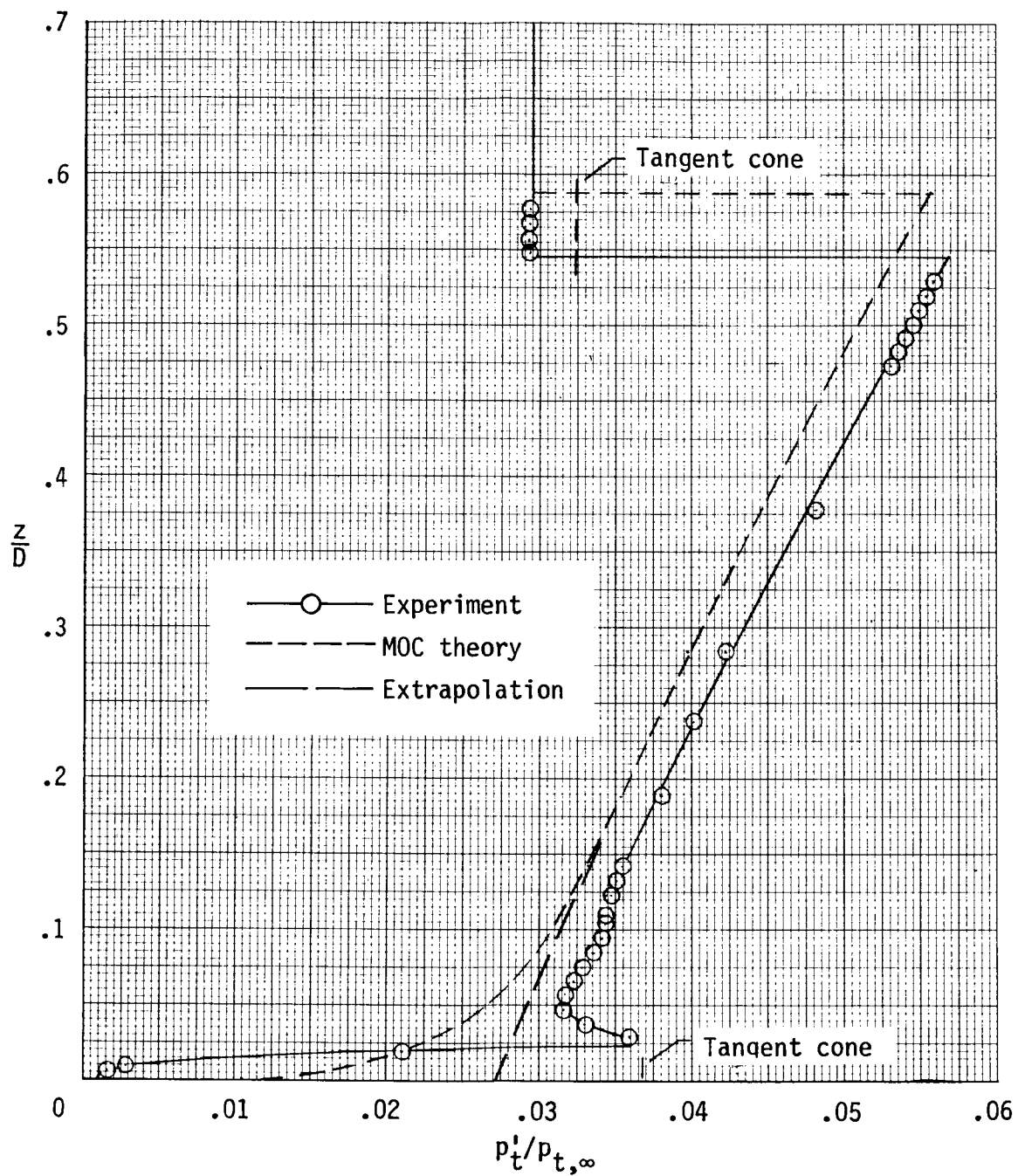
(b) $y/D = 0.118$.

Figure C5.- Continued.



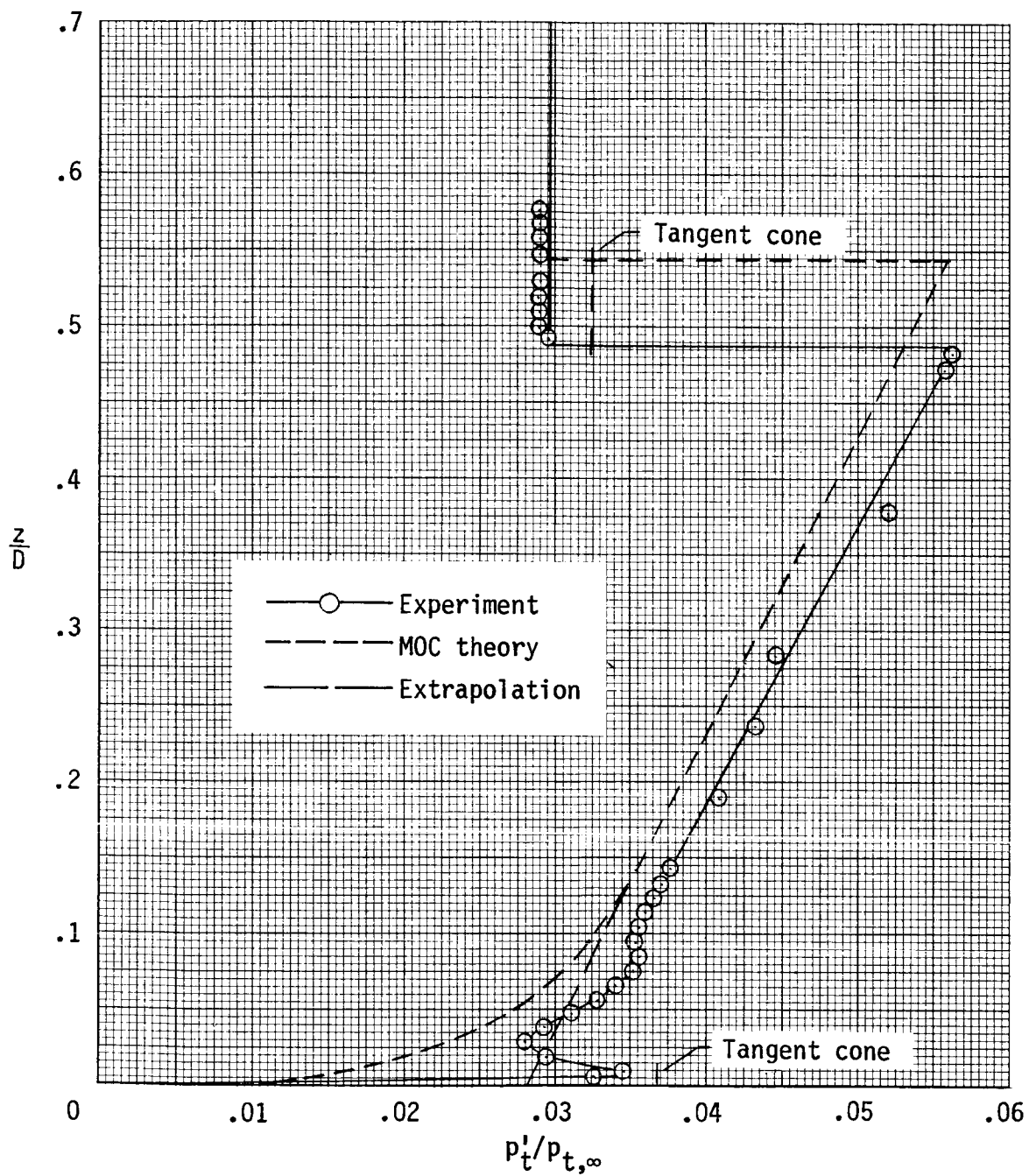
(c) $y/D = 0.236$.

Figure C5.- Continued.



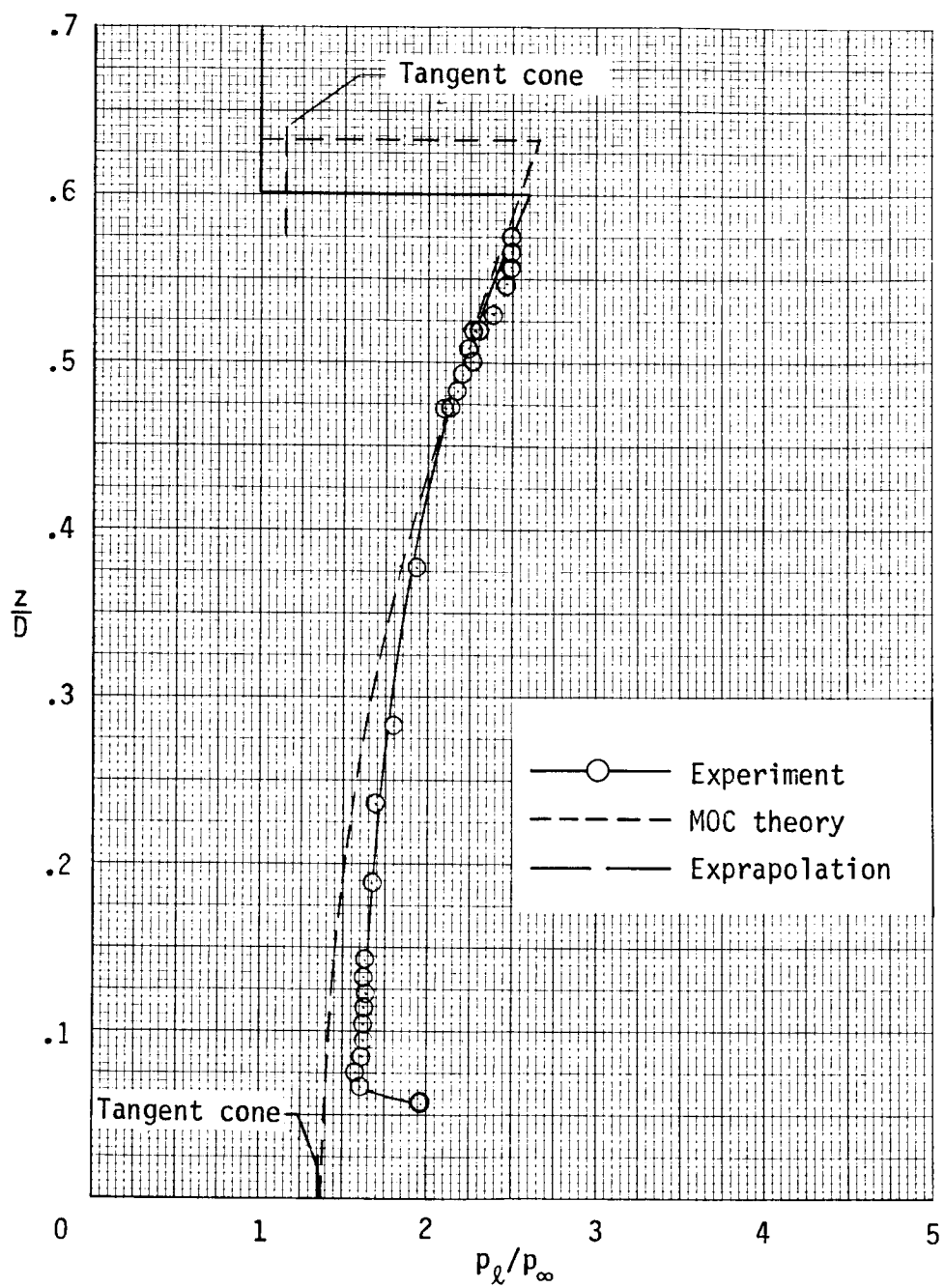
(d) $y/D = 0.354$.

Figure C5.- Continued.



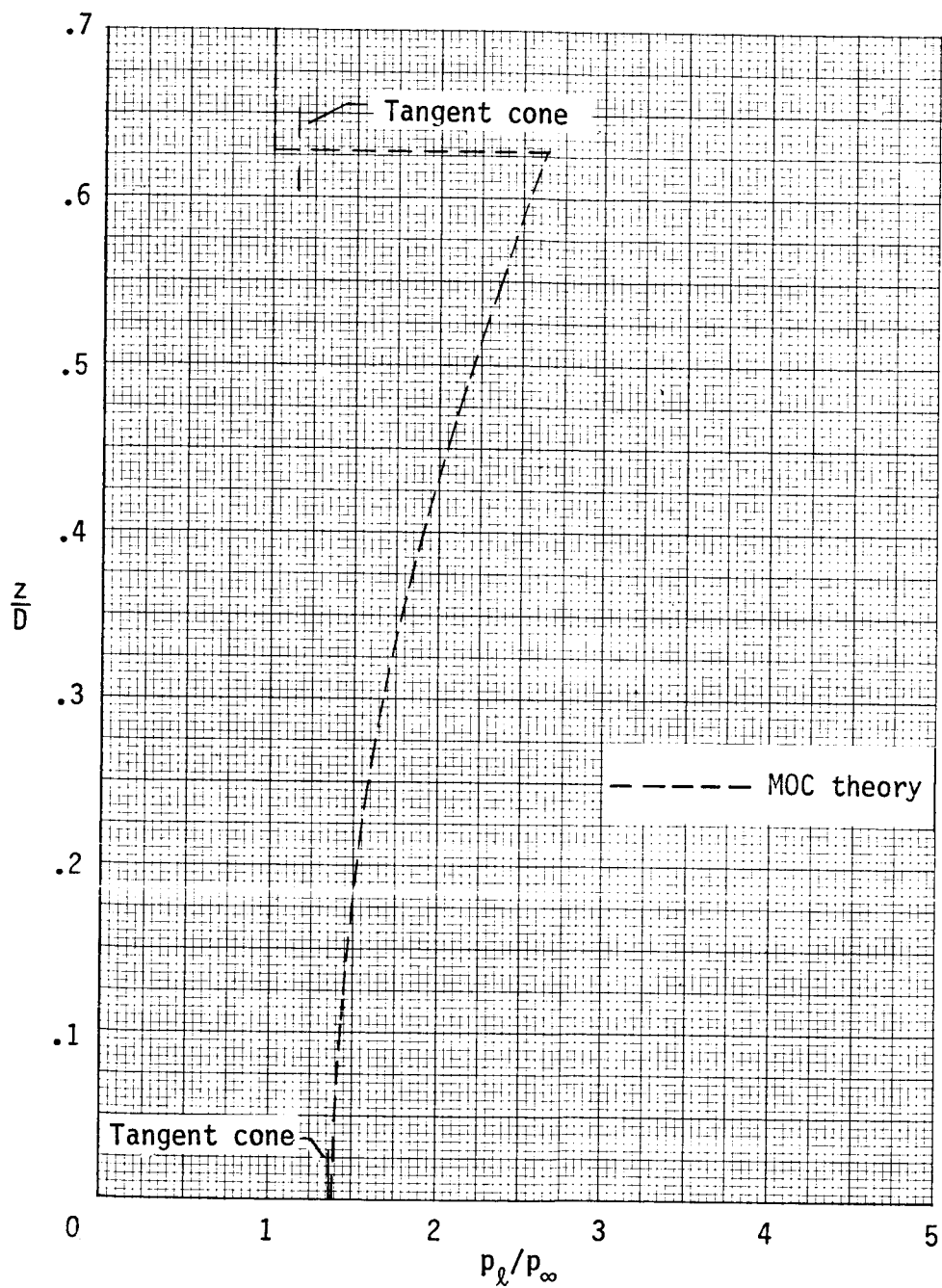
(e) $y/D = 0.472$.

Figure C5.- Concluded.



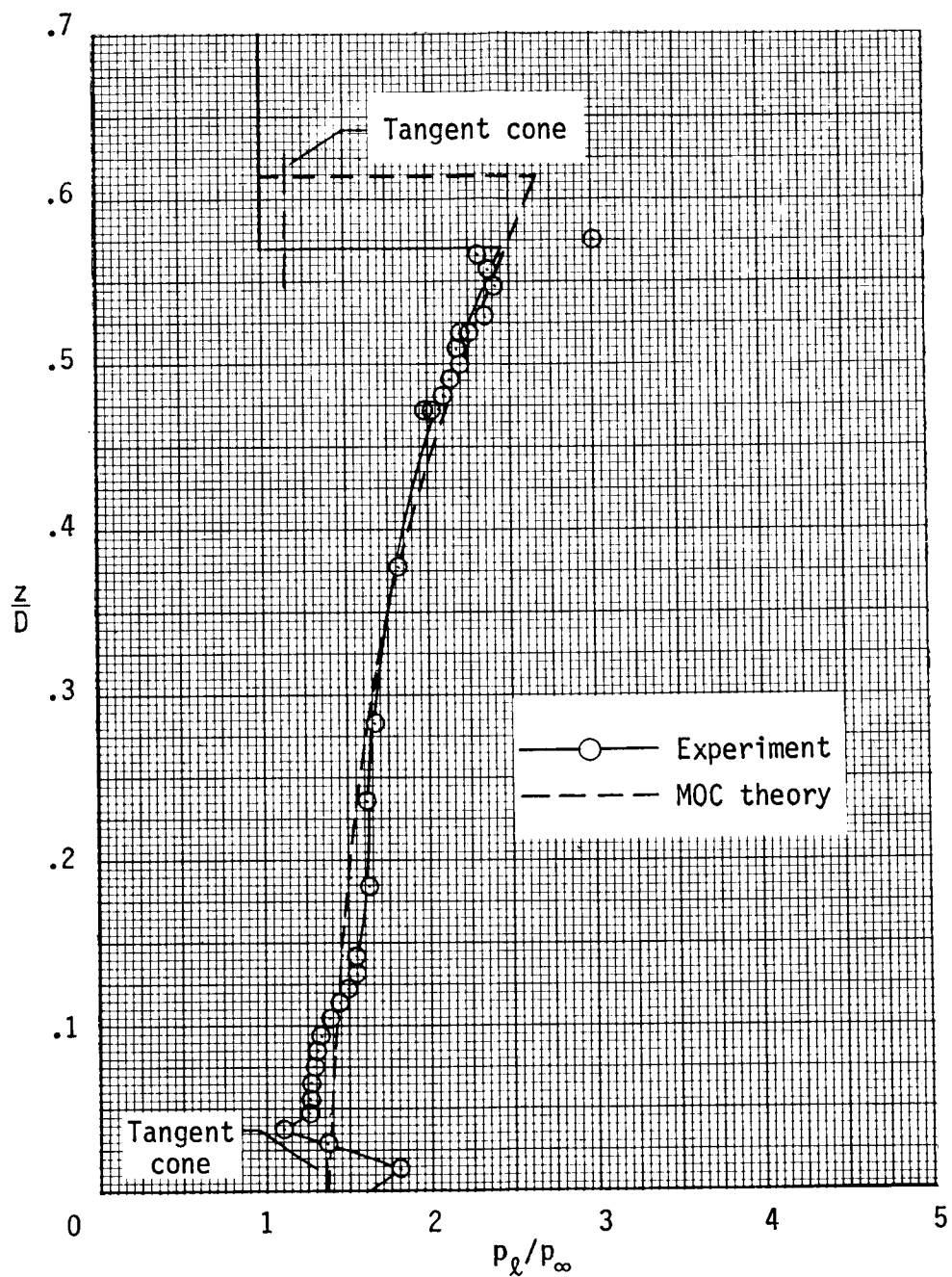
(a) $y/D = 0$.

Figure C6.- Static pressure survey at forward survey station ($x/D = 3.5$) at $\alpha = 4^\circ$.



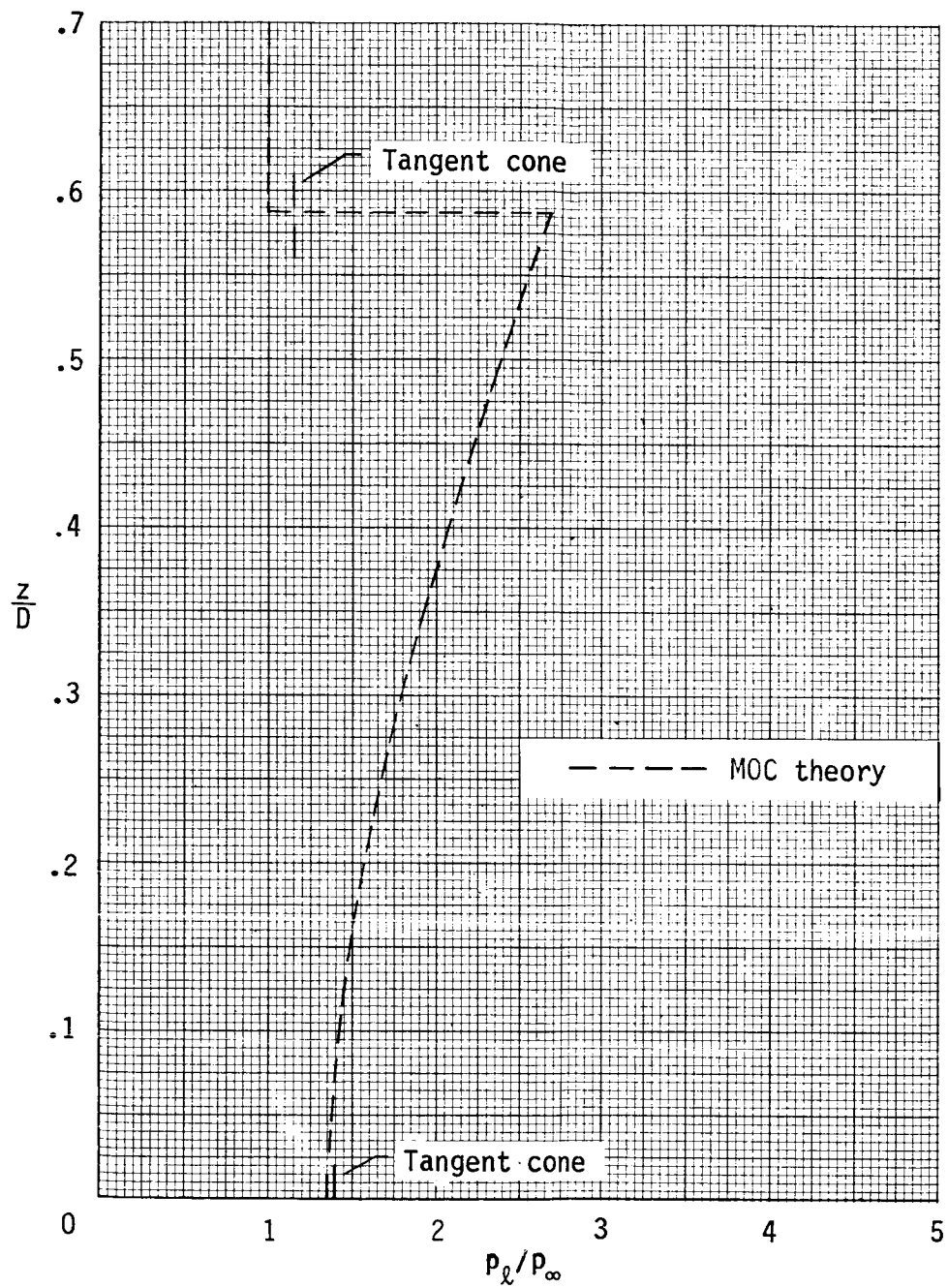
(b) $y/D = 0.118$.

Figure C6.- Continued.



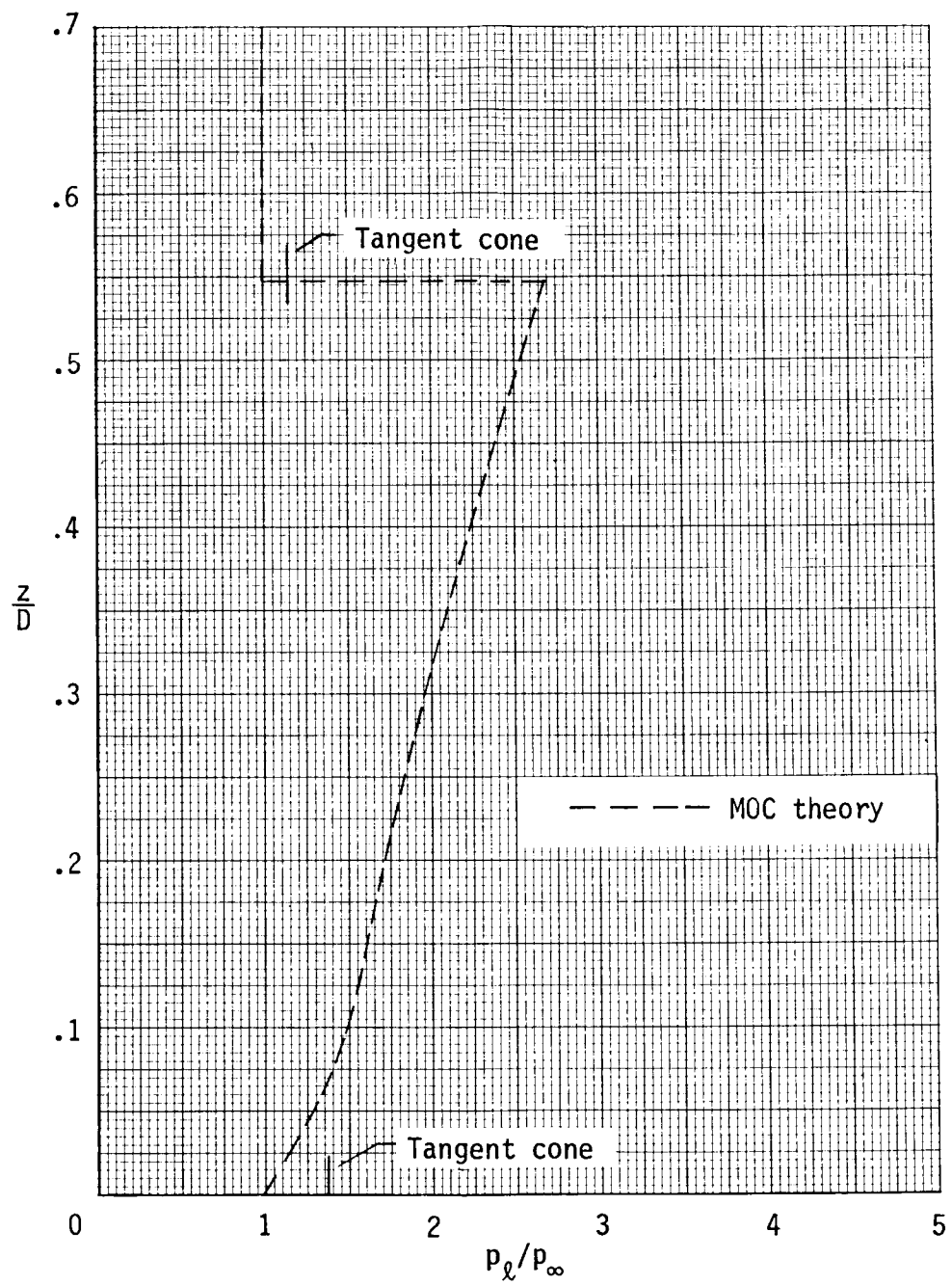
(c) $y/D = 0.236$.

Figure C6.- Continued.



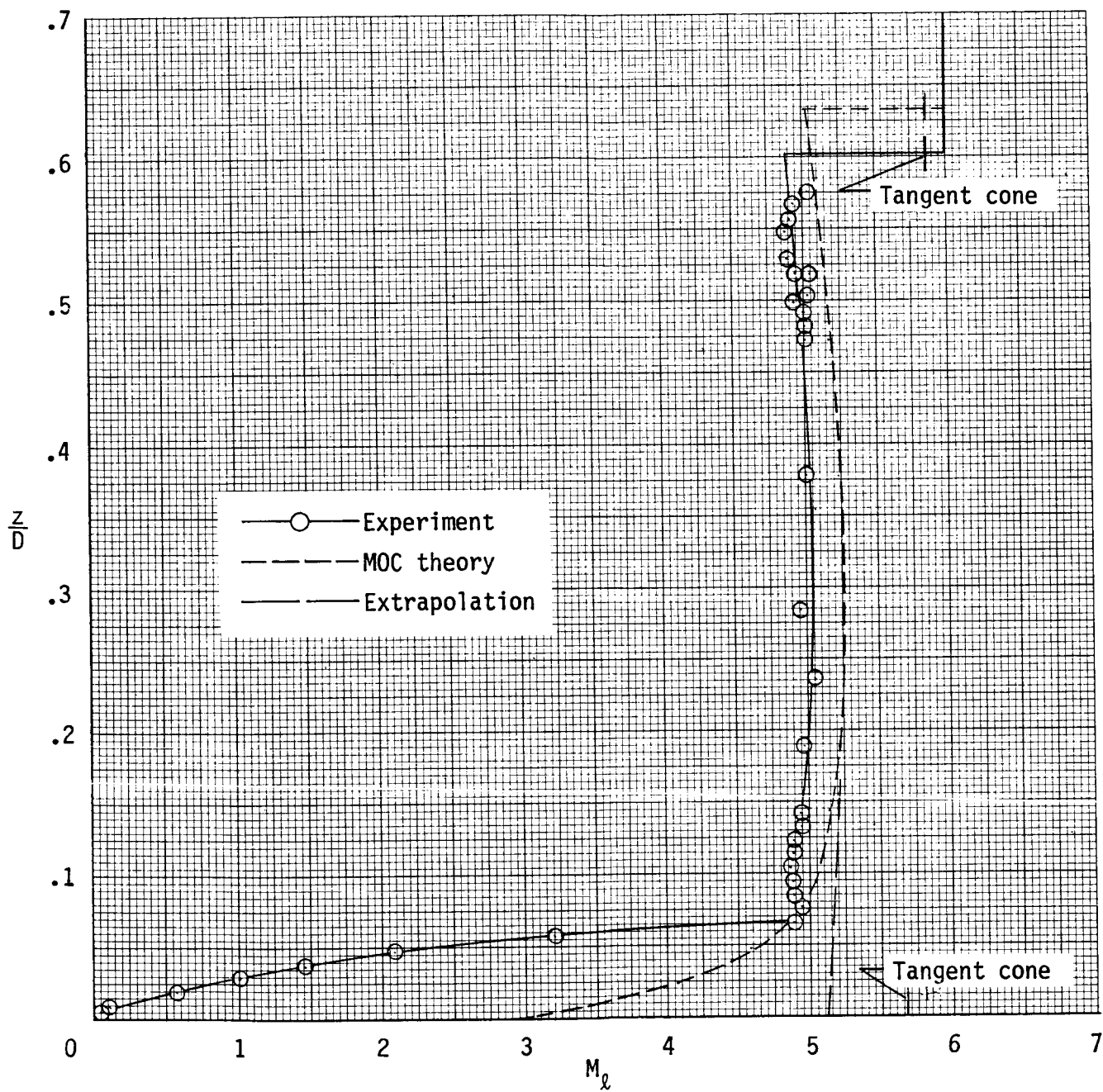
(d) $y/D = 0.354$.

Figure C6.- Continued.



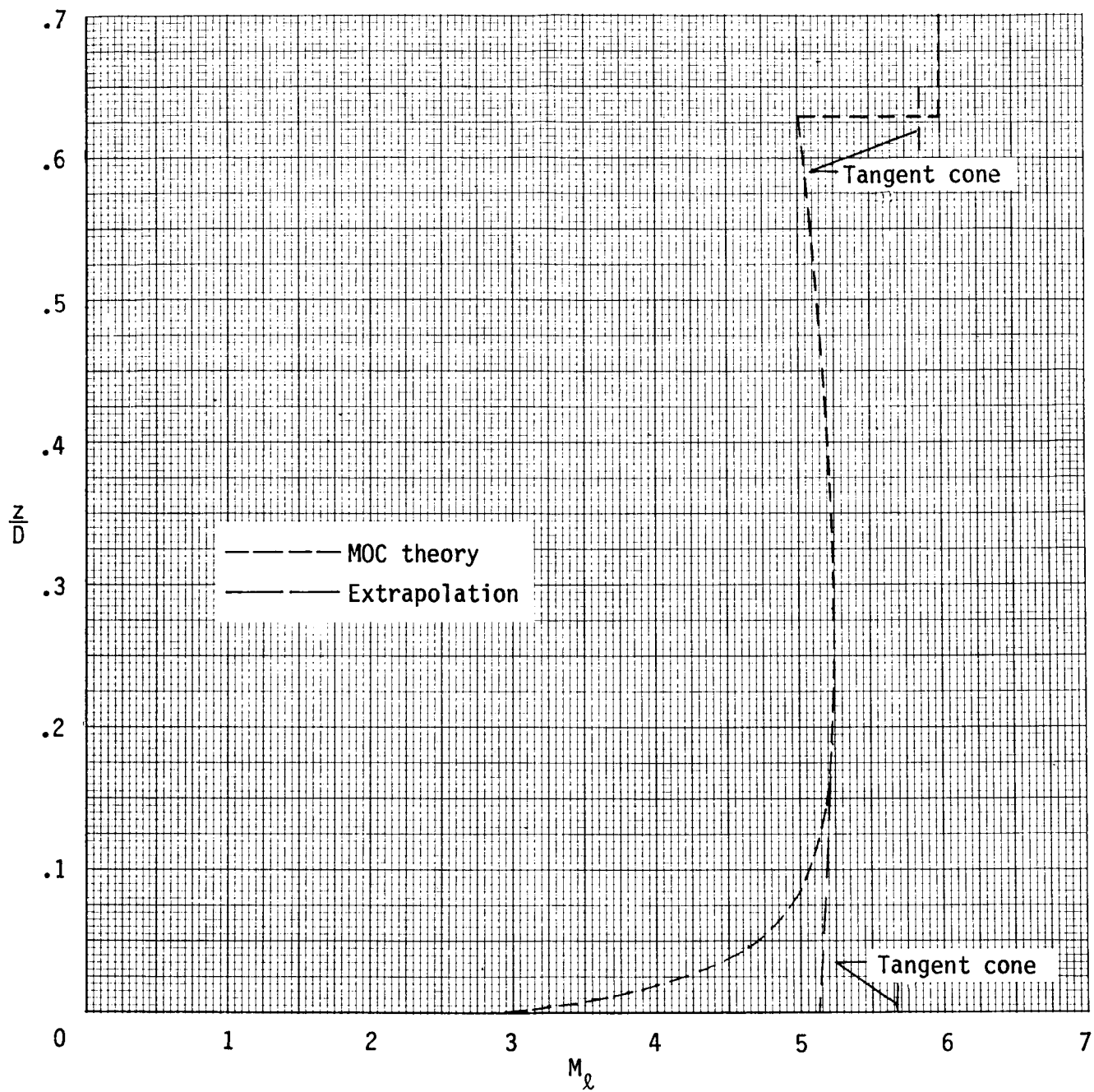
(e) $y/D = 0.472$.

Figure C6.- Concluded.



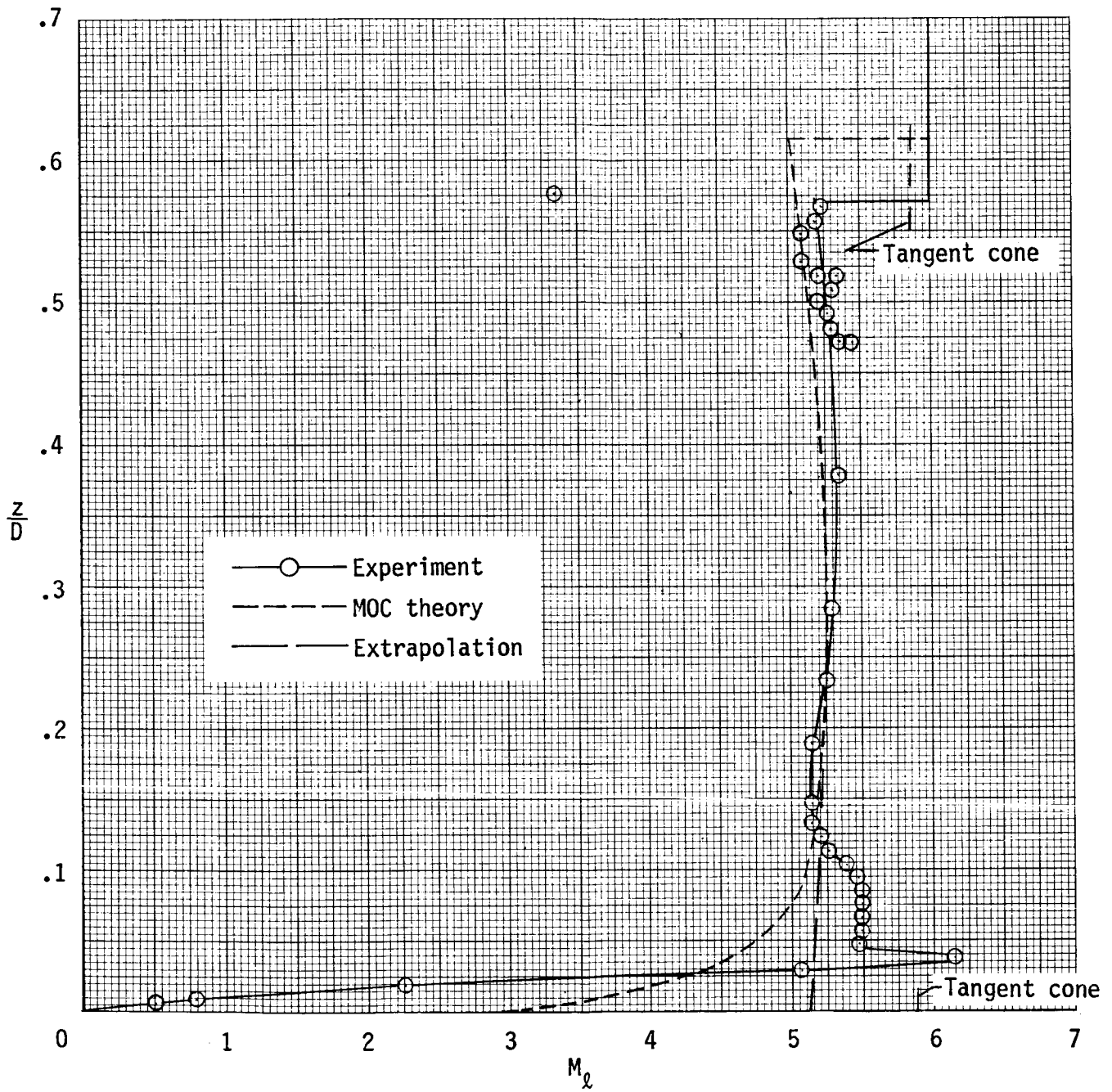
(a) $y/D = 0$.

Figure C7.- Local Mach number distribution at forward survey station
($x/D = 3.5$) at $\alpha = 4^\circ$.



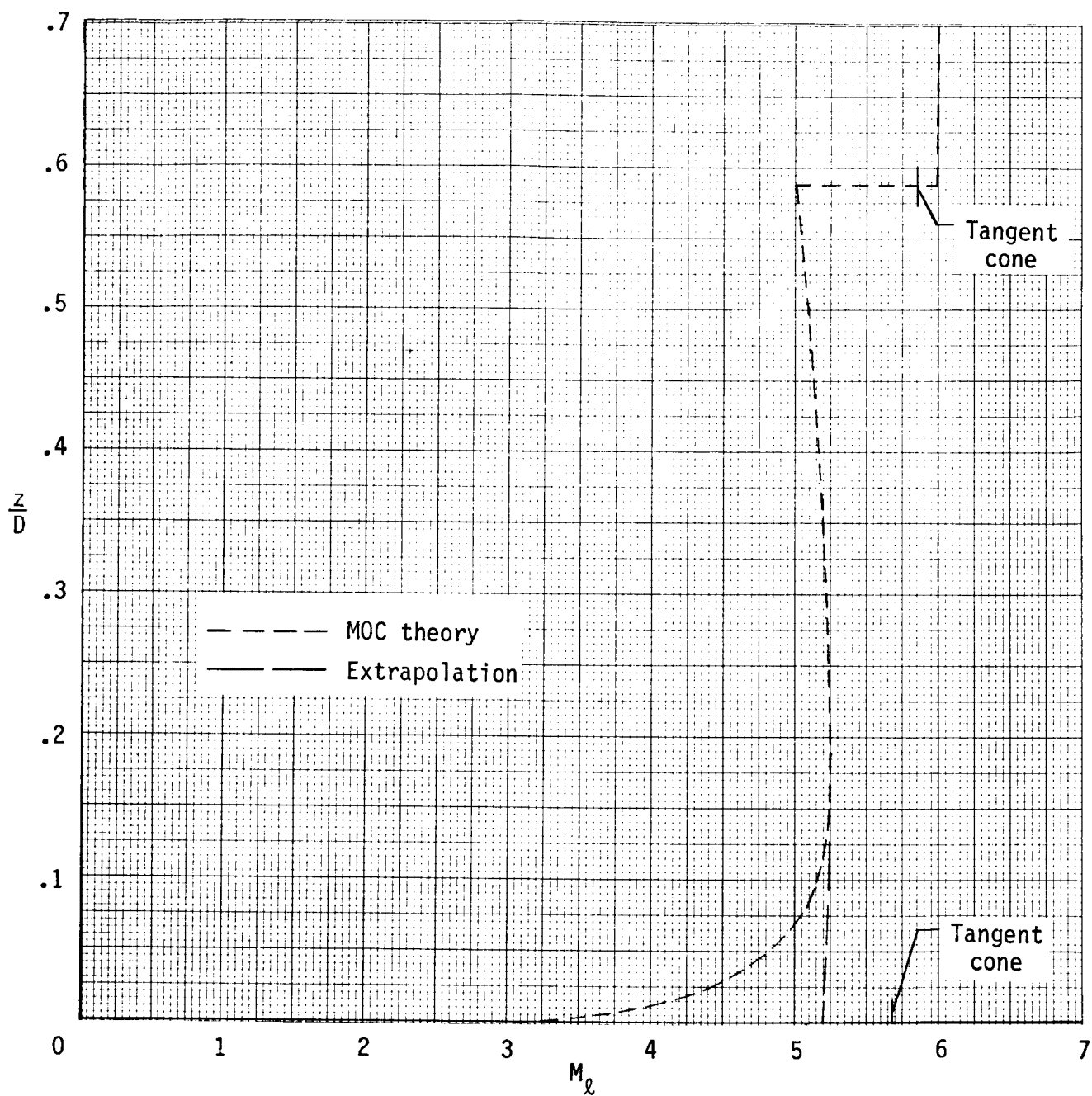
(b) $y/D = 0.118$.

Figure C7.- Continued.



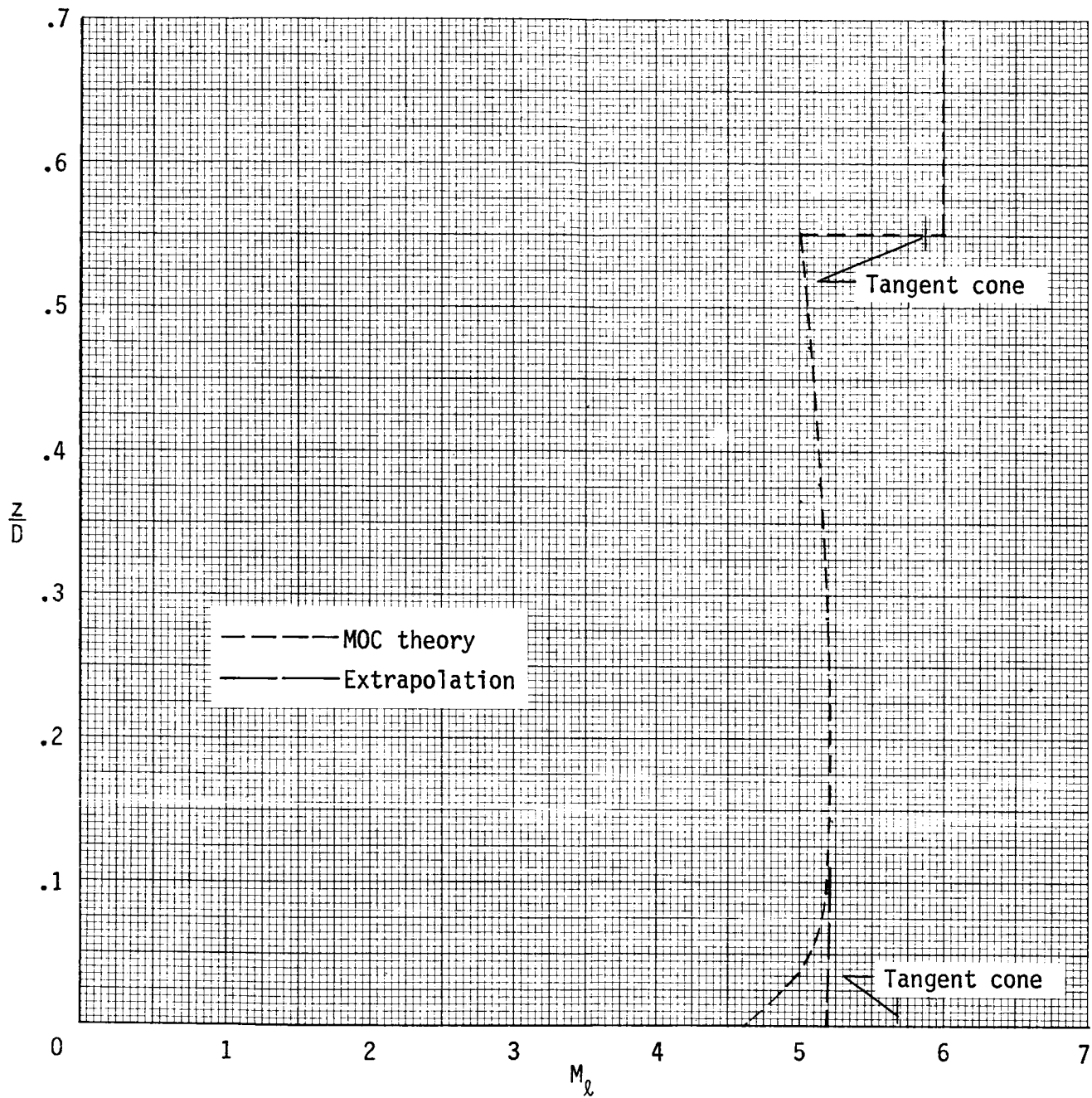
(c) $y/D = 0.236$.

Figure C7.- Continued.



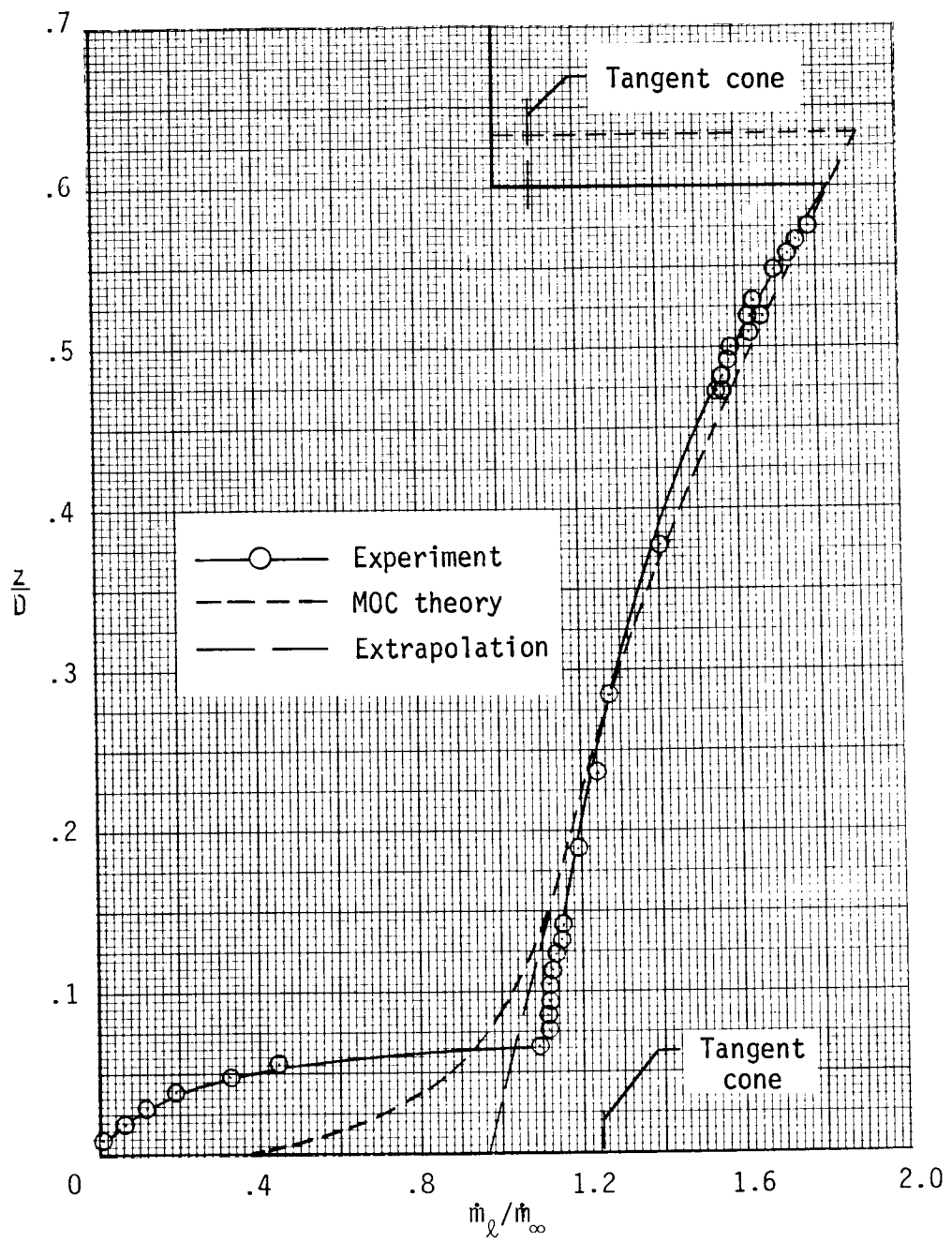
(d) $y/D = 0.354$.

Figure C7.- Continued.



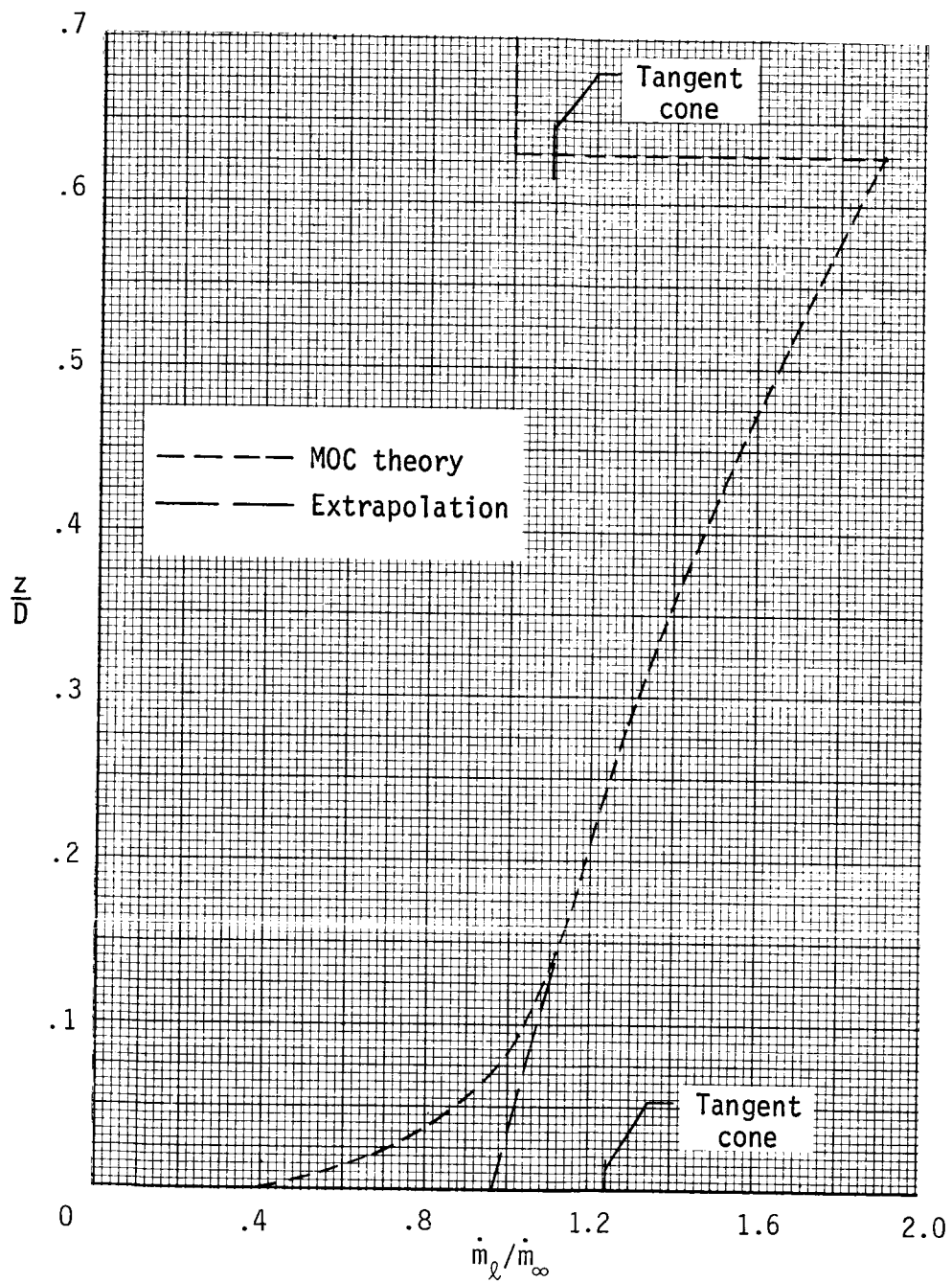
(e) $y/D = 0.472$.

Figure C7.- Concluded.



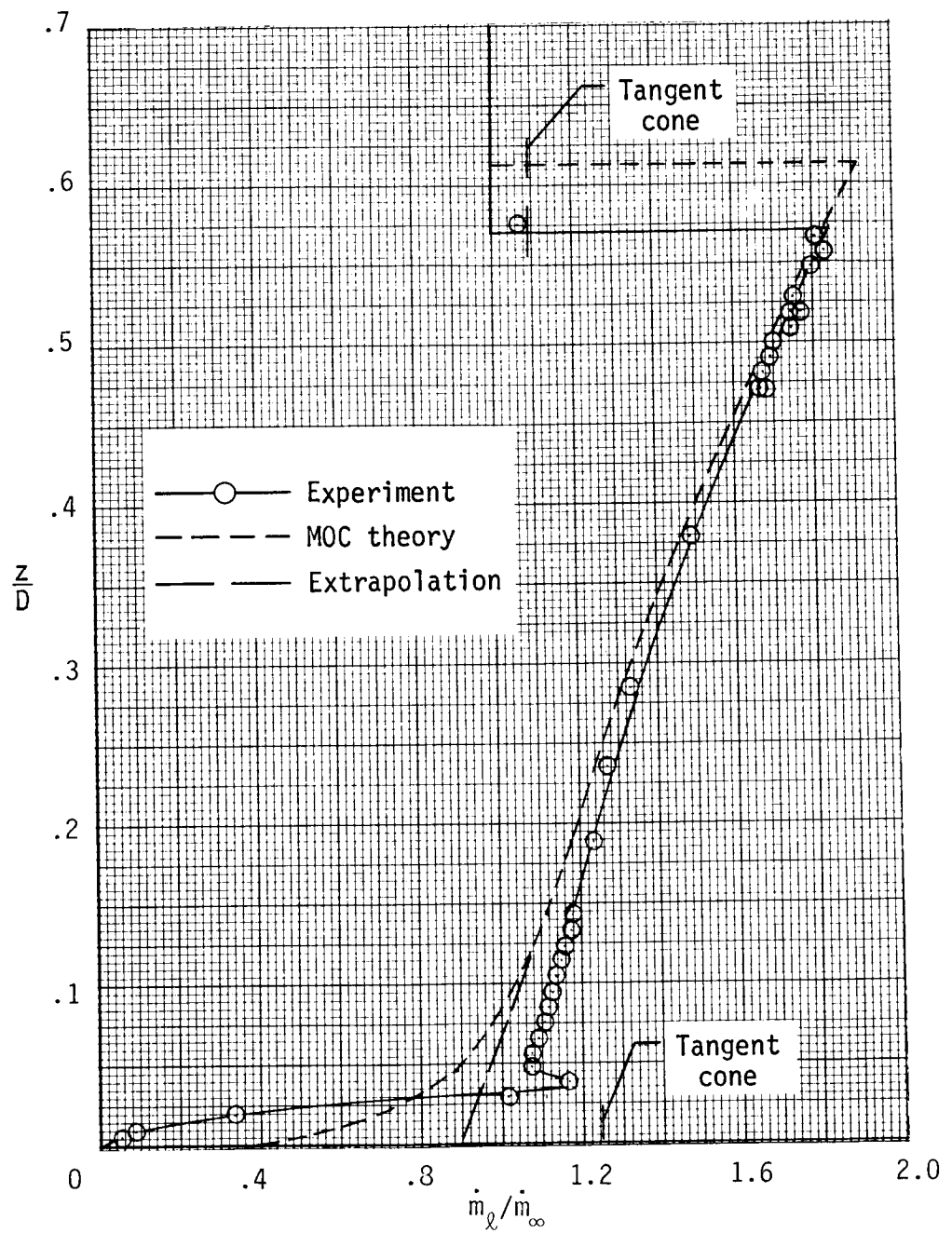
(a) $y/D = 0$.

Figure C8.- Local mass flow ratios at forward survey station
($x/D = 3.5$) at $\alpha = 4^\circ$.



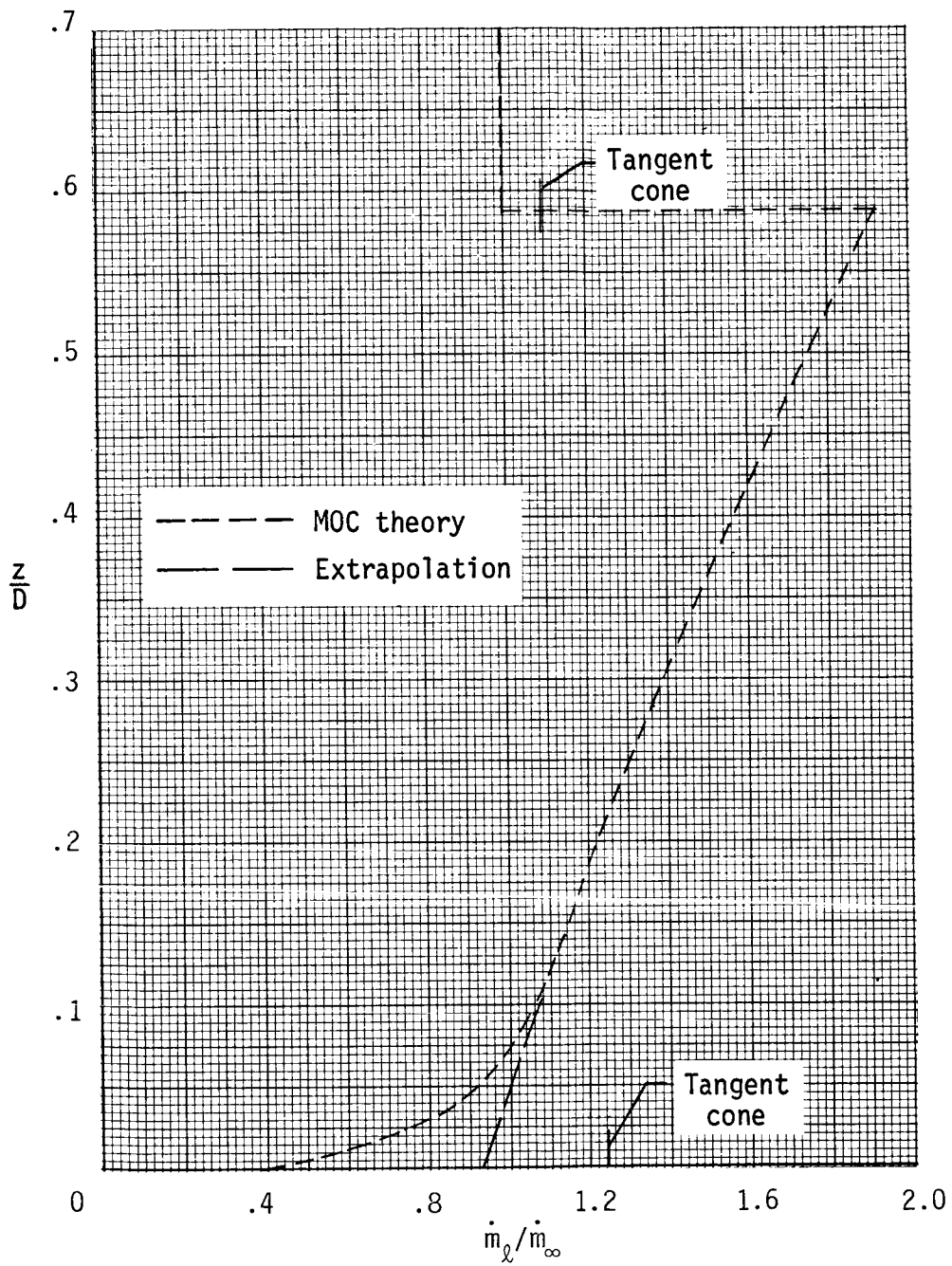
(b) $y/D = 0.118$.

Figure C8.- Continued.



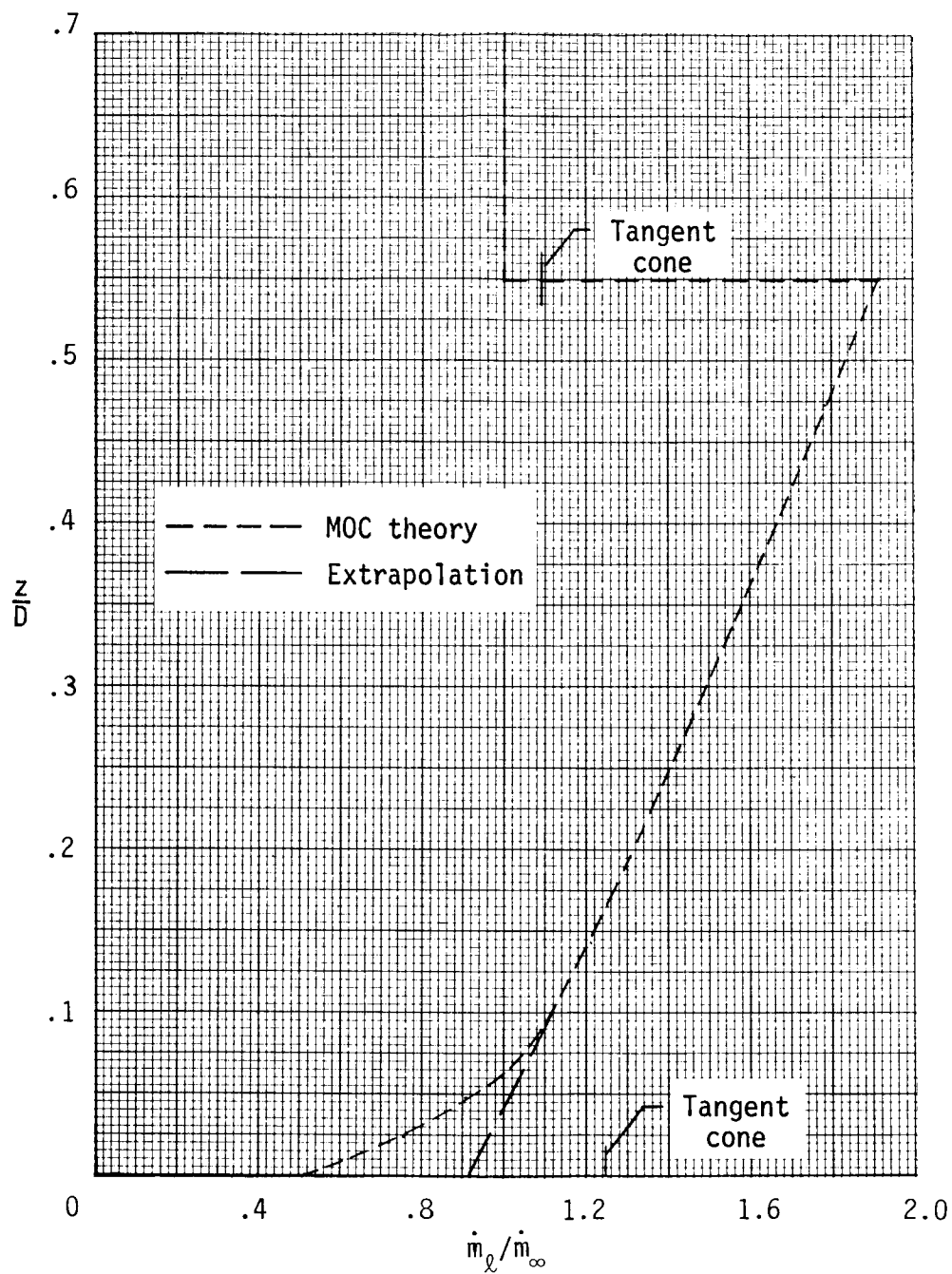
(c) $y/D = 0.236$.

Figure C8.- Continued.



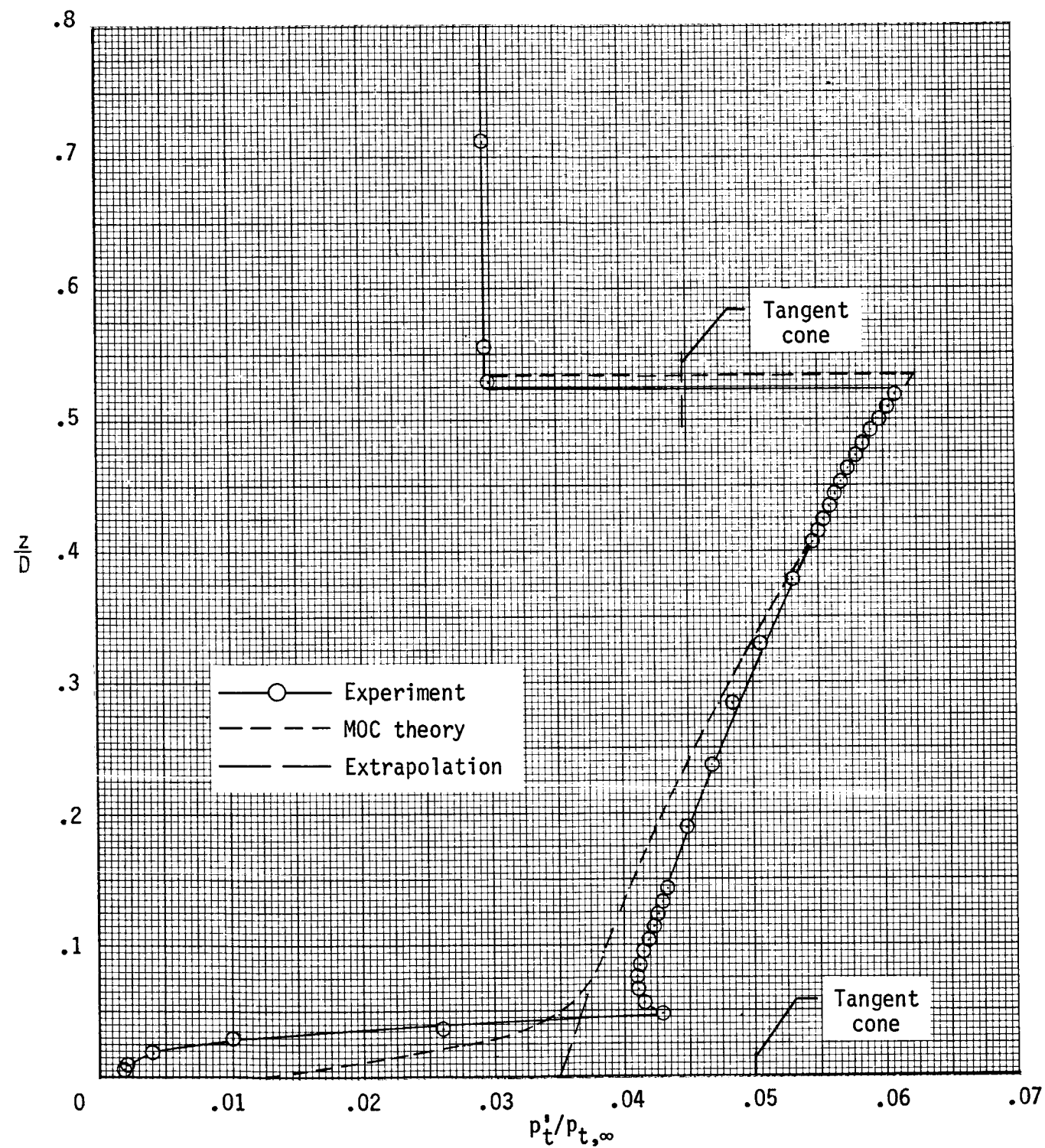
(d) $y/D = 0.354$.

Figure C8.- Continued.



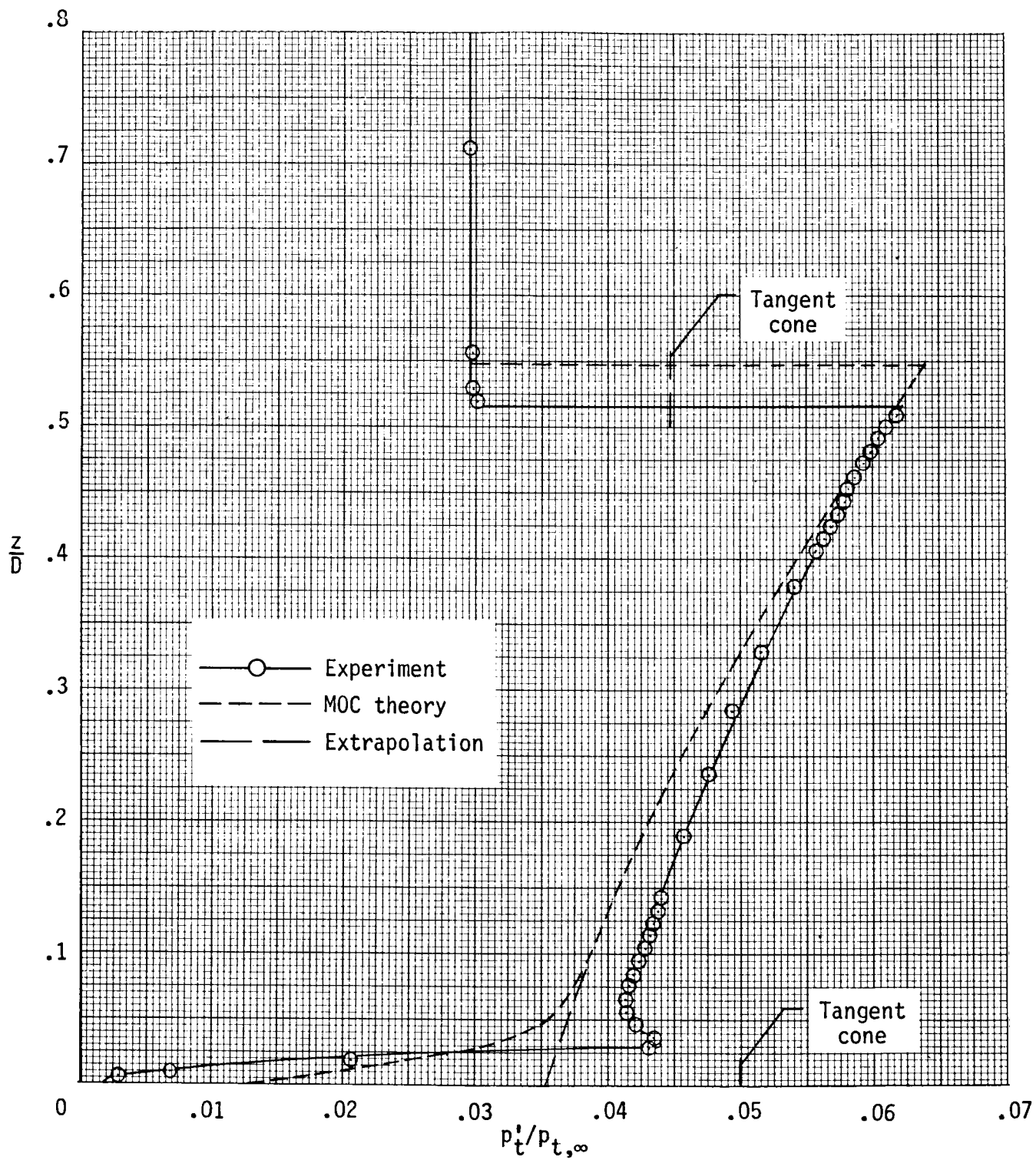
(e) $y/D = 0.472$.

Figure C8.- Concluded.



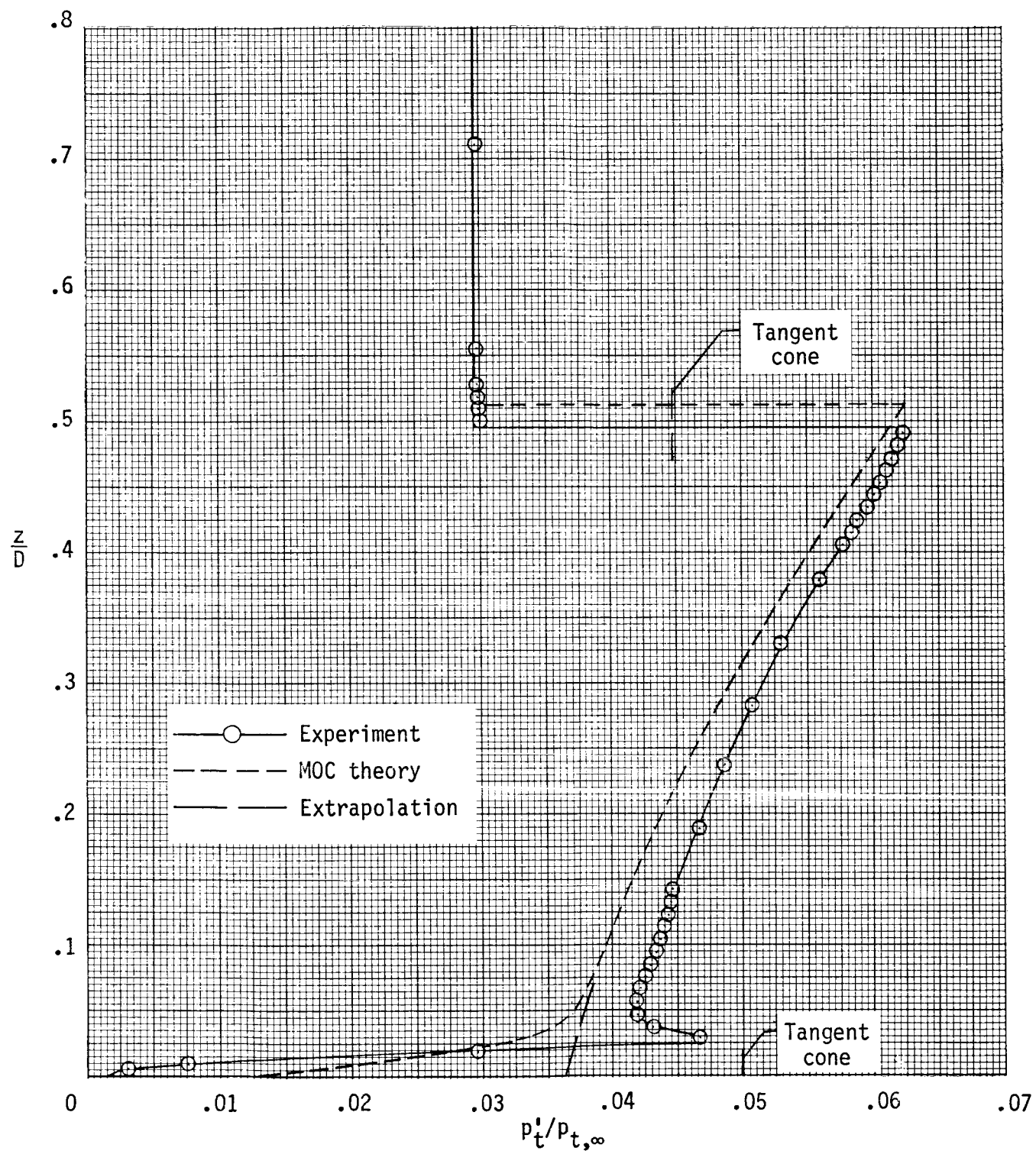
(a) $y/D = 0$.

Figure C9.- pitot pressure survey at forward survey station
($x/D = 3.5$) at $\alpha = 8^\circ$.



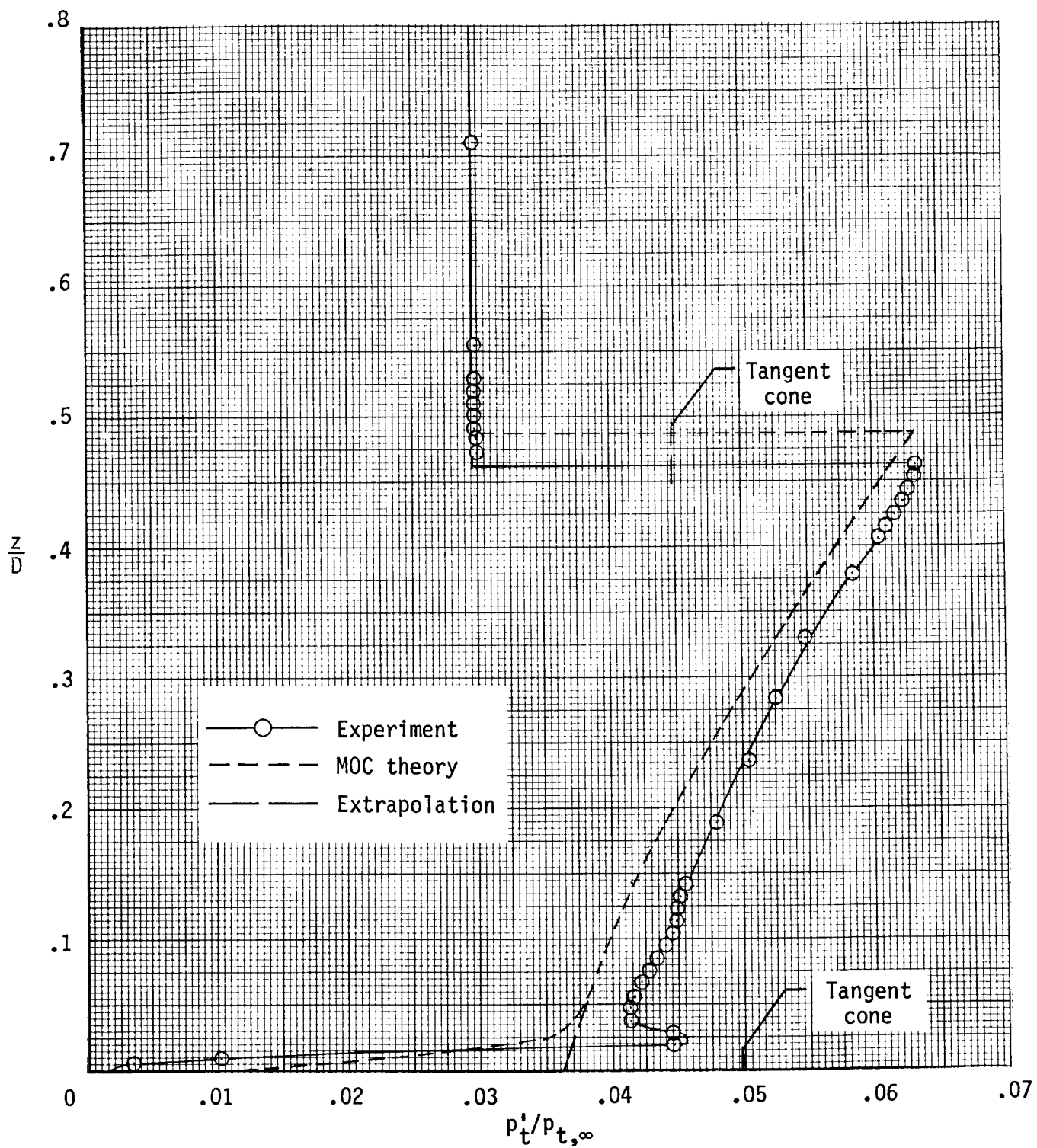
(b) $y/D = 0.118$.

Figure C9.- Continued.



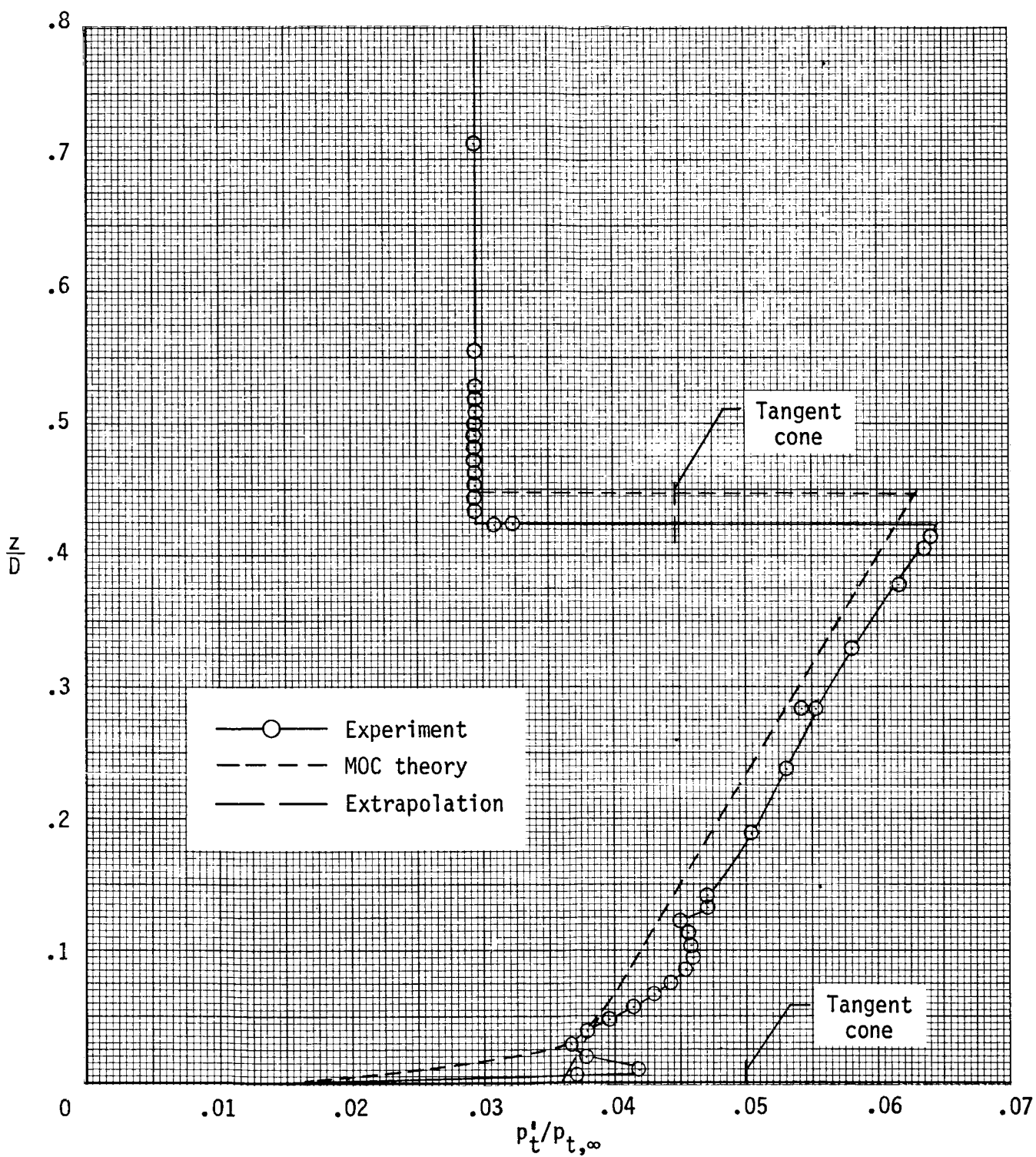
(c) $y/D = 0.236$.

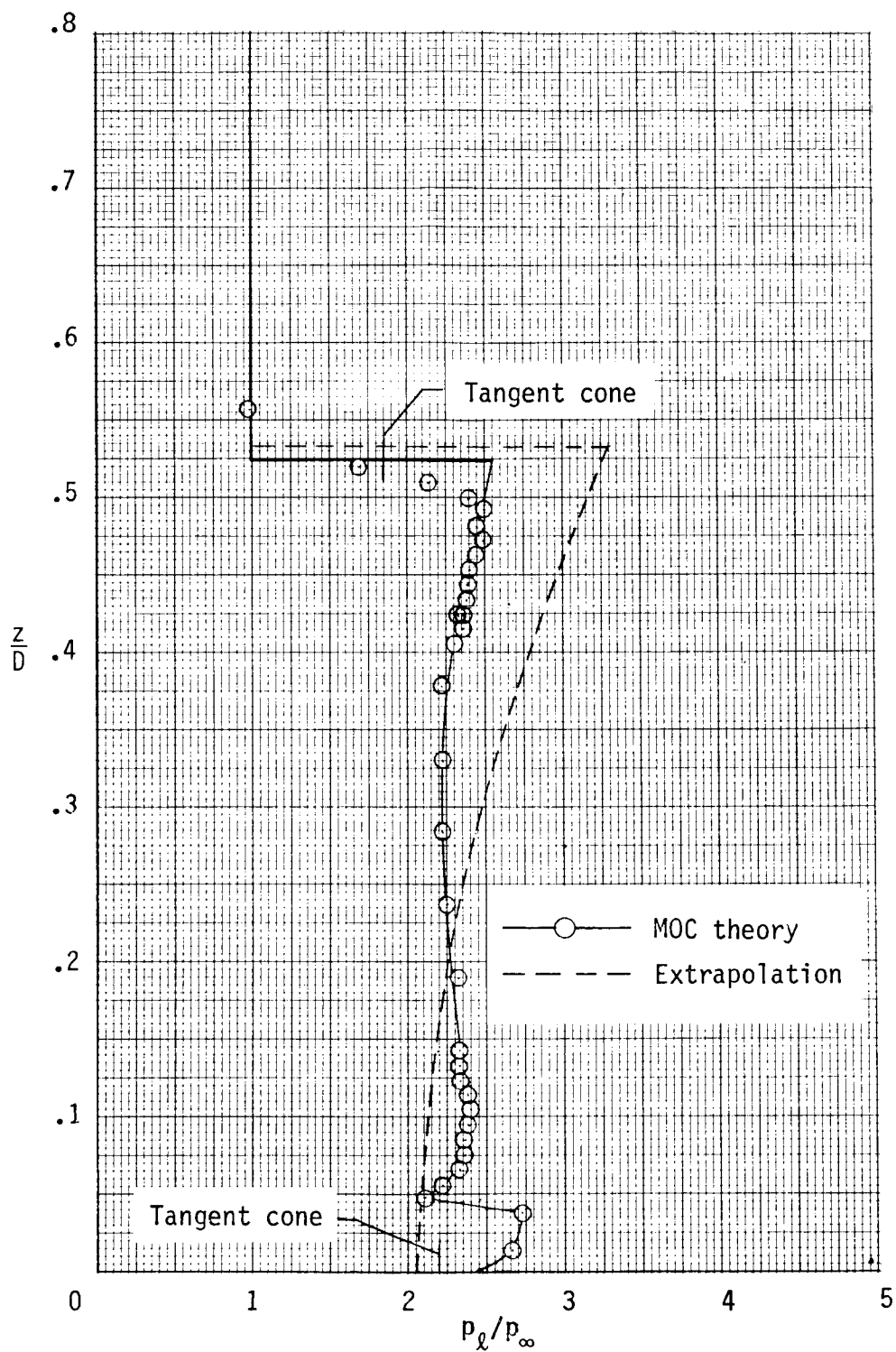
Figure C9.- Continued.



(d) $y/D = 0.354$.

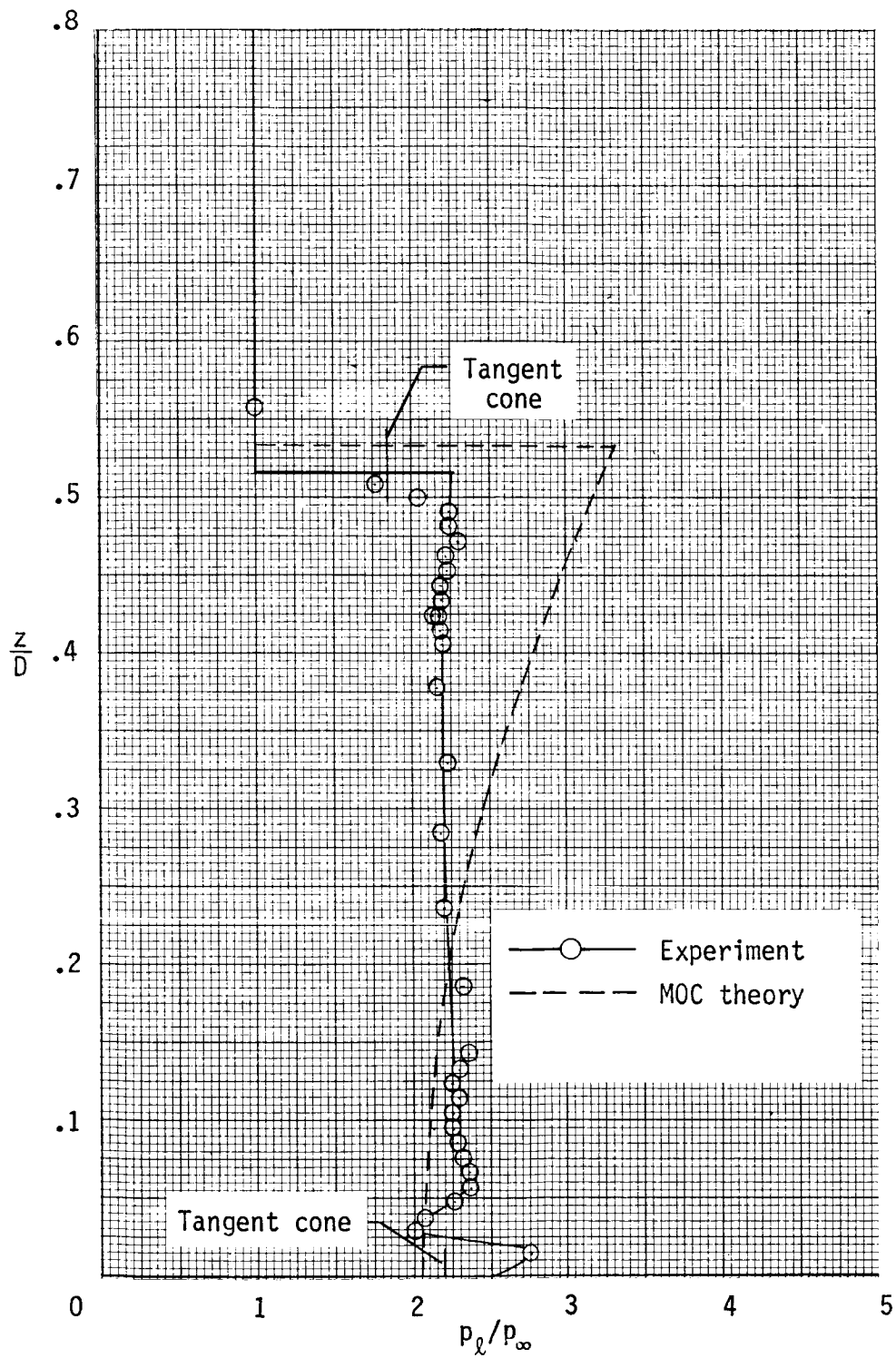
Figure C9.- Continued.





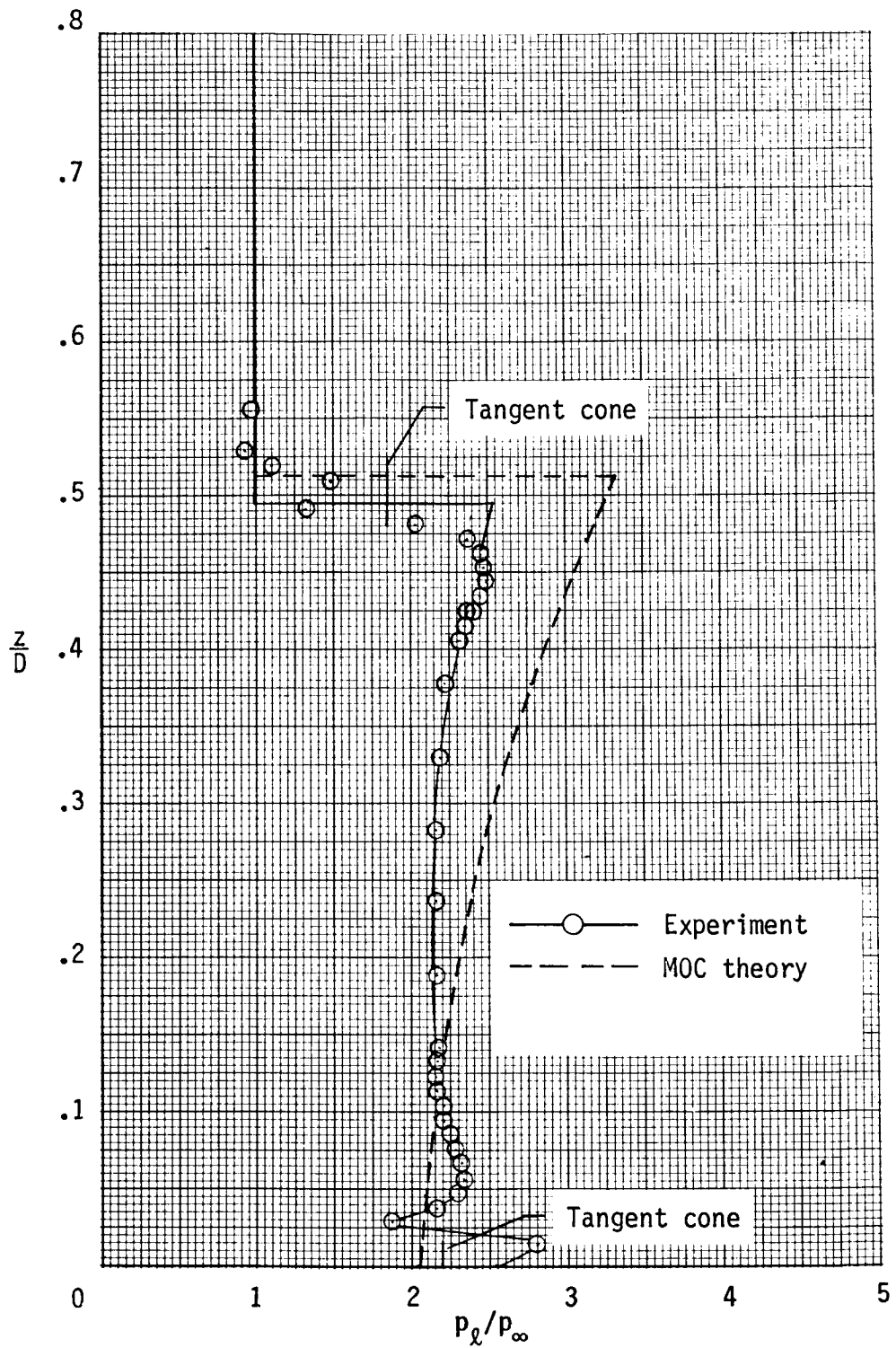
(a) $y/D = 0$.

Figure C10.- Static pressure survey at forward survey station
($x/D = 3.5$) at $\alpha = 8^\circ$.



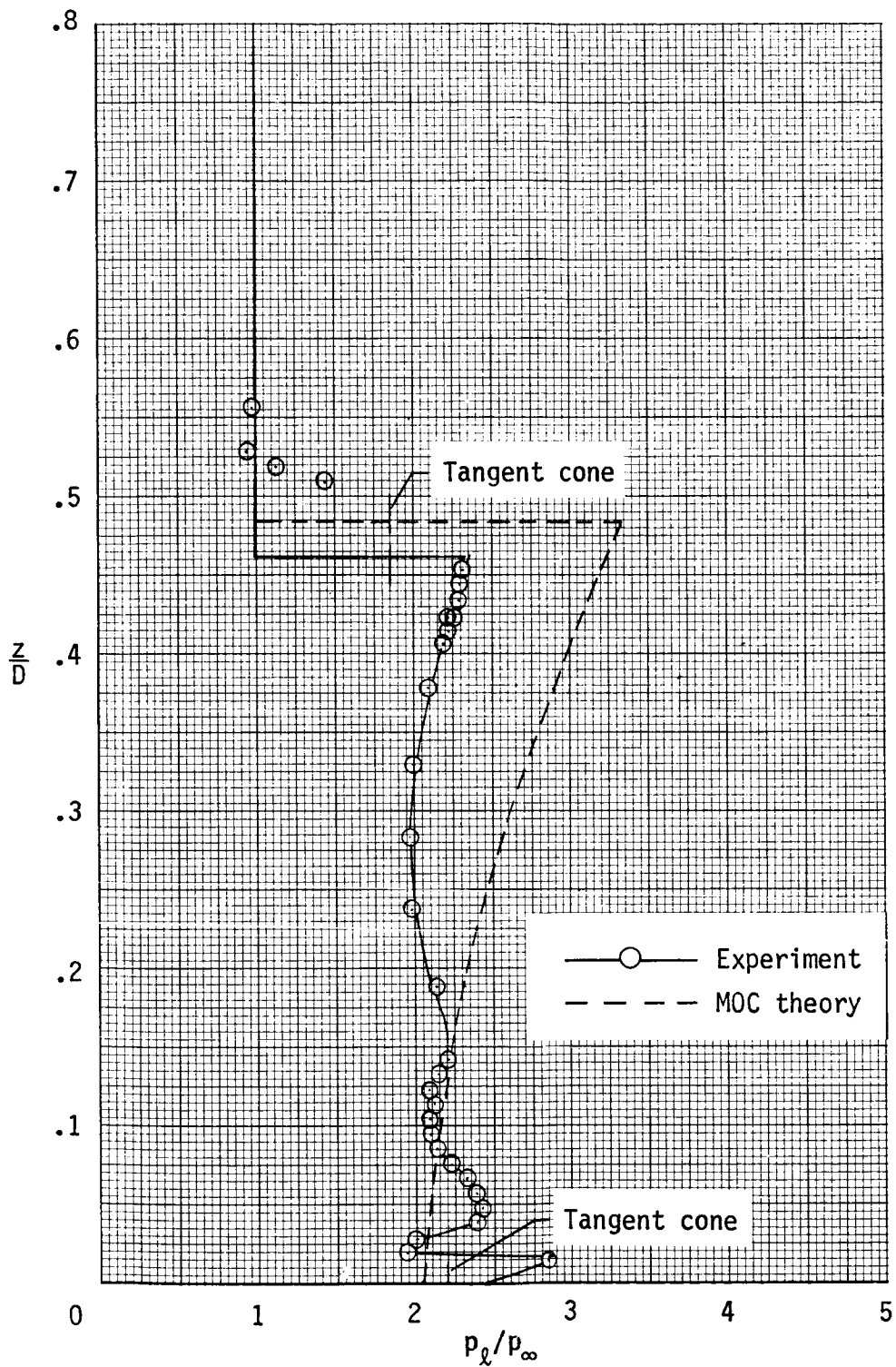
(b) $y/D = 0.118$.

Figure C10.- Continued.



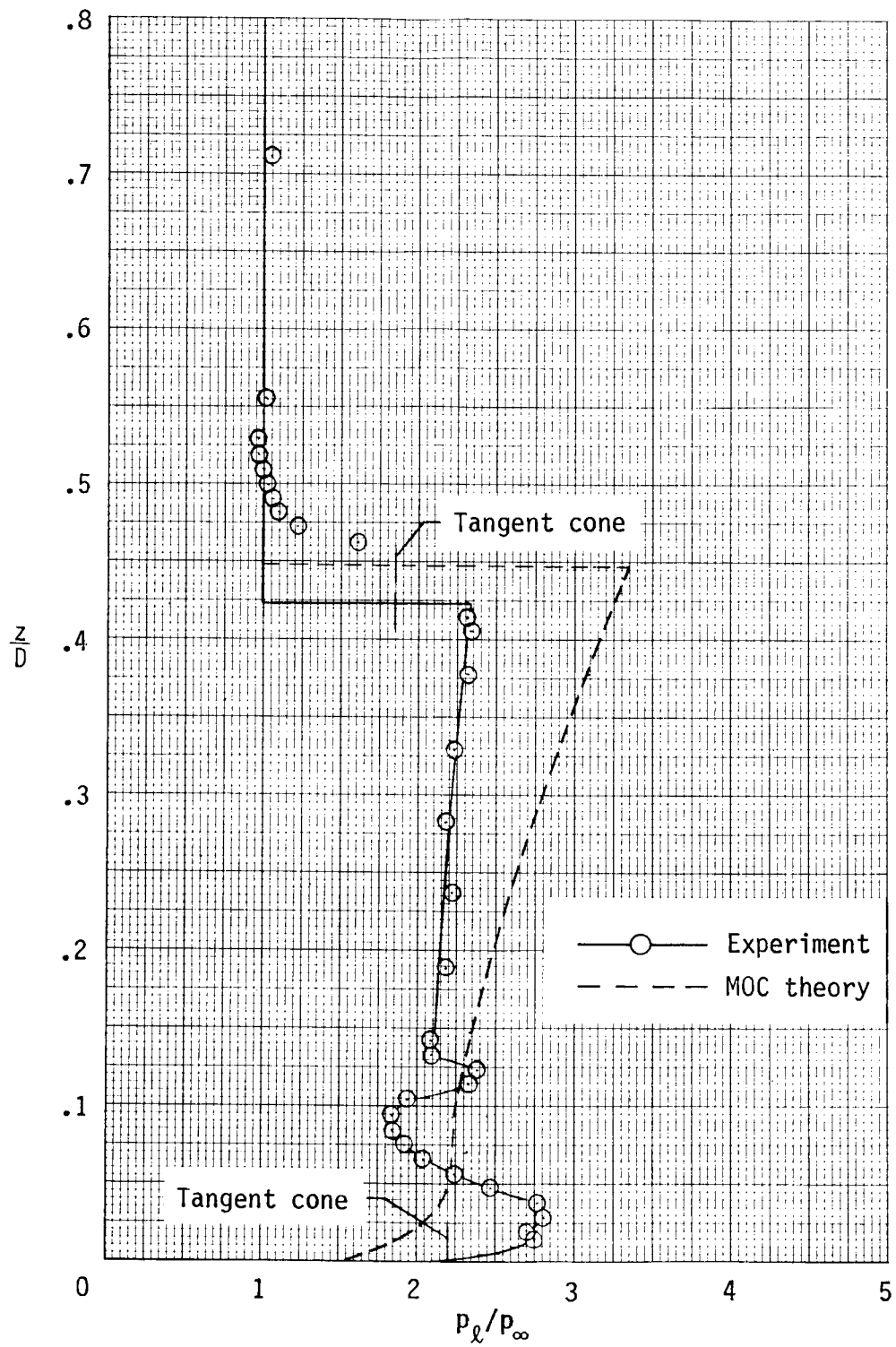
(c) $y/D = 0.236$.

Figure C10.- Continued.



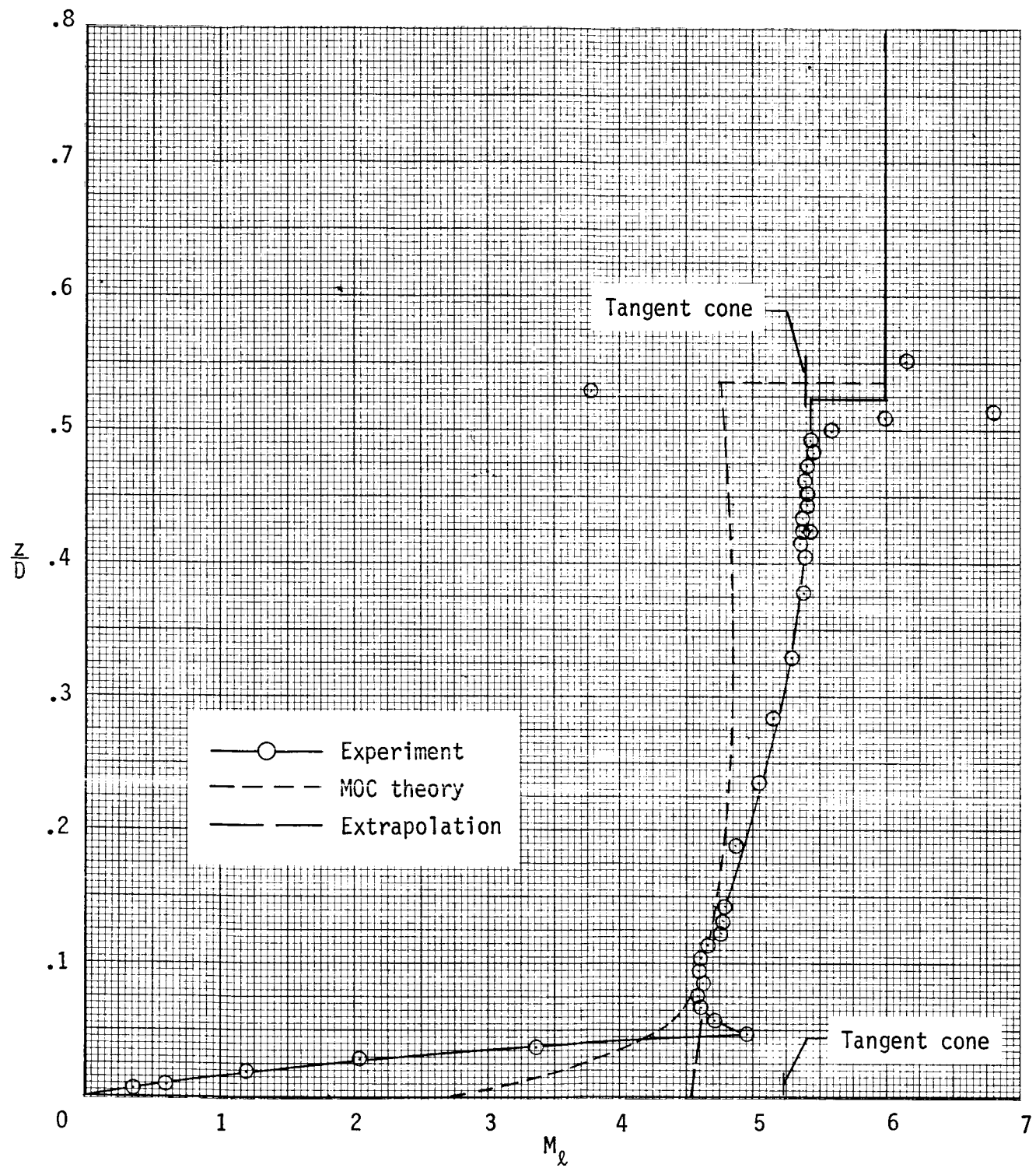
(d) $y/D = 0.354$.

Figure C10.- Continued.



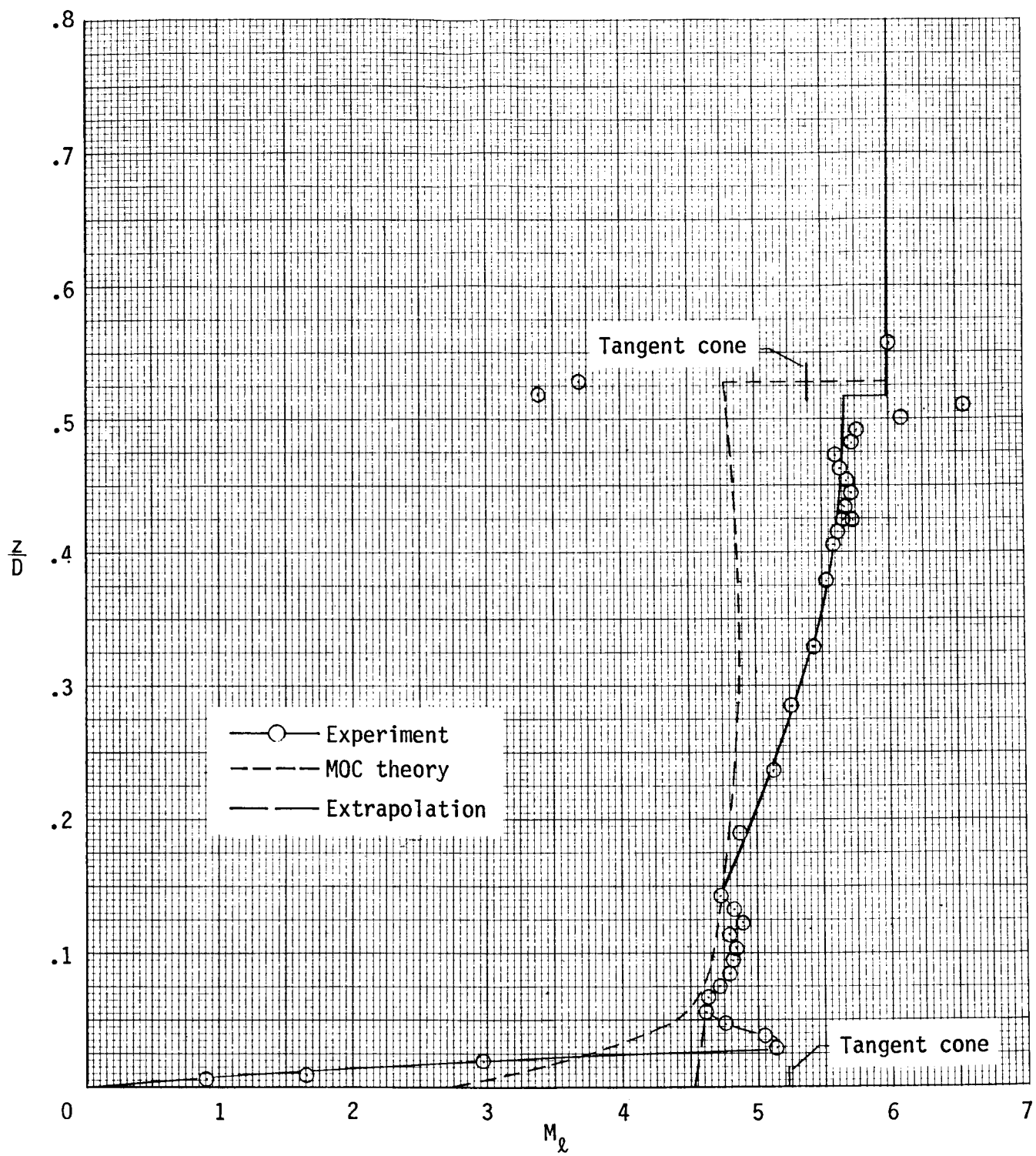
(e) $y/D = 0.472$.

Figure C10.- Concluded.



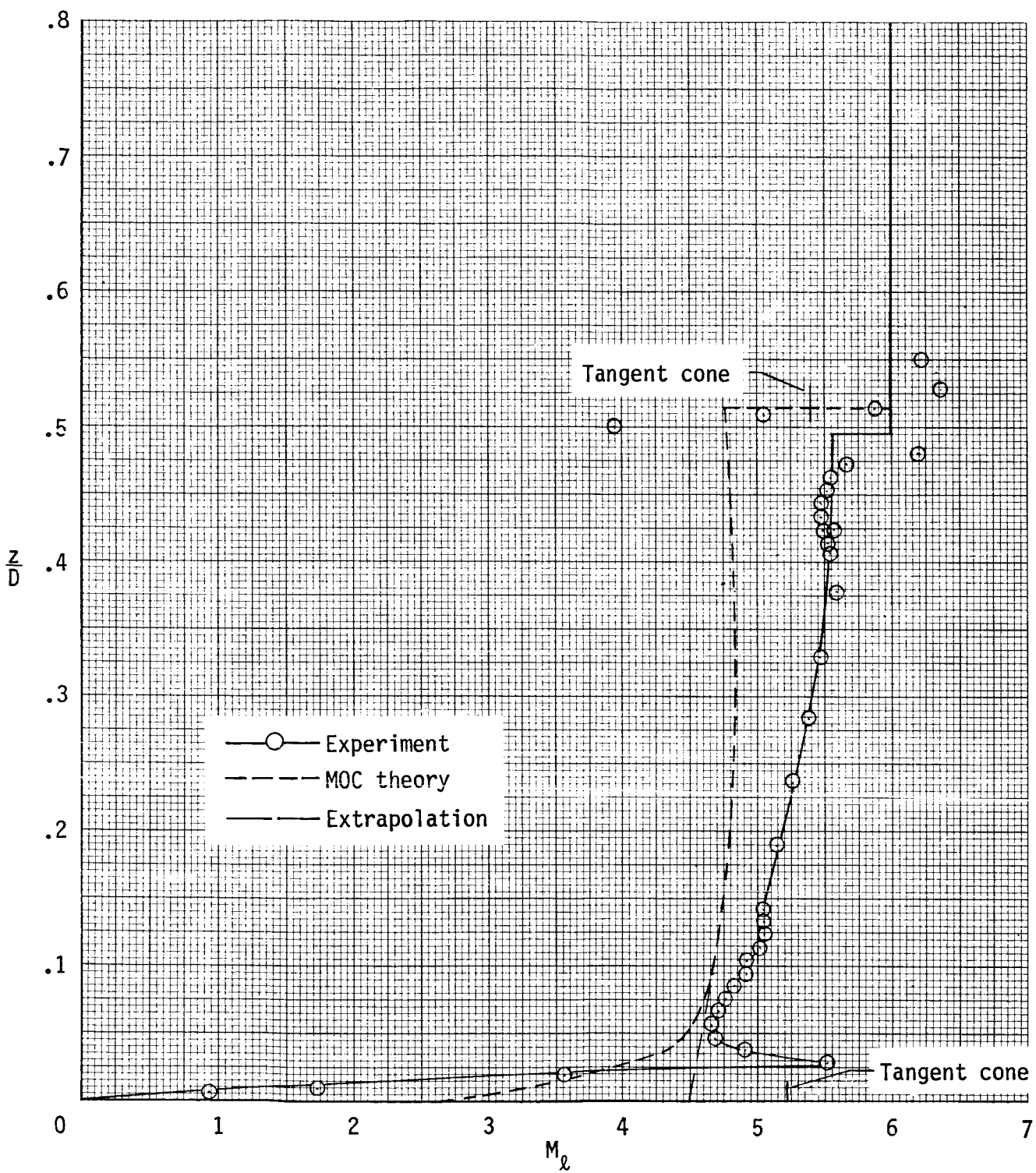
(a) $y/D = 0$.

Figure C11.- Local Mach number distribution at forward survey station
($x/D = 3.5$) at $\alpha = 8^\circ$.



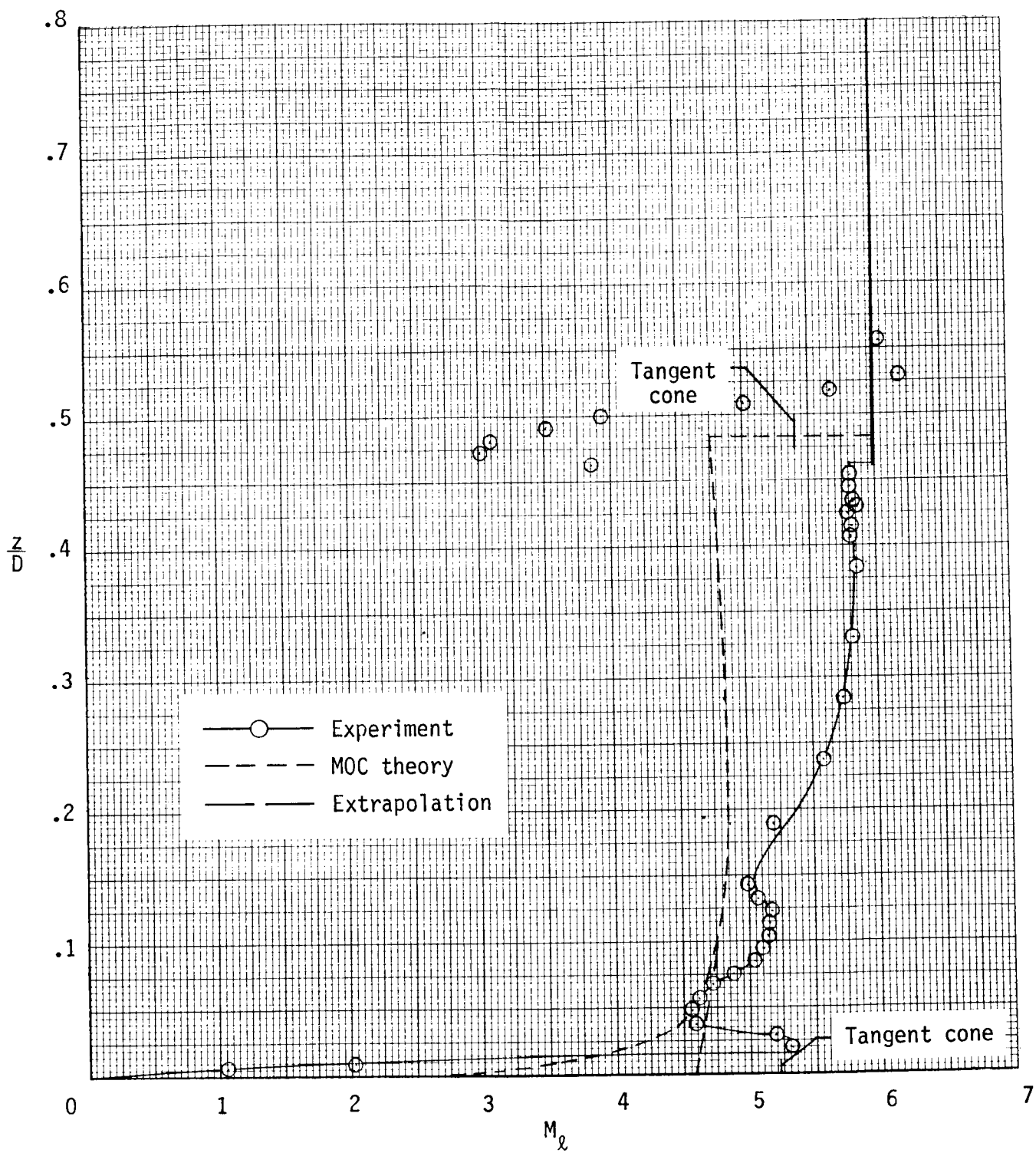
(b) $y/D = 0.118$.

Figure C11.- Continued.



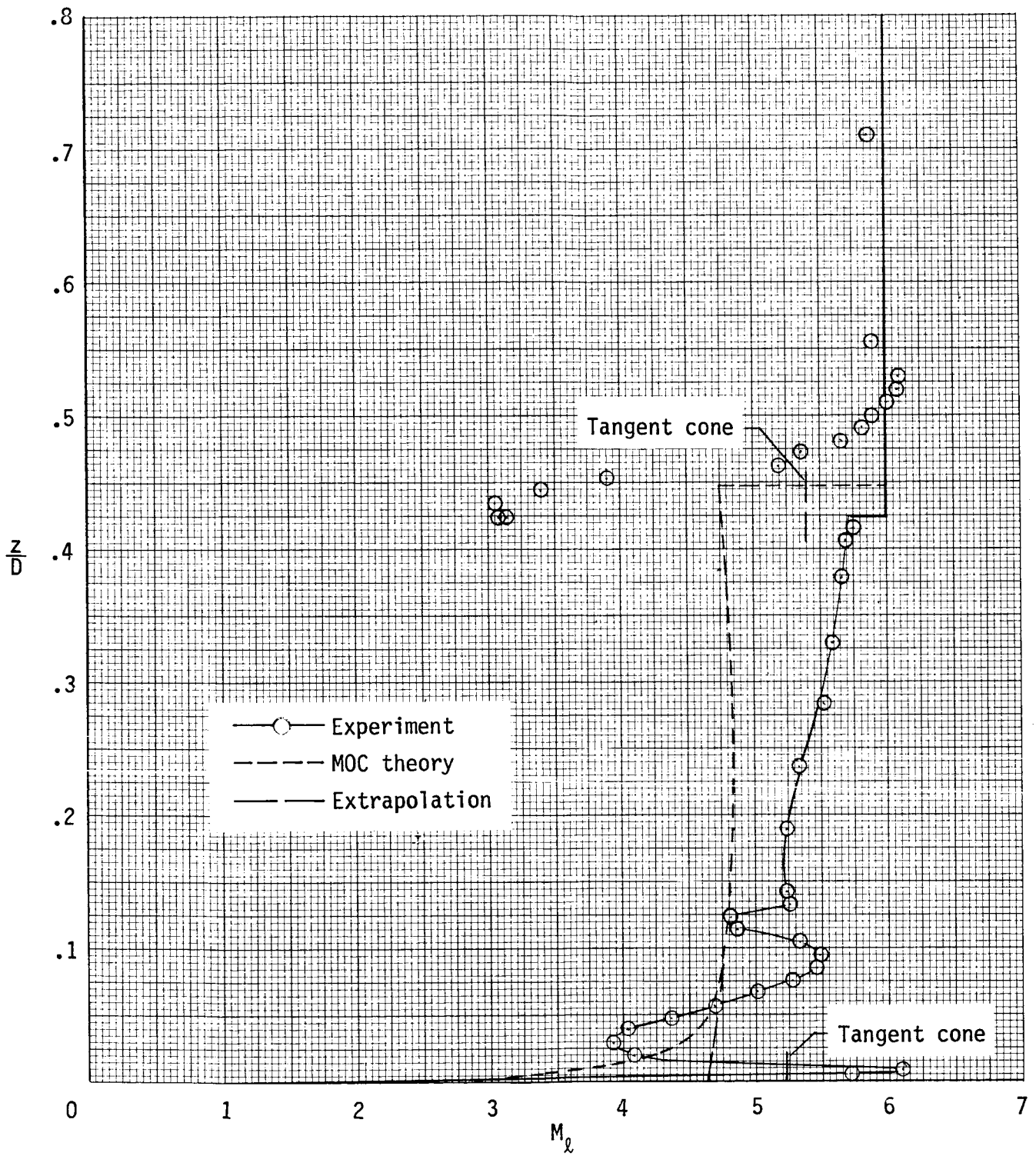
(c) $y/D = 0.236$.

Figure C11.- Continued.



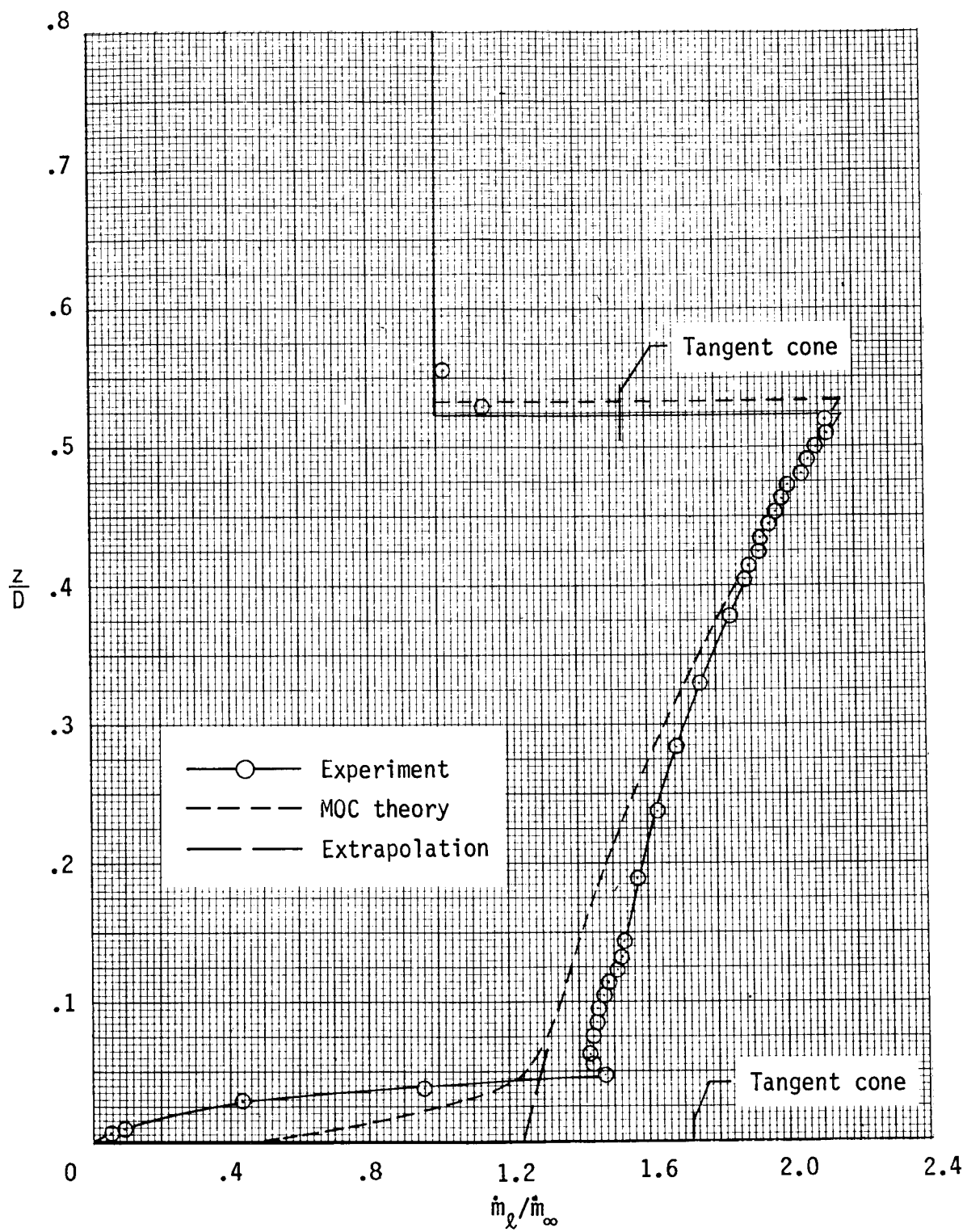
(d) $y/D = 0.354$.

Figure C11.-- Continued.



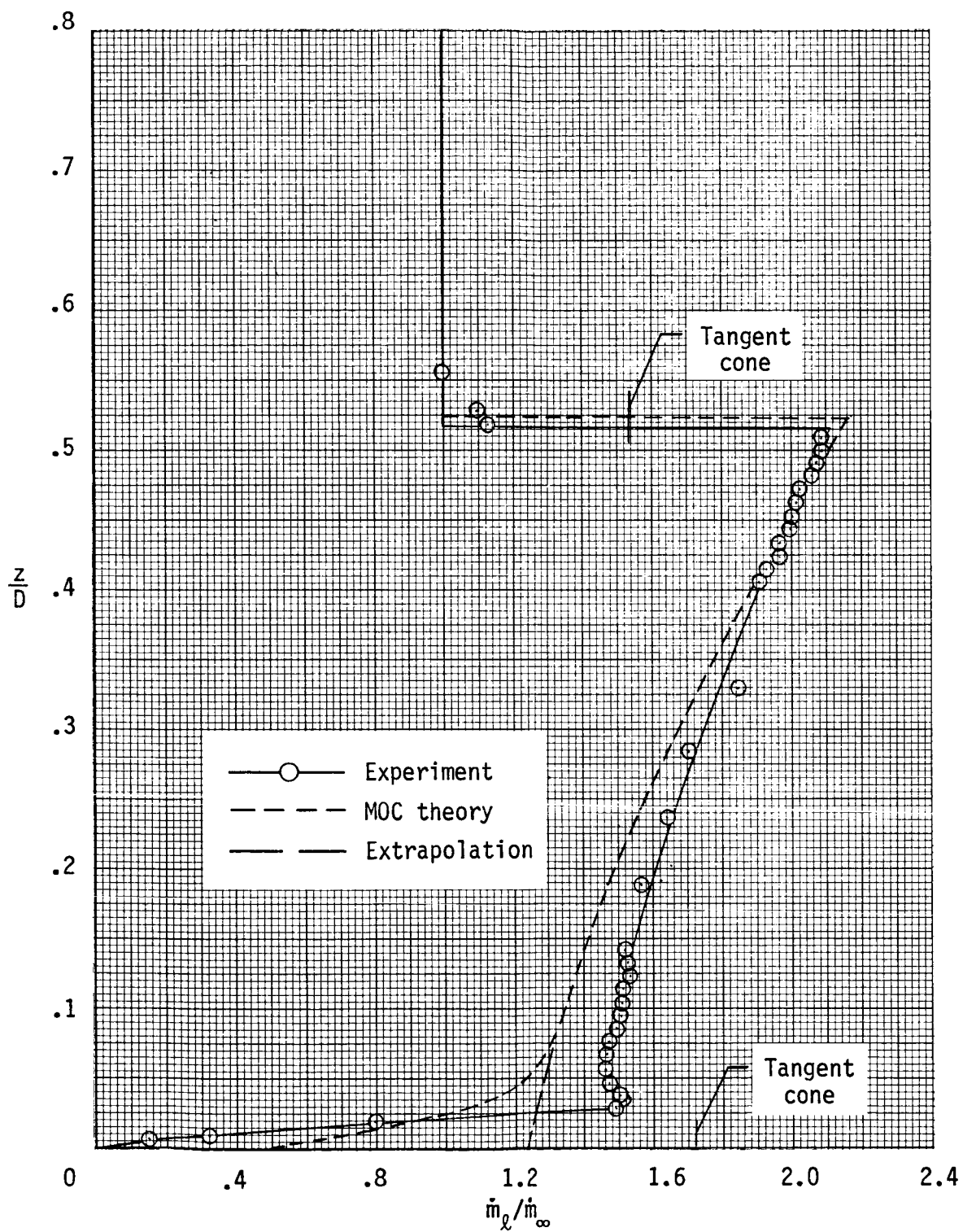
(e) $y/D = 0.472$.

Figure C11.- Concluded.



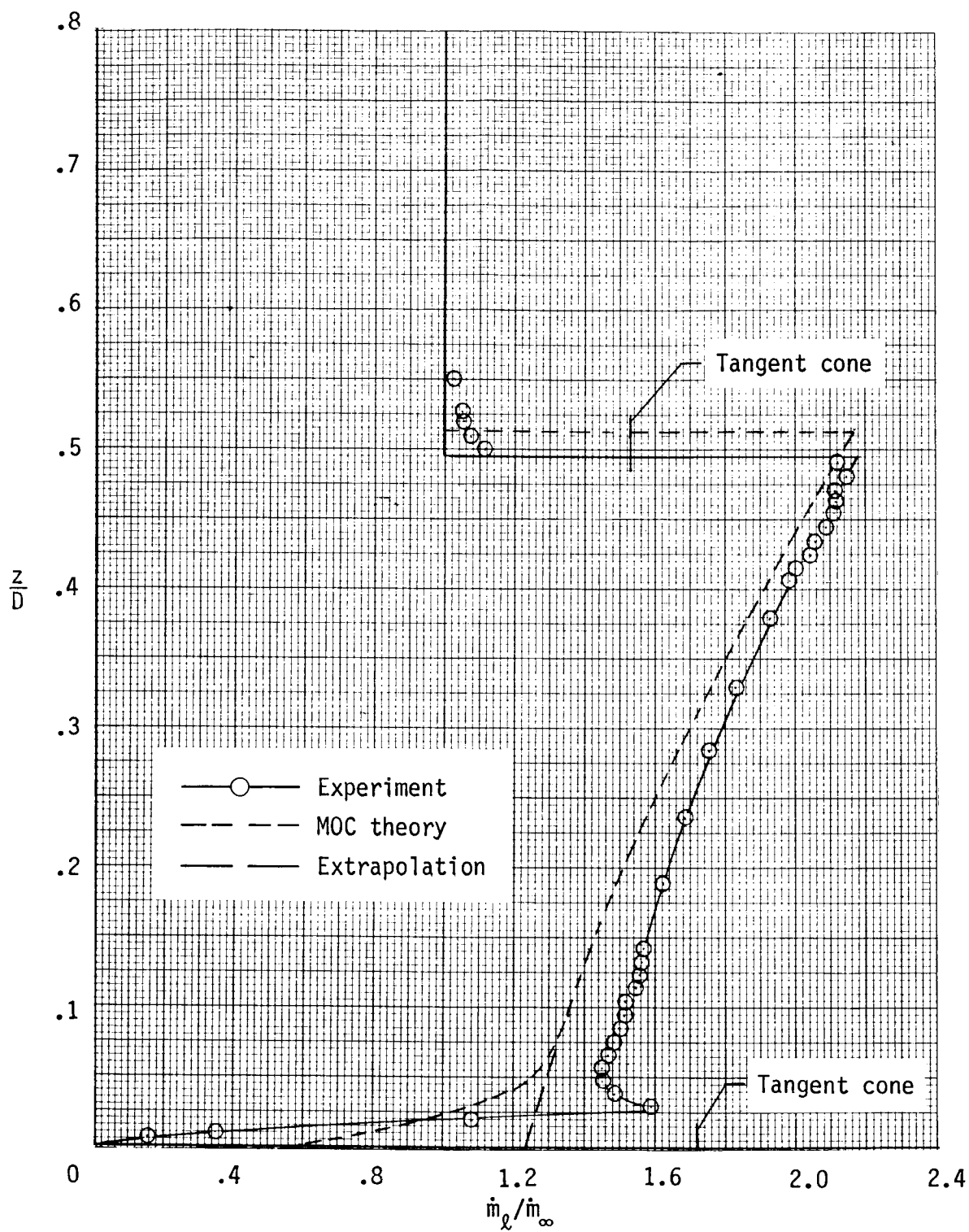
(a) $y/D = 0$.

Figure C12.- Local mass flow ratios at forward survey station ($x/D = 3.5$) at $\alpha = 8^\circ$.



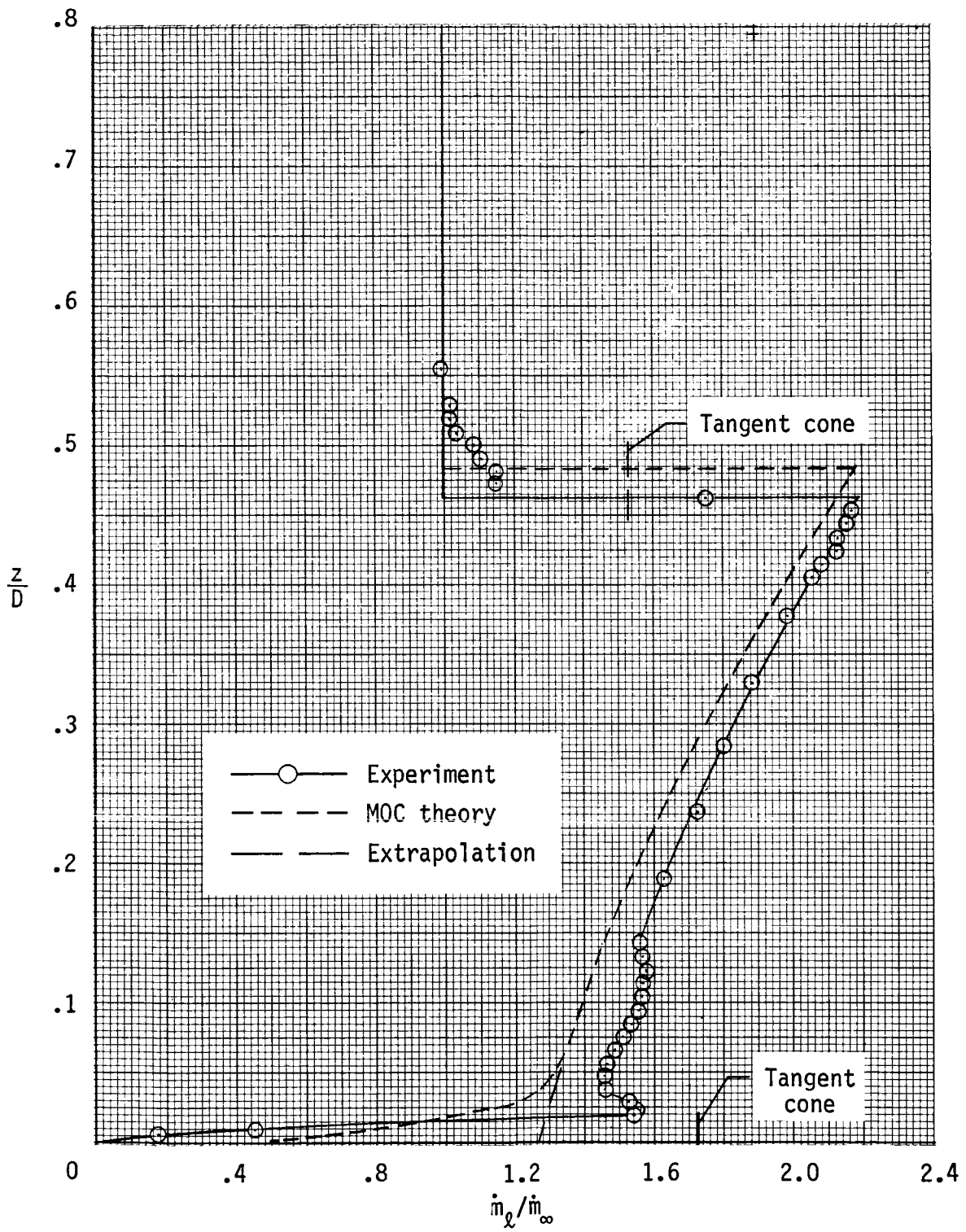
(b) $y/D = 0.118$.

Figure C12.- Continued.



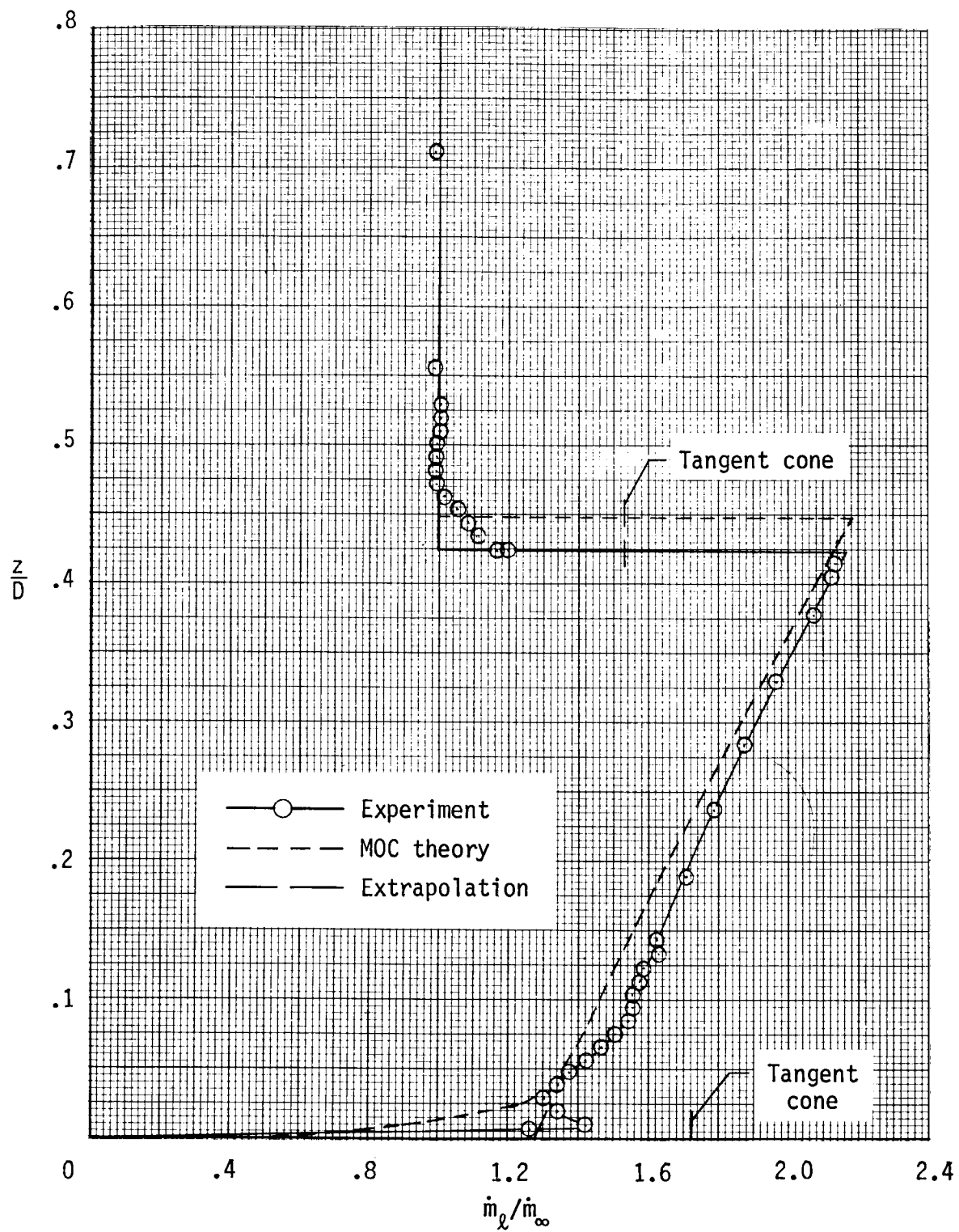
(c) $y/D = 0.236$.

Figure C12.- Continued.



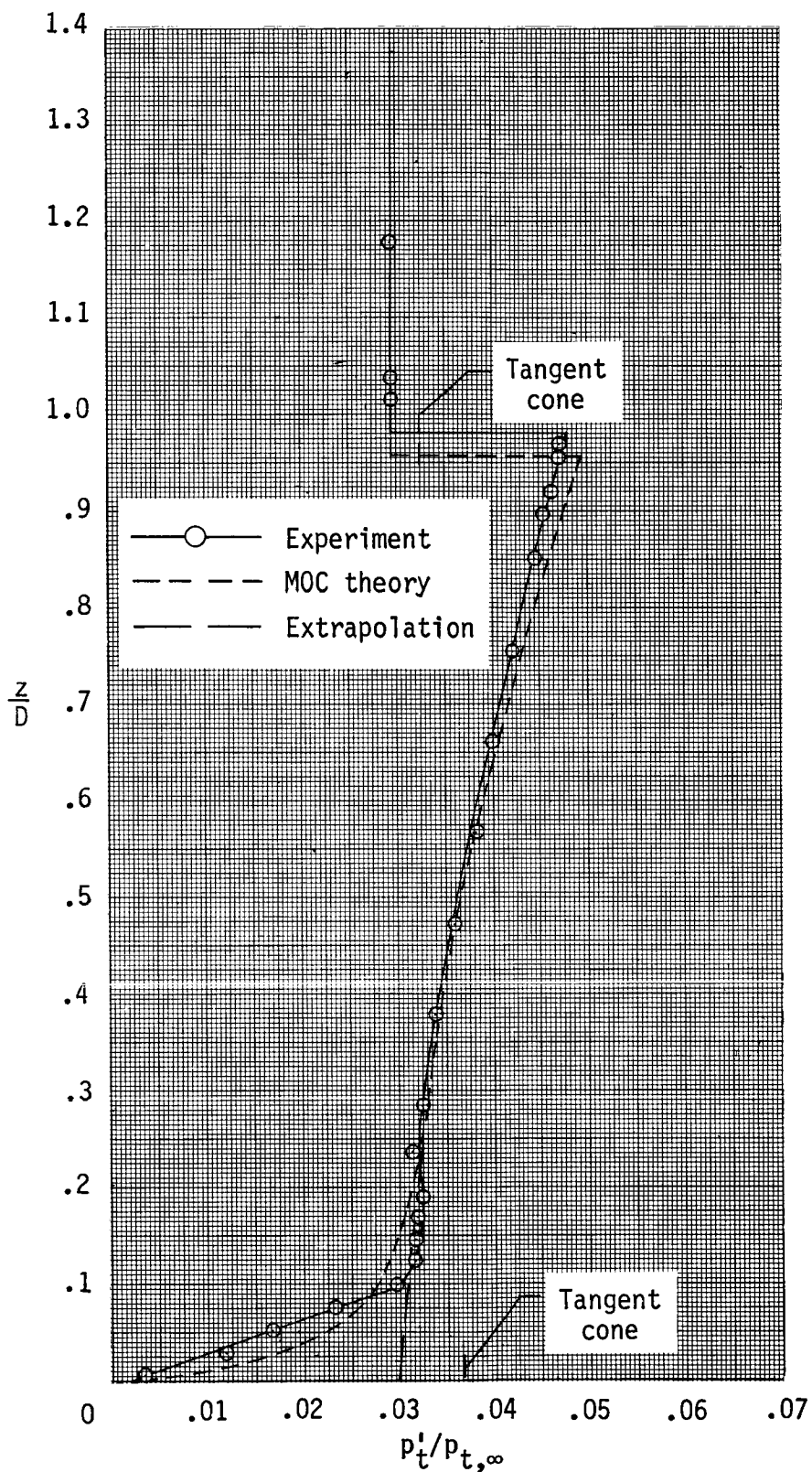
(d) $y/D = 0.354$.

Figure C12.- Continued.



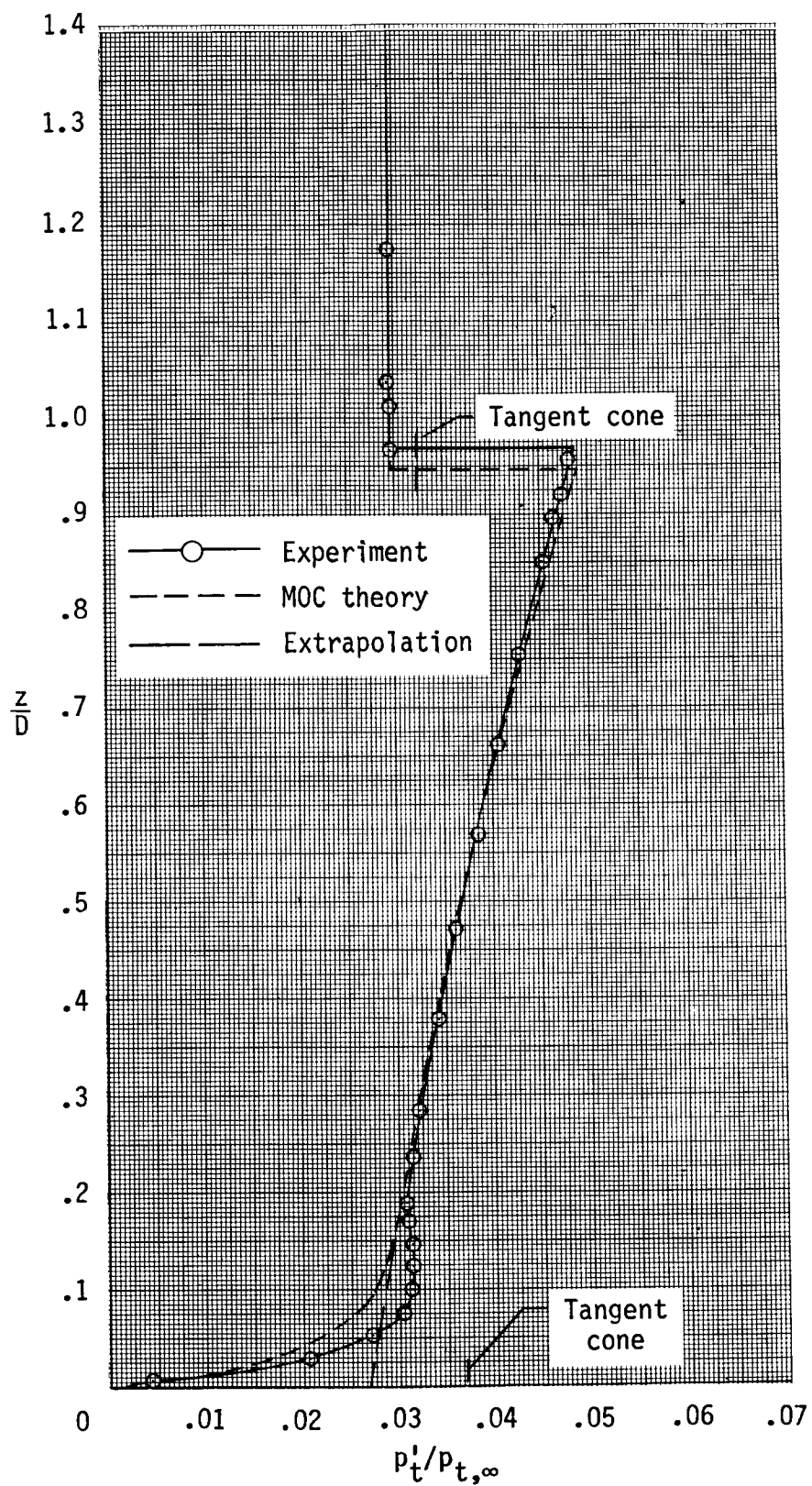
(e) $y/D = 0.472$.

Figure C12.- Concluded.



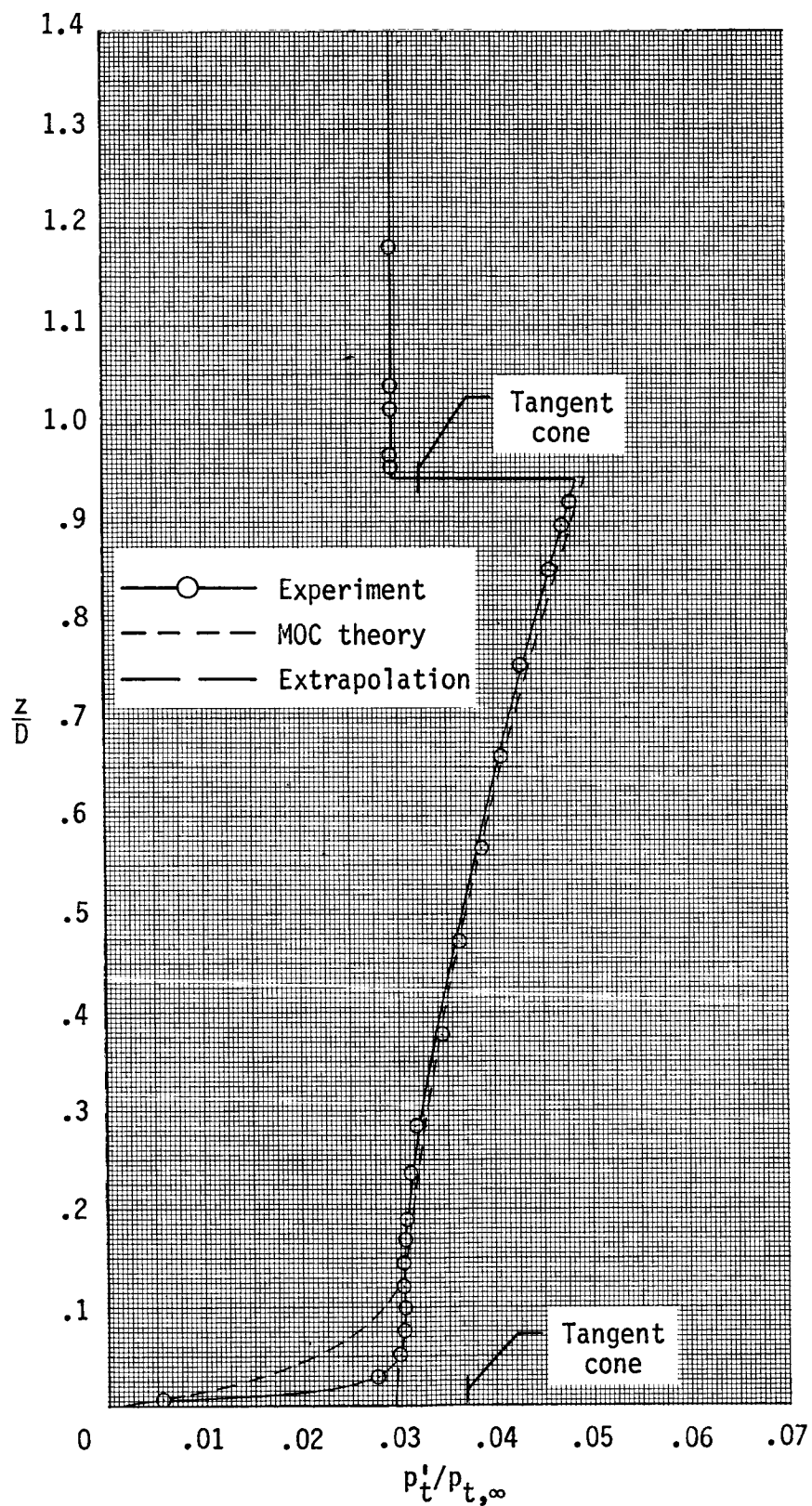
(a) $y/D = 0$.

Figure C13.- Pitot pressure survey at aft survey station
($x/D = 5.4$) at $\alpha = 4^\circ$.



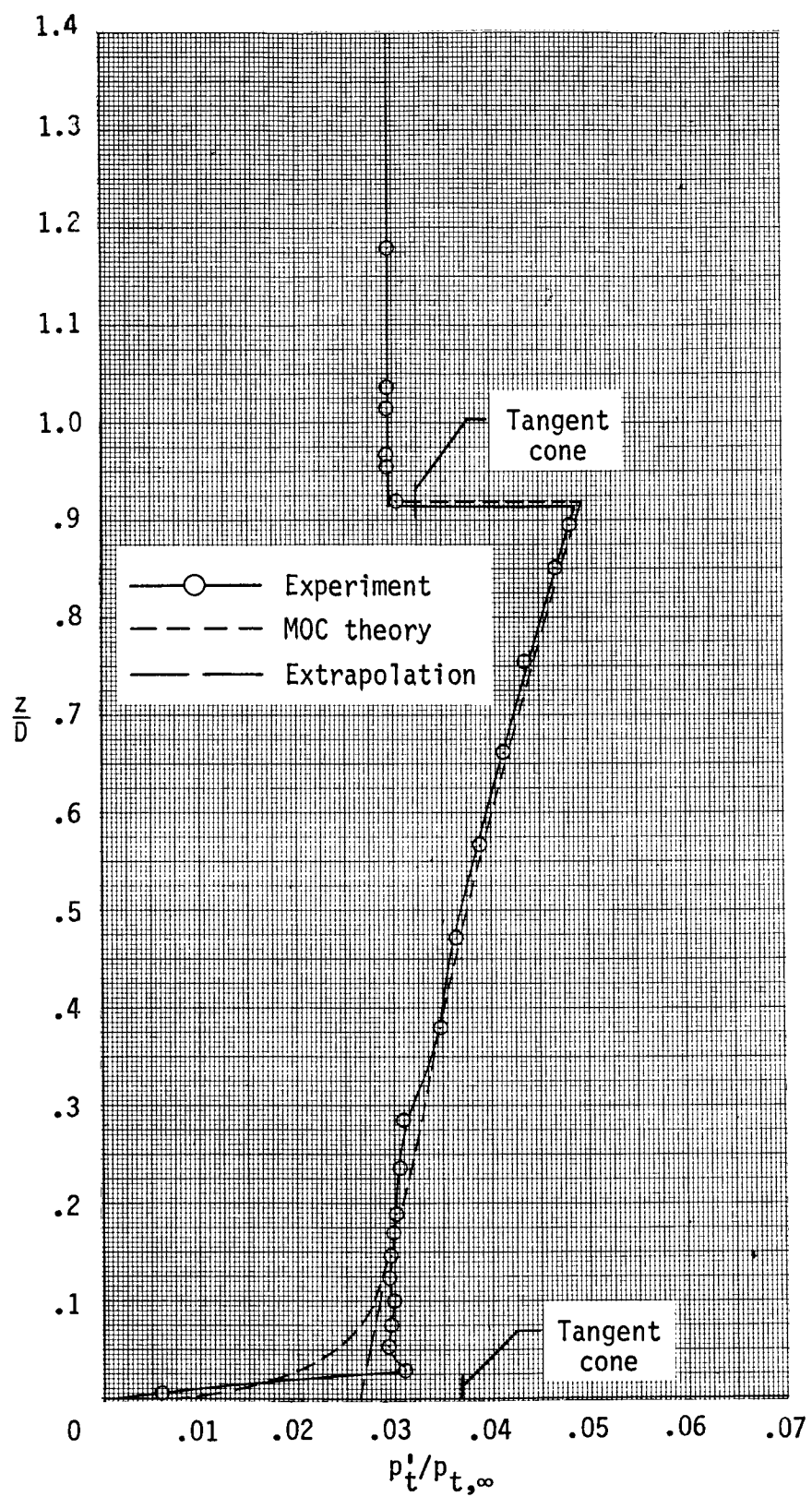
(b) $y/D = 0.118$.

Figure C13.- Continued.



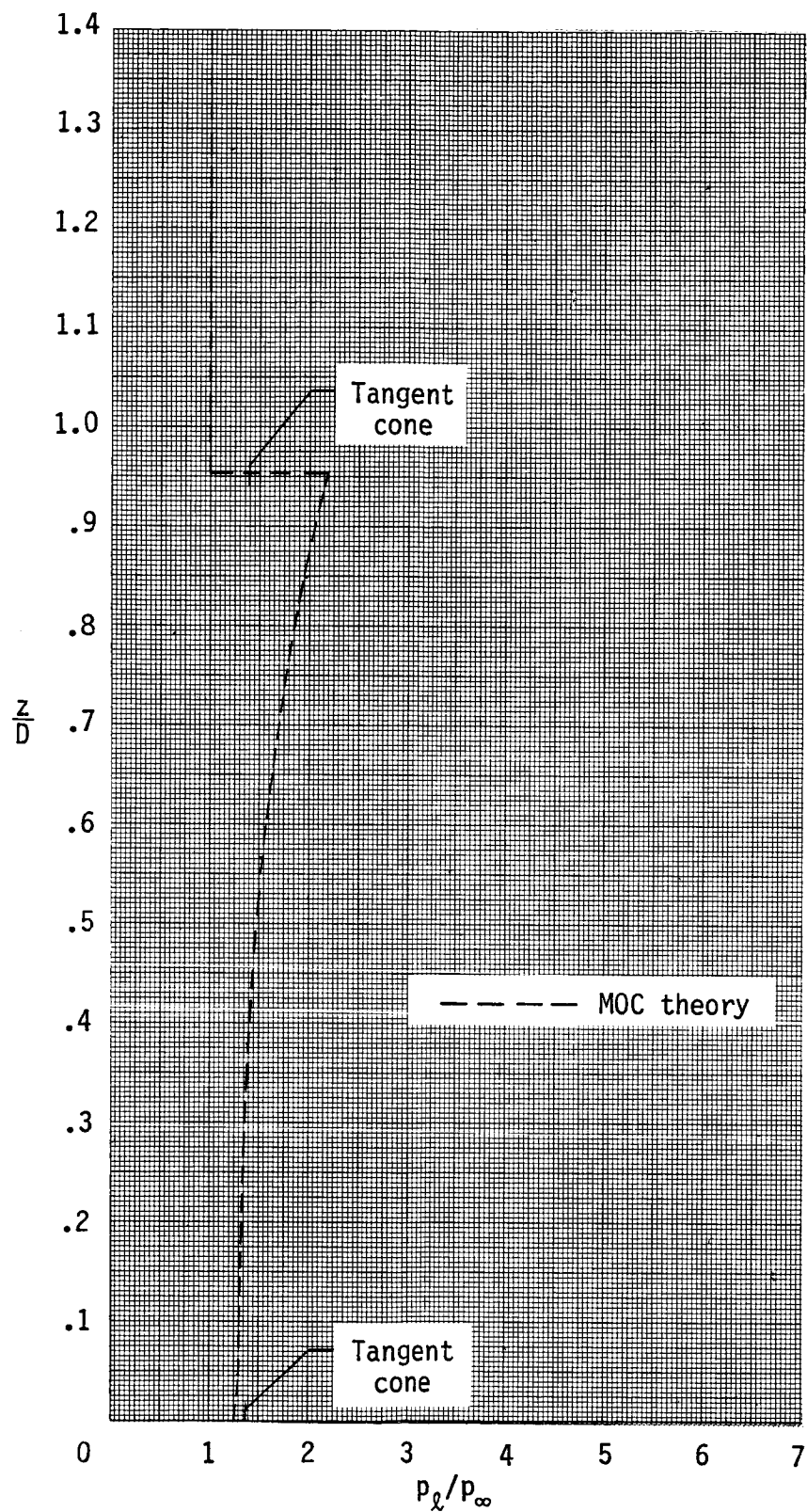
(c) $y/D = 0.236$.

Figure C13.- Continued.



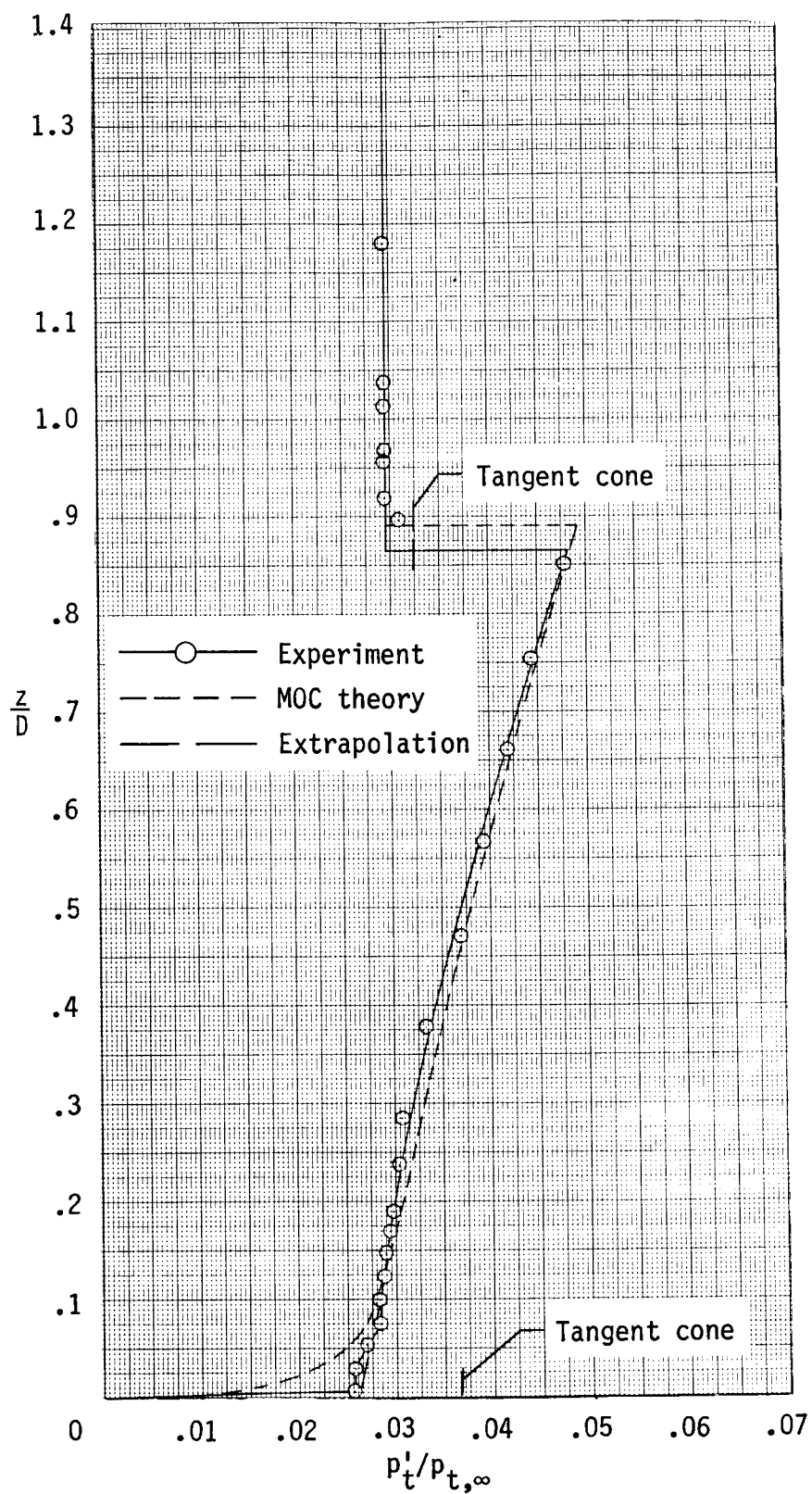
(d) $y/D = 0.354$.

Figure C13.- Continued.



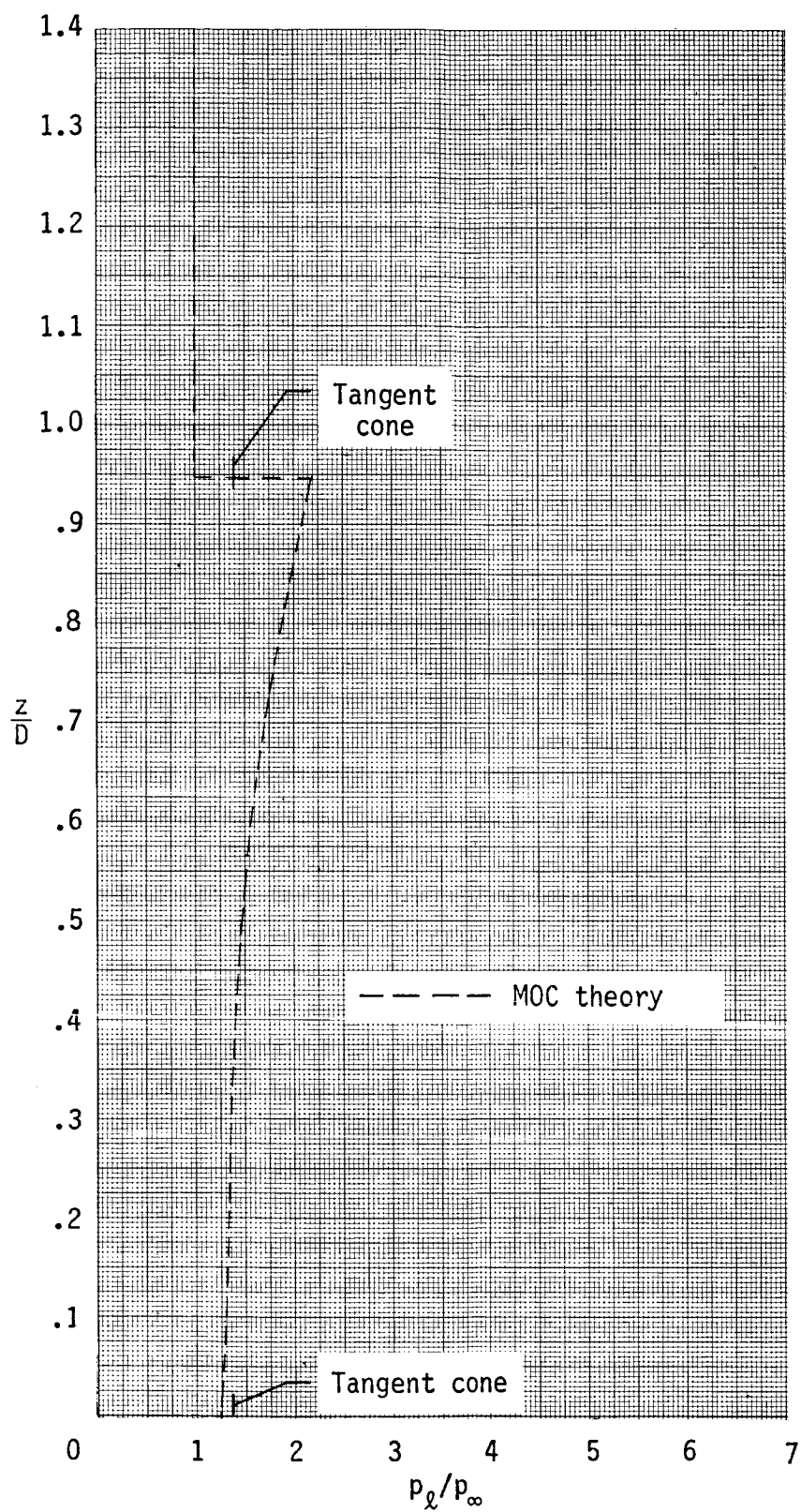
(a) $y/D = 0$.

Figure C14.- Static pressure survey at aft survey station
($x/D = 5.4$) at $\alpha = 4^\circ$.



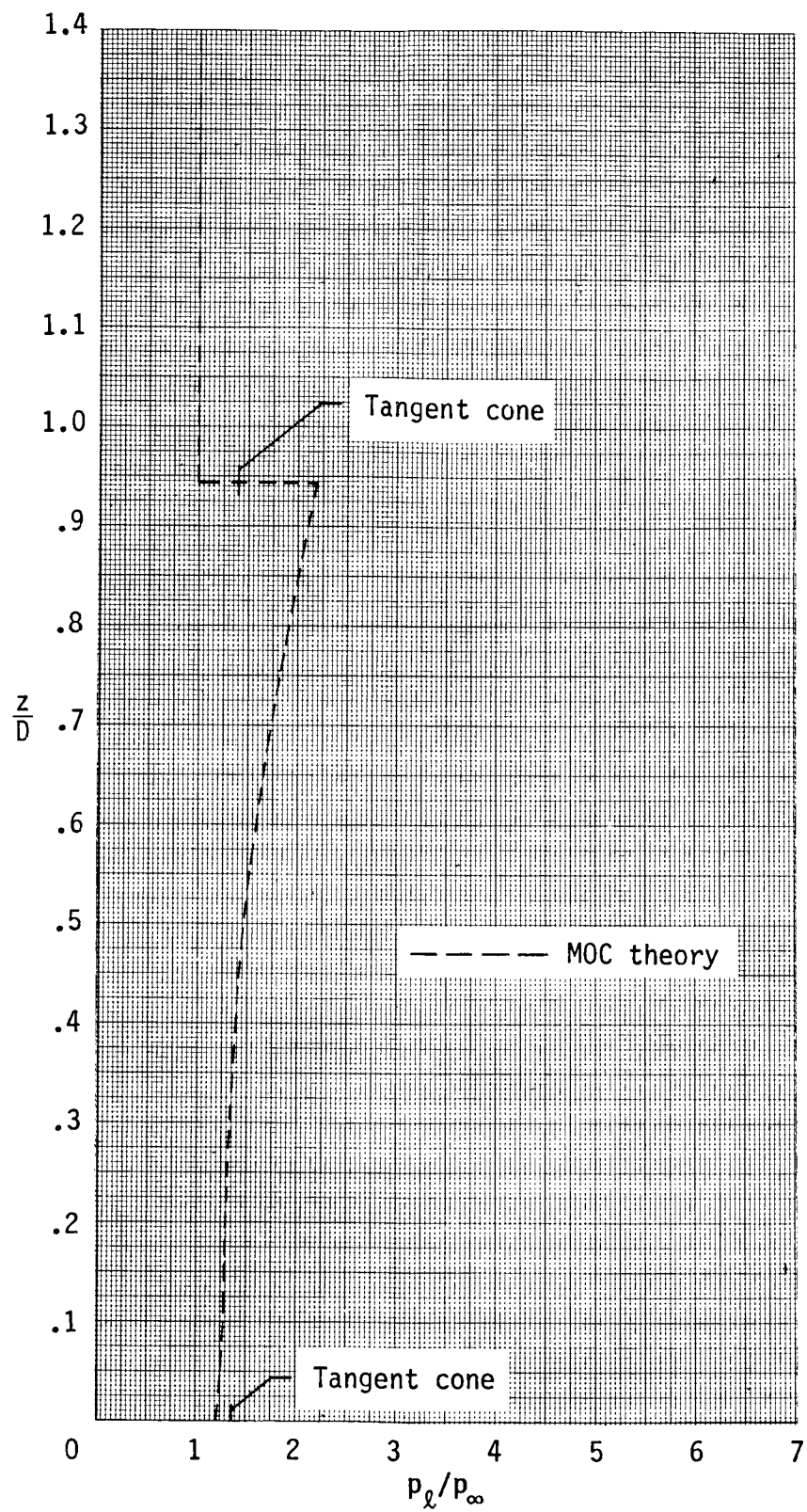
(e) $y/D = 0.472$.

Figure C13.- Concluded.



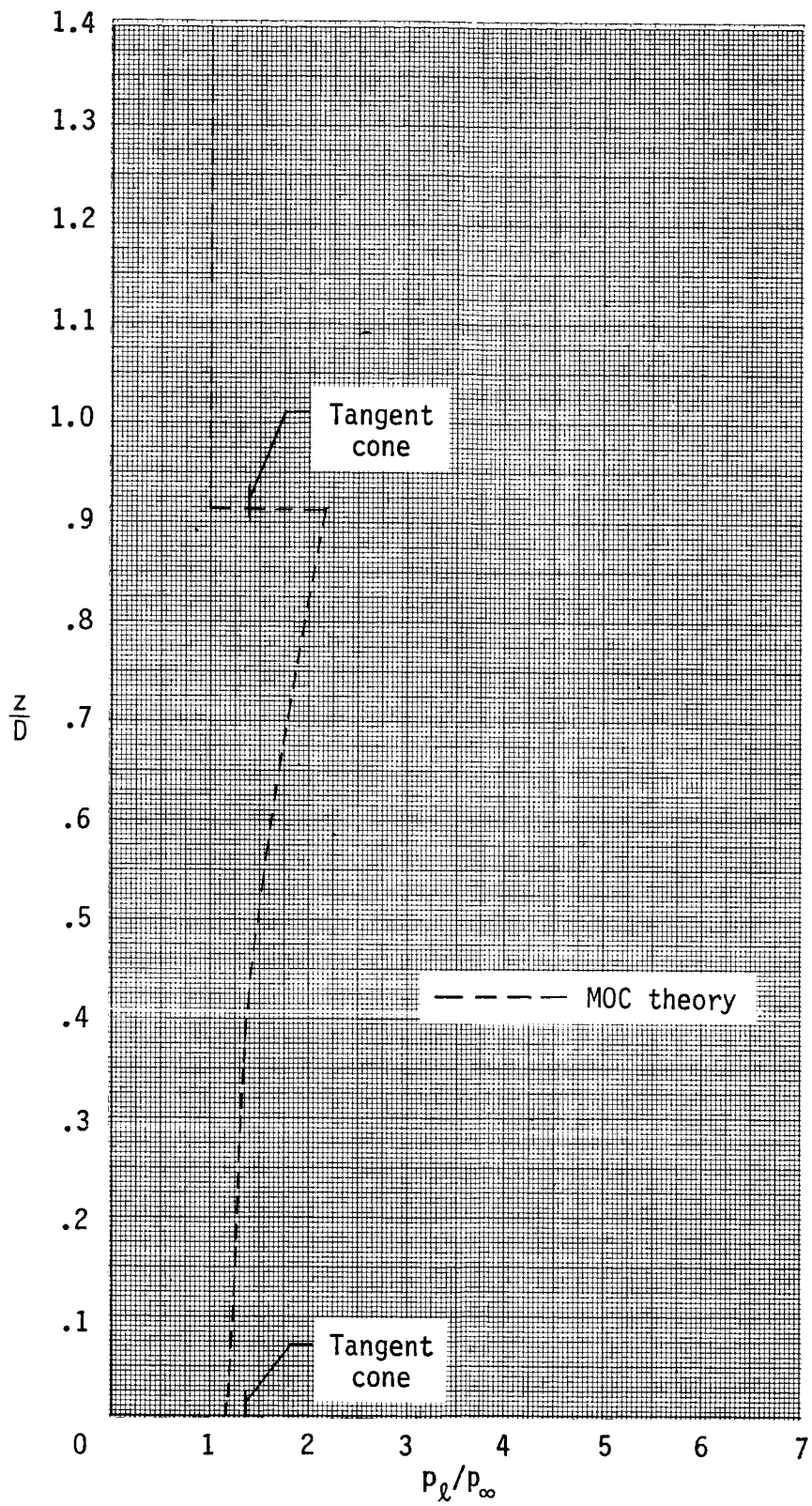
(b) $y/D = 0.118$.

Figure C14.- Continued.



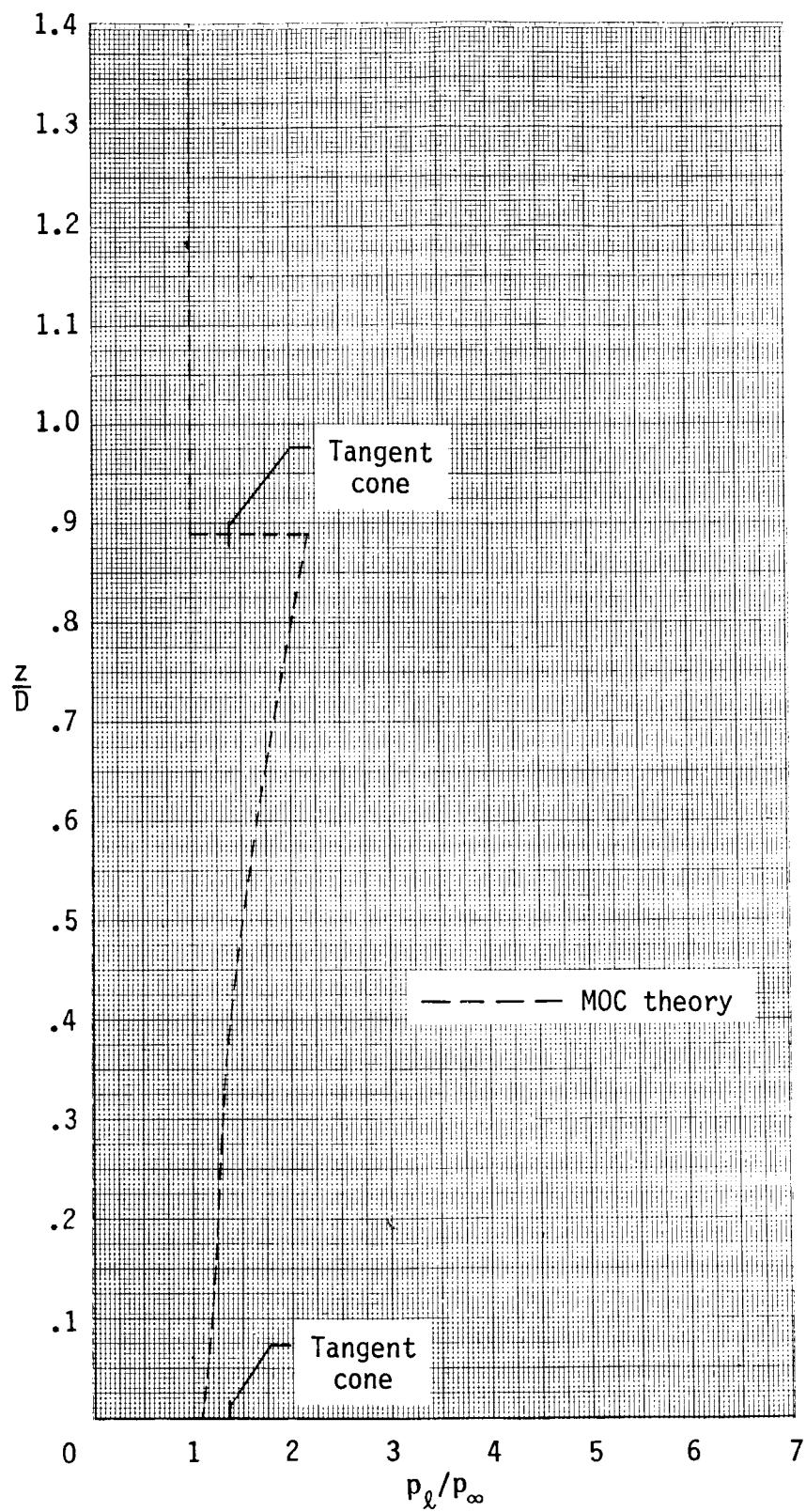
(c) $y/D = 0.236$.

Figure C14.- Continued.



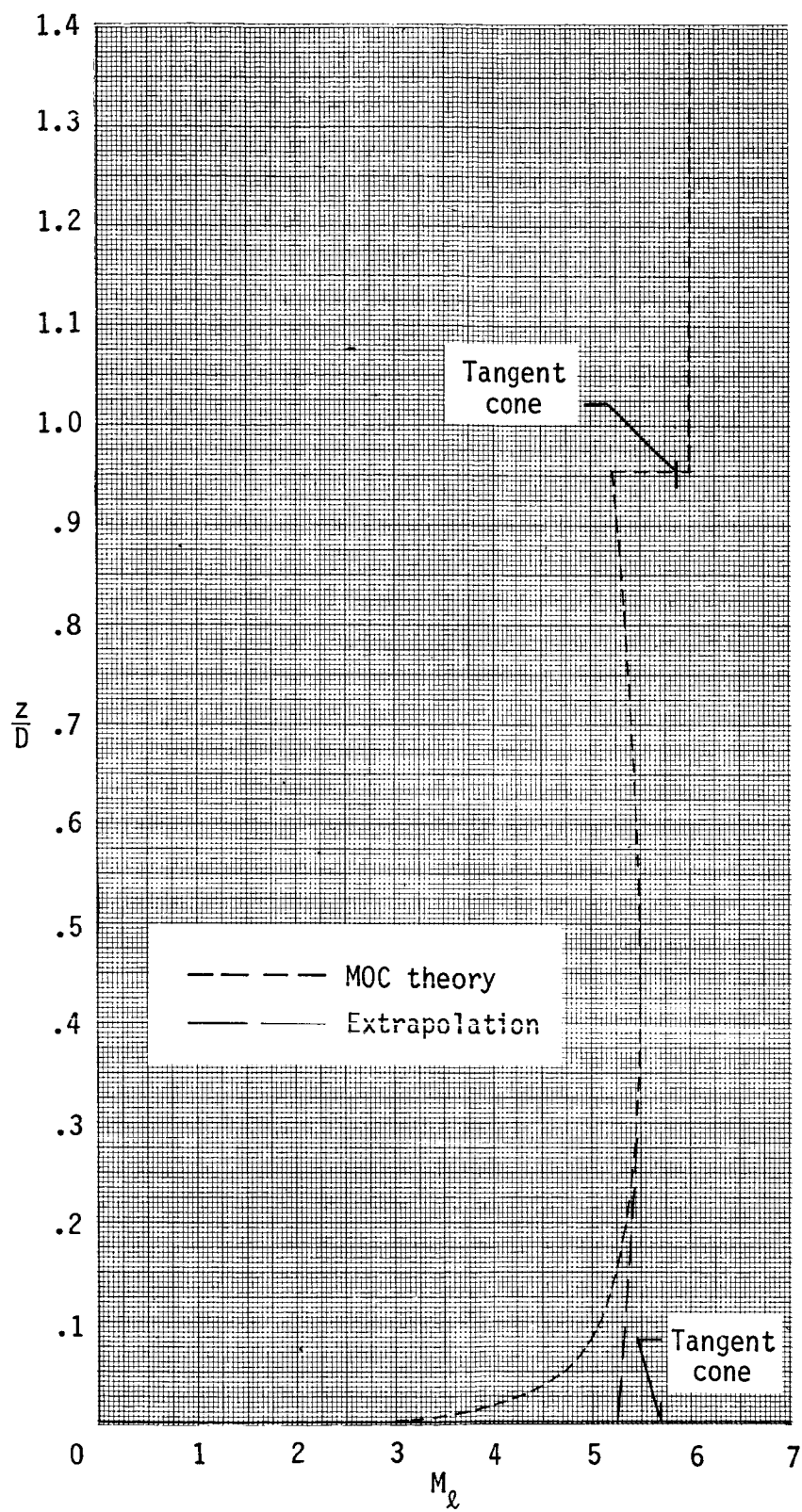
(d) $y/D = 0.354$.

Figure C14.- Continued.



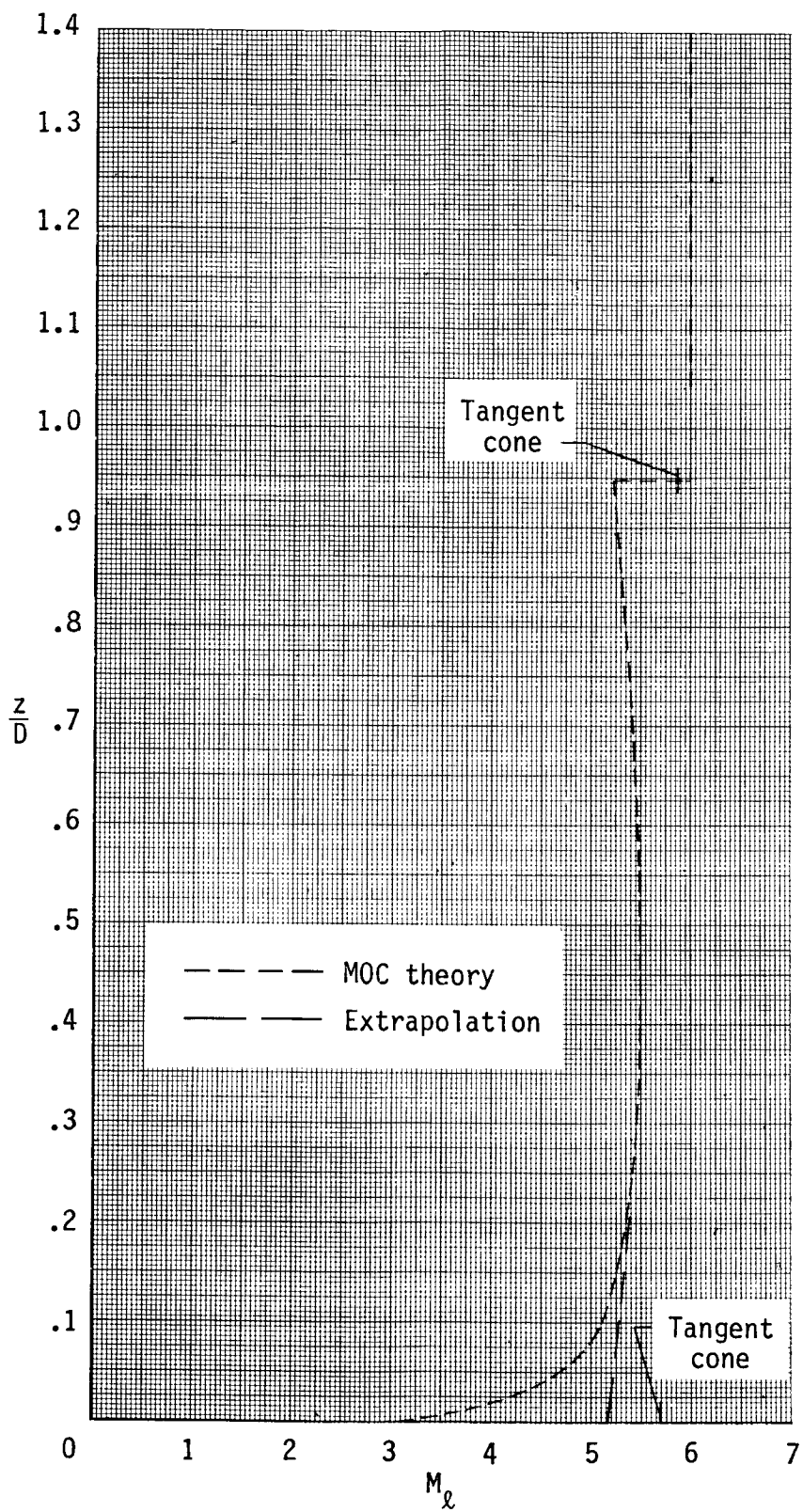
(e) $y/D = 0.472$.

Figure C14.- Concluded.



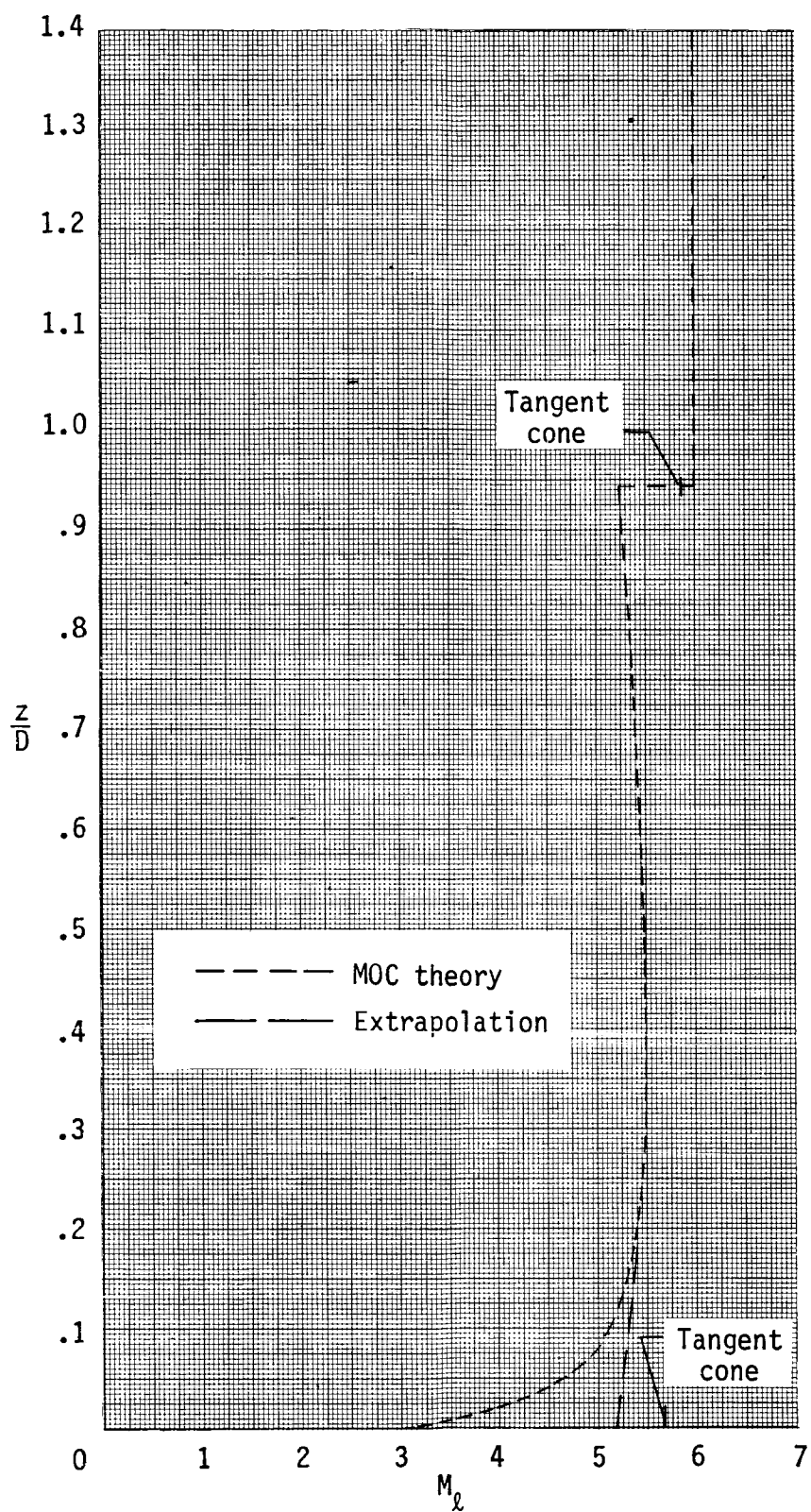
(a) $y/D = 0$.

Figure C15.- Local Mach number distribution at aft survey station
($x/D = 5.4$) at $\alpha = 4^\circ$.



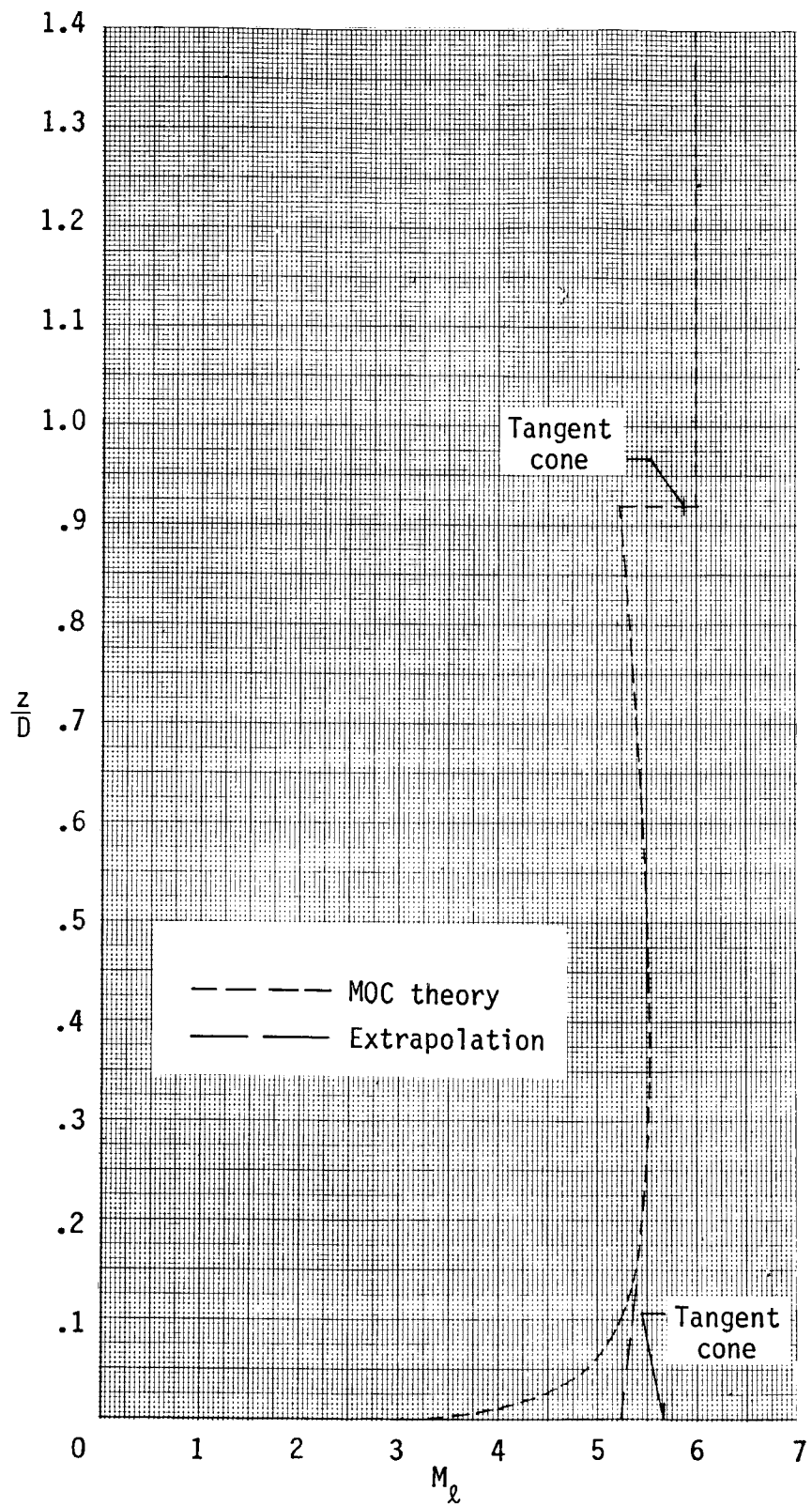
(b) $y/D = 0.118$.

Figure C15.- Continued.



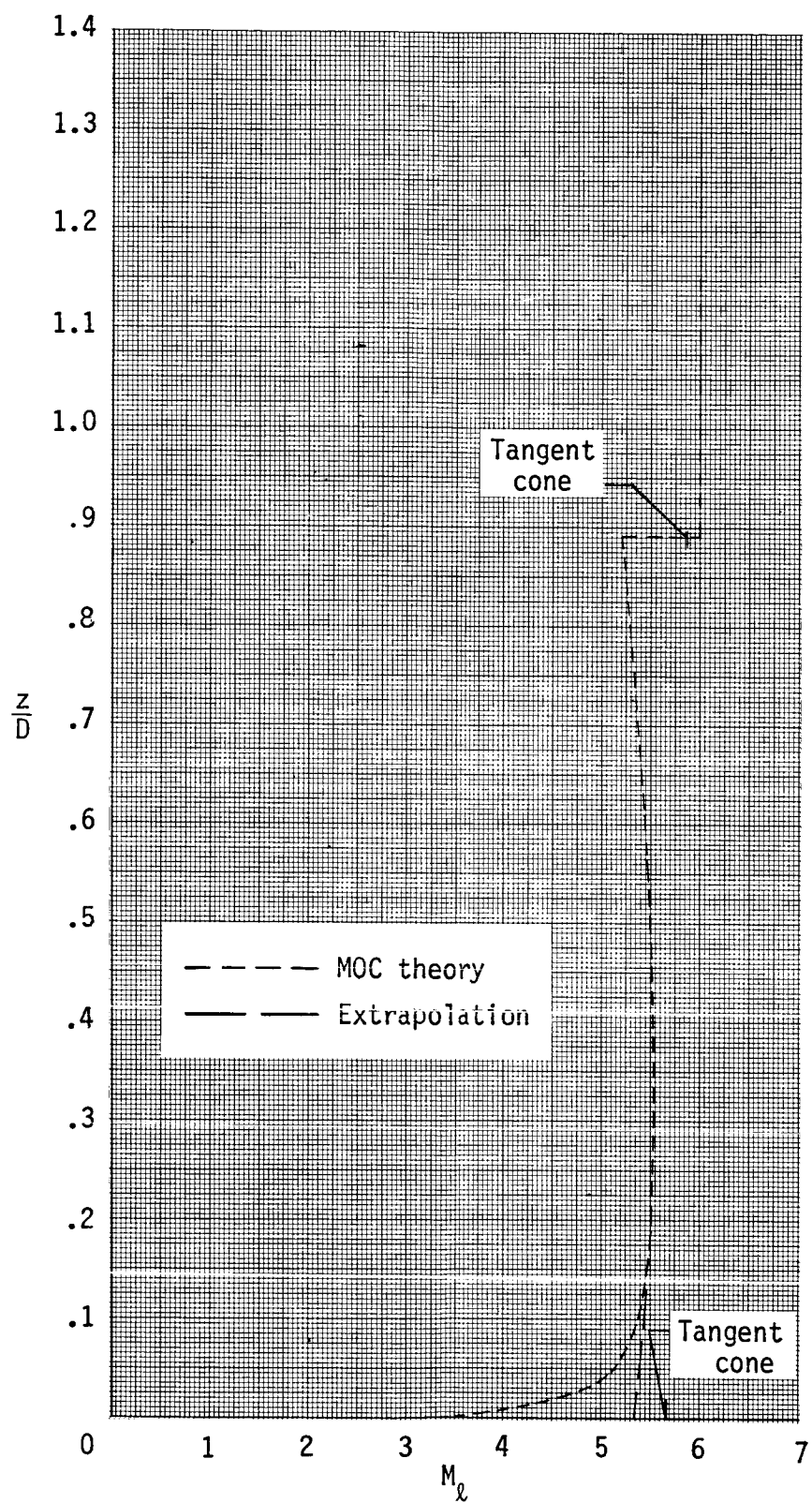
(c) $y/D = 0.236$.

Figure C15.- Continued.



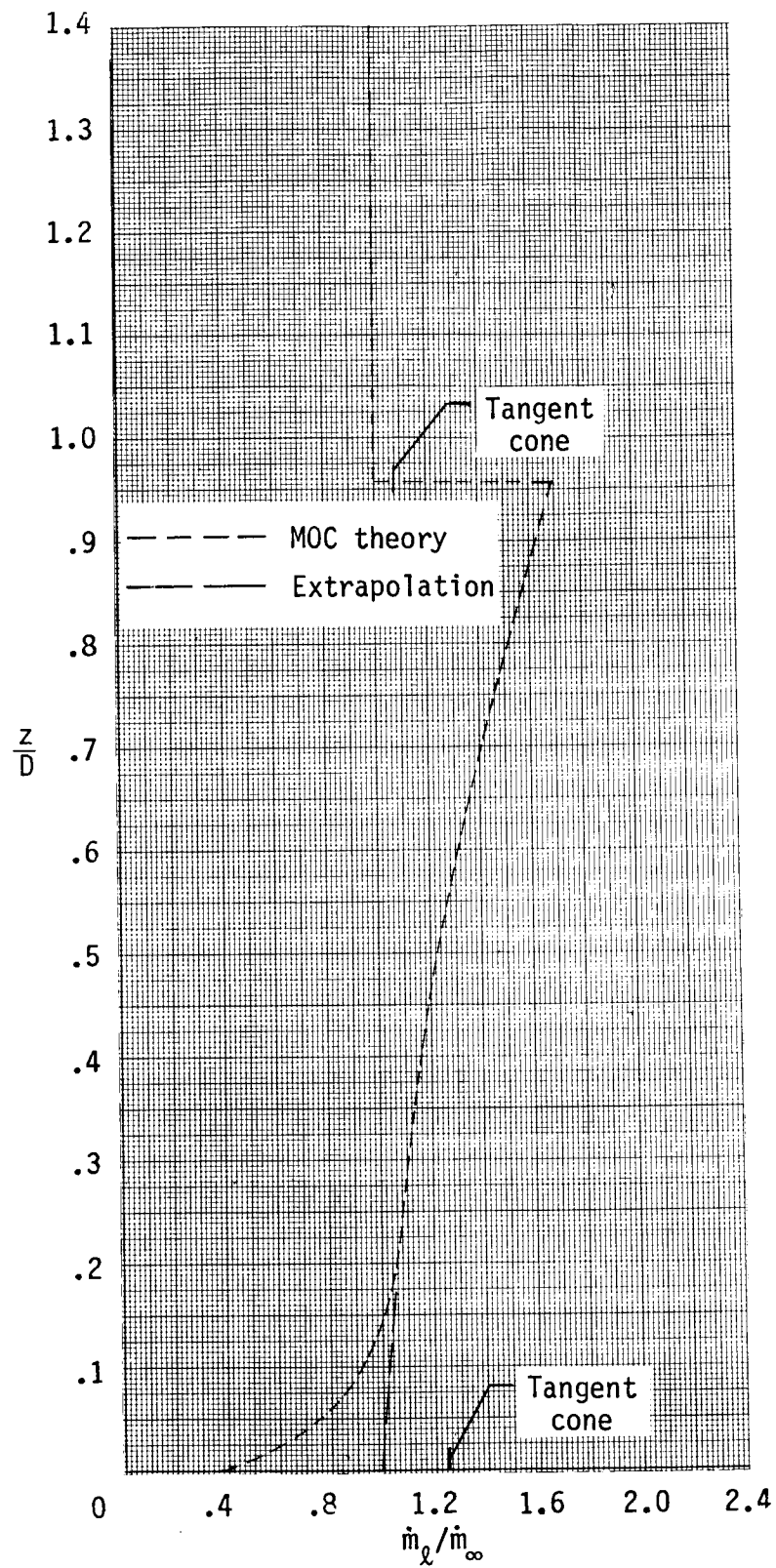
(d) $y/D = 0.354$.

Figure C15.- Continued.



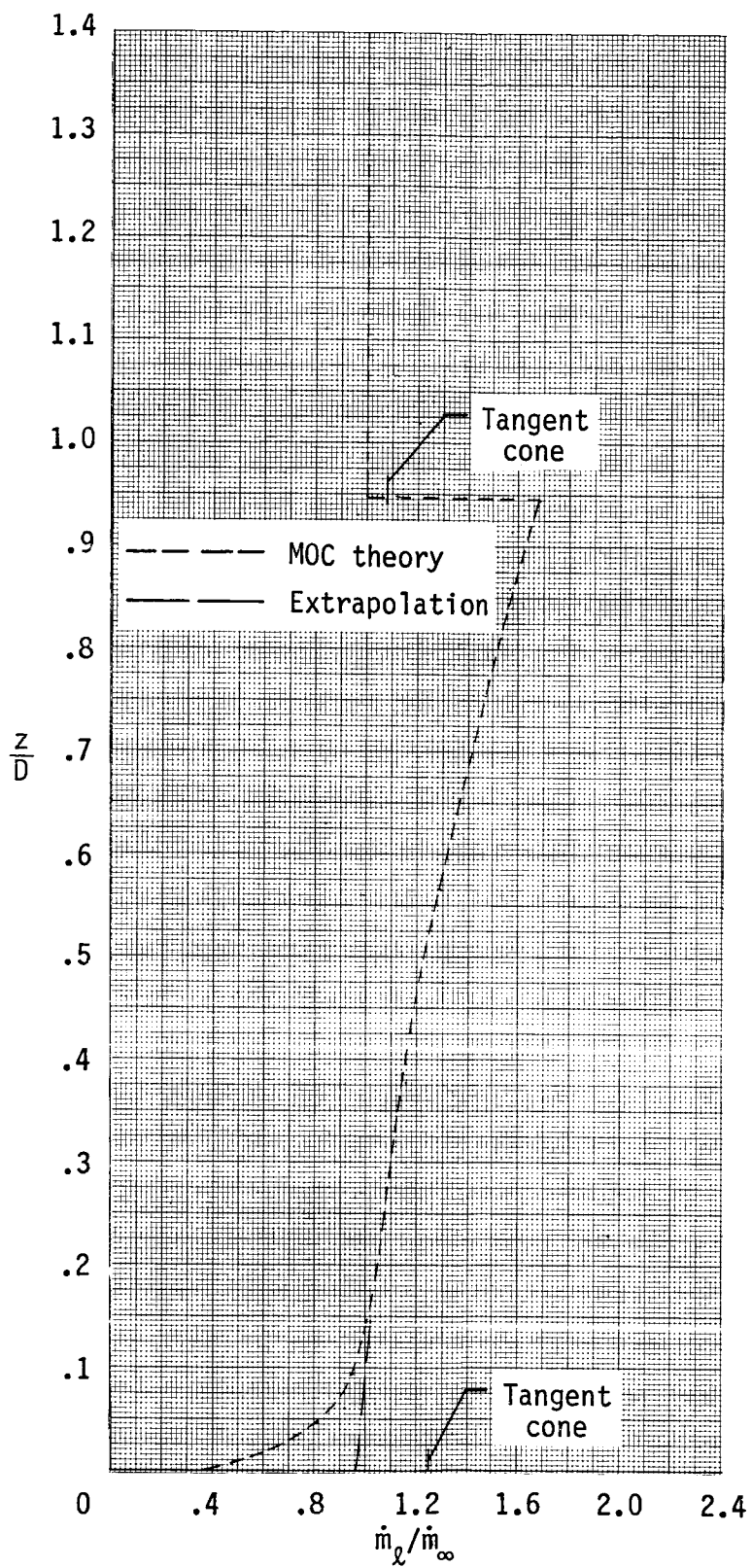
(e) $y/D = 0.472$.

Figure C15.- Concluded.



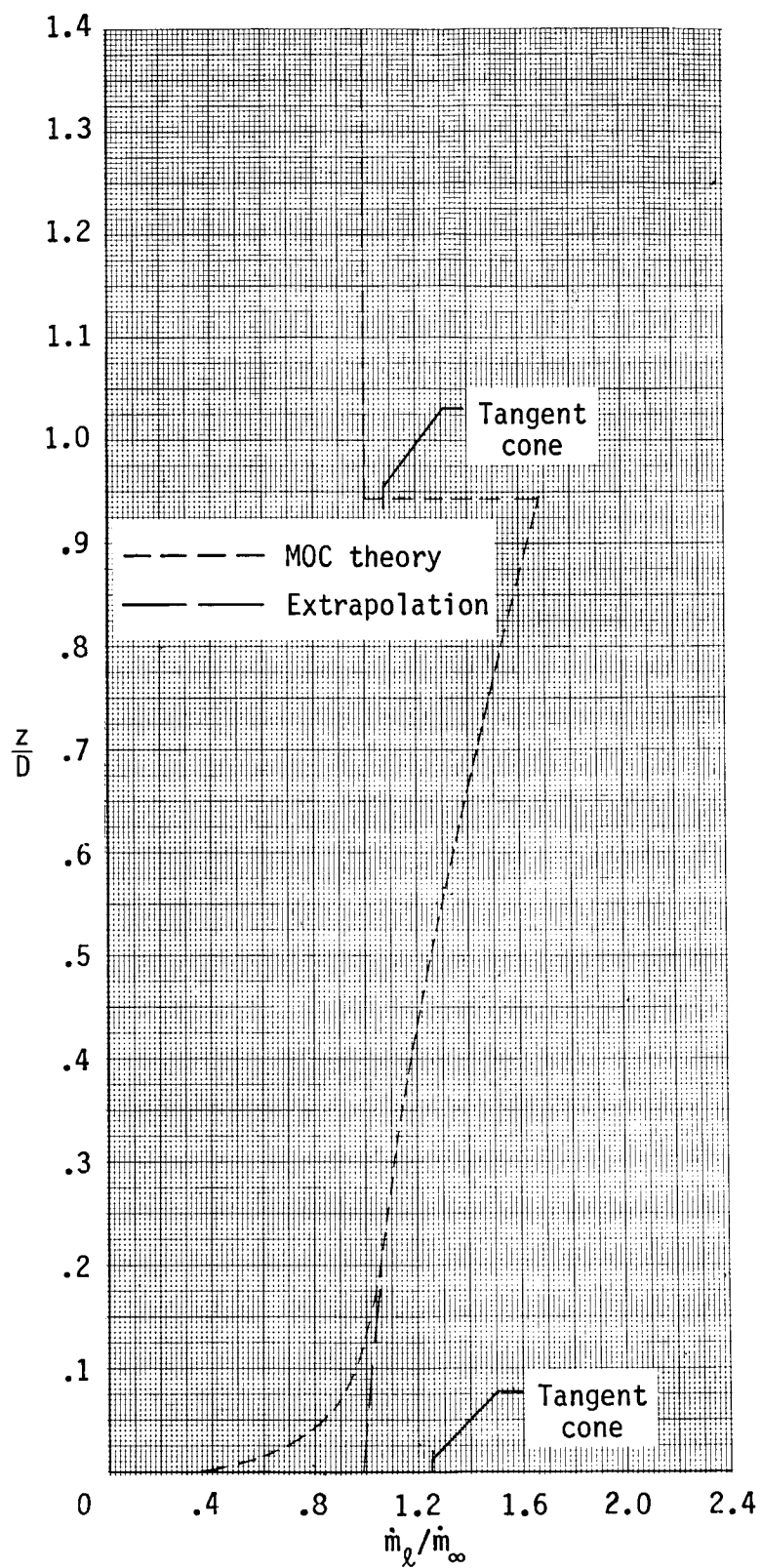
(a) $y/D = 0$.

Figure C16.- Local mass flow ratios at aft survey station
($x/D = 5.4$) at $\alpha = 4^\circ$.



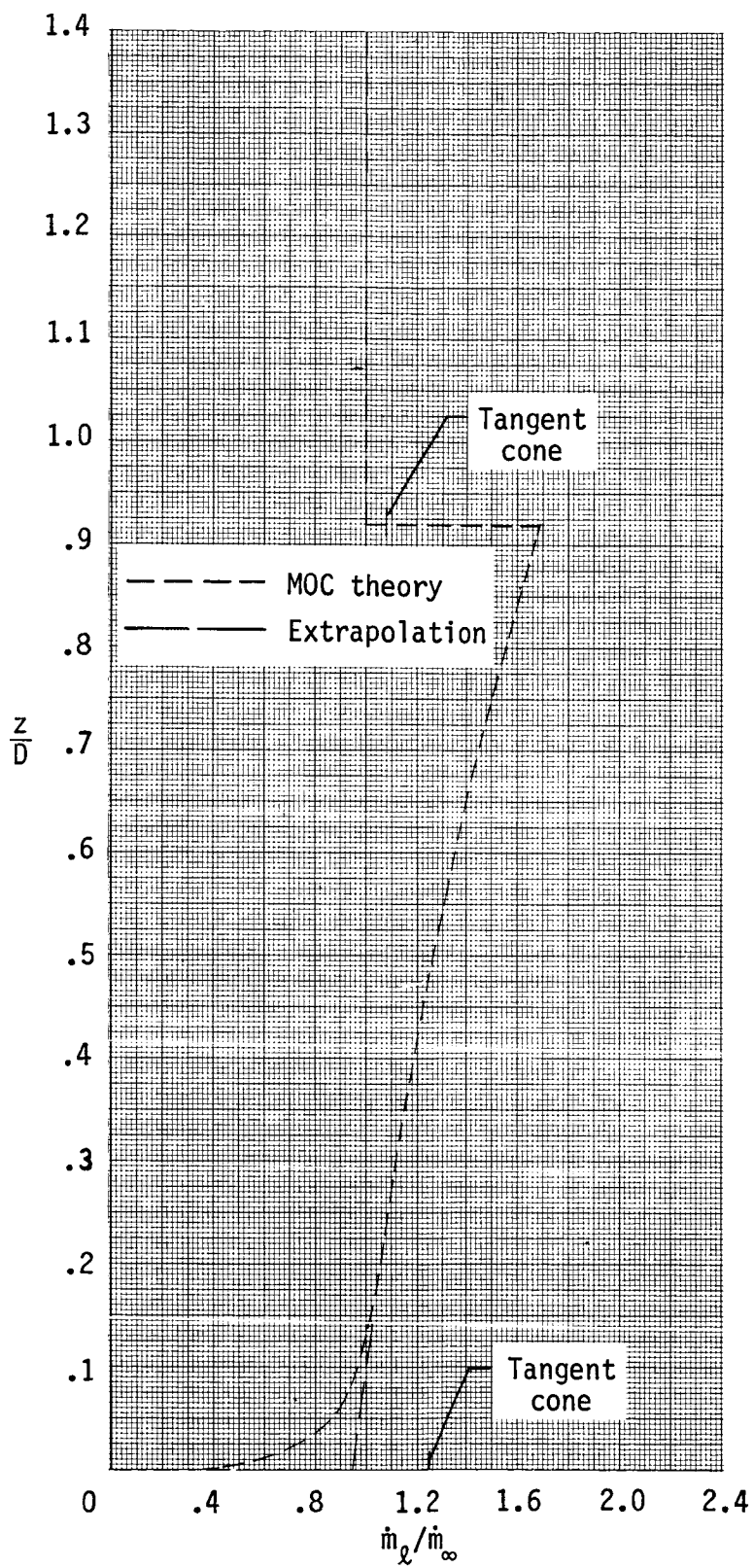
(b) $y/D = 0.118$.

Figure C16.- Continued.



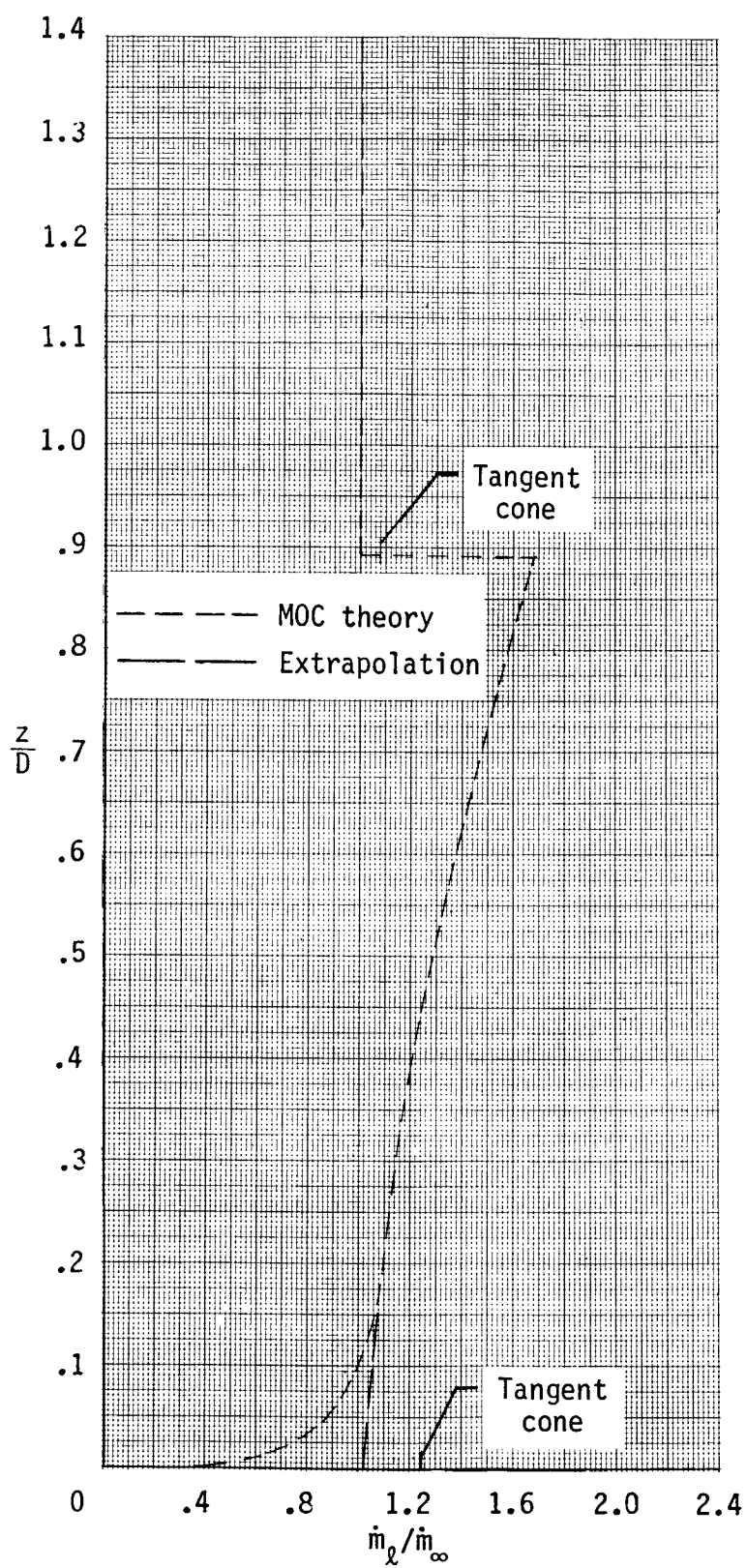
(c) $y/D = 0.236$.

Figure C16.-- Continued.



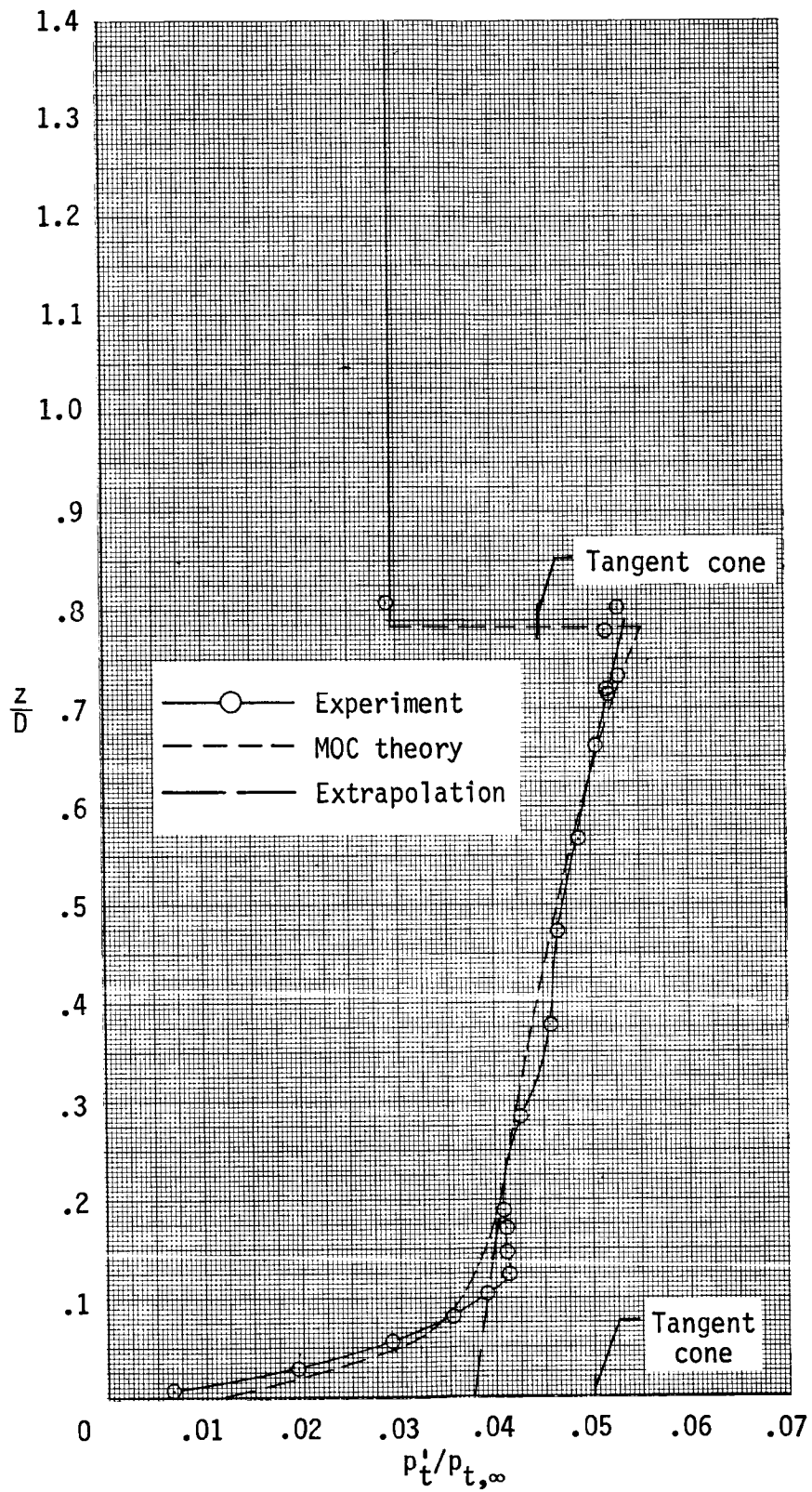
(d) $y/D = 0.354$.

Figure C16.- Continued.



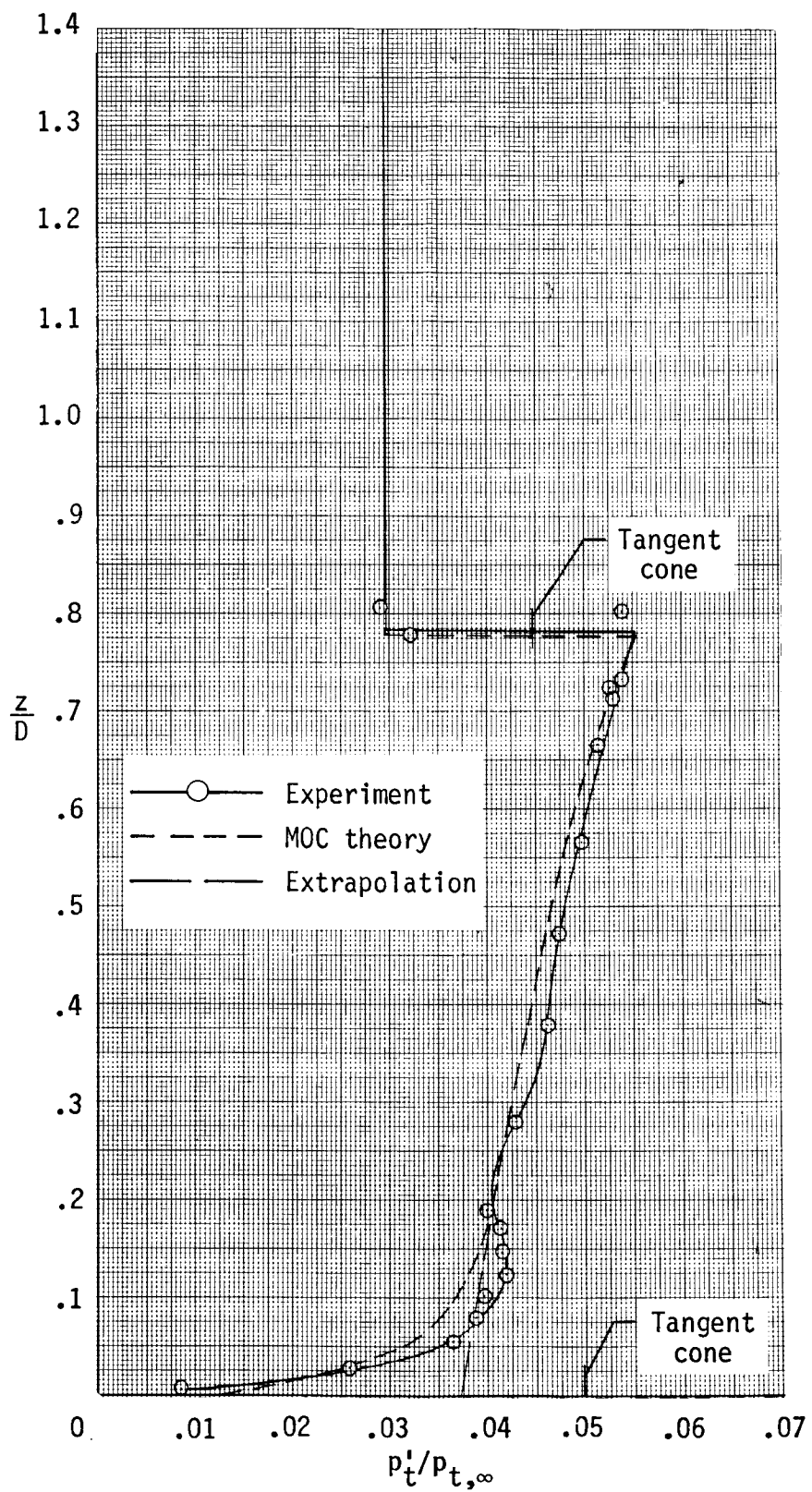
(e) $y/D = 0.472$.

Figure C16.- Concluded.



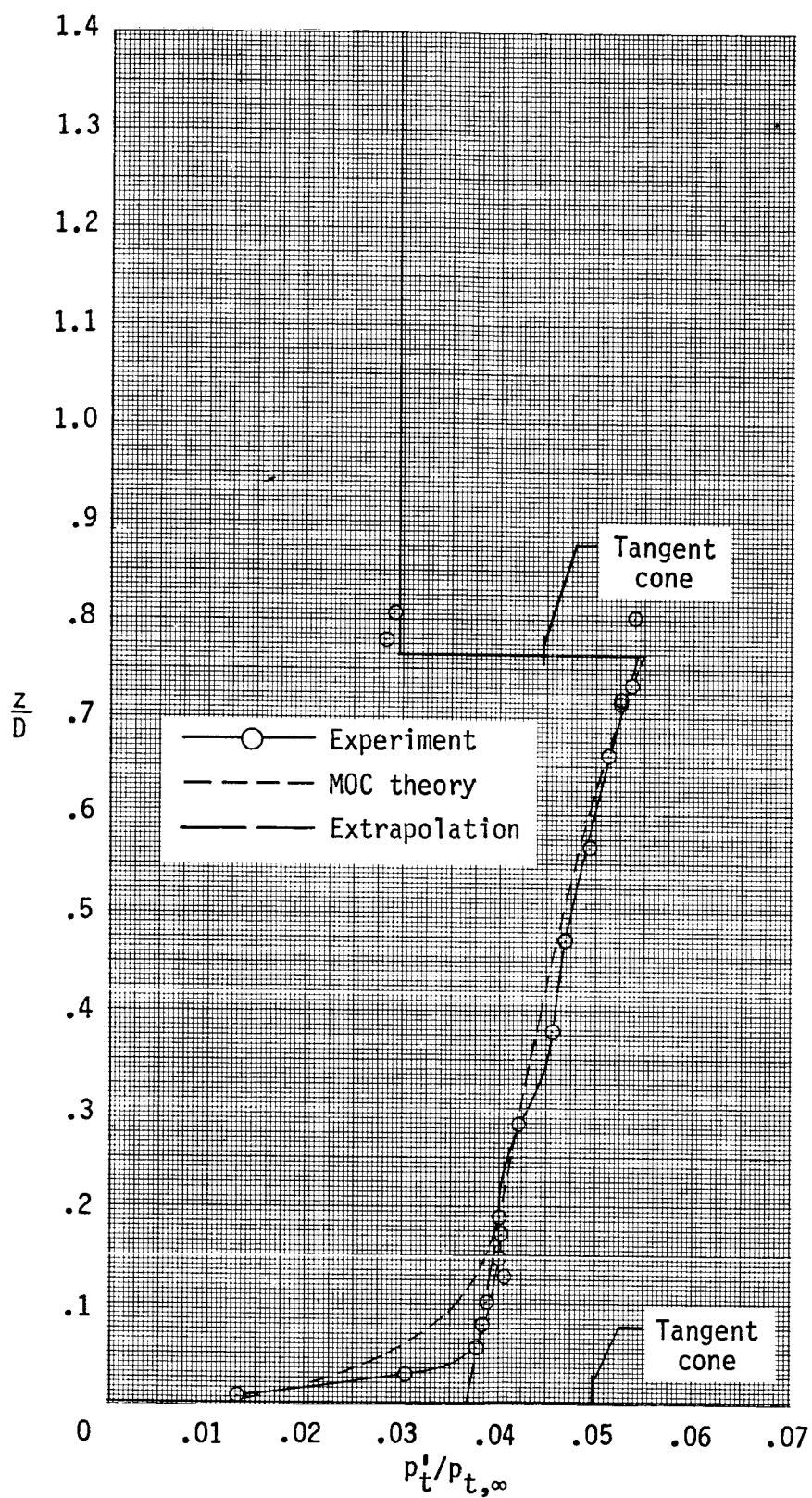
(a) $y/D = 0$.

Figure C17.- Pitot pressure survey at aft survey station
($x/D = 5.4$) at $\alpha = 8^\circ$.



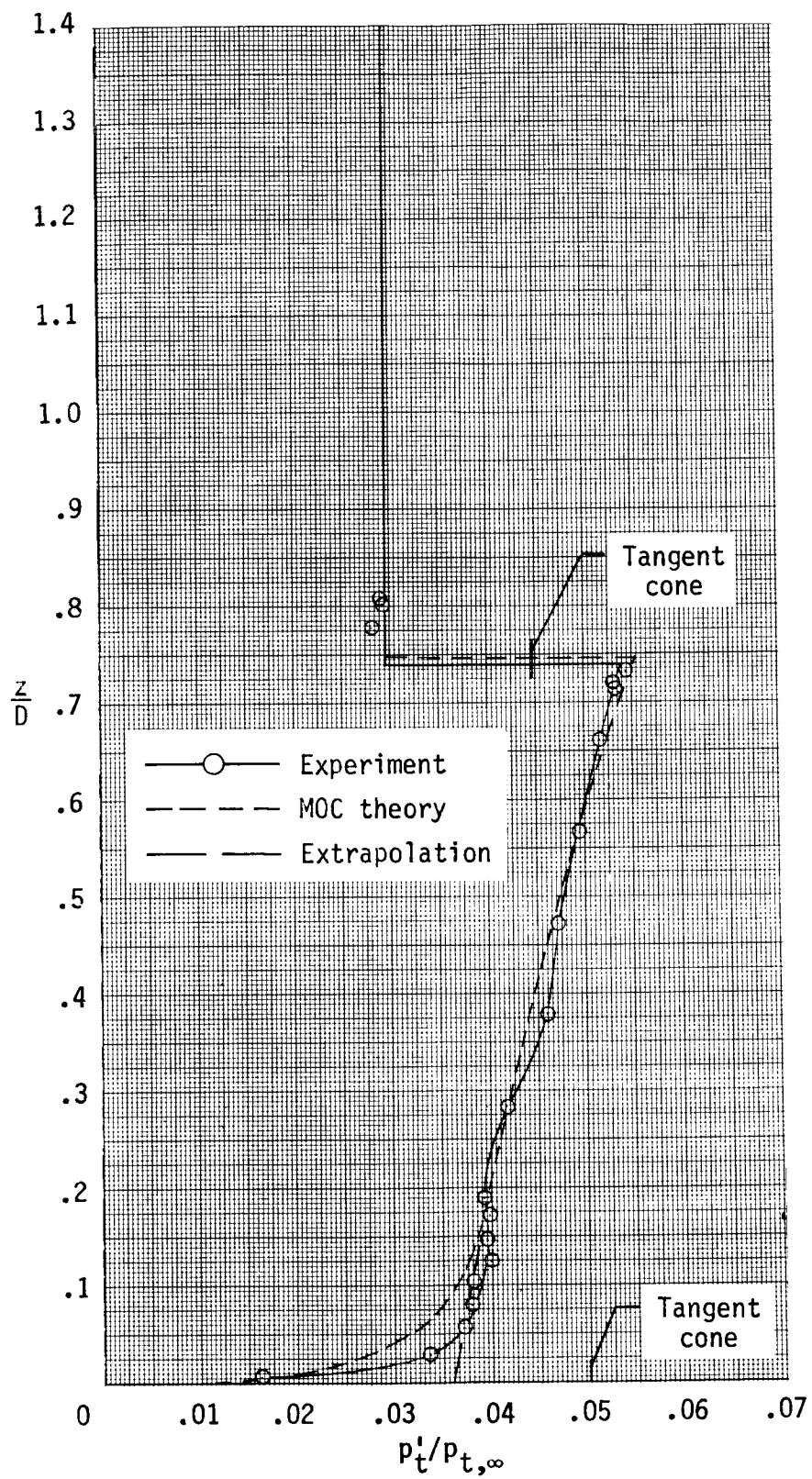
(b) $y/D = 0.118$.

Figure C17.- Continued.



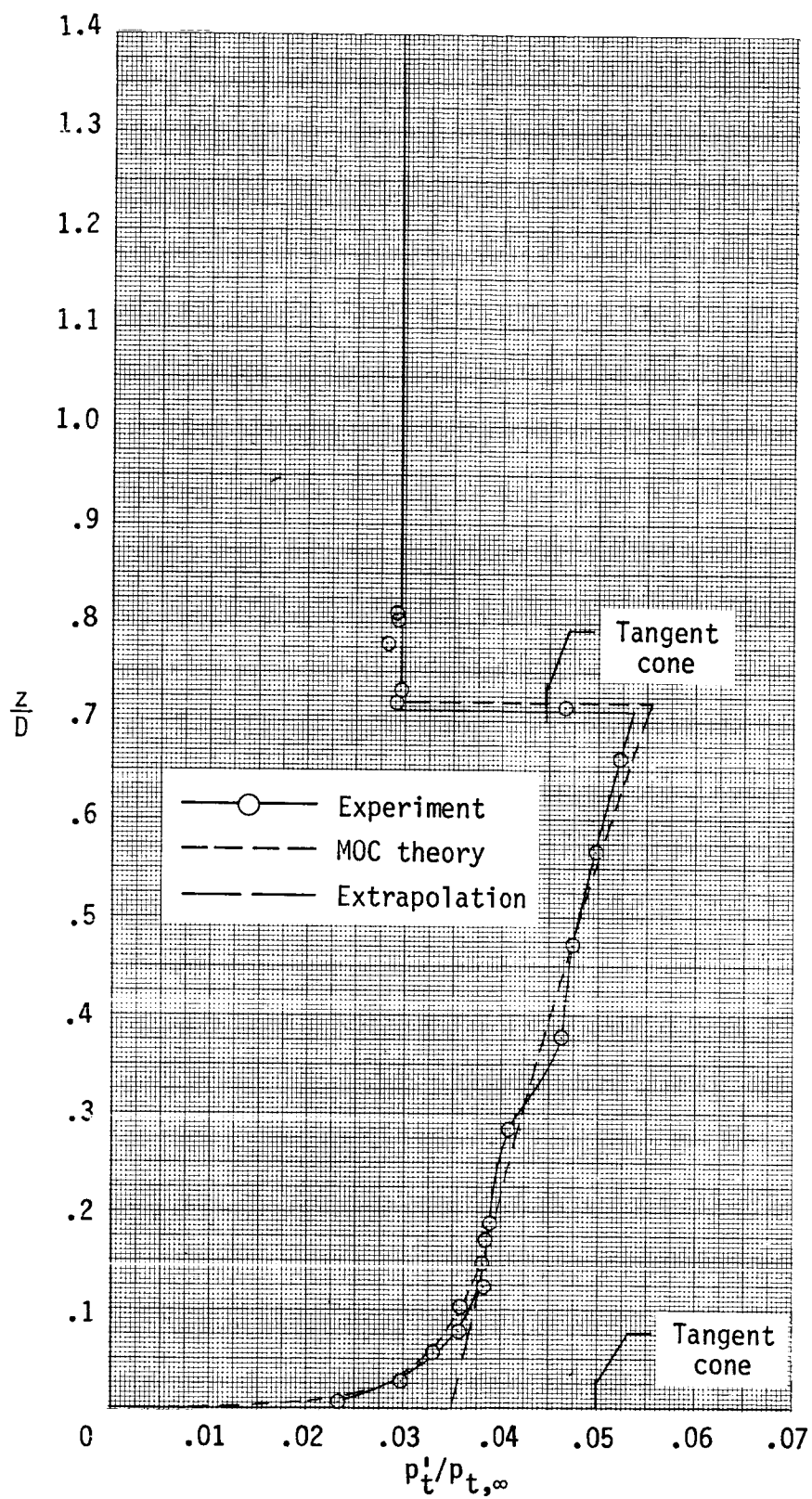
(c) $y/D = 0.236$.

Figure C17.- Continued.



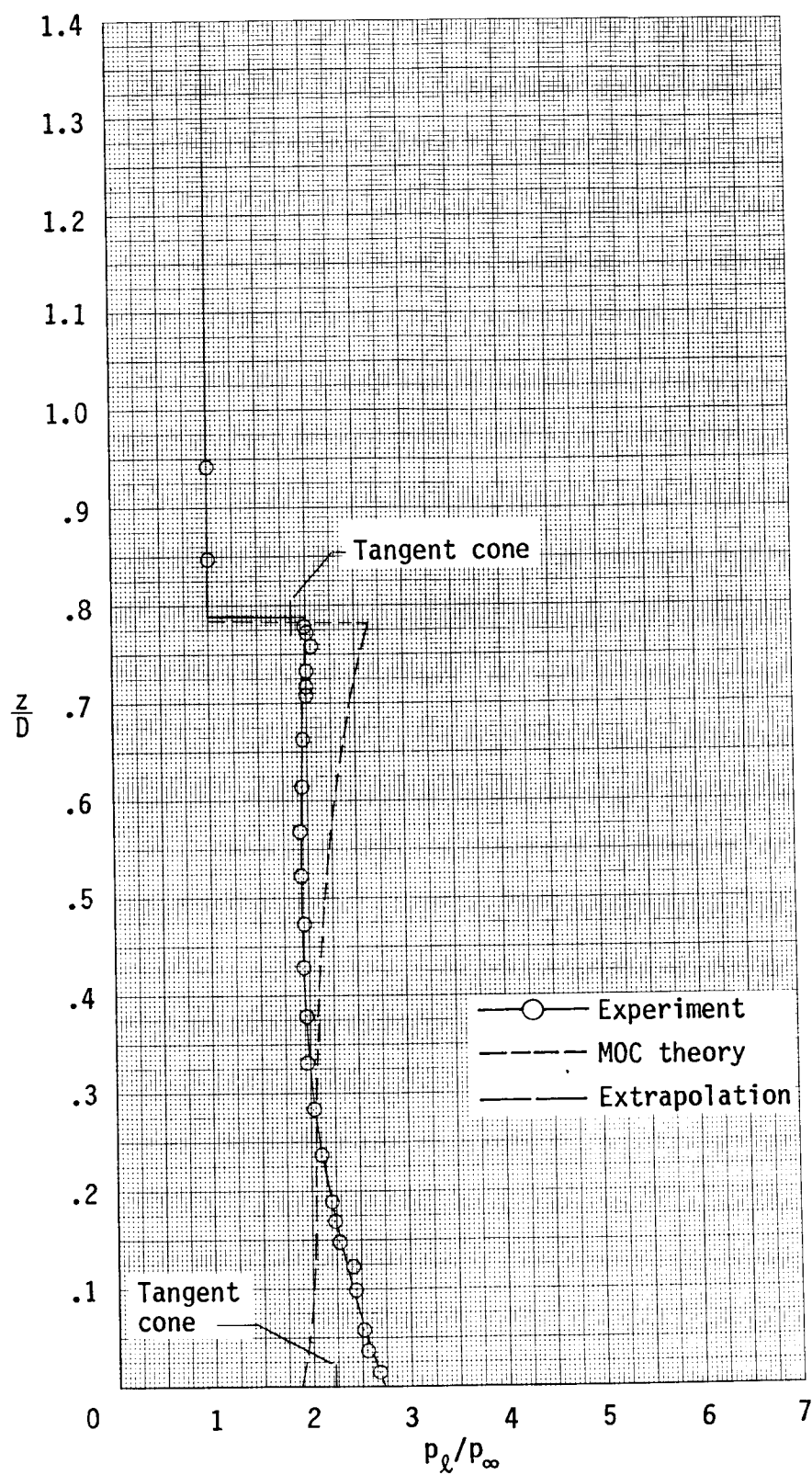
(d) $y/D = 0.354$.

Figure C17.- Continued.



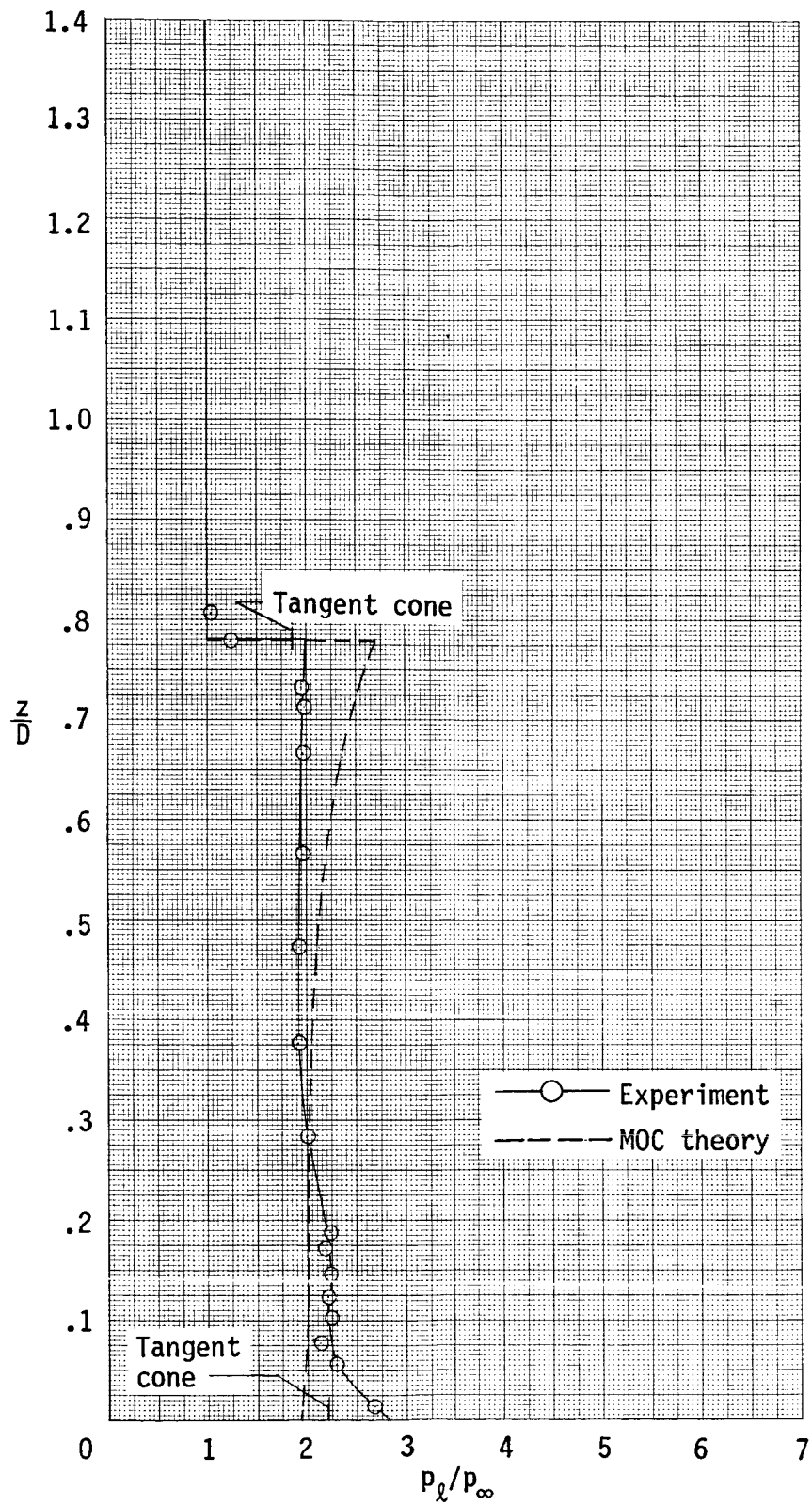
(e) $y/D = 0.472$.

Figure C17.- Concluded.



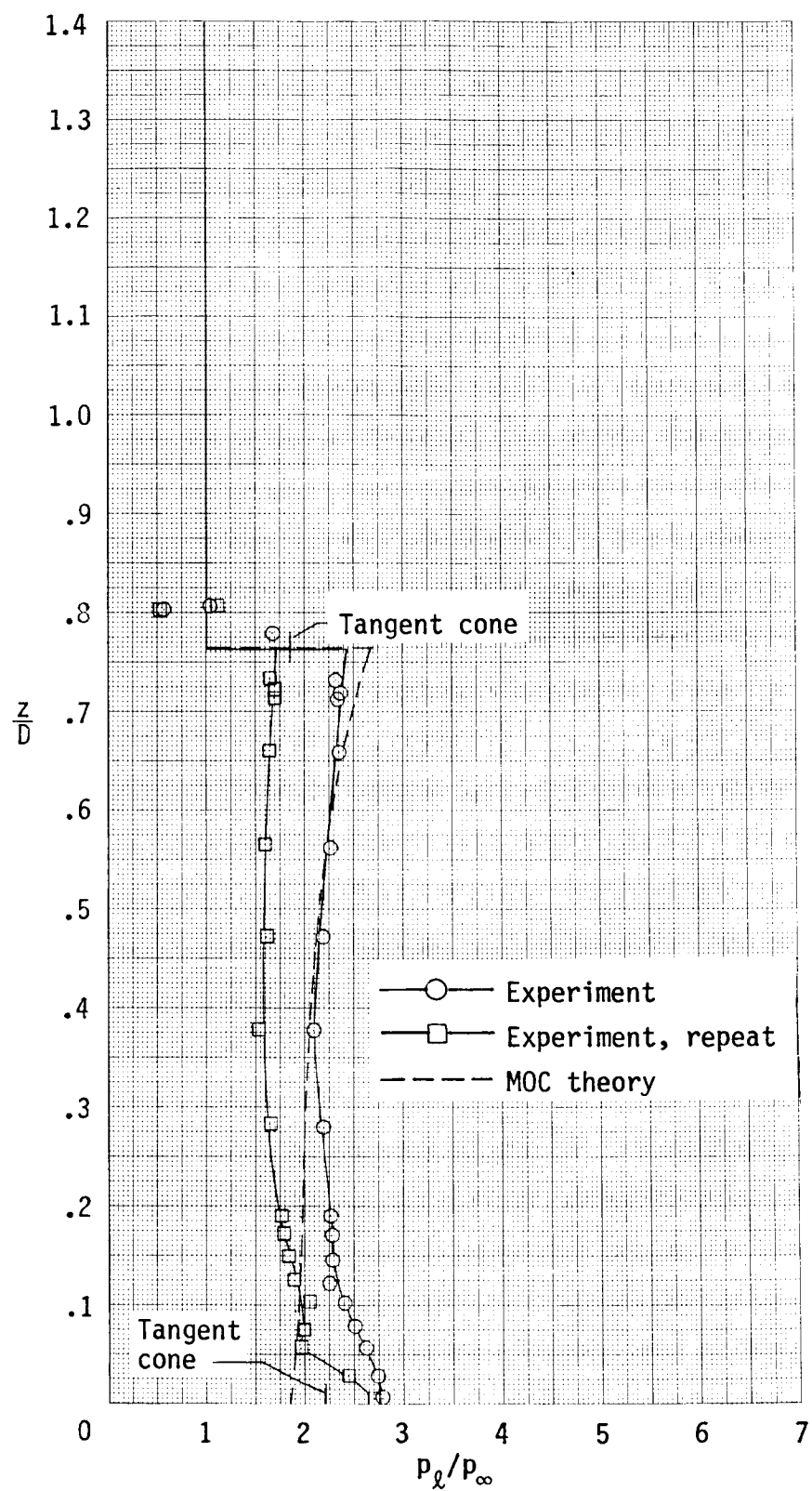
(a) $y/D = 0$.

Figure C18.- Static pressure survey at aft survey station
($x/D = 5.4$) at $\alpha = 8^\circ$.



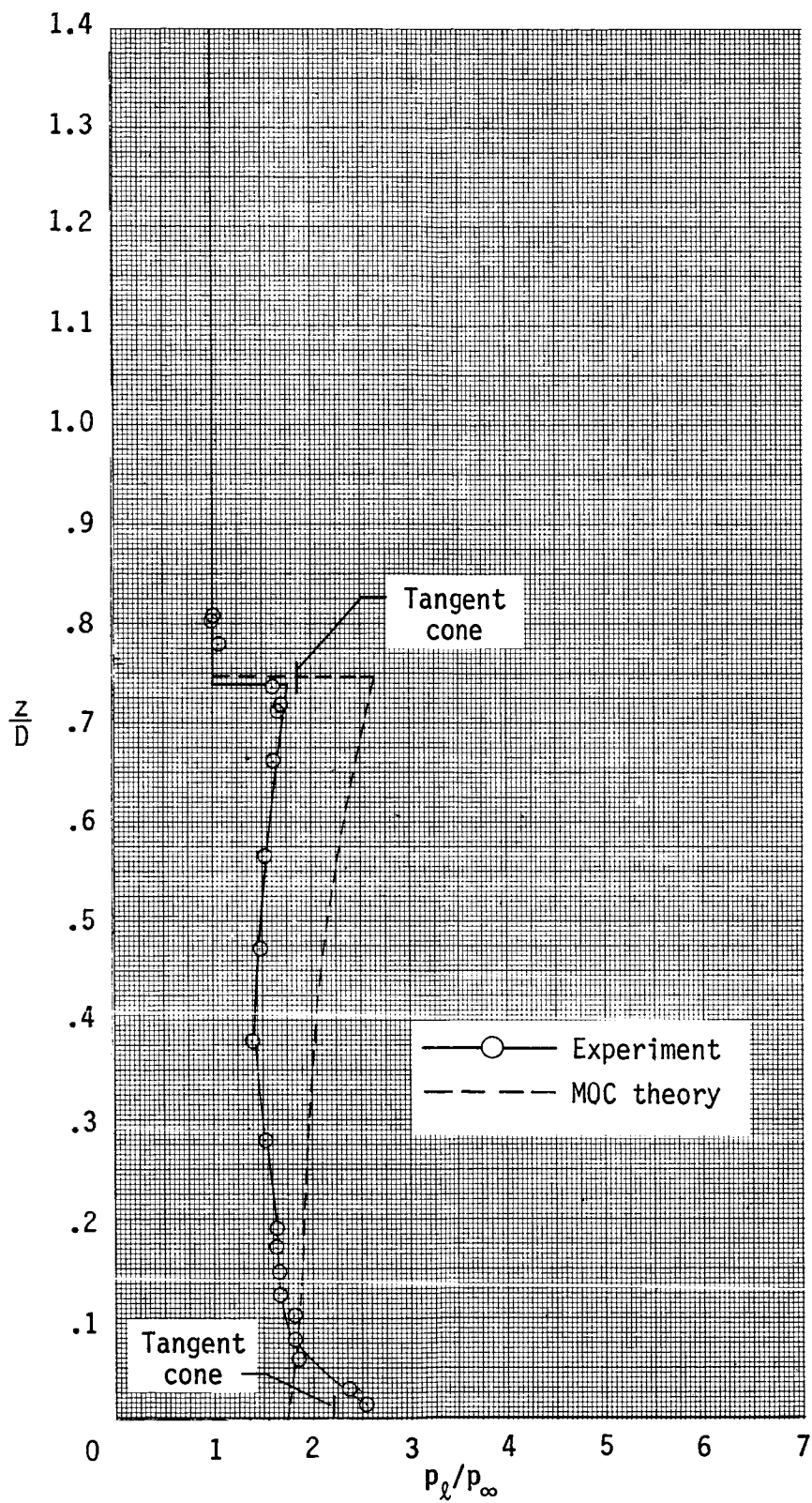
(b) $y/D = 0.118$.

Figure C18.- Continued.



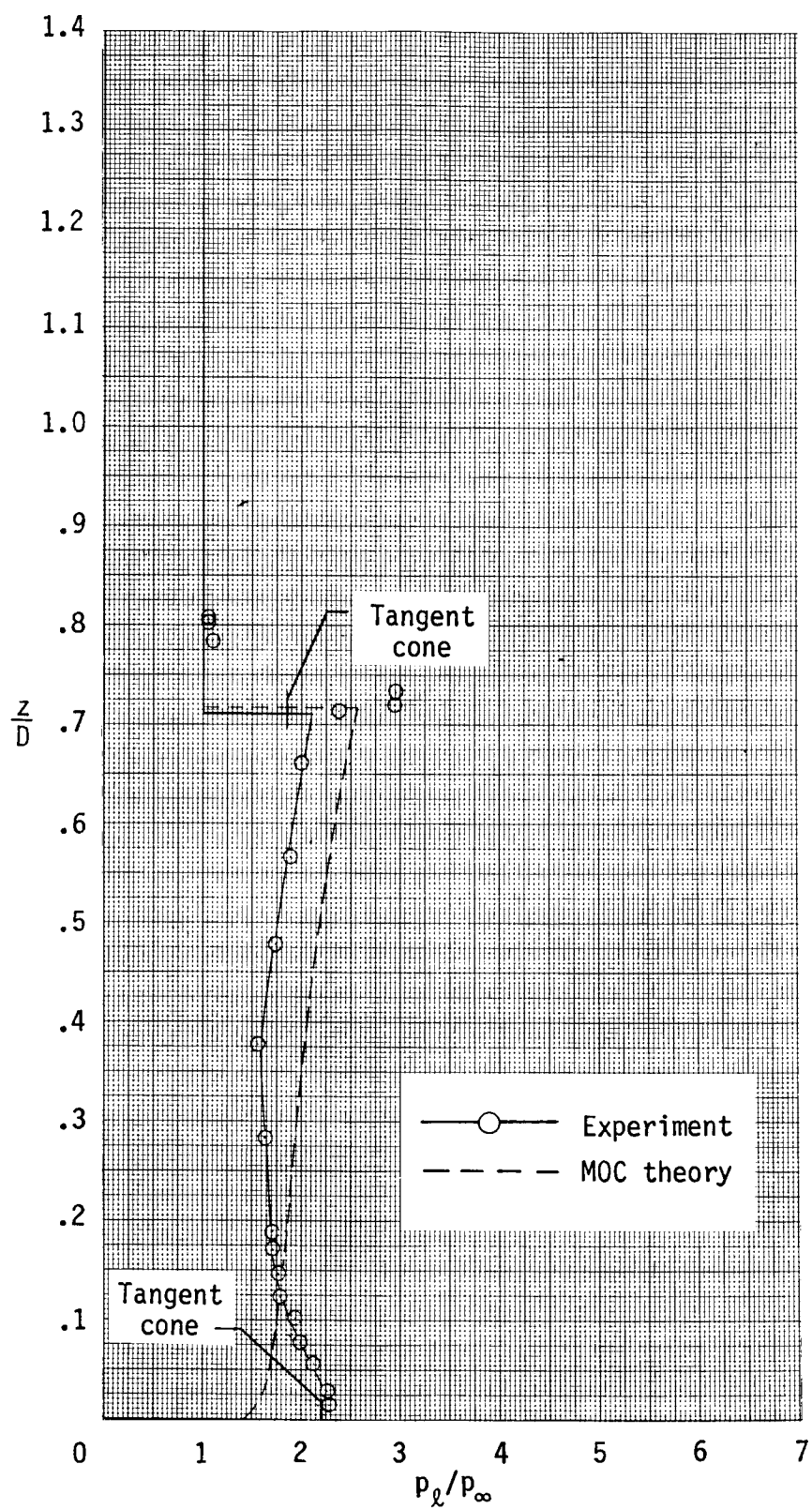
(c) $y/D = 0.236$.

Figure C18.- Continued.



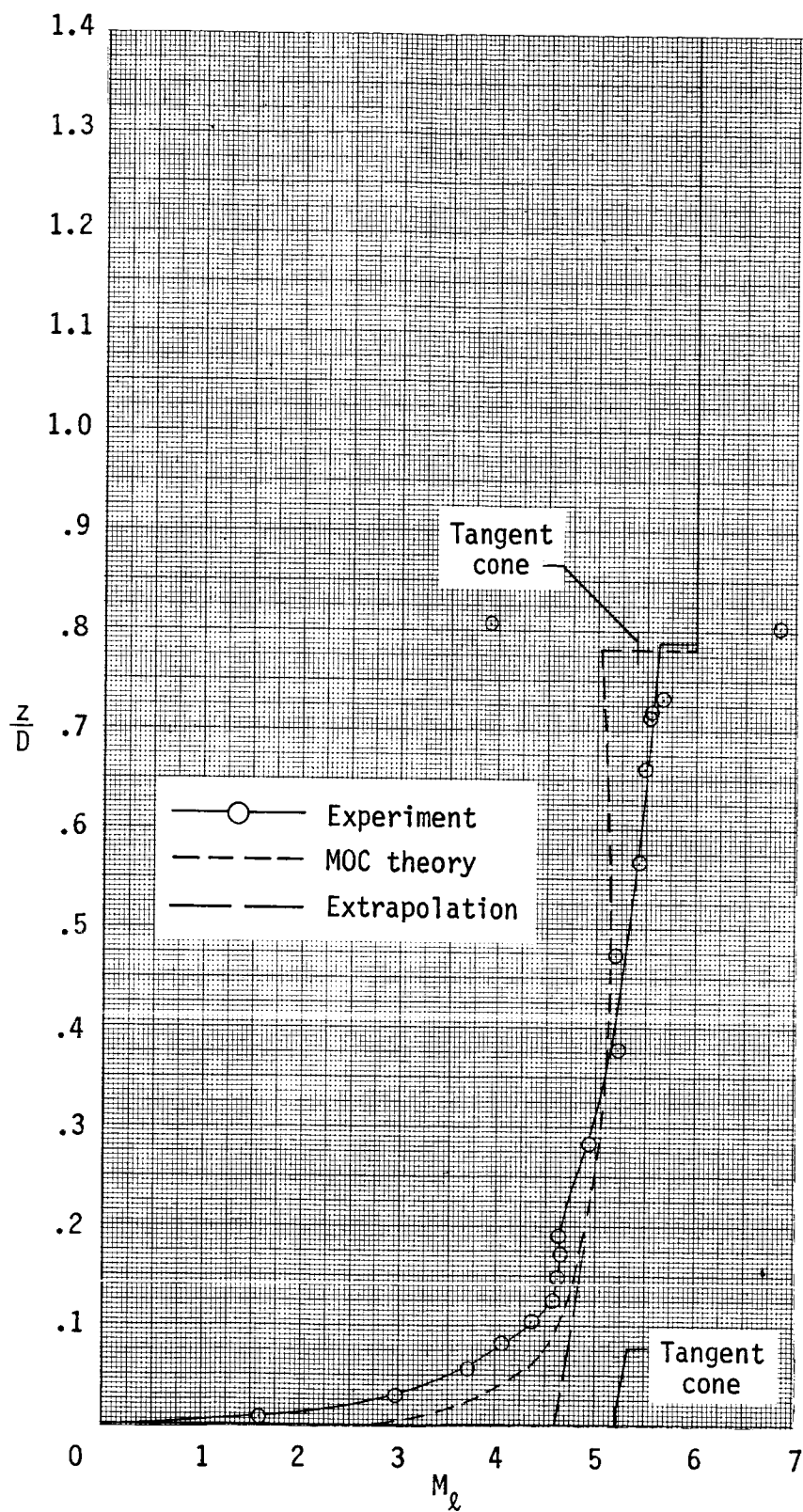
(d) $y/D = 0.354$.

Figure C18.- Continued.



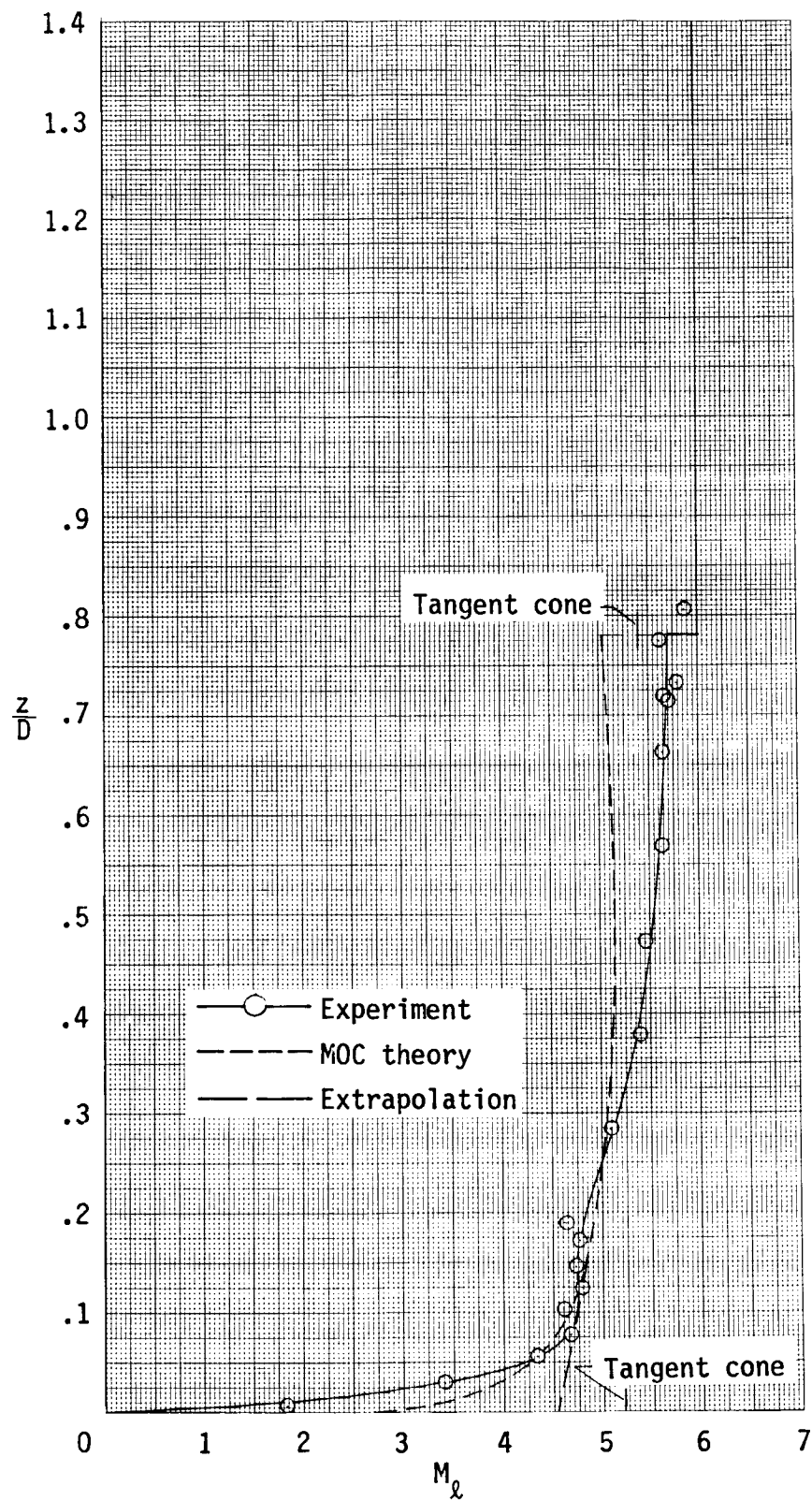
(e) $y/D = 0.472$.

Figure C18.- Concluded.



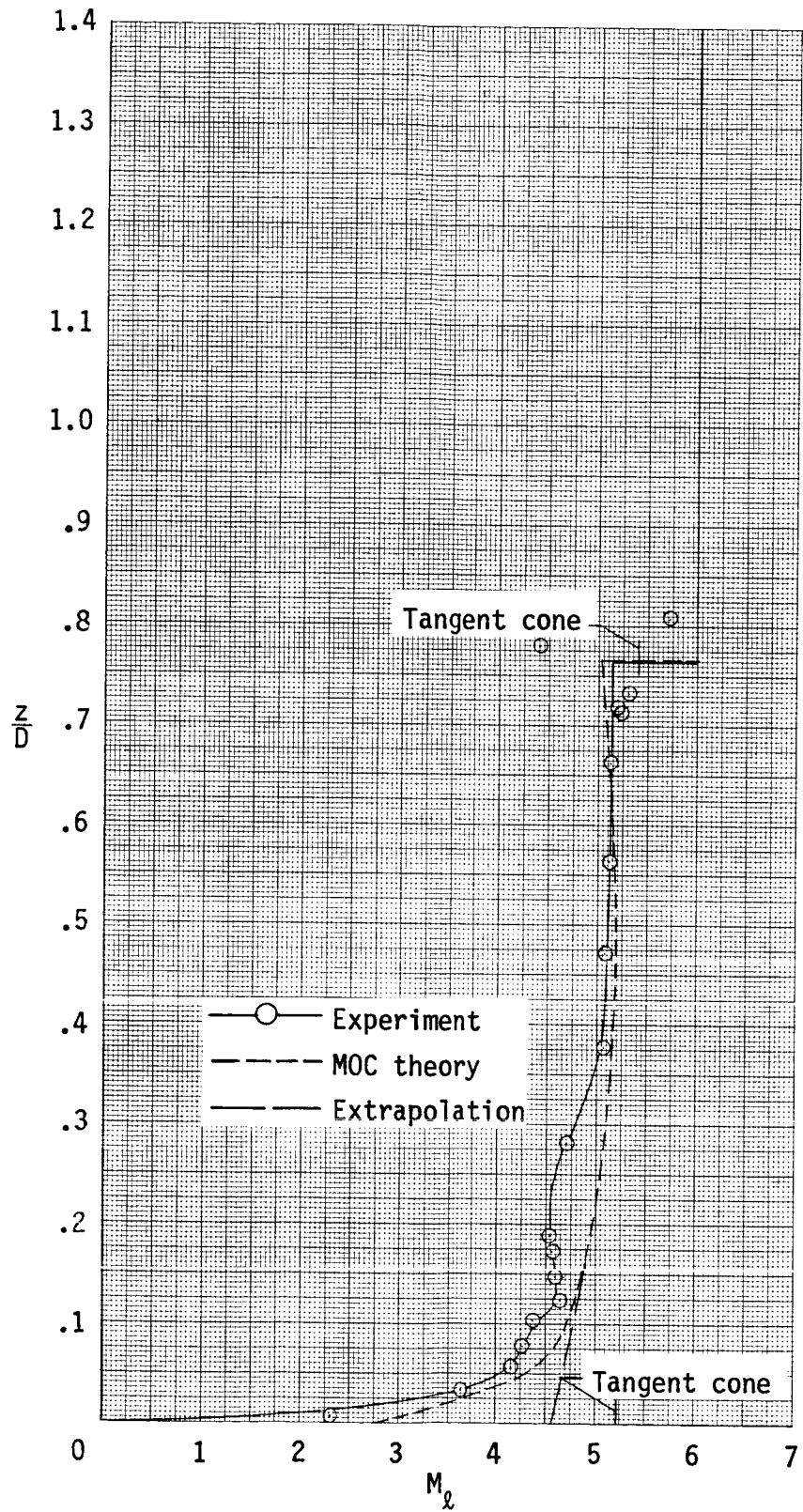
(a) $y/D = 0$.

Figure C19.- Local Mach number distribution at aft survey station ($x/D = 5.4$) at $\alpha = 8^\circ$.



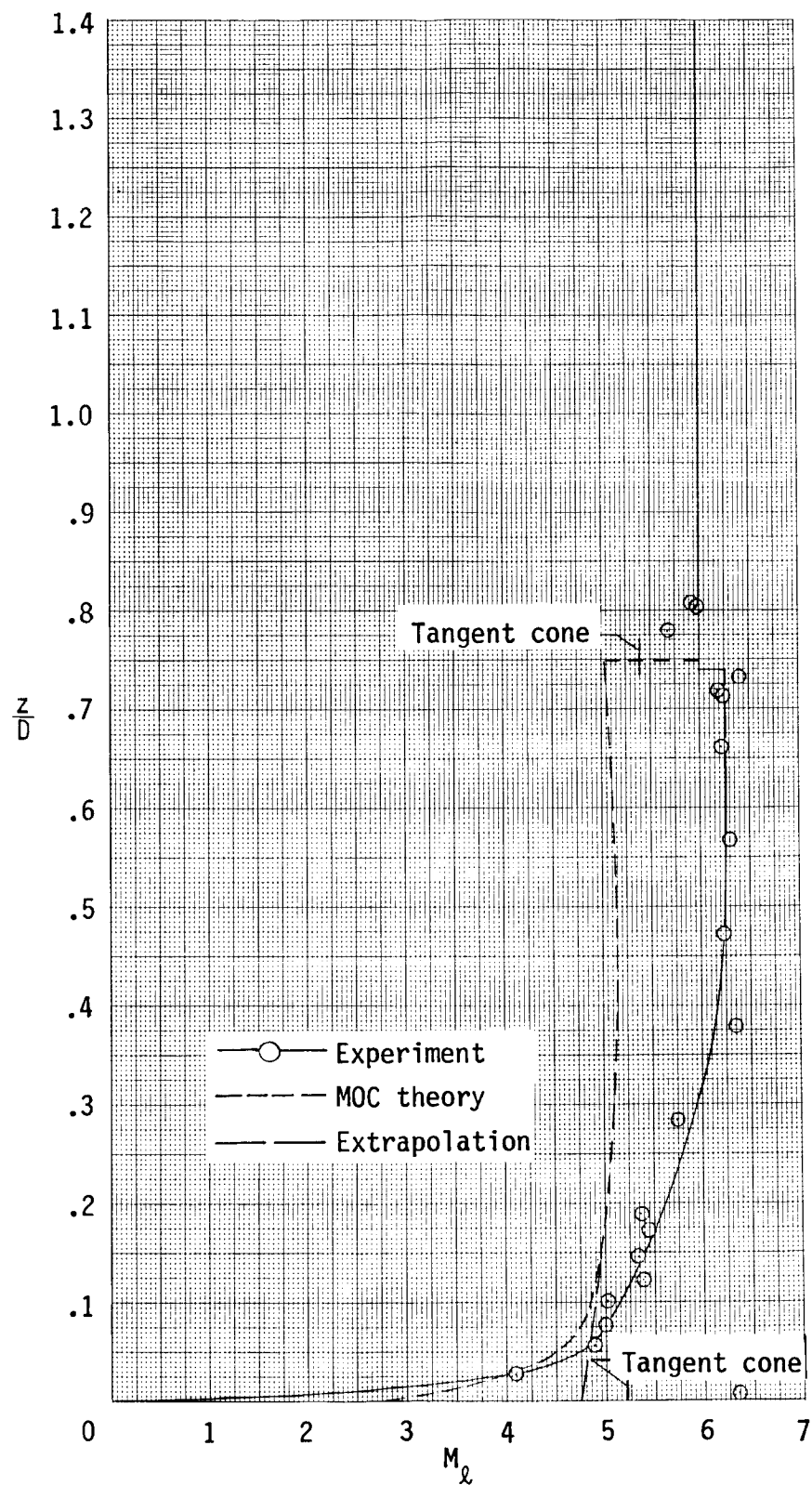
(b) $y/D = 0.118$.

Figure C19.- Continued.



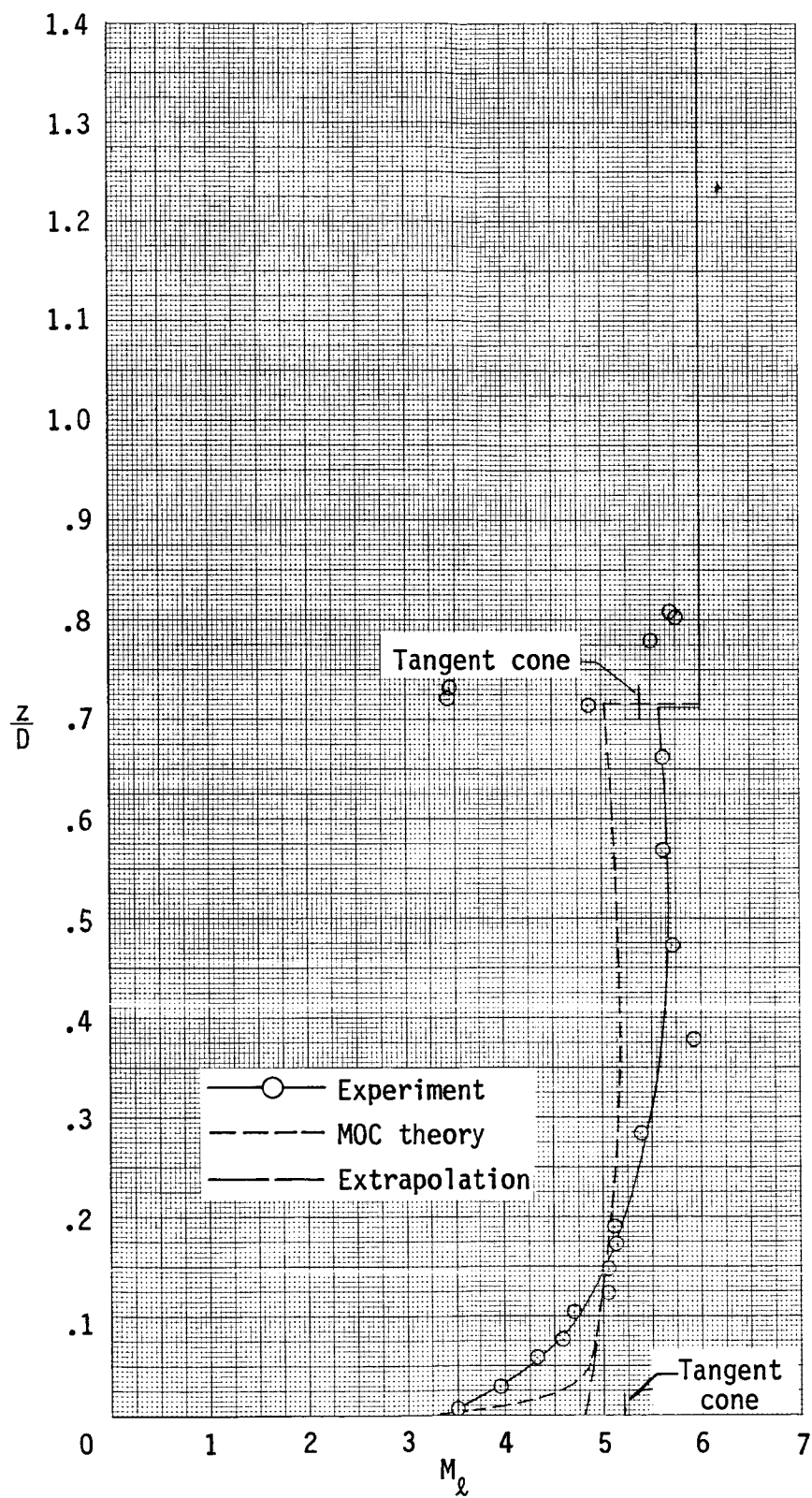
(c) $y/D = 0.236$.

Figure C19.- Continued.



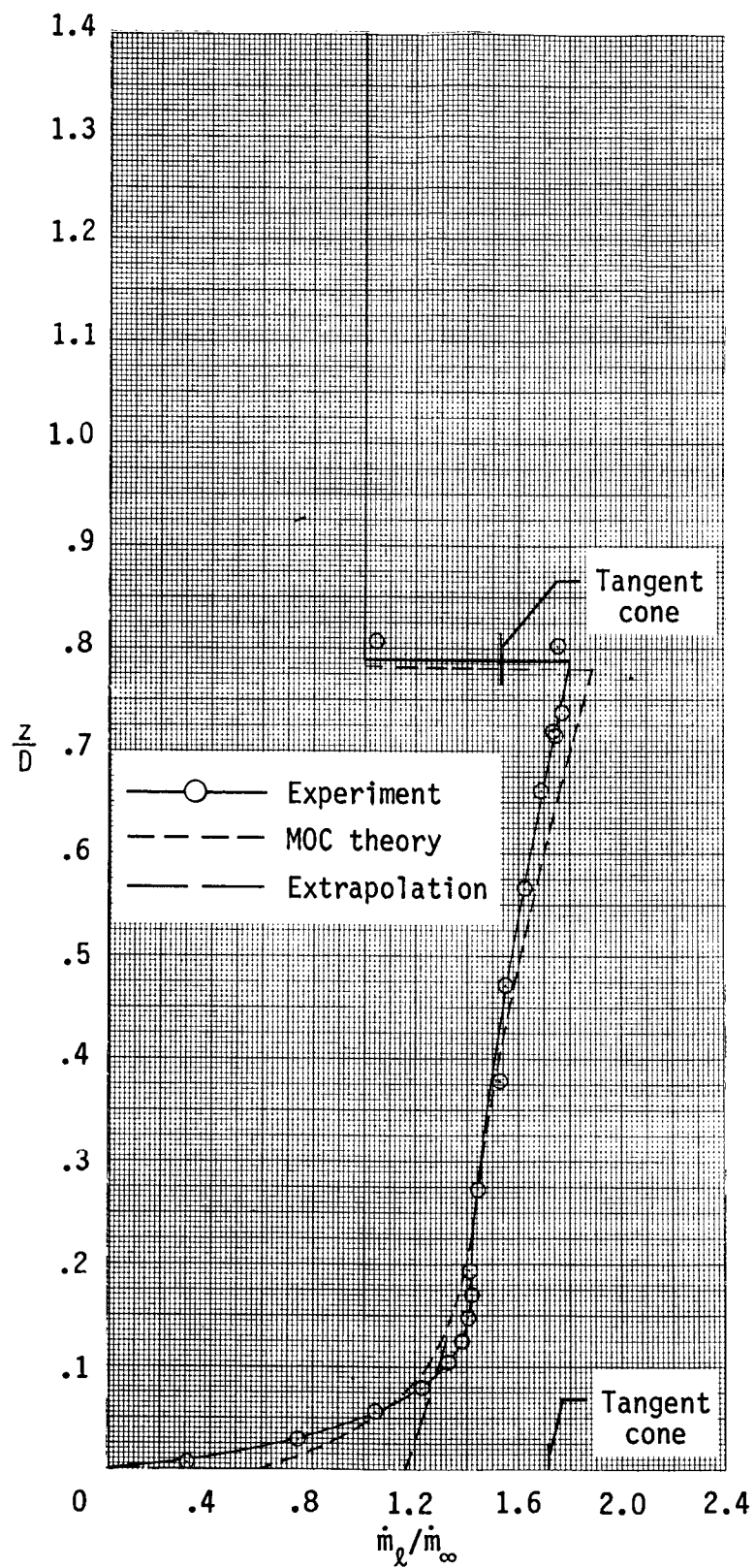
(d) $y/D = 0.354$.

Figure C19.- Continued.



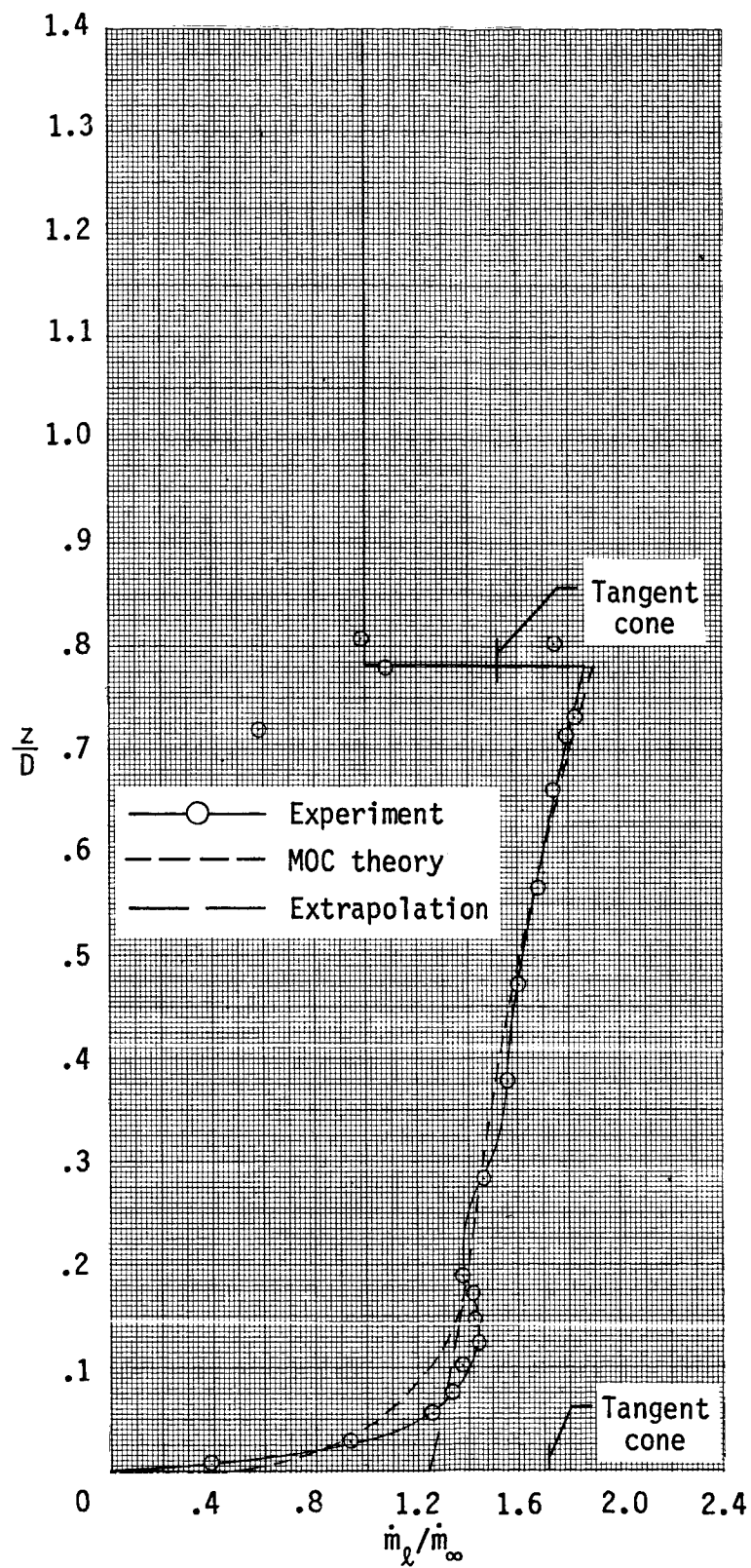
(e) $y/D = 0.472$.

Figure C19.- Concluded.



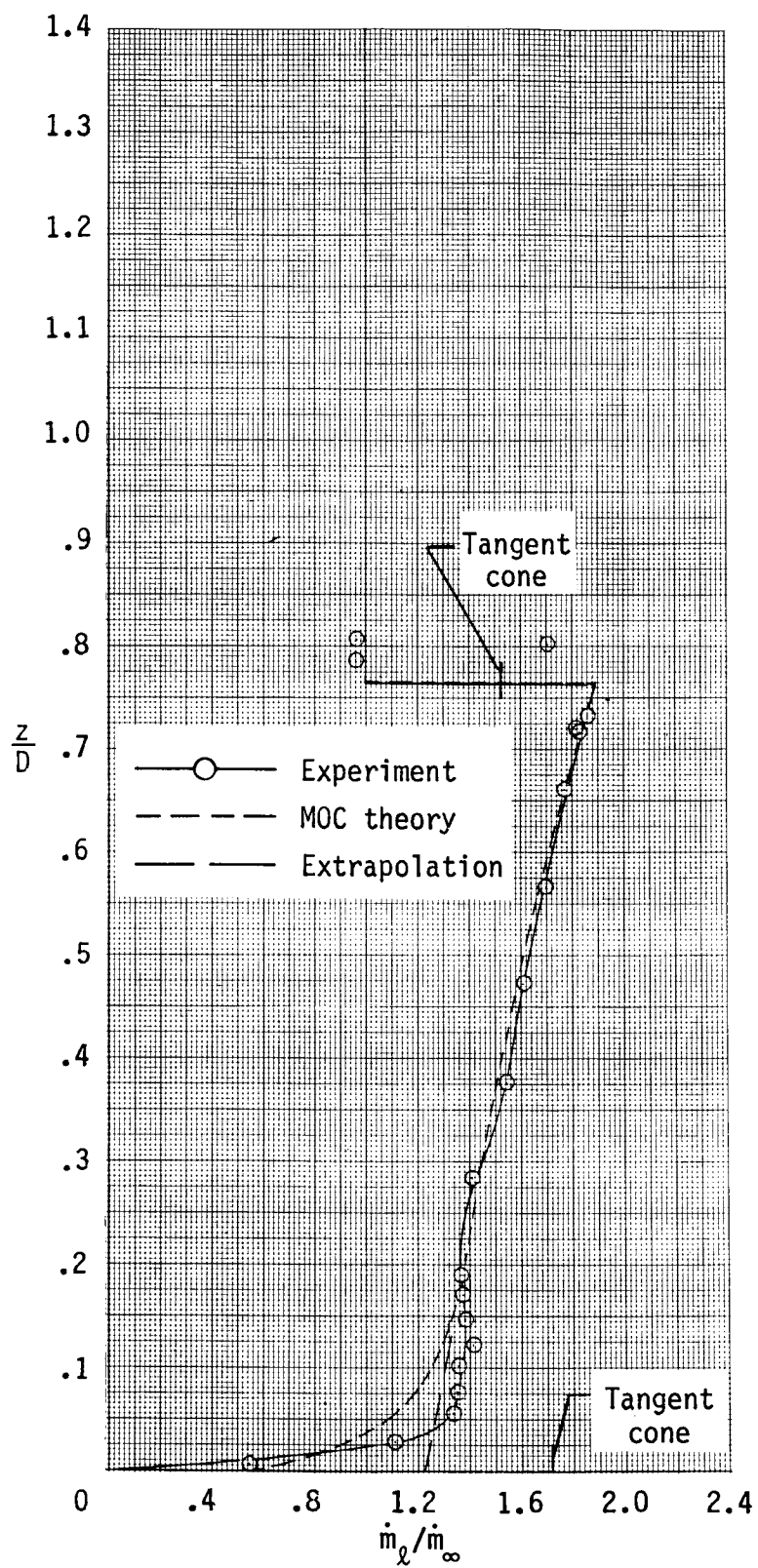
(a) $y/D = 0$.

Figure C20.- Local mass flow ratios at aft survey station
($x/D = 5.4$) at $\alpha = 8^\circ$.



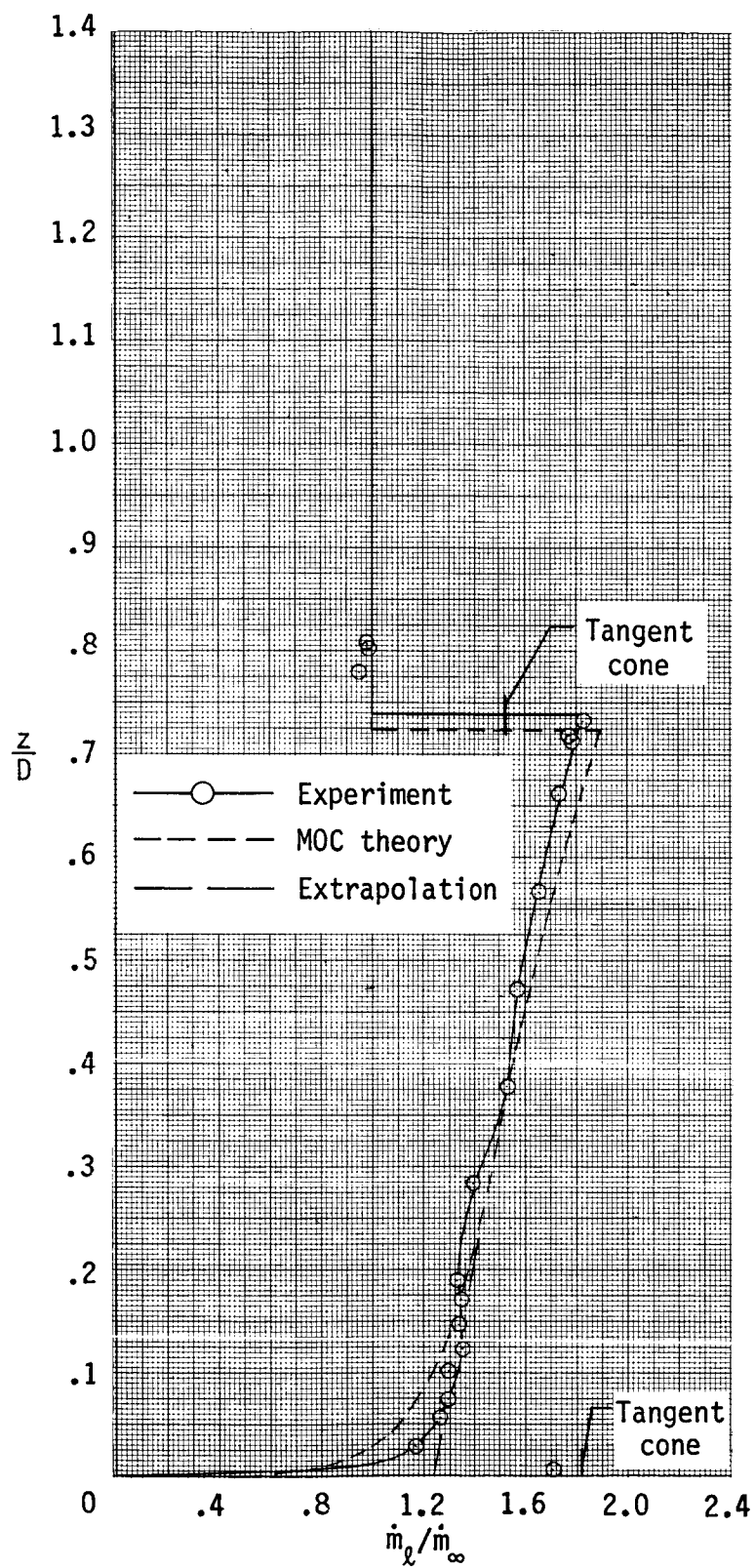
(b) $y/D = 0.118$.

Figure C20.- Continued.



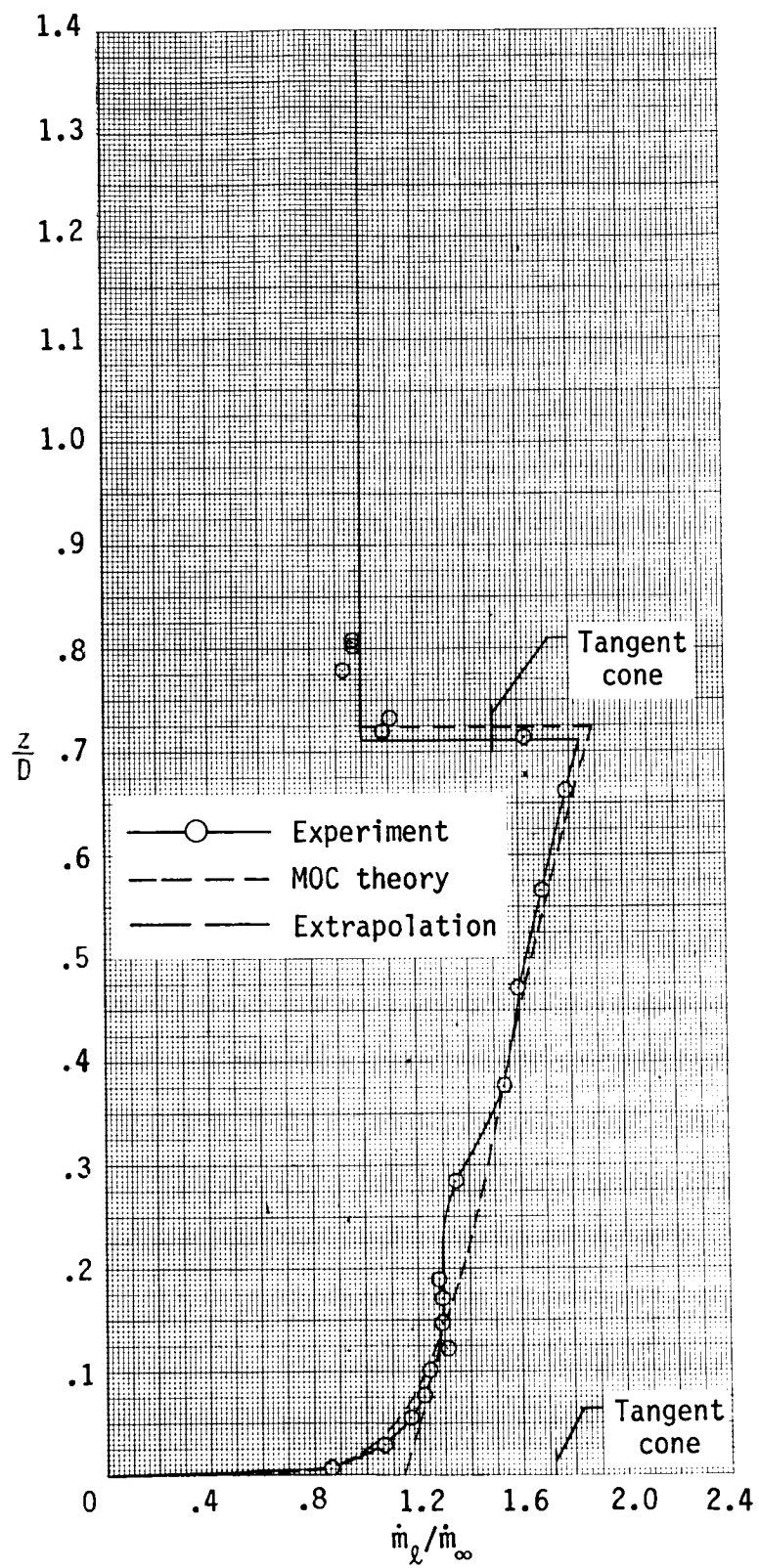
(c) $y/D = 0.236$.

Figure C20.- Continued.



(d) $y/D = 0.354$.

Figure C20.- Continued.



(e) $y/D = 0.472$.

Figure C20.- Concluded.

REFERENCES

1. Dillon, J. L.; Marcum, D. C., Jr.; Johnston, P. J.; and Hunt, J. L.: Aerodynamic and Inlet Flow Characteristics of Several Hypersonic Airbreathing Missile Concepts. AIAA-80-0255, Jan. 1980.
2. Hunt, James L.; Johnston, Patrick J.; Cabbage, James M.; Marcum, Don C.; and Carlson, Charles H.: A Mach 6, Airbreathing Surface-to-Air Missile (HYSAM). 1980 JANNAF Propulsion Meeting - Volume II, Karen L. Strange, ed., CPIA Publ. 315 (Contract N00024-78-C-5384), Appl. Phys. Lab., Johns Hopkins Univ., Mar. 1980, pp. 321-385.
3. Hunt, J. L.; Johnston, P. J.; Cabbage, J. M.; Dillon, J. L.; Richie, C. B.; Marcum, D. C., Jr.; and Carlson, C. H.: Hypersonic Airbreathing Missile Concepts Under Study at NASA Langley Research Center. AIAA-82-0316, Jan. 1982.
4. Henry, John R.; and Anderson, Griffin Y.: Design Considerations for the Airframe-Integrated Scramjet. NASA TM X-2895, 1973.
5. Pinckney, S. Z.: A Short Static-Pressure Probe Design for Supersonic Flow. NASA TN D-7978, 1975.
6. Sims, Joseph L.: Tables for Supersonic Flow Around Right Circular Cones at Zero Angle of Attack. NASA SP-3004, 1964.
7. Dennard, John S.; and Spencer, Patricia B.: Ideal-Gas Tables for Oblique-Shock Flow Parameters in Air at Mach Numbers From 1.05 to 12.0. NASA TN D-2221, 1964.
8. Chu, C. W.; and Powers, S. A.: The Calculation of Three-Dimensional Supersonic Flows Around Spherically-Capped Smooth Bodies and Wings. Volumes I and II. AFFDL-TR-72-91, Vols. I and II, U.S. Air Force, Sept. 1972.
9. Fischer, Michael C.; and Maddalon, Dal V.: Experimental Laminar, Transitional, and Turbulent Boundary-Layer Profiles on a Wedge at Local Mach Number 6.5 and Comparisons With Theory. NASA TN D-6462, 1971.
10. Lawing, Pierce L.; and Johnson, Charles B.: Inlet Boundary-Layer Shapes on Four Aircraft Forebodies at Mach 6. J. Aircr., vol. 15, no. 1, Jan. 1978, pp. 62-63.
11. Johnson, Charles B.; and Lawing, Pierce L.: Mach 6 Flowfield Survey at the Engine Inlet of a Research Airplane. J. Aircr., vol. 14, no. 4, Apr. 1977, pp. 412-414.
12. Persh, Jerome; and Lee, Roland: Tabulation of Compressible Turbulent Boundary Layer Parameters. NAVORD Rep. 4282, U.S. Navy, May 1, 1956.
13. Shapiro, Ascher H.: The Dynamics and Thermodynamics of Compressible Fluid Flow. Volume II. Ronald Press Co., c.1954.

14. Dougherty, N. S., Jr.; and Fisher, D. F.: Boundary-Layer Transition on a 10-Deg Cone: Wind Tunnel/Flight Correlation. AIAA-80-0154, Jan. 1980.
15. Stallings, Robert L., Jr.; and Lamb, Milton: Effects of Roughness Size on the Position of Boundary-Layer Transition and on the Aerodynamic Characteristics of a 55° Swept Delta Wing at Supersonic Speeds. NASA TP-1027, 1977.
16. Ashby, George C., Jr.; and Harris, Julius E.: Boundary-Layer Transition and Displacement-Thickness Effects on Zero-Lift Drag of a Series of Power-Law Bodies at Mach 6. NASA TN D-7723, 1974.
17. Beckwith, Ivan E.; Creel, Theodore R., Jr.; Chen, Fang-Jenq; and Kendall, James M.: Free Stream Noise and Transition Measurements in a Mach 3.5 Pilot Quiet Tunnel. AIAA-83-0042, Jan. 1983.
18. Morrisette, E. Leon; Stone, David R.; and Whitehead, Allen H., Jr.: Boundary-Layer Tripping With Emphasis on Hypersonic Flows. Viscous Drag Reduction, C. Sinclair Wells, ed., Plenum Press, 1969, pp. 33-51.
19. Huffman, G. David: Theory, Performance and Design of Flow Direction and Mach Number Probes. AFATL-TR-81-44, U.S. Air Force, Apr. 1981. (Available from DTIC as AD B063 871L.)
20. Behrens, Wilhelm: Viscous Interaction Effects on a Static Pressure Probe at $M = 6$. AIAA J., vol. 1, no. 12, Dec. 1963, pp. 2864-2866.
21. Wagner, Richard D., Jr.; and Watson, Ralph: Reynolds Number Effects on the Induced Pressures of Cylindrical Bodies With Different Nose Shapes and Nose Drag Coefficients in Helium at a Mach Number of 24. NASA TR R-182, 1963.
22. Ames Research Staff: Equations, Tables, and Charts for Compressible Flow. NACA Rep. 1135, 1953. (Supersedes NACA TN 1428.)
23. Anderson, John D., Jr.: Fundamentals of Aerodynamics. McGraw-Hill Book Co., c.1984.

1. Report No. NASA TP-2491		2. Government Accession No.		3. Recipient's Catalog No.	
4. Title and Subtitle Mach 6 Flow Field Surveys Beneath the Forebody of an Airbreathing Missile				5. Report Date March 1986	
				6. Performing Organization Code 505-43-23-03	
7. Author(s) Patrick J. Johnston and James L. Hunt				8. Performing Organization Report No. L-15973	
				10. Work Unit No.	
9. Performing Organization Name and Address NASA Langley Research Center Hampton, VA 23665-5225				11. Contract or Grant No.	
				13. Type of Report and Period Covered Technical Paper	
12. Sponsoring Agency Name and Address National Aeronautics and Space Administration Washington, DC 20546-0001				14. Sponsoring Agency Code	
15. Supplementary Notes					
16. Abstract Wall static, local stream static, and pitot pressure surveys were made on the windward side of a hypersonic airbreathing missile at full-scale length Reynolds numbers. In the inviscid part of the flow field, the experimental mass flow ratios agreed with trends predicted by a three-dimensional method-of-characteristics solution. At a longitudinal station 3.5 diameters downstream of the nose, the boundary layer was transitional or turbulent at zero incidence but became laminar as the angle of attack increased. The bell-shaped distribution of the boundary layer across the width of the body affected the mass flow distribution out to the bow shock and decreased the mass flow available to the engine inlet.					
17. Key Words (Suggested by Authors(s)) Airbreathing missile Flow field survey Boundary layer Hypersonic				18. Distribution Statement Unclassified - Unlimited	
				Subject Category 02	
19. Security Classif.(of this report) Unclassified		20. Security Classif.(of this page) Unclassified		21. No. of Pages 153	
				22. Price A08	

National Aeronautics and
Space Administration
Code NIT-4

Washington, D.C.
20546-0001

Official Business
Penalty for Private Use, \$300

BULK RATE
POSTAGE & FEES PAID
NASA
Permit No. G-27

NASA

POSTMASTER:

**If Undeliverable (Section 158
Postal Manual) Do Not Return**